

**NONADIABATIC COLLISIONS OF PROTON WITH CO
AND O₂ MOLECULES : A QUANTUM MECHANICAL
STUDY**

A THESIS

submitted by

F GEORGE DENSINGH XAVIER

for the award of the degree

of

DOCTOR OF PHILOSOPHY



DEPARTMENT OF CHEMISTRY

INDIAN INSTITUTE OF TECHNOLOGY MADRAS

CHENNAI 600 036 INDIA

MAY 2010

THESIS CERTIFICATE

This is to certify that the thesis titled **NONADIABATIC COLLISIONS OF PROTON WITH CO AND O₂ MOLECULES : A QUANTUM MECHANICAL STUDY**, submitted by **F GEORGE DENSINGH XAVIER**, to the **Indian Institute of Technology, Madras, Chennai**, for the award of the degree of **Doctor of Philosophy**, is a bona fide record of the research work done by him under our supervision. The contents of this thesis, in full or in parts, have not been submitted to any other Institute or University for the award of any degree or diploma.

IIT Madras, Chennai 600036.

Date:

Research Guide

Dr. Sanjay Kumar

ACKNOWLEDGEMENTS

I am happy to share a word of appreciation through this thesis that my research supervisor **Prof. Sanjay Kumar** constantly pour on me the spirit of research in a truly systematic way to develop and nurture the habit of scientific enquiry and learning. In this section I take immense pleasure in remembering his contribution towards the goal of achieving my Ph.D degree.

I greatly remember, at this point of time, **Prof. M. S. Gopinathan**, former HOD of Chemistry, in moulding my scientific career through his innovative teaching methodology during course work and instilling in me a strong commitment towards hard work. Without his involvement this Ph.D would have been a dream to me forever.

I thank the present HOD **Prof. R. Dhamodharan** and former HODs **Late Prof. G. Sundararajan** and **Prof. M. N. S. Rao** in enabling me in completing official formalities required for the Ph.D degree. I thank **Prof. Mangala Sunder Krishnan** for offering us a course on chemical kinetics and dynamics which was useful to all of us. I also express my gratitudes to teachings who taught me the principles of physical, inorganic, organic chemistry.

I greatly appreciate the guidance and suggestions given by my docotral committee members namely, **Prof. N. Chandrakumar** and **Prof. A. K. Mishra** of Chemistry department and **Prof. C. Vijayan** and **Prof. Prem. B. Bisht** of Physics department during periodic evaluation of my work.

At the International level, I sincerely acknowledge the help I got during my first seminar preparation, from the following people : **Prof. Richar N Zare (Stanford University), Prof. George C Schatz (NorthWestern University), Prof. Stuart C Althorpe (Cambridge University), Prof. Daiqian Xie (Nanjing University) Prof. David E Manolopoulos (Oxford University)** and many more.

I thank people from the computer center, especially, **Mr. Ravichandran, Mr. Sourirajan, Mr. Ananthkumar** etc. for their help in using high performance computing systems which are intergral part of my research life.

I thank **Dr. R. B. C. Pillai**, Department of Chemistry for his useful suggestions during my lab teaching assignments. I also thank **Mr. RamKumar, Mr. Narayanan, Mr. Bhoopathy, Mr. Esakimuthu** and others for their help during my lab teaching assignments.

I am grateful to **Dr. Susithra Selvam** in helping me out in my initial days in successfully completing the course work of **Prof. A. K. Mishra** and also in writing my synopsis report and other matters. I thank my senior labmates **Dr. Amar Kumar Dora, Dr. T. J. Dhilipkumar and Dr. Saieswari Amaran** and junior lab mate **V. C. saheer** for their encouragement and continued support in my early days of reseach and also thank other fellow mates working theoretical chemistry, namely, **Mr. Atul Kumar Srivastava, Mr. Manoj Kumar Pandey, Mr. Akbar Ali, Mr. Vinayak** for their continued support and cooperation throughtout. I thank research scholars working in other areas of research especially **Mr. Hariharan, Dr. Jeyakumar, Mr. Velkannan** and many more scholars for their support and goodwill.

Many other may have helped me in various ways in my day to day life during my entire stay in IITM. My apology to them is always extended to them if they find their names

missing in this section.

Finally, I rememeber the contribution made by my parents, brothers and sister in achieving what I am today. I dedicate this piece of research work to them.

I greatfully acknowledge the financial support given by both IITM and CSIR during my stay at IITM, without which this research work is impossible.

F. George Densingh Xavier

ABSTRACT

KEYWORDS: *ab initio* potential energy surfaces, inelastic vibrational excitations, vibrational charge transfer, nonadiabatic coupling matrix elements, differential cross section

Nonadiabatic phenomena are ubiquitous in nature. The dynamics of proton-molecule collisions often evolve on highly coupled electronic potential energy surfaces leading to inelastic and charge transfer processes. In this thesis, we have investigated the quantum dynamics of energy transfer processes involving the inelastic vibrational excitations and the vibrational charge transfer collisions in the $\text{H}^+ + \text{CO}$ and the $\text{H}^+ + \text{O}_2$ systems on our newly obtained quasi-diabatic *ab initio* potential energy surfaces for collision energies 0-30 eV and compared the collision attributes with the earlier theoretical results as well as the available state-to-state experimental data obtained from the molecular beam study and H^+/H energy-loss spectra.

We have described the computational details of the *ab initio* potential energy surfaces at the configuration interaction level of accuracy employing the correlation consistent polarized valence triple zeta basis sets.

We report the details of time-independent quantum dynamics calculations for the inelastic vibrational excitations and vibrational charge transfer processes under the framework of vibrational close-coupling rotational infinite order sudden approximation.

To the best of our knowledge the present *ab initio* global adiabatic and quasi-diabatic potential energy surfaces for the ground and the first excited electronic states for the $\text{H}^+ + \text{CO}$ system are being presented perhaps for the first time in the literature. The present theoretical results are found to be in good agreement with those of experiments for the inelastic vibrational excitations and they are in overall qualitative agreement for charge transfer channel in the experimental trend. It is suggested that quantitative agreement between theory and experiment can be achieved by modelling the dynamics as a three- and four-state process. For the $\text{H}^+ + \text{O}_2$ system, quantum dynamics with the two-state (the ground and the first excited electronic states) coupling yields results in general agreement with the experiments. Significant improvement is achieved when the dynamics is carried out with four-state (the ground and the lowest three excited electronic states) coupling. However, some quantitative agreement between theory and experiment is still lacking, which can be settled through an elaborate and more refined (over a fine mesh of molecular orientation) computations within the VCC-RIOSAs framework.

A summary of the present study is given at the end with the concluding remarks and the future direction of research followed by bibliography.

TABLE OF CONTENTS

ACKNOWLEDGEMENTS	i
ABSTRACT	iv
LIST OF TABLES	xii
LIST OF FIGURES	xxii
ABBREVIATIONS	xxiii
NOTATION	xxv
1 INTRODUCTION	1
1.1 Review on experimental studies	3
1.2 Review on theoretical studies	5
1.3 Scope of the thesis	11
2 BORN-OPPENHEIMER APPROXIMATION AND QUASIDIABATIZATION PROCEDURE	17
2.1 The breakdown of Born-Oppenheimer approximation	17
2.2 Diabatization procedures	24
3 THE TIME INDEPENDENT QUANTUM DYNAMICS STUDY - THE VCC- RIOSA SCHEME	31
3.1 The full close-coupling method	31
3.2 The infinite-order sudden approximation(IOSA)	37
3.3 Application of VCC-RIOSA in ion(atom)-molecule collisions	42
4 NONADIABATIC DYNAMICS ON THE TWO COUPLED ELECTRONIC PESs : THE H⁺ + CO SYSTEM	44
4.1 Present focus	44

4.2	<i>Ab initio</i> adiabatic PESs	45
4.3	Asymptotic interaction potential	60
4.4	<i>Ab initio</i> quasi-diabatic PESs	61
4.5	Vibrational coupling matrix elements ($V_{vv'}/v''(R; \gamma)$)	71
4.6	Quantum dynamics within the VCC-RIOSAs approach	76
4.6.1	Dynamics at $E_{cm}=9.5$ eV	78
4.6.1.1	The orientation opacities	78
4.6.1.2	Rotationally-summed total differential cross section	80
4.6.1.3	Rotationally-summed state-selective differential cross section (DCS)	83
4.6.1.4	Transition Probability	84
4.6.1.5	Average vibrational energy transfer	86
4.6.1.6	Integral cross section	88
4.6.2	Dynamics at $E_{cm}=28.96$ eV	89
4.6.2.1	The orientation opacities	89
4.6.2.2	Rotationally-summed total differential cross section	91
4.6.2.3	Rotationally-summed state-selected differential cross section (DCS)	93
4.6.2.4	Transition probability	95
4.6.2.5	Average vibrational energy transfer	97
4.6.2.6	Integral cross section	98
4.6.3	Dynamics : A comparison between 9.5eV and 28.96eV	99
4.6.3.1	Rotationally-summed state-selective differential cross section (DCS)	100
4.6.3.2	Transition probability	102
4.6.3.3	Average vibrational energy transfer	103
4.6.3.4	Integral cross section	105
4.7	Summary	106
5	NONADIABATIC DYNAMICS ON THE TWO COUPLED ELECTRONIC PESs : THE H⁺ + O₂ SYSTEM	109
5.1	Present focus	109
5.2	<i>Ab initio</i> PECs	111

5.3	<i>Ab initio</i> PESs	120
5.4	Coupling PESs and NACME	127
5.5	Asymptotic interaction potential	130
5.6	Vibrational coupling matrix elements ($V_{vv'}/v''(R; \gamma)$)	131
5.7	Quantum Dynamics	134
5.7.1	Dynamics at $E_{cm}=9.5$ eV	135
5.7.1.1	The orientation opacities	135
5.7.1.2	Rotationally-summed state-selective differential cross section (DCS)	138
5.7.1.3	Transition Probability	140
5.7.1.4	Average vibrational energy transfer	142
5.7.1.5	Integral cross section	143
5.7.2	Dynamics at $E_{cm}=23$ eV	145
5.7.2.1	The orientation opacities	145
5.7.2.2	Rotationally-summed state-selective differential cross section (DCS)	148
5.7.2.3	Transition Probability	152
5.7.2.4	Average vibrational energy transfer	156
5.7.2.5	Integral cross section	158
5.8	Summary	160
6	NONADIABATIC DYNAMICS ON THE FOUR COUPLED ELECTRONIC PESs : THE $H^+ + O_2$ SYSTEM	162
6.1	Present focus	162
6.2	<i>Ab initio</i> PECs	163
6.3	<i>Ab initio</i> PESs	168
6.4	Coupling PESs and NACME	172
6.5	Vibrational coupling matrix elements ($V_{vv''}/v'''(R; \gamma)$)	176
6.6	Quantum dynamics	178
6.6.1	Dynamics at $E_{cm}=9.5$ eV	179
6.6.1.1	The orientation opacities	179
6.6.1.2	Rotationally-summed state-selective differential cross section (DCS)	182

6.6.1.3	Transition Probability	185
6.6.1.4	Average vibrational energy transfer	187
6.6.1.5	Integral cross section	188
6.6.2	Dynamics at $E_{cm}=23$ eV	190
6.6.2.1	The orientation opacities	190
6.6.2.2	Rotationally-summed state-selective differential cross section (DCS)	193
6.6.2.3	Transition Probability	196
6.6.2.4	Average vibrational energy transfer	201
6.6.2.5	Integral cross section	203
6.6.3	Dynamics : A comparison between 9.5eV and 23eV	204
6.6.3.1	The orientation opacities	205
6.6.3.2	Rotationally-summed state-selective differential cross section(DCS)	206
6.6.3.3	Transition Probability	207
6.6.3.4	Average vibrational energy transfer	209
6.6.3.5	Integral cross section	210
6.7	Summary	211
7	SUMMARY AND CONCLUSIONS	215
7.1	Concluding Remarks	215
7.2	Future direction of research	219
A	VALIDITY OF VCC-RIOSSA IN THE PRESENT CALCULATIONS	221
A.1	Numerical test calculations on the validity of IOSA in the $H^+ + CO$ system	226

LIST OF TABLES

4.1	Comparison of computed molecular properties of CO and CO ⁺ with experiments. r_{eq} is equilibrium bond distance. D_0 is the dissociation energy in the GS. I.P is the ionization potential. $\Delta E_{rot}^{0 \rightarrow 1}$ is the energy of first rotational excitation, $j = 0 \rightarrow j = 1$ expressed in milli eV in the GS. $\Delta E_{vib}^{0 \rightarrow 1}$ is the energy of first vibrational excitation, $v = 0 \rightarrow v = 1$ in the GS. $\Delta E_{elec}^{0 \rightarrow 1}$ is the energy of first electronic excitation from $v = 0$ of the GS to $v' = 0$ of the first ES and D is the dipole moment for the GS expressed in atomic units.	48
4.2	Equilibrium geometry (collinear) data for the bound HCO ⁺ and HOC ⁺ ions. The bond distances are in Å.	49
4.3	Calculated minimum energy geometries for H ⁺ – CO. r_m is the distance between the atoms of the diatom, R_m is the distance between the center of mass of the diatom and the proton, γ is the angle between r_m and R_m , ϵ is the well depth.	49
4.4	Comparison of endoergicicy of VCT process relative to IVE process with experimental as well as theoretical data	51
4.5	The local energy minima of the adiabtic GS PES and the well depth at each local minima relative to the asymptotic products is listed out as a function of Jacobi coordinates (R, r, γ)	59
4.6	Values of coefficients (a.u) used in Eq. (4.4) for the prediction of μ , Q , α_0 and α_2 as a function of r	61
4.7	VCC-RIOSAs state-to-state integral cross section (absolute values) for the IVE channel, H ⁺ + CO($v = 0$) \longrightarrow H ⁺ + CO(v') and the VCT channel, H ⁺ + CO($v = 0$) \longrightarrow H(² S) + CO ⁺ (v'') at the $E_{cm} = 9.5$ eV.	88
4.8	VCC-RIOSAs state-to-state integral cross section (absolute values) for the IVE channel, H ⁺ + CO($v = 0$) \longrightarrow H ⁺ + CO(v') and the VCT channel, H ⁺ + CO($v = 0$) \longrightarrow H(² S) + CO ⁺ (v'') at the $E_{cm} = 28.96$ eV.	98
4.9	VCC-RIOSAs state-to-state integral cross section (absolute values) for the IVE channel, H ⁺ + CO($v = 0$) \longrightarrow H ⁺ + CO(v') and the VCT channel, H ⁺ + CO($v = 0$) \longrightarrow H(² S) + CO ⁺ (v'') at the $E_{cm} = 28.96$ eV and $E_{cm} = 9.5$ eV.	105
5.1	The symmetrywise arrangement of orbitals in eV at the SCF level at the reference geometry $R_{ref} = 16a_0$ of the H ⁺ + O ₂ system. The occupational pattern of electrons is given in parenthesis.	113
5.2	Comparison of electronic energies for three molecular orientations at different levels of methodologies at r_e	115

5.3	The computed molecular properties of O_2 and O_2^+ are compared with the experimental values. r_{eq} is the equilibrium bond length, E_{eq} is the electronic energy at equilibrium bond length, D_o is the dissociation energy, P.A is the proton affinity relative to asymptote $H^+ + O_2(X^3\Sigma_g^-)$, I.P is the ionization potential, $\Delta E_{rot}^{0\rightarrow 1}$ is the energy of first rotational excitation, $\Delta E_{vib}^{0\rightarrow 1}$ is the energy of first vibrational excitation and ΔE_{elec} is the energy of first electronic excitation, $O_2(1\Delta_g \leftarrow 3\Sigma_g^-)$, $O_2^+(4\Pi_u \rightarrow 2\Pi_g)$, $O_2^+(2\Pi_u \rightarrow 4\Pi_u)$ and $O_2^+(4\Sigma_g^- \rightarrow 4\Pi_u)$. All properties are computed using MRCI level of accuracy and <i>cc-pVTZ</i> basis set.	116
5.4	The calculated energy difference ΔE between the first H/O_2^+ channel and the H^+/O_2 channel at r_{eq} and at $R = 15a_o$ for various γ values.	120
5.5	The computed well depth (eV) present in first ES PEC at $r_{eq} = 2.293a_o$ at different γ for off-collinear geometries. The earlier reported computed values is about roughly 1 eV (Staemmler and Gianturco, 1985). R (bohr) is the location at which shallow well exists.	120
5.6	The number of <i>ab initio</i> points per electronic state for all γ values and the grand total computed using <i>cc-pVTZ</i> basis set and MRCI level of accuracy for the $H + O_2$ system.	122
5.7	The local energy minima of the adiabatic GS PES and the well depth at each local minima relative to the asymptotic products is listed out as a function of Jacobi coordinates (R, r, γ)	126
5.8	Computed equilibrium geometry parameters in the valence coordinates of the $[HO_2]^+$ ion in the GS ($1^3A''$).	126
5.9	Values of coefficients (in a.u) used in Eq. (5.2) for the generation of Q, α_0 and α_2 as a function of r of O_2	131
5.10	Measured relative transition probabilities (Noll and Toennies, 1986) for vibrational excitation of O_2 by proton impact at $E_{lab} = 23.7$ eV for various scattering angles compared with our computed values for the inelastic channel, $H^+ + O_2(v = 0) \rightarrow H^+ + O_2(v')$ upto $v' = 5$ levels.	154
5.11	The computed vibrational transition probabilities for the charge transfer process $H^+ + O_2(v = 0) \rightarrow H(^2S) + O_2^+(v'')$ at $E_{cm} = 23$ eV compared with the experimental values (Noll and Toennies, 1986) for the scattering angle $\theta_{cm} = 0^\circ - 11^\circ$	155
5.12	The VCC-RIOSAs absolute state-to-state integral cross section (σ) for the IVE channel, $H^+ + O_2(v = 0) \rightarrow H^+ + O_2(v')$ and the VCT channel, $H^+ + O_2(v = 0) \rightarrow H(^2S) + O_2^+(v'')$ at $E_{cm} = 9.5$ eV and $E_{cm} = 23$ eV.	159
6.1	The computed vibrational energy level spacing $\Delta E_{vib}^{v+1\rightarrow v}$ (eV) of $O_2(3\Sigma_g^-)$, $O_2^+(2\Pi_g)$, $O_2^+(4\Pi_u)$ and $O_2^+(4\Sigma_g^-)$ from their corresponding PECs for first 20 states and $\Delta E_{vib}^{1\rightarrow 0}$ transition have been given in bold	165

6.2	The computed well depth and its location in terms of R coordinate for first VCT, $H^+ + O_2(X^3\Sigma_g^-, v = 0) \longrightarrow H(^2S) + O_2^+(X^2\Pi_g, v'')$, second VCT, $H^+ + O_2(X^3\Sigma_g^-, v = 0) \longrightarrow H(^2S) + O_2^+(X^4\Pi_u, v''')$ and third VCT, $H^+ + O_2(X^3\Sigma_g^-, v = 0) \longrightarrow H(^2S) + O_2^+(X^4\Sigma_g^-, v''')$ process given at $r = r_{eq} = 2.293a_0$ as a function of γ with the data under titles $O_2^+(^2\Pi_g)$, $O_2^+(^4\Pi_u)$ and $O_2^+(^4\Sigma_g^-)$ denoting the well depth in eV. The maximum well depth, its location and the mean well depth for each process is indicated in bold font.	168
6.3	Measured relative transition probabilities (Noll and Toennies, 1986) for vibrational excitation of O_2 by proton impact at $E_{lab} = 23.7$ eV for various scattering angles compared with our computed values for the inelastic channel, $H^+ + O_2(v = 0) \longrightarrow H^+ + O_2(v')$ upto $v' = 5$ levels.	199
6.4	The computed vibrational transition probabilities for the charge transfer process $H^+ + O_2(v = 0) \longrightarrow H(^2S) + O_2^+(v'')$ at $E_{cm} = 23$ eV compared with the experimental values (Noll and Toennies, 1986) for the scattering angle $\theta_{cm} = 0^\circ - 11^\circ$	200
6.5	The VCC-RIOSAs absolute state-to-state integral cross section (σ) for the IVE channel, $H^+ + O_2(v = 0) \longrightarrow H^+ + O_2(v')$ and the VCT channel, $H^+ + O_2(v = 0) \longrightarrow H(^2S) + O_2^+(v'')$ at $E_{cm} = 9.5$ eV and $E_{cm} = 23$ eV for different vibrational states of $O_2(v')$ and $O_2^+(v'')$	211

LIST OF FIGURES

1.1	Comparison of PECs (left) as a function of R for $\gamma = 45^\circ$ at r_{eq} computed by Grimbert <i>et al.</i> (1988), Schneider <i>et al.</i> (1988) and Saieswari and Kumar (2009) and as a function of R for $\gamma = 0^\circ, 45^\circ$ and 90° (right) computed by Grimbert <i>et al.</i> (1988) and Saieswari and Kumar (2009)	14
3.1	Jacobi coordinates	32
4.1	The adiabatic GS and first ES PECs for $\gamma = 0^\circ, 90^\circ$ and 180° as a function of R for $r = r_{eq} = 2.13a_0$	50
4.2	The adiabatic GS and first ES PECs for $\gamma = 0^\circ, 90^\circ$ and 180° as a function of r at R fixed at $3a_0$ and $5a_0$. The energy is in atomic units and r is in the units of bohr	53
4.3	Comparison between our adiabatic GS and first ES PECs for $\gamma = 0^\circ, 90^\circ$ and 180° as a function of R at $r = r_{eq} = 2.13a_0$. The available PECs of Kimura <i>et al.</i> (2000) have also been reproduced.	54
4.4	The adiabatic PESs as a function R and r for $\gamma = 0^\circ, 90^\circ$ and 180° for the GS and the first ES PESs. The distances are in bohr and energy in atomic units (hartrees)	55
4.5	Contour diagrams of the GS (left) and ES (right) PESs of the $H^+ + CO$ system as a function of R and r for $\gamma = 0^\circ, 90^\circ, 180^\circ$	56
4.6	The adiabatic GS and ES PES as a function R and γ for fixed $r = r_{eq} = 2.13a_0$. The R is in bohr and γ is in degrees and energy in atomic units (hartrees)	57
4.7	Contour diagrams of the GS (left) and ES (right) PES of HCO^+ system as a function of R and γ for fixed $r = r_{eq} = 2.13a_0$	58
4.8	The splined minimum energy pathway of adiabatic GS showing minimum and maximum during the interconversion process, $HOC^+ \rightleftharpoons HCO^+$	58
4.9	The first-order NACME as a function R for a fixed $r = r_{eq} = 2.13a_0$ for $\gamma = 0^\circ, 90^\circ$ and 180° orientations between GS and first ES PESs and compared with Kimura <i>et al.</i> (2000). The R are in bohr units and first order NACME $\langle \phi_1^a \frac{d}{dR} \phi_2^a \rangle$ in a.u.	65
4.10	First-order NACME between the GS and the first ES PESs as a function R and r for $\gamma = 0^\circ, 90^\circ$ and 180° orientations. The R and r are in bohr units and the NACME values are in a.u.	66

4.11	The mixing angle as a function R and r for $\gamma = 0^\circ, 90^\circ$ and 180° orientations between GS and first ES PESs. The R and r are in bohr units and mixing angle in degrees	67
4.12	The quasidiabatic PECs as a function R (distance of H^+ from the cm of CO) at $r_{eq} = 2.13a_0$ for $\gamma = 0^\circ, 90^\circ$ and 180° orientations for GS and first ES superposed with the corresponding adiabatic PECs for comparison . .	68
4.13	The diabatic PESs as a function R and r for $\gamma = 0^\circ, 90^\circ$ and 180° orientations for GS and first ES PESs. The lengths are in bohr and energy in atomic units (hartrees).	69
4.14	The coupling potential as a function R and r for $\gamma = 0^\circ, 90^\circ$ and 180° orientations between GS and first ES PESs. The R and r are in bohr units and coupling potential V_{12}^d in a.u.	70
4.15	Vibrational coupling matrix elements ($V_{vv'}$) for the IVE channel, $H^+ + CO(v = 0) \longrightarrow H^+ + CO(v')$, as a function of R for $\gamma = 0^\circ, 90^\circ, 180^\circ$. Elastic channel V_{00} (left panel) and Inelastic channel $V_{0v'}$ (right panel). See the text	72
4.16	Vibrational coupling matrix elements ($V_{vv''}$) for the VCT channel, $H^+ + CO(v = 0) \longrightarrow H(^2S) + CO^+(v'')$, as a function of R for $\gamma = 0^\circ, 90^\circ, 180^\circ$. VCT channel V_{00} (left panel) and VCT channel $V_{0v''}$ (right panel)	74
4.17	Vibrational coupling matrix elements ($V_{v'v''}$) in the vibrational manifold of charge transfer channel, $H^+ + CO(v') \rightleftharpoons H(^2S) + CO^+(v'')$, as a function of R for $\gamma = 0^\circ, 90^\circ, 180^\circ$. The reversible arrow denotes that process can occur in both directions	75
4.18	Opacity function (Eq. (3.34)) as a function of partial wave, l (in the units of \hbar) for three excitations, $v = 0 \rightarrow v' = 0, v = 0 \rightarrow v' = 1, v = 0 \rightarrow v' = 2$ for the IVE channel, $H^+ + CO(v = 0) \longrightarrow H^+ + CO(v')$ (left panel) and for three excitations, $v = 0 \rightarrow v'' = 0, v = 0 \rightarrow v'' = 1, v = 0 \rightarrow v'' = 2$ for the VCT channel, $H^+ + CO(v = 0) \longrightarrow H(^2S) + CO^+(v'')$ (right panel) at the collision energy of $E_{cm} = 9.5$ eV	79
4.19	The computed TDCS for IVE and VCT channels at $E_{cm} = 9.5$ eV as a function of scattering angle θ_{cm} (deg). The numbers in the ordinate are the powers of 10. There is no experimental data available to compare with at this collision energy	82
4.20	The computed state-selective rotationally summed DCS for IVE and VCT channels at $E_{cm} = 9.5$ eV as a function of scattering angle θ_{cm} (deg) for the first six states and the numbers in the ordinate are the powers of 10. There is no experimental data available to compare with at this collision energy .	84
4.21	State-selective transition probability for IVE (left) for the first three states $v' = 0, v' = 1, v' = 2$ and VCT (right) for the first three states $v'' = 0, v'' = 1, v'' = 2$ as a function of scattering angle θ_{cm} at the collision energy $E_{cm} = 9.5$ eV. The transition probability for IVE is compared with experimental data (Gianturco, Gierz, and Toennies, 1981). See the text. .	85

- 4.22 The computed average vibrational energy transfer $\overline{\Delta E}_{vib}$ (eV) for the IVE (left) and the VCT (right) as a function of scattering angle θ_{cm} at the collision energy $E_{cm} = 9.5$ eV. The theoretical values gives excellent agreement with the experiments (Gianturco, Gierz, and Toennies, 1981) for the IVE channel and no experimental data are available at this collision energy for VCT channel 87
- 4.23 The computed integral cross section $\sigma(\text{\AA}^2/\text{sr})$ for the IVE and the VCT as a function of vibrational energy levels at the collision energy $E_{cm} = 9.5$ eV. The two curves run parallel to each other with a crossing at higher vibrational levels. The integral cross section for the IVE process is of higher magnitude than VCT process. Note that the numbers on the Y-axis indicate powers of 10. 88
- 4.24 Opacity function (Eq. (3.34)) as a function of partial wave, l (in the units of \hbar) for three excitations, $v = 0 \rightarrow v' = 0, v = 0 \rightarrow v' = 1, v = 0 \rightarrow v' = 2$ for the IVE channel, $\text{H}^+ + \text{CO}(v = 0) \rightarrow \text{H}^+ + \text{CO}(v')$ (left column) and for three excitations, $v = 0 \rightarrow v'' = 0, v = 0 \rightarrow v'' = 1, v = 0 \rightarrow v'' = 2$ for the VCT channel, $\text{H}^+ + \text{CO}(v = 0) \rightarrow \text{H}(^2\text{S}) + \text{CO}^+(v'')$ (right column) at the collision energy of $E_{cm} = 28.96$ eV 90
- 4.25 The computed TDCS for IVE, $\text{H}^+ + \text{CO}(v = 0) \rightarrow \text{H}^+ + \text{CO}(\Sigma v')$, and VCT, $\text{H}^+ + \text{CO}(v = 0) \rightarrow \text{H}(^2\text{S}) + \text{CO}^+(\Sigma v'')$, channels at $E_{cm} = 28.96$ eV as a function of scattering angle $\theta_{cm}(\text{deg})$. The numbers in the ordinate are the powers of 10. The experimental data (Niedner-Schatteburg and Toennies, 1992) along with error bars for few points for charge transfer process is shown for IVE(\circ) and VCT(\bullet) at this collision energy. The experimental data were normalized at $\theta_{cm} = 9.3881^\circ$ 92
- 4.26 The computed state-selective rotationally summed DCS for IVE and VCT channels at $E_{cm} = 28.96$ eV as a function of scattering angle $\theta_{cm}(\text{deg})$ for the first six states and the numbers in the ordinate are the powers of 10. The experimental data (Krutein and Linder, 1979) are available along with error bars for the IVE channel for first three states, $v = 0 \rightarrow v' = 0(\times), v = 0 \rightarrow v' = 1(\bullet), v = 0 \rightarrow v' = 2(\blacktriangle)$, and the experimental data are normalised at $\theta_{cm} = 9.3881^\circ$. There is no experimental data available for VCT channel $E_{cm} = 28.96$ eV. 94
- 4.27 The computed transition probability $P_{0v'/v''}$ for IVE and VCT channels at $E_{cm} = 28.96$ eV as a function of scattering angle $\theta_{cm}(\text{deg})$ for the first three states. The experimental data (Krutein and Linder, 1979) are available along with error bars for the IVE channel for first three excitations, $v = 0 \rightarrow v' = 0(\times), v = 0 \rightarrow v' = 1(\bullet), v = 0 \rightarrow v' = 2(\blacktriangle)$. There is no experimental data available for VCT channel and hence we show the plots in full range. 96

4.28	The computed average vibrational energy transfer $\overline{\Delta E}_{vib}$ (eV) for IVE (left) and VCT (right) as a function of scattering angle θ_{cm} at the collision energy $E_{cm} = 28.96$ eV. The theoretical values gives excellent agreement with the experimental data with error bars (Krutein and Linder, 1979) for the IVE channel and no experimental data are available at this collision energy for VCT channel	97
4.29	The computed integral cross section $\sigma(\text{\AA}^2/\text{sr})$ for IVE and VCT as a function of vibrational energy levels at the collision energy $E_{cm} = 28.96$ eV. The two curves run parallel to each other with a crossing at slightly higher vibrational levels and intially the integral cross section for IVE process is of higher magnitude than VCT process. Note that the numbers on the Y-axis indicate powers of 10.	99
4.30	A comparision between the TDCS and DCS at two different collision energies.	100
4.31	The computed transition probability $P_{0 \rightarrow v'/v''}$ for IVE channel, $\text{H}^+ + \text{CO}(v = 0) \rightarrow \text{H}^+ + \text{CO}(v')$ for the first three excitations, $v = 0 \rightarrow v' = 0, v = 0 \rightarrow v' = 1, v = 0 \rightarrow v' = 2$, and VCT channel, $\text{H}^+ + \text{CO}(v = 0) \rightarrow \text{H}(^2\text{S}) + \text{CO}^+(v'')$, for the first three excitations, $v = 0 \rightarrow v'' = 0, v = 0 \rightarrow v'' = 1, v = 0 \rightarrow v'' = 2$ at $E_{cm} = 28.96$ eV and $E_{cm} = 9.5$ eV as a function of scattering angle $\theta_{cm}(\text{deg})$	102
4.32	The computed average vibrational energy transfer $\overline{\Delta E}_{vib}$ (eV) for IVE channel, $\text{H}^+ + \text{CO}(v = 0) \rightarrow \text{H}^+ + \text{CO}(v')$ and VCT channel, $\text{H}^+ + \text{CO}(v = 0) \rightarrow \text{H}(^2\text{S}) + \text{CO}^+(v'')$, at $E_{cm} = 28.96$ eV and $E_{cm} = 9.5$ eV as a function of scattering angle $\theta_{cm}(\text{deg})$. Note the jump in $E_{cm} = 28.96$ eV.	104
4.33	The computed VCC-RIOSAs state-to-state integral cross section $\sigma(\text{\AA}^2)$ for IVE channel, $\text{H}^+ + \text{CO}(v = 0) \rightarrow \text{H}^+ + \text{CO}(v')$ and VCT channel, $\text{H}^+ + \text{CO}(v = 0) \rightarrow \text{H}(^2\text{S}) + \text{CO}^+(v'')$, at $E_{cm} = 28.96$ eV and $E_{cm} = 9.5$ eV as a function of scattering angle $\theta_{cm}(\text{deg})$. Note that ICS for the VCT channel for 28.96 eV and 9.5 eV remains the same and Y-ordinates are powers of 10	106
5.1	<i>Ab initio</i> adiabatic PECs of the GS and the first ES for $\gamma = 0^\circ$ and 90° orientations as a function of R for a fixed $r = r_{eq} = 2.293a_0$ (left panel) and as a function of r (right) for a fixed $R = 4.0a_0$ (right panel). Note the presence of crossings between the two electronic states of different symmetries in all four cases.	118
5.2	<i>Ab initio</i> adiabatic (solid) and diabatic (dashed) PECs of the GS and the first ES for $\gamma = 15^\circ, 45^\circ, 75^\circ$ as a function of R for a fixed $r = r_{eq} = 2.293a_0$ (left panel) and as a function of r for a fixed $R = 4.0a_0$ (right panel). Note the presence of avoided crossings in the adiabatic curves and crossings in the quasi-diabatic curves in both the right and the left panels and the asymptotic relationships at large R . A small shallow well is present in the upper adiabatic curves and is slightly seen for $\gamma = 75^\circ$	119

5.3	<i>Ab initio</i> smoothed adiabatic PESs of the GS ($1^3\Sigma^-/1^3B_1$) and the first ES ($1^3\Pi/1^3A_2$) for $\gamma = 0^\circ$ and 90° orientations as a function of R and r . Note the presence of crossings between the two electronic surfaces of different symmetries.	121
5.4	<i>Ab initio</i> adiabatic (left panel) and the corresponding quasi-diabatic (right panel) as a function of R and r for $\gamma = 15^\circ, \gamma = 45^\circ$ and $\gamma = 75^\circ$. Note that there exists avoided crossings in the adiabatic PESs (left panel) which are replaced by direct surface crossings in the diabatic PESs (right panel).	123
5.5	<i>Ab initio</i> adiabatic GS and the first ES PESs as a function of γ and R at $r = r_{eq} = 2.293a_0$	125
5.6	The splined minimum energy pathway of adiabatic GS showing minimum and maximum peaks during the interconversion process, $\text{HOO}^+ \rightleftharpoons \text{OOH}^+$	127
5.7	Coupling PESs (right panel) and NACME (left panel) as a function of R and r for a fixed γ . Since there is no radial couplings for the collinear and perpendicular geometries, coupling potential and NACME are not applicable to these orientations.	128
5.8	Coupling potential and NACME as a function of γ and R at $r = r_{eq} = 2.293a_0$. The γ range begins with 15° and ends with 75° because there is no radial couplings for 0° and 90°	129
5.9	Vibrational coupling matrix elements (VCME) as a function of R for $\gamma = 15^\circ, \gamma = 45^\circ$ and $\gamma = 75^\circ$ for the IVE ($V_{0v'}$) channel $\text{H}^+ + \text{O}_2(v=0) \longrightarrow \text{H}^+ + \text{O}_2(v')$ (left panel) and the VCT ($V_{0v''}$) channel $\text{H}^+ + \text{O}_2(v=0) \longrightarrow \text{H}(^2\text{S}) + \text{O}_2^+(v'')$ (right panel).	132
5.10	The vibrational coupling matrix elements ($V_{v'v''}$) for the VCT as a function of R for $\gamma = 15^\circ, 45^\circ$ and 75° orientations for the mixed channels, $\text{H}^+ + \text{O}_2(v') \longrightarrow \text{H}(^2\text{S}) + \text{O}_2^+(v'')$	134
5.11	The opacity function as a function of partial waves (l , in the units of \hbar) for $\gamma = 0^\circ, \gamma = 45^\circ$ and $\gamma = 90^\circ$ for the IVE channel, $\text{H}^+ + \text{O}_2(v=0) \longrightarrow \text{H}^+ + \text{O}_2(v')$ (left panel) and for $\gamma = 15^\circ, \gamma = 45^\circ$ and $\gamma = 75^\circ$ for the VCT channel $\text{H}^+ + \text{O}_2(v=0) \longrightarrow \text{H}(^2\text{S}) + \text{O}_2^+(v'')$ (right panel).	137
5.12	Opacity function for all γ values for the elastic collisions for IVE channel $\text{H}^+ + \text{O}_2(v=0) \longrightarrow \text{H}^+ + \text{O}_2(v')$ (left) and for first charge transfer collisions for VCT channel $\text{H}^+ + \text{O}_2(v=0) \longrightarrow \text{H}(^2\text{S}) + \text{O}_2^+(v'')$ (right).	138
5.13	Rotationally-summed total differential cross section (TDCS) and rotationally-summed state-to-state DCS as function of θ_{cm} for the IVE channel $\text{H}^+ + \text{O}_2(v=0) \longrightarrow \text{H}^+ + \text{O}_2(v')$ (left) and for the VCT channel $\text{H}^+ + \text{O}_2(v=0) \longrightarrow \text{H}(^2\text{S}) + \text{O}_2^+(v'')$ (right) at $E_{cm} = 9.5$ eV. The number in the ordinate indicate the powers of 10. There are no experimental data available to compare with theoretical results at this collision energy.	139

5.14	The transition probability for the IVE channel $P_{0 \rightarrow v'}(\theta_{cm})$, $H^+ + O_2(v = 0) \longrightarrow H^+ + O_2(v')$, (left) and for the VCT channel $P_{0 \rightarrow v''}(\theta_{cm})$, $H^+ + O_2(v = 0) \longrightarrow H(^2S) + O_2^+(v'')$ (right) at $E_{cm} = 9.5$ eV as a function of θ_{cm} . Theory and experiments are compared only for the IVE channel (Gianturco, Gierz, and Toennies, 1981). No experimental data are available for the VCT channel.	141
5.15	Average vibrational energy transfer $\overline{\Delta E}_{vib}(\theta_{cm})$ (in eV) as a function of scattering angle θ_{cm} for the IVE (left) and the VCT (right) channels at $E_{cm} = 9.5$ eV. Theory and experiment (Gianturco, Gierz, and Toennies, 1981) are compared for the IVE channel.	143
5.16	Rotationally-summed state-to-state integral cross section (σ) for the IVE (left) and the VCT (right) processes as a function of final vibrational energy levels of O_2 and O_2^+ , respectively at $E_{cm} = 9.5$ eV. Note that the ground vibrational state of $O_2(X^3\Sigma_g^-)$ is the initial state. The numbers in the ordinate indicate powers of 10.	144
5.17	The VCC-RIOSAs absolute rotationally-summed state-to-state integral cross section (σ) for the IVE channel, $H^+ + O_2(v = 0) \longrightarrow H^+ + O_2(v')$, and the VCT channel, $H^+ + O_2(v = 0) \longrightarrow H(^2S) + O_2^+(v'')$ at the $E_{cm} = 9.5$ eV for different vibrational states of $O_2(v')$ and $O_2^+(v'')$	144
5.18	Opacity function as a function of partial waves (l , in the unit of \hbar) at $E_{cm} = 23$ eV for $\gamma = 0^\circ, \gamma = 45^\circ$ and $\gamma = 90^\circ$ for the IVE channel $H^+ + O_2(X^3\Sigma_g^-, v = 0) \longrightarrow H^+ + O_2(X^3\Sigma_g^-, v')$ (left panel), and orientations for the VCT channel $H^+ + O_2(X^3\Sigma_g^-, v = 0) \longrightarrow H(^2S) + O_2^+(X^2\Pi_g, v'')$ (right panel).	146
5.19	Opacity functions for all γ values at $E_{cm} = 23$ eV for the elastic collisions in the IVE channel $H^+ + O_2(v = 0) \longrightarrow H^+ + O_2(v' = 0)$ (left) and for first charge transfer collisions in the VCT channel $H^+ + O_2(v = 0) \longrightarrow H(^2S) + O_2^+(v'' = 0)$ (right).	147
5.20	Rotationally-summed total differential cross section (TDCS) and rotationally-summed state-to-state DCS as function of θ_{cm} for IVE channel $H^+ + O_2(v = 0) \longrightarrow H^+ + O_2(v')$ at $E_{cm} = 23$ eV along with experimental results (Noll and Toennies, 1986) and other two earlier theoretical works (Sidis, Grimbert, Sizun, and Baer, 1989; Gianturco, Palma, Semprini, Stefani, and Baer, 1990). The numbers in the ordinate denote powers of 10. See the text.	149
5.21	Rotationally-summed total differential cross section (TDCS) and rotationally-summed state-to-state DCS as function of θ_{cm} for the IVE channel $H^+ + O_2(v = 0) \longrightarrow H^+ + O_2(v')$ and the VCT channel $H^+ + O_2(v = 0) \longrightarrow H(^2S) + O_2^+(v'' = 0)$ at $E_{cm} = 23$ eV. These results have been reproduced from the earlier theoretical study (Saieswari and Kumar, 2007 <i>b</i> , 2008 <i>a</i> , 2009). The numbers in the ordinate denote powers of 10.	150

5.22	Rotationally-summed total differential cross section (TDCS) and rotationally-summed state-to-state DCS as function of θ_{cm} for the VCT channel $H^+ + O_2(v = 0) \longrightarrow H(^2S) + O_2^+(v'' = 0)$ at $E_{cm} = 23$ eV along with experimental results (Noll and Toennies, 1986) and other two earlier theoretical results (Sidis, Grimbert, Sizun, and Baer, 1989; Gianturco, Palma, Semprini, Stefani, and Baer, 1990). The numbers in the ordinate denote powers of 10. See the text.	151
5.23	The transition probability, $P_{0 \rightarrow v'}(\theta_{cm})$, for IVE (left) and VCT (right) channel compared with experiment (Noll and Toennies, 1986) along with earlier theoretical works (Staemmler and Gianturco, 1985; Gianturco, Palma, Semprini, Stefani, and Baer, 1990).	153
5.24	Average vibrational energy transfer $\overline{\Delta E_{vib}}$ (in eV) as a function of θ_{cm} at $E_{cm} = 23$ eV for the IVE (top) and the VCT (bottom) channels along with experimental data (Noll and Toennies, 1986) as well as earlier theoretical results (Gianturco, Palma, Semprini, Stefani, and Baer, 1990). Note the scaling factor ($\times 0.66$) in the data of Gianturco <i>et al.</i> . See the text.	157
5.25	Rotationally-summed integral cross section (σ) for the IVE (top left) and VCT (top right) processes as a function of vibrational energy levels of O_2 and O_2^+ respectively at $E_{cm} = 23$ eV and comparison at two collision energies (bottom row). The numbers in the ordinate indicate powers of 10.	158
6.1	<i>Ab initio</i> adiabatic PECs of GS, the first, the second and the third ESs for $\gamma = 0^\circ$ and 90° as a function of R for a fixed $r = r_{eq} = 2.293a_o$ (left panel) and as a function of r for a fixed $R = 4.0a_o$ (right panel). Note the presence of crossings between the lowest two electronic states of different symmetries.	164
6.2	<i>Ab initio</i> adiabatic (solid line) and quasi-diabatic (dashed line) PECs of GS, first ES, second ES and third ES for $\gamma = 15^\circ, 45^\circ$ and 75° orientations as a function of R (left panel) for a fixed $r = r_{eq} = 2.293a_o$ and as a function of r (right panel) for a fixed $R = 4.0a_o$. Note the presence of various crossings and avoided crossings between the PECs of symmetry $^3A''$. The presence of shallow well in the second and third ES PECs as function of R lends support to the second and third charge transfer processes. See text.	166
6.3	<i>Ab initio</i> adiabatic PESs for $\gamma = 0^\circ$ and $\gamma = 90^\circ$ as a function of r and R . The symmetry labelling differs due to the point group difference, $C_{\infty v}$ and C_{2v} , respectively. Note that there is direct surface crossing between the GS PES and first ES PES which are of different symmetry in both cases.	169
6.4	<i>Ab initio</i> adiabatic (left panel) and quasi-diabatic (right panel) PESs for $\gamma = 15^\circ, 45^\circ, 75^\circ$ as a function of r and R for four low lying electronic states of symmetries, $1^3A''$, $2^3A''$, $3^3A''$ and $4^3A''$ respectively. Note that there is a direct crossing of two low lying surfaces of same symmetry, $^3A''$	170

6.5	<i>Ab initio</i> adiabatic GS, first ES PES, second ES PES and third ES PES as a function of γ and R at $r = r_{eq} = 2.293a_0$. Note the large energy gap between the first ES and second ES PES.	171
6.6	Coupling between GS and second ES PESs (left panel) and coupling between GS and third ES PESs (right panel) as a function of R and r for $\gamma = 15^\circ, 45^\circ, 75^\circ$	173
6.7	Coupling between first ES and second ES PESs (left panel) and coupling between first ES and third ES PESs (right panel) as a function of R and r for $\gamma = 15^\circ, 45^\circ, 75^\circ$	174
6.8	Coupling between second and third ES PESs (left panel) and NACME between second and third ES PESs (right panel) as a function of R and r for $\gamma = 15^\circ, 45^\circ, 75^\circ$	175
6.9	Coupling between second and third ES PESs (left) and NACME between second and third ES PESs (right) as a function of R and γ for $r = r_{eq} = 2.293a_0$	176
6.10	The vibrational coupling matrix elements as a function of R for $\gamma = 0^\circ, \gamma = 45^\circ$ and $\gamma = 90^\circ$ orientations for the second VCT ($V_{0v''''}$) channel $H^+ + O_2(X^3\Sigma_g^-, v = 0) \longrightarrow H(^2S) + O_2^+(X^4\Pi_u, v''')$ (left panel) and the third VCT ($V_{0v''''}$) channel $H^+ + O_2(X^3\Sigma_g^-, v = 0) \longrightarrow H(^2S) + O_2^+(X^4\Sigma_g^-, v''''')$ (right panel).	177
6.11	The opacity function as a function of partial waves (l , in the units of \hbar) for $\gamma = 0^\circ, \gamma = 45^\circ$ and $\gamma = 90^\circ$ orientations for the IVE channel, $H^+ + O_2(X^3\Sigma_g^-, v = 0) \longrightarrow H^+ + O_2(X^3\Sigma_g^-, v')$ (left panel) and for $\gamma = 15^\circ, \gamma = 45^\circ$ and $\gamma = 75^\circ$ orientations for the first VCT channel, $H^+ + O_2(X^3\Sigma_g^-, v = 0) \longrightarrow H(^2S) + O_2^+(X^2\Pi_g, v'')$ (right panel) at $E_{cm} = 9.5$ eV.	180
6.12	The comparison of opacity function among all the molecular orientations for the elastic collisions for the IVE channel $H^+ + O_2(X^3\Sigma_g^-, v = 0) \longrightarrow H^+ + O_2(X^3\Sigma_g^-, v')$ (left) and for first charge transfer collisions for the first VCT channel $H^+ + O_2(X^3\Sigma_g^-, v = 0) \longrightarrow H(^2S) + O_2^+(X^2\Pi_g, v'')$ (right) at $E_{cm} = 9.5$ eV.	181
6.13	Rotationally-summed differential cross section (TDCS) and rotationally-summed state-to-state DCS as function of θ_{cm} for the IVE channel $H^+ + O_2(X^3\Sigma_g^-, v = 0) \longrightarrow H^+ + O_2(X^3\Sigma_g^-, v')$ (left) and for the first VCT channel $H^+ + O_2(X^3\Sigma_g^-, v = 0) \longrightarrow H(^2S) + O_2^+(X^2\Pi_g, v'')$ (right) at $E_{cm} = 9.5$ eV. The number in the ordinate indicate the powers of 10. There are no experimental data available to compare with theoretical results at this collision energy.	183
6.14	The transition probability for the IVE channel (left) $P_{0 \rightarrow v'}(\theta_{cm})$, $H^+ + O_2(v = 0) \longrightarrow H^+ + O_2(v')$ and for the first VCT channel (right) $P_{0 \rightarrow v''}(\theta_{cm})$, $H^+ + O_2(v = 0) \longrightarrow H(^2S) + O_2^+(v'')$ at $E_{cm} = 9.5$ eV as a function of θ_{cm} . Theory and experiments are compared in the IVE channel alone (Gianturco, Gierz, and Toennies, 1981) and no experimental data are available for VCT channel.	186

6.15	Average vibrational energy transfer $\overline{\Delta E_{vib}}(\theta_{cm})$ in eV as a function of scattering angle (θ_{cm}) for the IVE (left) and the first VCT (right) channels at $E_{cm} = 9.5$ eV. Theory and experiment (Gianturco, Gierz, and Toennies, 1981) are compared in the IVE channel	187
6.16	Integral cross section (σ) for the IVE, $H^+ + O_2(X^3\Sigma_g^-, v = 0) \longrightarrow H^+ + O_2(X^3\Sigma_g^-, v')$ (left) and VCT, $H^+ + O_2(X^3\Sigma_g^-, v = 0) \longrightarrow H^+ + O_2(X^2\Pi_g, v'')$ (right) processes as a function of vibrational energy levels of $O_2(^3\Sigma_g^-)$ and $O_2(^2\Pi_g)$ respectively at $E_{cm} = 9.5$ eV. The numbers in the ordinate indicate powers of 10.	189
6.17	The VCC-RIOS absolute state-to-state integral cross section (σ) for the IVE channel, $H^+ + O_2(X^3\Sigma_g^-, v = 0) \longrightarrow H^+ + O_2(X^3\Sigma_g^-, v')$ and the VCT channel, $H^+ + O_2(X^3\Sigma_g^-, v = 0) \longrightarrow H(^2S) + O_2^+(X^2\Pi_g, v'')$ at the $E_{cm} = 9.5$ eV for different vibrational states of $O_2(v')$ and $O_2^+(v'')$	189
6.18	The opacity function as a function of partial waves (l , in the units of \hbar) for $\gamma = 0^\circ, \gamma = 45^\circ$ and $\gamma = 90^\circ$ orientations for the IVE channel, $H^+ + O_2(X^3\Sigma_g^-, v = 0) \longrightarrow H^+ + O_2(X^3\Sigma_g^-, v')$ (left panel) and for $\gamma = 15^\circ, \gamma = 45^\circ$ and $\gamma = 75^\circ$ orientations for the VCT channel, $H^+ + O_2(X^3\Sigma_g^-, v = 0) \longrightarrow H(^2S) + O_2^+(X^2\Pi_g, v'')$ (right panel) at $E_{cm} = 23$ eV.	191
6.19	The comparison of opacity function among all the molecular orientations for the elastic collisions for IVE channel $H^+ + O_2(X^3\Sigma_g^-, v = 0) \longrightarrow H^+ + O_2(X^3\Sigma_g^-, v')$ (left) and for first charge transfer collisions for the first VCT channel $H^+ + O_2(X^3\Sigma_g^-, v = 0) \longrightarrow H(^2S) + O_2^+(X^2\Pi_g, v'')$ (right) at $E_{cm} = 23$ eV.	192
6.20	Rotationally-summed total differential cross section (TDCS) and rotationally-summed state-to-state DCS as function of θ_{cm} for IVE channel $H^+ + O_2(X^3\Sigma_g^-, v = 0) \longrightarrow H^+ + O_2(X^3\Sigma_g^-, v')$ at $E_{cm} = 23$ eV along with the experimental and other two earlier theoretical results (Sidis, Grimbert, Sizun, and Baer, 1989; Gianturco, Palma, Semprini, Stefani, and Baer, 1990). The numbers in the ordinate denote powers of 10. See the text.	194
6.21	Rotationally-summed total differential cross section (TDCS) and rotationally-summed state-to-state DCS as function of θ_{cm} for the first VCT channel $H^+ + O_2(X^3\Sigma_g^-, v = 0) \longrightarrow H(^2S) + O_2^+(X^2\Pi_g, v'')$ at $E_{cm} = 23$ eV along with experimental results and other two earlier theoretical works (Sidis, Grimbert, Sizun, and Baer, 1989; Gianturco, Palma, Semprini, Stefani, and Baer, 1990). The numbers in the ordinate denote powers of 10. See the text.	195
6.22	The transition probability, $P_{0 \rightarrow v'}(\theta_{cm})$, for IVE (left) and VCT (right) channel compared with experiment (Noll and Toennies, 1986) along with earlier theoretical works (Staemmler and Gianturco, 1985; Gianturco, Palma, Semprini, Stefani, and Baer, 1990). See the text.	197

6.23	Average vibrational energy transfer $\overline{\Delta E_{vib}}(\theta_{cm})$ (in eV) as a function of scattering angle (θ_{cm}) at $E_{cm} = 23$ eV for the IVE (top) and the first VCT (bottom) channels along with experimental data (Noll and Toennies, 1986) as well as earlier theoretical work (Gianturco, Palma, Semprini, Stefani, and Baer, 1990).	202
6.24	Integral cross section (σ) for the IVE (left) and VCT (right) processes as a function of vibrational energy levels of O_2 and O_2^+ respectively at $E_{cm} = 23$ eV. The numbers in the ordinate indicate powers of 10.	204
6.25	The VCC-RIOSAs absolute rotationally-summed state-to-state integral cross section (σ) for the IVE channel, $H^+ + O_2(X^3\Sigma_g^-, v = 0) \longrightarrow H^+ + O_2(X^3\Sigma_g^-, v')$ and the VCT channel, $H^+ + O_2(X^3\Sigma_g^-, v = 0) \longrightarrow H(^2S) + O_2^+(X^2\Pi_g, v'')$ at the $E_{cm} = 23$ eV for different vibrational states of $O_2(v')$ and $O_2^+(v'')$	204
6.26	The comparison of opacity function between $E_{cm} = 9.5$ eV and $E_{cm} = 23$ eV for the elastic collisions for IVE channel (left) $H^+ + O_2(v = 0) \longrightarrow H^+ + O_2(v')$ for $\gamma = 0^\circ, 45^\circ, 90^\circ$ and for first charge transfer collisions for VCT channel (right) $H^+ + O_2(v = 0) \longrightarrow H(^2S) + O_2^+(v'')$ for $\gamma = 15^\circ, 45^\circ, 75^\circ$	205
6.27	The comparison of state-to-state differential cross section (DCSs) and TDCS between $E_{cm} = 9.5$ eV and $E_{cm} = 23$ eV for IVE channel (left) $H^+ + O_2(v = 0) \longrightarrow H^+ + O_2(v')$ and for first VCT channel (right) $H^+ + O_2(v = 0) \longrightarrow H(^2S) + O_2^+(v'')$ as a function of scattering angle (θ_{cm}) (deg).	206
6.28	The transition probability for the IVE channel (left) $P_{0 \rightarrow v'}(\theta_{cm})$, $H^+ + O_2(v = 0) \longrightarrow H^+ + O_2(v')$ and for VCT channel (right) $P_{0 \rightarrow v''}(\theta_{cm})$, $H^+ + O_2(v = 0) \longrightarrow H(^2S) + O_2^+(v'')$ at $E_{cm} = 9.5$ eV and $E_{cm} = 23$ eV as a function of scattering angle θ_{cm}	208
6.29	Average vibrational energy transfer $\overline{\Delta E_{vib}}(\theta_{cm})$ in eV as a function of scattering angle (θ_{cm}) for inelastic vibrational channel (IVE) (right), $H^+ + O_2(X^3\Sigma_g^-, v = 0) \longrightarrow H^+ + O_2(X^3\Sigma_g^-, v')$ and vibrational charge transfer (VCT) (left), $H^+ + O_2(X^3\Sigma_g^-, v = 0) \longrightarrow H(^2S) + O_2^+(X^2\Pi_g, v'')$ channels at $E_{cm} = 9.5$ eV and $E_{cm} = 23$ eV.	209
6.30	Integral cross section (σ) for the IVE (left) and VCT (right) processes as a function of vibrational energy levels of O_2 and O_2^+ respectively at $E_{cm} = 9.5$ eV and $E_{cm} = 23$ eV. The numbers in the ordinate indicate powers of 10.	210
A.1	IOS and CS partial cross sections as a function of the total angular momentum J for the $j = 0 \rightarrow j' = 0$ and $j = 0 \rightarrow j' = 1$ rotational excitations in the $H^+ + CO$ system at 28.96 eV.	226

ABBREVIATIONS

BO	Born-Oppenheimer
CASSCF	Complete active space self-consistent field
<i>cc-pVTZ</i>	Correlation consistent polarized valence triple zeta basis
<i>aug-cc-pVQZ</i>	Augmented correlation consistent polarized valence quadrupole zeta basis
CCSD(T)	Coupled cluster single and double excitation method with perturbative estimate for connected triples
CEPA	Coupled electron pair approximation
c.m	center-of-mass
CI	Configuration interaction
CSF	Configuration state function
DCS	Differential cross section
DIM	Diatomics-in-molecules
FWHM	Full width at half maximum
HF	Hartree-Fock
ICS	Integral cross section
IOSA	Infinite order sudden approximation
IVE	Inelastic vibrational excitation
KE	Kinetic energy
MO	Molecular orbital

MCSCF	Multiconfiguration self consistent field
MRCI	Multireference internally contracted configuration interaction
MRDCI	Multireference internally contracted configuration interaction with davidson correction
NACME	Nonadiabatic coupling matrix elements
VCT	Vibrational charge transfer
PES	Potential energy surface
PEC	Potential energy curve
GS	Ground state
ES	Excited state
FCI	Full configuration interaction
QCISD(T)	Quadratic configuration interaction single and double excitation for connected triples
RIOSA	Rotational infinite order sudden approximation
SCF	Self consistent field theory
TDCS	Total differential cross section
VCC-RIOSA	Vibrational close coupling- rotational infinite order sudden approximation
VCME	Vibrational coupling matrix elements

NOTATION

α	Mixing angle
γ	Jacobi angle
\mathbf{q}	Set of electronic coordinates
\mathbf{Q}	Set of nuclear coordinates
θ_{cm}	Scattering angle in center-of-mass frame
θ_{lab}	Scattering angle in laboratory frame
E_{cm}	Collision energy in center-of-mass frame
E_{lab}	Collision energy in laboratory frame
μ	Dipole moment
μ_{ABC}	Reduced mass of the triatomic system ABC
Q	Quadrupole moment
$\alpha_{0,2}$	Polarizability components
P_i	Legendre polynomials
l	Orbital angular momentum quantum number
j	Rotational angular momentum quantum number
v	Vibrational quantum number
n	Principal quantum number
∇^2	Laplacian operator
Ψ	Total wavefunction
ψ	Nuclear wavefunction
ϕ	Adiabatic (real) electronic wavefunction
$\tilde{\phi}$	Diabatic (real) electronic wavefunction
\hat{H}_{el}	Electronic Hamiltonian
$0 \rightarrow v'$	Vibrational excitation from $v = 0$ state to v' state
ΔE	Energy difference
V_{as}	Asymptotic potential
V^{in}	Interaction potential
$V_{11,12,22}^d$	Quasi-diabatic potential matrix elements
$V_{vv'}$	Vibrational coupling matrix elements
σ^I	Opacity function
$\frac{d\sigma}{d\omega}$	Differential cross section
$P_{0 \rightarrow v'}$	Transition probability
$\langle \Delta E_{vib} \rangle$	Average vibrational energy transfer
σ	Integral cross section

CHAPTER 1

INTRODUCTION

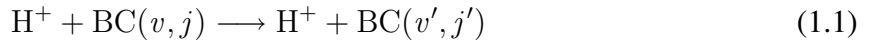
The proton is one of the simplest positive ions and its interactions with simple molecules are of fundamental importance in several areas of chemical and molecular physics and astrophysics. Being electronically structureless and positively charged it can easily deform the electronic cloud of the target molecule, thereby influencing the involvement of low-lying excited electronic state surfaces in the overall energy transfer processes.

Ion-molecule collisions occur dominantly in the interstellar spaces leading to the formation of many bound molecular ions. Bound protonated molecular ions like H_3^+ , N_2H^+ , HCO^+ , HOC^+ , HCS^+ , etc have been identified in the interstellar media (Herbst, 2001). On the other hand, the protons delivered by the solar flare enter the Earth's ionosphere with mean kinetic energy (KE) of $\sim 1\text{-}2$ KeV. These protons lose most of their KE by various inelastic processes, and finally reach the region of the stratosphere where they interact with several diatomic and polyatomic molecules in the KE range 0-100 eV (Niedner-Schatteburg and Toennies, 1992), yielding mostly elastic/inelastic and/or charge transfer processes. There have also been studies (Crutzen, Isaken, and Reid, 1975) which suggest that protons from the solar flare can deplete the stratosphere ozone by upto 15%. As a result, the proton-molecule interaction has been the subject of many experimental and theoretical studies, and a wealth of varied experimental information on inelastic vibrational (also rotational) and vibrational charge transfer excitations has become available over the years using the molecular beams and the proton energy-loss spectroscopy techniques (Udseth, Giese,

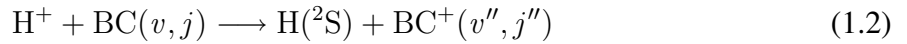
and Gentry, 1974; Hermann, Schmidt, and Linder, 1978; Krutein and Linder, 1979; Gianturco, Gierz, and Toennies, 1981; Noll and Toennies, 1986; Niedner, Noll, Toennies, and Schiler, 1987; Niedner-Schatteburg and Toennies, 1992). The focus has been on collision energies in the range 0-30 eV where extensive vibrational-rotational excitations of the target molecules occur along with possible vibrational charge transfer processes. There have been several experimental studies on proton collisions with diatomic and polyatomic targets such as H₂, N₂, O₂, CO, NO, HF, HCl, CH₄, SF₆, etc leading to an interesting finding of marked selectivity for vibrational excitations in apparently similar molecules. For example, the vibrational excitation of N₂ by H⁺ collisions is similar to that observed in CO and NO, while it is larger in H₂ and even larger in O₂, within similar collision energy range (Niedner-Schatteburg and Toennies, 1992; Hermann, Schmidt, and Linder, 1978; Krutein and Linder, 1979; Gianturco, Gierz, and Toennies, 1981). One also observes certain mode-selective vibrational excitation patterns in polyatomic molecules (Niedner-Schatteburg and Toennies, 1992). This intriguing observation can be explained mostly due to the participation of excited electronic states.

Proton-molecule interactions operate over a wide range of distances. For example, even when the proton is at a large distance from the molecule it can interact with it through the long-range tail of the interaction potential expressed in terms of charge-polarizability, charge-quadrupole, charge-dipole, etc. At shorter distances, the valence forces dominate the interactions, where it can strongly deform the electron cloud of the target molecule. As a result, the low-lying excited electronic potential energy surfaces (PESs) start interacting with the ground electronic state (GS) PES. Therefore, the dynamics of proton-molecule collisions quite often evolves on the coupled electronic PESs involving the GS and the low-lying excited electronic state (ES) PESs, thereby leading to the breakdown of the Born-Oppenheimer

(BO) approximation. The treatment of the breakdown of the BO approximation and the dynamics on coupled PESs pose quite challenging and involved tasks and is one of the contemporary theoretical problems (General Discussion, 2004). In the present study we have focussed on the following two dominant collision outcomes: the elastic/inelastic vibrational (rotational) excitations (IVE) of the diatom,



and the vibrational charge transfer (VCT) process,



where (v, j) denote the initial vibrational and rotational quantum numbers of BC and (v', j') and (v'', j'') denote the final vibrational and rotational quantum numbers of BC and BC^+ , respectively. Below, we review till date the experimental and theoretical studies carried out on the proton-diatom systems mostly for low and moderate collision energies in the range, 0-30 eV.

1.1 Review on experimental studies

Perhaps, the first experimental investigations on the proton-diatom systems were done by Udseth and coworkers (Udseth, Giese, and Gentry, 1974) at $E_{lab} = 12$ eV and $\theta_{cm} = 15^\circ$, but their energy resolution was too low to resolve the individual vibrational transitions. Early experimental studies were reported on the IVE processes in the $\text{H}^+ + \text{H}_2$ system in the late 1970's (Schmidt, Hermann, and Linder, 1976; Hermann, Schmidt, and Linder,

1978; Schmidt, Hermann, and Linder, 1978) at collision energies in the laboratory frame, $E_{lab} = 5 - 30$ eV, where they reported the state-resolved differential cross sections (DCS) and the corresponding transition probabilities for the vibrational states ($P_{0 \rightarrow v'}$) and the rotational states ($P_{0j \rightarrow v'j'}$) as a function of scattering angle (θ_{lab}). The state-resolved collisions attributes on both the IVE and the VCT processes for this system became available at $E_{lab} = 30$ eV in 1987 from the experiments of Toennies and coworkers (Niedner, Noll, Toennies, and Schiler, 1987) in the θ_{lab} range $0^\circ \leq \theta_{lab} \leq 18^\circ$. The IVE of H_2 with $v' \geq 4$ become quite effective to give rise to the VCT processes. Subsequently, Krutein and Linder (Krutein and Linder, 1979) carried out measurements for the vibrational excitations in N_2 , CO and NO at $E_{lab} = 30 - 80$ eV, and obtained vibrationally state-resolved DCSs at small θ_{lab} values (around the rainbow region) along with the corresponding $P_{0 \rightarrow v'}$ of vibrational excitation from the ground vibrational state $v = 0$ as a function of θ_{lab} . They were able to resolve the $v = 0 \rightarrow v' = 1(0 \rightarrow 1)$ and $v = 0 \rightarrow v' = 2(0 \rightarrow 2)$ excitations in CO and NO, but only $0 \rightarrow 1$ excitation in N_2 . The broadening of the proton energy-loss peaks, that is, Full Width Half maximum (FWHM) of peaks at $E_{lab} = 30$ eV and $\theta_{lab} = 5^\circ$ follows the following order : NO (155 meV) > CO (110 meV) > N_2 (100 meV) > Ne (80 meV), where the numbers in the parenthesis denote the FWHM values. This feature is due to the rotational excitations of the target molecules which remained unresolved in the experiments. It was concluded that the vibrational and rotational inelasticity increases in the order Ne < N_2 < CO < NO. The angular dependence of inelastic excitation by proton impact for $v' = 1$ at $E_{cm} = 77$ eV follows the order : NO > CO > N_2 . The average vibrational energy transfer $\langle \Delta E_{vib} \rangle$ follows the same order as that of angular dependency. Experimentally, the asymptotic CT channel, $H + CO^+$ is endoergic (≈ 0.42 eV) as compared to the asymptotic IVE channel, $H^+ + CO$ (Niedner-Schatteburg and Toennies, 1992). This is evident from the measurements of

Total differential cross section (TDCS) using proton and hydrogen atom detection at $E_{lab} = 30$ eV where the CT channel is almost an order of magnitude less probable compared to the IVE channel and is accessible by Demkov type of coupling (Demkov, 1964)

In the subsequent experiments (Gianturco, Gierz, and Toennies, 1981; Niedner-Schatteburg and Toennies, 1992) with N_2 , CO, NO and O_2 at $E_{cm} = 9.5$ eV, it was found that $P_{0 \rightarrow v'}$ and $\langle \Delta E_{vib} \rangle$ increased monotonically with θ_{cm} in the range, $5^\circ \leq \theta_{cm} \leq 21^\circ$, and in the order: $N_2 < CO < NO < O_2$. Noll and Toennies (Noll and Toennies, 1986) did detailed experiments on the $H^+ + O_2$ system for both the IVE and the VCT channels at $E_{lab} = 23.7$ eV in the range $0^\circ \leq \theta_{lab} \leq 11^\circ$. They observed a weak rainbow maximum at $\theta_{lab} = 11^\circ$ in the state resolved total differential cross section (TDCS) for the IVE channel by measuring the amount of scattered protons and two rainbow maxima located around $\theta_{lab} \approx 1^\circ$ and $\theta_{lab} = 8.5^\circ$ in the state-resolved TDCS for the VCT channel by measuring the amount of scattered hydrogen atoms with a suitable detector in their time-of-flight spectra. However from the theoretical point of view, there were no suitable explanation available as to how large amount of vibrational energy transfer, evident from the time-of-flight spectra, takes place in the collision process in the $H^+ + O_2$ system.

1.2 Review on theoretical studies

From the theoretical point of view, the most studied proton-diatom system is the $H^+ + H_2$ system. There is an avoided crossing between the first ES and the GS PES. The former electronic PES correlates to the VCT channel, $H(^2S) + H_2^+(^2\Sigma_g^+)$, in the asymptotic limit. There have been many theoretical studies in the past reporting semi-empirical and *ab initio* GS PES for the system along with the quantum dynamics studies for the IVE channel

(Schinke and McGuire, 1978*a,b*; Schinke, Dupuis, and Lester, 1980; Gianturco and Kumar, 1995*a,b*). In the absence of global *ab initio* PESs for the GS and ESs semiempirical diatomics-in-molecules (DIM) PESs were obtained for the system (Tully and Preston, 1971; Ushakov, Nobusada, and Osherov, 2001). Quantum dynamics study for both the IVE and the VCT processes were reported using the DIM PESs, which were able to predict the experimental data on an average quite satisfactorily at $E_{cm} = 20$ eV. However, there were some serious quantitative discrepancies which could not be resolved. Recently, global *ab initio* PESs for the GS and the first ES have been computed and quantum dynamics study predicts almost all the available experimental data for $E_{cm} \leq 20$ eV in near quantitative agreement (Saieswari and Kumar, 2007*b,c,a*, 2008*a,c,b,d*). It is worthpointing out that another set of *ab initio* PESs for the GS and the lowest two ESs have already been obtained by varandas and coworkers (Viegas, Alijah, and Varandas, 2007).

Interestingly, in the $H^+ + N_2$ system, the low-lying excited PESs are found to be well separated energetically from the GS PES (Gianturco, Kumar, and Schneider, 1996; Gianturco, Kumar, Ritschel, Vetter, and Zülicke, 1997). However, strong interactions occur among the excited states, which are assumed to be less significant in the energy transfer process in relation to the dynamics on the GS PES. Experiments performed in the E_{cm} range, 0 - 30 eV, also do not hint any significant amount of the VCT (Krutein and Linder, 1979). Exact quantum dynamical calculations for the IVE process in the vibrational close coupling rotational infinite-order sudden approximation (VCC-RIOSAs) (Schinke and McGuire, 1978*a*; Parker and Pack, 1978; Gianturco, 1979) framework have been performed using the GS PES (Gianturco, Kumar, and Schneider, 1996; Gianturco, Kumar, Ritschel, Vetter, and Zülicke, 1997) which resulted in good agreement with the experiments.

In the $H^+ + NO$ system, there exist a direct curve crossing between the GS PES, asymptotically correlating to $H^+ + NO(X^2\Pi)$, and the first ES PES, asymptotically correlating to $H(^2S) + NO^+(X^1\Sigma^+)$, in the collinear collision geometries, which turn out to be an avoided crossing in off-collinear geometries. There have been *ab initio* studies on this system but they have been focussed on the interaction well of the GS PES with a view to characterize the bound HNO^+ and HON^+ ions (Loew, Berkowitz, and Chang, 1978; McLean, Loew, and Berkowitz, 1978; Marian, Bruna, Buenker, and Peyerimhoff, 1977; Perić, Mladenović, Marian, and Bruna, 1982; Ben Houria, Gritli, Jaidane, Lakdhar, Chambaud, and Rosmus, 2001). There have been few attempts to study the nonadiabatic interactions between the GS and the first ES PESs but they were focussed in the neighbourhood of the conical intersections (Yarkony, 1989; Manaa and Yarkony, 1992). Very recently, global *ab initio* PESs including the nonadiabatic coupling elements for the system have been computed and quantum dynamics study have been reported comparing with the experimental data available only for the IVE channel at $E_{cm} = 9.5$ eV which are in good agreement (Saieswari and Kumar, 2008*b,d*)

The $H^+ + CO$ system is an important system from the astrophysics points of view ever since it was proposed (Klemperer, 1970) that bound molecular HCO^+ and HOC^+ ions could be likely source of an unidentified microwave line observed (Buhl and Snyder, 1970) from the interstellar space. The experimental observation in the laboratory of the rotational spectrum of the HCO^+ using microwave technique (Woods, Dixon, Saykally, and Szanto, 1975) confirmed its presence in the interstellar media, and perhaps it was the first polyatomic ion to be detected in the outer space. Since then, a large number of experimental studies as well as *ab initio* structural calculations have been performed to characterize these molecular ions (for details see ref. Mourik *et al.* (2000) and references therein). Early *ab initio*

studies (Hopkins, Holbrook, Yates, and Csizmadia, 1968; Wahlgren, Pearson, and Schaefer III, 1973; Bruna, 1975) on the system reported calculations on proton affinity of CO molecules and equilibrium structures of HCO^+ and HOC^+ in the GS at the SCF level of accuracy which predicted the collinear equilibrium geometry for both the ions. Using a larger basis set and employing the coupled electron pair approximation (CEPA) and coupled cluster single and double excitation method with perturbative estimate for connected triples (CCSD(T)), Botschwina and coworkers (Botschwina, 1989) computed the collinear equilibrium geometry parameters of the HCO^+ and HOC^+ ions. Choosing another large basis set [6-311+F(3df,2p)] Ma and coworkers reported (Ma, Smith, and Radom, 1992) QCISD(T) calculations on the equilibrium bond length and the energetics of the HCO^+ . Martin and coworkers (Martin, Taylor, and Lee, 1993) computed *ab initio* quartic force fields for the HCO^+ and the HOC^+ ions using coupled cluster methods and basis set of *spdf* and *spdfg* quality. Subsequently, Yamaguchi and coworkers (Yamaguchi, Richards, and Schaefer III, 1994) computed the equilibrium structures of the HCO^+ and HOC^+ ions employing the CCSD(T) calculations with another large TZ2P(*f,p*)+diff basis set. Puzzarini and coworkers (Puzzarini, Tarroni, Palmieri, Carter, and Dore, 1996) computed the GS PES of HCO^+ system near equilibrium geometry and they predicted the vibrational and rotational frequencies using variational calculations. Their study involved complete active space self-consistent field multireference configuration interaction (CASSCF-MRCI) calculations employing the *cc-pVQZ* basis set of Dunning (Dunning, 1989). Recently, using the same basis set and CCSD(T) method, Mladenović and coworkers (Mladenović and Schmatz, 1998) computed the three dimensional GS PES for the bound $\text{HCO}^+/\text{HOC}^+$ system. Their study involved prediction of rovibrational spectrum along with the number and densities of bound vibrational states in the system. In a more recent study, Grunenberg and coworkers (Grunenberg,

Streubel, Frantzius, and Marten, 2003) have performed CCSD(T)/*aug-cc-pVQZ* calculations to obtain total energies, bond lengths, harmonic frequencies etc. for $\text{HCO}^+/\text{HOC}^+$ molecular ions.

There have been also a few early *ab initio* calculations to construct the potential energy curves (PECs) for the system. PES for $\text{H}^+ + \text{CO}$ (CO fixed at its equilibrium geometry, r_{eq}) as a function of proton approaches for collinear and a few non-collinear geometries were reported for the ground as well as low-lying excited electronic states by Peyerimhoff and coworkers (Bruna, Peyerimhoff, and Buenker, 1975). Their study involved SCF calculations along with restricted configuration interaction (CI) computations for a few geometries. Subsequently, treating the CO molecule as rigid rotor, the GS PES was computed at the SCF level and model calculations of vibrational excitations were performed by Gianturco and coworkers (Gianturco *et al.*, 1980b) using the spherical component of their *ab initio* PES.

In the case of the $\text{H}^+ + \text{CO}$ system, an avoided crossing between the GS and the first ES PESs occurs in the asymptotic regions (Niedner-Schatteburg and Toennies, 1992) leading to the Demkov type of coupling (Demkov, 1964). The charge transfer (CT) channel, $\text{H}(^2\text{S}) + \text{CO}^+(\text{X}^2\Sigma^+)$, is endoergic by ~ 0.4 eV as compared to the IVE channel, $\text{H}^+ + \text{CO}(\text{X}^1\Sigma^+)$. Therefore, it is expected that probability of the CT processes would be less and that they would be accessible only by the Rosen-Zener-Demkov type of coupling (Rosen and Zener, 1932; Demkov, 1964). This is confirmed by measurements of total DCS (Niedner-Schatteburg and Toennies, 1992) for proton and H-atom detection in the $\text{H}^+ + \text{CO}$ scattering at $E_{lab} = 30$ eV where the CT was found to be almost an order of magnitude less probable than the elastic and the IVE processes. This suggests that the IVE process, to a large extent, would be governed by the GS PES. Recently, a three-dimensional global *ab initio*

GS PES was obtained for the system and quantum dynamics study within the framework of the vibrational close coupling rotational infinite sudden approximation (VCC-RIOSAs) was performed at $E_{lab} = 30$ eV in our group (Dhilip Kumar and Kumar, 2004) which yielded results in excellent agreement with those of experiments. However, the involvement of the first ES PES at this higher collision energy can not be ruled out. Hence, preliminary studies of CT dynamics were also carried in a restricted geometry including the lowest three ES PECs along with the GS PEC by our group (Dhilip Kumar, Saieswari, and Kumar, 2006) and in extended geometry including only the first ES PES by Lin *et al.* (Lin, Stancil, Li, Gu, Liebermann, Buenker, and Kimura, 2007).

The CT dynamics (electron capture) has been also studied in the system at very high collision energies ($E_{coll} = 10$ KeV/u) by Kimura *et al.* (Kimura, Gu, Hirsch, Buenker, and Stancil, 2000). They computed the GS as well as the first and the second ES PECs with CO fixed at its equilibrium geometry for the collinear and perpendicular approaches of H^+ using the MRCI method and employing the *cc-pVTZ* basis set. They also computed electron capture cross section and the DCSs for these molecular orientations along with the averaged DCS and compared the results with the experimental results of Gao *et al.* (Gao, Johnson, Hakes, Smith, and Stebbings, 1990).

In the $H^+ + O_2$ system, for the collinear and perpendicular geometries, there are direct curve crossings between the GS PES, asymptotically correlating to the IVE channel, $H^+ + O_2(X^3\Sigma_g^-)$ and the first ES PES, asymptotically correlating to the VCT channel, $H(^2S) + O_2^+(X^2\Pi_g)$. These crossing become avoided crossing in all off-collinear geometries, thus leading to a conical intersection (Domcke, Yarkony, and Köppel, 2004) between the respective PESs in the full dimensional nuclear configuration space. The GS and the first

ES PESs are strongly coupled via the Landau-Zener-Stuckelberg type of coupling (Landau, 1932; Zener, 1932; Stuckelberg, 1932). There have been many *ab initio* studies on this system but only in restricted geometries which could qualitatively explain some of the experimental observation like anomalous vibrational excitations in the system (Gianturco and Staemmler, 1981; Vazquez, Buenker, and Peyerimhoff, 1986) in terms of intermediate formation of O_2^+ through the CT process. Full three-dimensional global PESs for both the GS and the first ES became available from two different groups (i) Grimbert *et al.* (Grimbert, Lassier-Givers, and Sidis, 1988) and Schneider *et al.* (Schneider, Zülicke, DiGiacomo, Gianturco, Paidarová, and Polák, 1988), where the former obtained the diabatic PESs needed for the dynamics study by modelling the projected valence bond approach and the latter obtained the same using semi-empirical DIM approach. Quantum dynamics on these two sets of PESS qualitatively agree with the experiments (Sidis, Grimbert, Sizun, and Baer, 1989; Gianturco, Palma, Semprini, Stefani, and Baer, 1990).

1.3 Scope of the thesis

Quantum dynamics study on highly coupled electronic PESs is one of the contemporary and main theoretical challenges today. On the coupled electronic PESs the Schrödinger equation for nuclear motion can be written down either in an adiabatic or a diabatic representation of the wavefunction. In principle, one can carry out dynamics in the adiabatic representation. However, one generally faces the following difficulties in computations: (i) the magnitudes of nonadiabatic coupling terms grow very large over small regions of nuclear configurations near avoided crossings, (ii) they become singular at conical intersections, and (iii) it is generally difficult to deal with them since they are expressed in terms of KE operators and are

vectors in nature. Therefore, one makes an attempt to carry out the dynamics in a diabatic representation where one assumes that the electronic wavefunctions are independent of the nuclear coordinates or are almost independent (weakly varying functions) of nuclear coordinates. In this representation, the nonadiabatic coupling terms in the KE are transformed into the easily handled coupling potential terms which are scalar in nature.

Although the adiabatic representation of the wavefunction is unique, a unique transformation from the adiabatic to a diabatic representation and vice-versa does not exist for a multidimensional collision problem, except for the diatomic case. For a multidimensional case the nonadiabatic coupling terms cannot be made exactly zero. However, they can be made vanishingly small for a (quasi) diabatic representation. Therefore, different sets of quasi-diabatic PESs may correspond to the unique set of adiabatic PESs. There have been several attempts and suggestions to create quasi-diabatic PESs along with discussion about their exactness in the literature (For example, see (General Discussion, 2004) and references therein). *Ab initio* procedures have also been proposed to generate the quasi-diabatic PESs, and they have been used recently in studying the photodissociation dynamics on the coupled electronic PESs and successfully explaining the experimental observation for the H₂S system (Simah, Hartke, and Werner, 1999). In the present study, we adopt the *ab initio* procedures to generate the quasi-diabatic PESs for the considered system. In **chapter 2**, we briefly describe the adiabatic representation and the breakdown of BO approximation. We also briefly review the methods of diabatization including the *ab initio* procedures.

In the time-independent framework of the Schrödinger equation, the quantum dynamics of nuclear motion can be performed using the full close-coupling methods. However, they become computationally expensive at higher energies. However, one can still carry

out quantum dynamics by invoking some physically valid assumptions and approximations. One of the most valid treatments is the vibrational close-coupling rotational infinite order sudden approximation (VCC-RIOSAs). Since the scattering studies in the present study are in the range of 20 - 30 eV, we believe that the studies carried out in the VCC-RIOSAs framework would capture the physics of the collisions quite meaningfully and efficiently. The validity of the VCC-RIOSAs has been numerically tested at higher collision energy end and the details are given in the Appendix A. In **chapter 3**, the close-coupling method is described briefly followed by the discussion on the inclusion of effective approximation leading to the VCC-RIOSAs framework. The details of the various working equations are also described there.

As noted above, a proper theoretical understanding of the IVE and the VCT mechanisms are still lacking for the $H^+ + CO$ and the $H^+ + O_2$ systems. In fact, accurate *ab initio* descriptions of the electronic PESs and the associated couplings are still not available for these systems and therefore elaborate theoretical studies are desirable from both *ab initio* structural and quantum dynamics points of view. The present study focuses on a full theoretical understanding of energy transfer processes of IVE and VCT channels in collisions of H^+ with CO and O_2 molecules for collision energy range $E_{cm}=0 - 30$ eV. Our objective is to examine the dynamics of vibrationally-rotationally inelastic and vibrational charge transfer processes from the *first principles* of quantum mechanics. In this thesis, we report new results on the dynamical attributes obtained from employing the VCC-RIOSAs methodologies, and compare them with the available experimental results.

For the $H^+ + CO$ system *ab initio* PES has become available only for the GS and theoretical attempts have been made to predict only the collision attributes of IVE channel by

carrying out dynamics on the GS PES. In **chapter 4**, we present the details of *ab initio* PESs for the GS and the first ES along with the quantum dynamics results. We compare the computed collision attributes for the system with those of experiments which have become available from the experiments at $E_{cm} = 28.96$ eV.

For the $\text{H}^+ + \text{O}_2$ system, marked differences exist in the topologies of the available quasiadiabatic PESs. Fig. 1.1 shows some salient characteristics of the GS and the first ES PESs used in earlier calculations of Schneider *et al.* (1988), Grimbert *et al.* (1988) and Saieswari

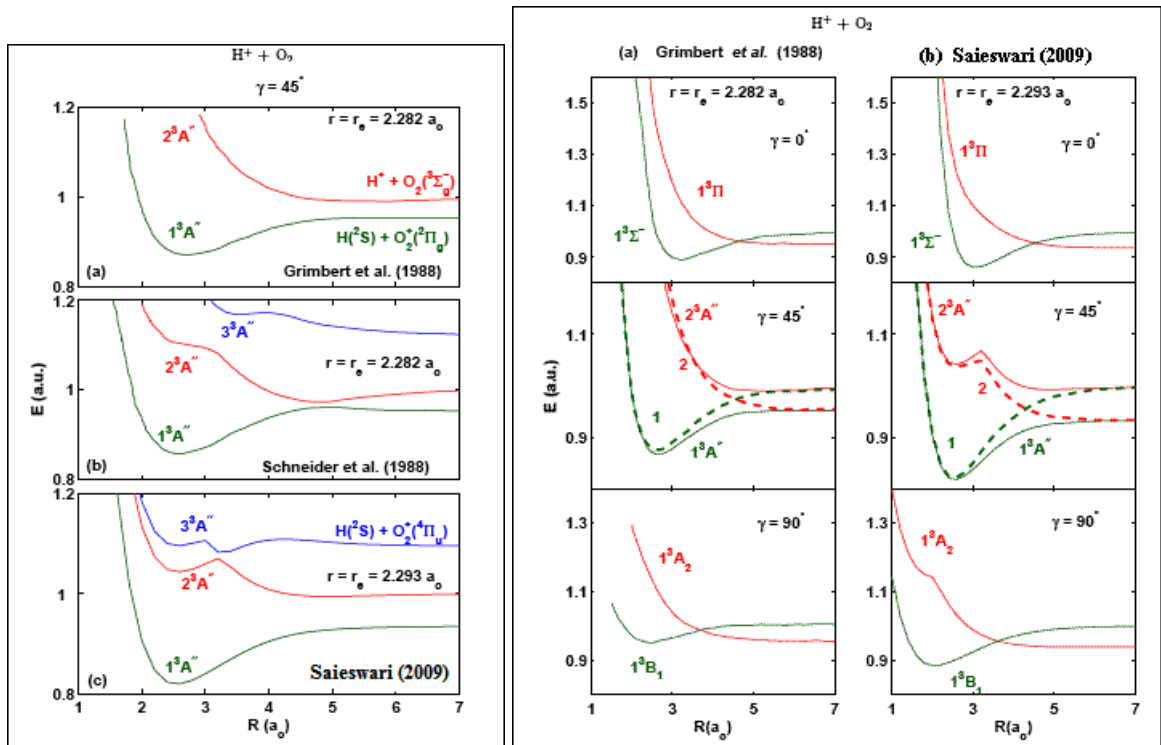


Figure 1.1: Comparison of PECs (left) as a function of R for $\gamma = 45^\circ$ at r_{eq} computed by Grimbert *et al.* (1988), Schneider *et al.* (1988) and Saieswari and Kumar (2009) and as a function of R for $\gamma = 0^\circ, 45^\circ$ and 90° (right) computed by Grimbert *et al.* (1988) and Saieswari and Kumar (2009)

and Kumar (2009). The available PECs have been reproduced in Fig. 1.1(left) as a function of R (distance of proton/hydrogen from the center of mass of diatom) from the internuclear distance of the diatom (r) fixed at its equilibrium value (r_{eq}) and angular approach (γ) of 45° of proton/hydrogen. Note that the r_{eq} values obtained/used are slightly different in the

early calculations and the calculations of Saieswari and Kumar which was determined to be $2.293a_0$. (Expt.value, $r_{eq}(O_2) = 2.286a_0$, (Huber and Herzberg, 1979)). The PECs obtained by model projected valence bond (Grimbert, Lassier-Givers, and Sidis, 1988) and the semi-empirical DIM (Schneider, Zülicke, DiGiacomo, Gianturco, Paidarová, and Polák, 1988) and MRCI (Saieswari and Kumar, 2009) are shown in Fig. 1.1 (left). The $3^3A''$ PEC is not available from the calculations of Grimbert *et al.*. For the sake of comparison the energy of $2^3A''$ is arbitrarily set equal to $1.0a_0$ at $R = 7.0a_0$. It is important to note that the ES PECs differ drastically. The first ES PEC ($2^3A''$) of Grimbert *et al.* remains repulsive while in the DIM and the *ab initio* calculations it shows an avoided crossing with the $3^3A''$ state. Although the avoided crossing is present in the DIM calculations it differs significantly in comparison with the *ab initio* calculations. From the interactions, it is clear that the $3^3A''$ state is also expected to play a role in the dynamics.

We further compare the adiabatic PECs of the GS and the first ES of Grimbert *et al.* and the corresponding *ab initio* PECs of Saieswari and Kumar in Fig. 1.1 (right) for $\gamma = 0^\circ, 45^\circ$ and 90° with $r = r_{eq}$. Here again for the sake of comparison, the energy corresponding to the channel $H^+ + O_2(X^3\Sigma_g^-)$ is set equal 1.0 a.u. at $R = 7.0a_0$. For $\gamma = 0^\circ$ and 90° there is a direct curve crossing which becomes an avoided crossing for $\gamma = 45^\circ$. The corresponding quasideadibatic PECs obtained in the calculations are also shown for $\gamma = 45^\circ$. One can see that the PECs in the two sets look similar except the associated character of avoided crossing for the $2^3A''$ state (originating from the interaction of $3^3A''$) seen in the *ab initio* calculations. In the *ab initio* calculations for the 2×2 , (that is, involving only the GS and the first ES) the computed PESs and the associated nonadiabatic couplings showed quite an irregular behaviour (in the regions of avoided crossing with low-lying ESs). However, the quantum dynamics was performed by strictly modelling a 2×2 coupled process by

smoothing the irregular behaviour of the PESs and the obtained results for the collision attributes were similar to the results obtained using earlier model projected valence bond PESs (Sidis *et al.*, 1989) and the semi-empirical DIM PESs (Gianturco *et al.*, 1990).

From the analysis of the interactions between the GS and the ESs, it is clear that $3^3A''$ state is also expected to play a role in the dynamics. In fact, the third ES $4^3A''$ also lies energetically close to the second ES $3^3A''$ and exhibits avoided crossing with it. At the experimental collision energy of 23 eV all these states are expected to play a role in influencing the collision dynamics. Therefore, there is a need (i) to look into the details of the topologies of *ab initio* PESs (ii) to examine the role of these ESs in influencing the IVE and the VCT processes.

In continuation of the earlier *ab initio* studies, in **chapter 5**, we first obtain the quasidiabatic PESs for the GS and the first ES but without smoothing the behaviour of NACMEs and analyse the quantum dynamics comparing the results with that of experiments. However, the analysis of the coupling and dynamics results suggests that at least two more low-lying ESs would also be involved in influencing the collision dynamics at the experimental collision energy of $E_{cm} = 23$ eV. Therefore, in **chapter 6**, a new set of extensive *ab initio* computations for the 4-state (the GS and the three lowest ESs) adiabatic PESs are reported. The corresponding 4-state quasidiabatic PESs and the coupling potential matrix is also obtained. Quantum dynamics results are improved considerably by the inclusion of two more ESs in the calculations. The detailed analysis and results are presented there.

A summary with conclusions of the present work along with future direction of the research is given in **chapter 7** and followed by Appendix and bibliography.

CHAPTER 2

BORN-OPPENHEIMER APPROXIMATION AND QUASIDIABATIZATION PROCEDURE

In this chapter, we briefly review the break down of the Born-oppenheimer (BO) approximation and the need to move from the adiabatic representation to a quasi-diabatic representation. The discussion on the various diabatization procedures suggested in the literature (Köppel, Domcke, and Cederbaum, 1984; Heumann, Weide, Duren, and Schinke, 1992; Sidis, 1992; Pacher, Cederbaum, and Köppel, 1993; Romero, Aguilar, and Gadea, 1999; Baer, 2002*a,b*; Child, 2002; Worth and Robb, 2002; Adhikari and Billing, 2002; Vibok, Halasz, Vertesi, S.Suhai, Baer, and Toennies, 2003; Köppel, 2004; Baer, Vertesi, Halasz, Vibok, and Suhai, 2004; Baragan, Errea, Macias, Mendez, Rabadan, Riera, Lucas, and Aguilar, 2004; Vertesi, Bene, Vibok, Halasz, and Baer, 2005) is also reviewed.

2.1 The breakdown of Born-Oppenheimer approximation

The validity of the adiabatic and the BO approximation in the nuclear configuration space has been well discussed and documented in the literature (Smith, 1969; Baer, 1975; Mead and Truhlar, 1982; Köppel, Domcke, and Cederbaum, 1984; Handy and Lee, 1996; Balakrishnan, Kalyanaraman, and Sathyamurthy, 1997; Adhikari and Billing, 2002; Baer, 2002*a,b*; Mahapatra and Köppel, 2002; General Discussion, 2004; Jasper, Zhu, Nangia, and Truhlar, 2004). Hence, we briefly summarize here only the necessary details of it.

The time independent Schrödinger equation is given by

$$\hat{H}_{tot} \Psi = E \Psi \quad (2.1)$$

where E is the total energy of the system, Ψ is the total wavefunction and \hat{H}_{tot} is the total Hamiltonian given as

$$\hat{H}_{tot} = \hat{T}_n + \hat{H}_{el}(\mathbf{q}, \mathbf{Q}) \quad (2.2)$$

where \hat{T}_n is the nuclear KE operator ($= -\frac{1}{2M} \nabla_Q^2$, M being the reduced mass of the system and ∇_Q^2 is the Laplacian operator) and $\hat{H}_{el}(\mathbf{q}, \mathbf{Q})$ is the electronic Hamiltonian, which is a function of both the electronic coordinates \mathbf{q} and nuclear coordinates \mathbf{Q} .

The total wavefunction (Ψ) can be expanded as

$$\Psi = \sum_{i=1}^N \psi_i(\mathbf{Q}) \phi_i(\mathbf{q}, \mathbf{Q}) \quad (2.3)$$

where $\{\psi_i(\mathbf{Q})\}$ and $\{\phi_i(\mathbf{q}, \mathbf{Q})\}$ are the set of orthogonal nuclear and real electronic wavefunctions, respectively. The orthogonality condition for the real electronic wavefunctions is defined as

$$\langle \phi_i(\mathbf{Q}) | \phi_j(\mathbf{Q}) \rangle = \int \phi_i^*(\mathbf{q}, \mathbf{Q}) \phi_j(\mathbf{q}, \mathbf{Q}) d\mathbf{q} = \delta_{ij} \quad (2.4)$$

Using Eq. (2.3) in Eq. (2.1), multiplying it from left by the electronic wavefunction $\phi_j^*(\mathbf{q}, \mathbf{Q})$ and integrating over the electronic coordinates \mathbf{q} we result in (Baer, 2002b; Mead and Truh-

lar, 1982)

$$\begin{aligned}
& -\frac{1}{2M} \left\{ \nabla_Q^2 \psi_j(\mathbf{Q}) + 2 \sum_{i=1}^N \vec{F}_{ji}(\mathbf{Q}) \vec{\nabla}_Q \psi_i(\mathbf{Q}) + \sum_{i=1}^N G_{ji}(\mathbf{Q}) \psi_i(\mathbf{Q}) \right\} \\
& + \sum_{i=1}^N U_{ji}(\mathbf{Q}) \psi_i(\mathbf{Q}) = E \psi_j(\mathbf{Q}) \quad j = 1, 2, 3, \dots, N
\end{aligned} \tag{2.5}$$

where

$$\vec{F}_{ji}(\mathbf{Q}) = \left\langle \phi_j(\mathbf{Q}) \left| \vec{\nabla}_Q \right| \phi_i(\mathbf{Q}) \right\rangle = \int \phi_j^*(\mathbf{q}, \mathbf{Q}) \vec{\nabla}_Q \phi_i(\mathbf{q}, \mathbf{Q}) d\mathbf{q} \tag{2.6}$$

are the first order nonadiabatic coupling matrix elements (NACME) which are vector quantities.

$$G_{ji}(\mathbf{Q}) = \left\langle \phi_j(\mathbf{Q}) \left| \nabla_Q^2 \right| \phi_i(\mathbf{Q}) \right\rangle = \int \phi_j^*(\mathbf{q}, \mathbf{Q}) \nabla_Q^2 \phi_i(\mathbf{q}, \mathbf{Q}) d\mathbf{q} \tag{2.7}$$

are the second order NACME values and are scalar quantities, and

$$\begin{aligned}
U_{ji}(\mathbf{Q}) &= \left\langle \phi_j(\mathbf{Q}) \left| \hat{H}_{el}(\mathbf{q}, \mathbf{Q}) \right| \phi_i(\mathbf{Q}) \right\rangle \\
&= \int \phi_j^*(\mathbf{q}, \mathbf{Q}) \hat{H}_{el}(\mathbf{q}, \mathbf{Q}) \phi_i(\mathbf{q}, \mathbf{Q}) d\mathbf{q}
\end{aligned} \tag{2.8}$$

are the adiabatic electronic (eigen) energies which are also scalar quantities. The matrix form

of Eq. (2.5) is given by

$$\begin{aligned}
& -\frac{1}{2M} \left\{ \nabla_Q^2 \hat{1} + 2 \begin{pmatrix} \vec{F}_{11} & \vec{F}_{12} & \dots & \vec{F}_{1N} \\ \vec{F}_{21} & \vec{F}_{22} & \dots & \vec{F}_{2N} \\ \vdots & \vdots & \ddots & \vdots \\ \vec{F}_{N1} & \vec{F}_{N2} & \dots & \vec{F}_{NN} \end{pmatrix} \vec{\nabla}_Q + \begin{pmatrix} G_{11} & G_{12} & \dots & G_{1N} \\ G_{21} & G_{22} & \dots & G_{2N} \\ \vdots & \vdots & \ddots & \vdots \\ G_{N1} & G_{N2} & \dots & G_{NN} \end{pmatrix} \right\} \\
& \begin{pmatrix} \psi_1 \\ \psi_2 \\ \vdots \\ \psi_N \end{pmatrix} + \begin{pmatrix} U_{11} & U_{12} & \dots & U_{1N} \\ U_{21} & U_{22} & \dots & U_{2N} \\ \vdots & \vdots & \ddots & \vdots \\ U_{N1} & U_{N2} & \dots & U_{NN} \end{pmatrix} \begin{pmatrix} \psi_1 \\ \psi_2 \\ \vdots \\ \psi_N \end{pmatrix} = E \hat{1} \begin{pmatrix} \psi_1 \\ \psi_2 \\ \vdots \\ \psi_N \end{pmatrix} \quad (2.9)
\end{aligned}$$

Since $\vec{\nabla}_Q$ is antihermitian and ϕ_i 's are real electronic wavefunctions we have

$$\begin{aligned}
\vec{F}_{ji}(\mathbf{Q}) &= -\vec{F}_{ij}(\mathbf{Q}) \\
\vec{F}_{ii}(\mathbf{Q}) &= 0
\end{aligned} \quad (2.10)$$

Using Eq. (2.4) and Eq. (2.10) in Eq. (2.9) we get

$$\begin{aligned}
& -\frac{1}{2M} \left\{ \nabla_Q^2 \hat{1} + 2 \begin{pmatrix} 0 & \vec{F}_{12} & \dots & \vec{F}_{1N} \\ -\vec{F}_{21} & 0 & \dots & \vec{F}_{2N} \\ \vdots & \vdots & \ddots & \vdots \\ -\vec{F}_{N1} & -\vec{F}_{N2} & \dots & 0 \end{pmatrix} \vec{\nabla}_Q + \begin{pmatrix} G_{11} & G_{12} & \dots & G_{1N} \\ G_{21} & G_{22} & \dots & G_{2N} \\ \vdots & \vdots & \ddots & \vdots \\ G_{N1} & G_{N2} & \dots & G_{NN} \end{pmatrix} \right\} \\
& \begin{pmatrix} \psi_1 \\ \psi_2 \\ \vdots \\ \psi_N \end{pmatrix} + \begin{pmatrix} U_{11} & 0 & \dots & 0 \\ 0 & U_{22} & \dots & 0 \\ \vdots & \vdots & \ddots & \vdots \\ 0 & 0 & \dots & U_{NN} \end{pmatrix} \begin{pmatrix} \psi_1 \\ \psi_2 \\ \vdots \\ \psi_N \end{pmatrix} = E \hat{1} \begin{pmatrix} \psi_1 \\ \psi_2 \\ \vdots \\ \psi_N \end{pmatrix} \quad (2.11)
\end{aligned}$$

Thus, in the adiabatic representation (that is, using the set of $\psi_i(\mathbf{Q})$'s and $\psi_i(\mathbf{q}, \mathbf{Q})$'s) the potential matrix becomes diagonal and the nuclear kinetic energy matrix becomes non-diagonal due to the non-zero nature of the first order and the second order NACME values. These NACME values can be considered to be negligible if the PESs involved in our study are well separated energetically from each other. The $G_{ji}(\mathbf{Q})$ generally have a very small magnitude and can be neglected (Smith, 1969). From the Hellman-Feynman relation, the

$\vec{F}_{ji}(\mathbf{Q})$ is given by

$$\left\langle \phi_j(\mathbf{Q}) \left| \vec{\nabla}_Q \right| \phi_i(\mathbf{Q}) \right\rangle = \frac{\left\langle \phi_j(\mathbf{q}, \mathbf{Q}) \left| \frac{\partial \hat{H}_{el}}{\partial Q} \right| \phi_i(\mathbf{q}, \mathbf{Q}) \right\rangle}{U_{ii} - U_{jj}} \quad (2.12)$$

Thus, if the energy gap $U_{ii} - U_{jj}$ is very large, then the NACME values become very small and can be safely neglected in computations. Invoking the BO approximation, in which the electronic and nuclear motions are decoupled, that is,

$$\begin{aligned} \vec{\nabla}_Q \phi_i(\mathbf{q}, \mathbf{Q}) &= \vec{\nabla}_Q \phi_i(\mathbf{q}; \mathbf{Q}) = 0 \\ \vec{\nabla}_Q^2 \phi_i(\mathbf{q}, \mathbf{Q}) &= \vec{\nabla}_Q^2 \phi_i(\mathbf{q}; \mathbf{Q}) = 0, \end{aligned} \quad (2.13)$$

the electronic wavefunction ($\phi_i(\mathbf{q}, \mathbf{Q})$) is assumed to be parametrically dependent on the nuclear coordinates ($\phi_i(\mathbf{q}; \mathbf{Q})$). Using Eq. (2.13) in Eq. (2.11) and assuming that the energy gap between the PESs involved are reasonably large, leads to the simplest form given below

$$-\frac{1}{2M} \nabla_Q^2 \psi_i + U_{ii} \psi_i = E \psi_i \quad (2.14)$$

where U_{ii} are the adiabatic energies mentioned in Eq. (2.11). The details of the computations, in generating these adiabatic *ab initio* PESs for the $\text{H}^+ + \text{CO}$ and the $\text{H}^+ + \text{O}_2$ systems are described in **chapter 4**, **chapter 5** and **chapter 6**, respectively.

In the adiabatic picture, if there exists an avoided crossing or a direct crossing between two PESs for certain nuclear configuration space, then the (adiabatic) energy gap ($U_{ii} - U_{jj}$) becomes reasonably small for the former case but it becomes zero for the latter case. Thus, it leads to very high magnitude or even singularities in the first order NACME values (see Eq. (2.12)). Hence, handling these first order NACME values, which are also vector quan-

titles, becomes extremely difficult computationally. When PESs are strongly coupled the nuclear and electronic motions can not be decoupled, thereby leading to the breakdown of BO approximation

$$\begin{aligned}\vec{\nabla}_Q \phi_i(\mathbf{q}; \mathbf{Q}) &\neq 0 \\ \nabla_Q^2 \phi_i(\mathbf{q}; \mathbf{Q}) &\neq 0\end{aligned}\tag{2.15}$$

To overcome this problem one can choose a set of real wavefunctions $\{\tilde{\psi}_i(\mathbf{Q})\}$'s and $\{\tilde{\phi}_i(\mathbf{q}, \mathbf{Q})\}$'s which vary as little as possible with respect to the nuclear coordinates. Such type of wavefunctions are called diabatic wavefunctions. The adiabatic and diabatic wavefunctions are related by a unitary transformation matrix \mathbf{A} (defined in the next section) as

$$\begin{aligned}\{\psi_i(\mathbf{Q})\} &= \mathbf{A}^\dagger \{\tilde{\psi}_i(\mathbf{Q})\} \\ \{\tilde{\phi}_i(\mathbf{q}, \mathbf{Q})\} &= \mathbf{A} \{\phi_i(\mathbf{q}, \mathbf{Q})\}\end{aligned}\tag{2.16}$$

On following the same algebra mentioned above, with these diabatic wavefunctions, Eq. (2.6), Eq. (2.7) and Eq. (2.8) get modified as

$$\tilde{F}_{ji}(\mathbf{Q}) = \langle \tilde{\phi}_j(\mathbf{Q}) | \vec{\nabla}_Q | \tilde{\phi}_i(\mathbf{Q}) \rangle = \int \tilde{\phi}_j^*(\mathbf{q}, \mathbf{Q}) \vec{\nabla}_Q \tilde{\phi}_i(\mathbf{q}, \mathbf{Q}) d\mathbf{q}\tag{2.17}$$

$$\tilde{G}_{ji}(\mathbf{Q}) = \langle \tilde{\phi}_j(\mathbf{Q}) | \nabla_Q^2 | \tilde{\phi}_i(\mathbf{Q}) \rangle = \int \tilde{\phi}_j^*(\mathbf{q}, \mathbf{Q}) \nabla_Q^2 \tilde{\phi}_i(\mathbf{q}, \mathbf{Q}) d\mathbf{q}\tag{2.18}$$

$$\begin{aligned}
\tilde{U}_{ji}(\mathbf{Q}) &= \left\langle \tilde{\phi}_j(\mathbf{Q}) \left| \hat{H}_{el}(\mathbf{q}, \mathbf{Q}) \right| \tilde{\phi}_i(\mathbf{Q}) \right\rangle \\
&= \int \tilde{\phi}_j^*(\mathbf{q}, \mathbf{Q}) \hat{H}_{el}(\mathbf{q}, \mathbf{Q}) \tilde{\phi}_i(\mathbf{q}, \mathbf{Q}) d\mathbf{q}
\end{aligned} \tag{2.19}$$

Since the diabatic electronic wavefunctions are assumed to be (nearly) independent with respect to nuclear motion

$$\begin{aligned}
\vec{\nabla}_Q \tilde{\phi}_i(\mathbf{q}; \mathbf{Q}) &\cong 0 \\
\nabla_Q^2 \tilde{\phi}_i(\mathbf{q}; \mathbf{Q}) &\cong 0
\end{aligned} \tag{2.20}$$

Also, the set $\{\tilde{\phi}_i(\mathbf{q}, \mathbf{Q})\}$ are real (diabatic) electronic wavefunctions, therefore, the condition in Eq. (2.10) also holds for them. Using the above two conditions, we find that all the matrix elements of $\{\tilde{F}_{ji}(\mathbf{Q})\}$ and $\{\tilde{G}_{ji}(\mathbf{Q})\}$ are (nearly) zero, whereas the potential matrix $\{\tilde{U}_{ji}(\mathbf{Q})\}$ remains non-diagonal, since the diabatic electronic wavefunctions $\{\tilde{\phi}_i(\mathbf{q}, \mathbf{Q})\}$ are not the eigenfunctions of the electronic Hamiltonian (\hat{H}_{el}) . Hereafter, let $\{\tilde{U}_{ji}\}$ be denoted as $\{V_{ji}^d\}$. Hence, Eq. (2.9) takes the following form

$$\left\{ -\frac{1}{2M} \nabla_Q^2 \hat{1} + \begin{pmatrix} V_{11}^d & V_{12}^d & \cdots & V_{1N}^d \\ V_{21}^d & V_{22}^d & \cdots & V_{2N}^d \\ \vdots & \vdots & \ddots & \vdots \\ V_{N1}^d & V_{N2}^d & \cdots & V_{NN}^d \end{pmatrix} \right\} \begin{pmatrix} \tilde{\psi}_1 \\ \tilde{\psi}_2 \\ \vdots \\ \tilde{\psi}_N \end{pmatrix} = E \hat{1} \begin{pmatrix} \tilde{\psi}_1 \\ \tilde{\psi}_2 \\ \vdots \\ \tilde{\psi}_N \end{pmatrix} \tag{2.21}$$

Thus, in the diabatic representation ($\{\tilde{\psi}_i(\mathbf{Q})\}$'s and $\{\tilde{\phi}_i(\mathbf{q}, \mathbf{Q})\}$'s), the potential matrix becomes non-diagonal due to the presence of the coupling terms V_{ij}^d and the nuclear kinetic energy matrix becomes diagonal.

In the adiabatic representation, the couplings between (among) the electronic states appear in the nuclear kinetic energy part (as vectors), whereas in the diabatic representation

the same coupling is transformed to the potential energy part (as scalars). Hence, for computational convenience, the dynamics is performed on these diabatic PESs.

2.2 Diabatization procedures

Although the adiabatic representation ($\{\psi_i(\mathbf{Q})\}$'s and $\{\phi_i(\mathbf{q}, \mathbf{Q})\}$'s) is unique, a unique transformation from the adiabatic to a diabatic representation and vice-versa does not exist for a multidimensional collision problem except for the diatomic case. For a 2×2 case, where two electronic states are coupled, the transformation matrix \mathbf{A} is given by

$$\mathbf{A} = \begin{pmatrix} \cos(\alpha(\mathbf{Q})) & \sin(\alpha(\mathbf{Q})) \\ -\sin(\alpha(\mathbf{Q})) & \cos(\alpha(\mathbf{Q})) \end{pmatrix} \quad (2.22)$$

where $\alpha(\mathbf{Q})$ is called as the mixing angle which describes the mixing between the two electronic states involved and is a function of nuclear coordinates. For a 2×2 case, the adiabatic electronic wavefunction and the diabatic electronic wavefunctions are related as described in Eq. (2.16), that is,

$$\begin{pmatrix} \tilde{\phi}_i(\mathbf{q}, \mathbf{Q}) \\ \tilde{\phi}_j(\mathbf{q}, \mathbf{Q}) \end{pmatrix} = \begin{pmatrix} \cos(\alpha(\mathbf{Q})) & \sin(\alpha(\mathbf{Q})) \\ -\sin(\alpha(\mathbf{Q})) & \cos(\alpha(\mathbf{Q})) \end{pmatrix} \begin{pmatrix} \phi_i(\mathbf{q}, \mathbf{Q}) \\ \phi_j(\mathbf{q}, \mathbf{Q}) \end{pmatrix} \quad (2.23)$$

Using Eq. (2.23) in Eq. (2.16) and following the algebra, we have the relation

$$\langle \phi_i(\mathbf{q}, \mathbf{Q}) | \vec{\nabla}_Q | \phi_j(\mathbf{q}, \mathbf{Q}) \rangle = \vec{\nabla}_Q(\alpha(\mathbf{Q})) = \left(\frac{\partial \alpha(\mathbf{Q})}{\partial Q} \right) \quad (2.24)$$

Thus mixing angle can be obtained in principle by the integration of the first order NACME values with respect to the nuclear coordinates $\{\mathbf{Q}\}$,

$$\begin{aligned}
\alpha(\mathbf{Q}) &= \alpha_{Q_0} + \int_{Q_{ref}}^Q \left\langle \phi_i(\mathbf{q}, \mathbf{Q}) \left| \vec{\nabla}_{Q'} \right| \phi_j(\mathbf{q}, \mathbf{Q}) \right\rangle dQ' \\
&= \alpha_{Q_0} + \int_{Q_{1ref}}^{Q_1} \left\langle \phi_i(\mathbf{q}, \mathbf{Q}) \left| \frac{\partial}{\partial Q'_1} \right| \phi_j(\mathbf{q}, \mathbf{Q}) \right\rangle dQ'_1 + \\
&\quad \int_{Q_{2ref}}^{Q_2} \left\langle \phi_i(\mathbf{q}, \mathbf{Q}) \left| \frac{\partial}{\partial Q'_2} \right| \phi_j(\mathbf{q}, \mathbf{Q}) \right\rangle dQ'_2 + \dots
\end{aligned} \tag{2.25}$$

The relation between the adiabatic potential matrix $\{U_{ii}\}$'s and the diabatic potential matrix $\{V_{ij}^d\}$'s for the 2×2 case is given as

$$\begin{pmatrix} V_{ii}^d & V_{ij}^d \\ V_{ji}^d & V_{jj}^d \end{pmatrix} = A^\dagger \begin{pmatrix} U_{ii} & 0 \\ 0 & U_{jj} \end{pmatrix} A \tag{2.26}$$

On further solving the above equation we obtain the relation

$$\begin{aligned}
V_{ii}^d &= U_{ii} \cos^2(\alpha(\mathbf{Q})) + U_{jj} \sin^2(\alpha(\mathbf{Q})) \\
V_{jj}^d &= U_{ii} \sin^2(\alpha(\mathbf{Q})) + U_{jj} \cos^2(\alpha(\mathbf{Q})) \\
V_{ij}^d &= V_{ji}^d = (U_{ii} - U_{jj}) \cos(\alpha(\mathbf{Q})) \sin(\alpha(\mathbf{Q}))
\end{aligned} \tag{2.27}$$

The above procedure, which is mainly applicable for a 2×2 case, can be extended for an $N \times N$ case, where N electronic states are coupled. A detailed discussion of the $N \times N$ case has been discussed recently by Vertesi *et al.* (Vertesi, Bene, Vibok, Halasz, and Baer, 2005), where the N -state adiabatic-to-diabatic transformation have been applied to three- and five-state *ab initio* calculations for the $H + H_2$ system. For polyatomic systems, where there exist more than one nuclear degrees of freedom, the integral in the above equation is not path independent (Mead and Truhlar, 1982; Baer, 2002b). Therefore, the diabatic states can not

be defined uniquely and the coupling matrix elements cannot be made exactly zero for all nuclear geometries.

The derivatives $\vec{\nabla}_Q(\alpha(\mathbf{Q}))$ and $\langle \phi_i(\mathbf{q}, \mathbf{Q}) | \vec{\nabla}_Q | \phi_j(\mathbf{q}, \mathbf{Q}) \rangle$ in Eq. (2.24) can be obtained by numerical differentiation using the finite difference method (Galloy and Lorquet, 1977; Desouter-Lecomte, Galloy, Lorquet, and Vaz Pires, 1979; Hirsch, Bruna, Buenker, and Peyerimhoff, 1980; Werner and Meyer, 1981; Buenker, Hirsch, Peyerimhoff, Bruna, Römelt, Bettendorf, and Petrongolo, 1982; Werner, Follmeg, and Alexander, 1988; Werner, Follmeg, Alexander, and Lemoine, 1989)

$$\left(\frac{\partial \alpha(\mathbf{Q})}{\partial Q} \right) \cong \frac{\alpha(Q_0 + \Delta Q) - \alpha(Q_0 - \Delta Q)}{2\Delta Q} \quad (2.28)$$

$$\langle \phi_i(\mathbf{q}, \mathbf{Q}) | \vec{\nabla}_Q | \phi_j(\mathbf{q}, \mathbf{Q}) \rangle \cong \frac{1}{2\Delta Q} \langle \phi_i(Q_0 + \Delta Q) | \phi_j(Q_0 - \Delta Q) \rangle \quad (2.29)$$

where ΔQ is the small increment in the nuclear coordinates. The overlap matrix in Eq. (2.29) can be evaluated in complete analogy to transition matrix elements between the wavefunctions with nonorthogonal orbitals. That is, in this procedure, the orbitals are determined at the reference geometry, then the calculations are performed at the displaced geometries. The transition density matrices between the states at the reference geometry and the displaced geometries are then obtained. In using this method, one should choose ΔQ in such a way that the calculated coupling matrix elements are numerically converged. This procedure has been employed in the nonadiabatic studies for He-CN collision (Werner, Follmeg, and Alexander, 1988; Werner, Follmeg, Alexander, and Lemoine, 1989) and for photodissociation of H₂S (Heumann, Weide, Duren, and Schinke, 1992; Simah, Hartke, and Werner, 1999). Once the NACME values are obtained as a function of all the nuclear coordinates

$\{\mathbf{Q}\}$, the mixing angle can be obtained by integrating them numerically as described in Eq. (2.25) (Top and Baer, 1977; Baer and Beswick, 1979; Baer, 1983; Köppel, Domcke, and Cederbaum, 1984).

The computation of (quasi)diabatic potential matrix in the above procedure is based on the a priori information on the NACME values which demand further computational requirements. Therefore, it is desirable to use a direct diabatization scheme that avoids the computation of the NACMEs completely. These methods are either based on diagonalization of some property matrix (Werner and Meyer, 1981; Heumann and Schinke, 1994) or on an analysis of the CI vectors (Desouter-Lecomte, Dehareng, and Lorquet, 1987; Werner, Follmeg, and Alexander, 1988; Pacher, Cederbaum, and Köppel, 1988; Werner, Follmeg, Alexander, and Lemoine, 1989; Hirsch, Buenker, and Petrongolo, 1990; Petrongolo, Hirsch, and Buenker, 1990; Kozin and Jensen, 1994)

In earlier studies, the mixing angle ($\alpha(\mathbf{Q})$) was obtained from the coefficients of the CI vectors of the adiabatic wavefunctions. For example, in the case of A + BC collisions having $\Sigma - \Pi$ electronic states, these will be crossing in the collinear geometries. For the off-collinear geometries the Σ -state will correlate with A' state (we call it as 1A'), while the degeneracy of the Π -state will be lifted resulting into A' + A'' (we call it as 1A'' and 2A'). The 1A' and 2A' electronic states will have avoided crossing for off-collinear geometries. If the adiabatic electronic wavefunctions of 1A' and 2A' are represented as

$$\begin{aligned}\phi_1 &= \sum_k c_k^1 \zeta_k^1 \\ \phi_2 &= \sum_k c_k^2 \zeta_k^2\end{aligned}\tag{2.30}$$

where c_k 's and ζ_k 's are the CI coefficients and configuration state functions (CSF), respec-

tively. ϕ_1 and ϕ_2 will have contributions of CSFs describing the $1A'$ and $2A'$ states, and one can obtain the mixing angle from the c_k 's of either wavefunctions. For an example, using ϕ_1 wavefunction α can be obtained as

$$\alpha = \sin^{-1} \left[\frac{\sum_{k'} (c_k^1)^2}{\sum_k (c_k^1)^2} \right]^{\frac{1}{2}} \quad (2.31)$$

Note that in the numerator the summation is over the coefficients of configurations belonging to $1A'$ only and that α is also a function of nuclear geometry.

An improvement in this procedure has been proposed recently (Simah, Hartke, and Werner, 1999), where it is assumed that the CI vectors representing the diabatic states are approximately geometry independent, which implies that the change of orbitals as function of geometry can be neglected. This condition is met by the invariance of the CI/MRCI energies with respect to the unitary transformation among the active orbitals to minimize the geometry dependence of the orbitals. Following the generalization of the method proposed by Domcke and Woywod (Domcke and Woywod, 1993), this was achieved for a 2×2 case by maximizing the overlap $|\langle \phi_i(\mathbf{Q}') | \phi_i(\mathbf{Q}) \rangle|^2 + |\langle \phi_j(\mathbf{Q}') | \phi_j(\mathbf{Q}) \rangle|^2$ for all pairs of active orbitals i, j at a considered geometry \mathbf{Q} with those in a neighborhood geometry \mathbf{Q}' using a 2×2 Jacobi rotation technique (Simah, Hartke, and Werner, 1999). In an alternative way, one can achieve the unitary transformation for the active orbitals as

$$\mathbf{T} = \mathbf{S} (\mathbf{S}^\dagger \mathbf{S})^{-\frac{1}{2}} \quad (2.32)$$

where $S_{ij} = \langle \phi_i(\mathbf{Q}) | \phi_j(\mathbf{Q}') \rangle$ is the overlap matrix of the active orbitals at the two geometries. It has been found (Simah, Hartke, and Werner, 1999) that for the 2×2 case the two

methods yield identical results.

One can also achieve diabaticization via block diagonalization of a generalized Fock matrix (Domcke, Woywod, and Stengle, 1994). Considering a case of M states with resulting diabatic electronic wavefunctions denoted as $\tilde{\phi}_m$ which are constructed in basis of N configuration state function (CSF) as

$$\tilde{\phi}_m = \sum_l^N d_{lm} \tilde{\chi}_l \quad (2.33)$$

for $m = 1, \dots, M$, where d is an $N \times M$ matrix and it is related to corresponding coefficient matrix c of the adiabatic electronic wavefunctions through the transformation $\mathbf{d} = \mathbf{c}\mathbf{A}$. \mathbf{A} is an $M \times M$ matrix which can be determined from the condition that \mathbf{d} remains as close as possible to the matrix \mathbf{d}^{ref} at a reference geometry at which the adiabatic and diabatic wavefunctions become identical. The unitary matrix \mathbf{A} can be obtained from the relation,

$$\mathbf{A} = \mathbf{B} (\mathbf{B}^\dagger \mathbf{B})^{-\frac{1}{2}} \quad (2.34)$$

with $\mathbf{B} = \mathbf{c}^\dagger \mathbf{d}^{ref}$. This procedure is closely related to the block diagonalization of Pacher *et al.* (Pacher, Cederbaum, and Köppel, 1988).

This procedure was applied for the photodissociation of H_2S on electronically coupled PESs by computing the quasidiabatic PESs and the coupling potentials and quantum dynamics using the quasidiabatic potential matrix was able to explain the experimental observations (Simah, Hartke, and Werner, 1999). It is also worth pointing out here that Balint-Kurti *et al.* (see in: General Discussion (2004)) have also recently computed the quasidiabatic PECs corresponding to the five lowest adiabatic PECs in O_3 system using the same procedure. Recently, a new set of quasidiabatic potential matrix (2×2) was also obtained for

the $\text{H}^+ + \text{H}_2$ system and quantum dynamics yielded results in near quantitative agreement settling some long-standing discrepancies between theory and experiments (Saieswari and Kumar, 2007*c,a*, 2008*c*).

In our present study, we have employed the above *ab initio* procedure (see Eq. (2.34)) to compute diabatic potential matrix and/or mixing angle (Simah, Hartke, and Werner, 1999; Heumann, Weide, Duren, and Schinke, 1992) using the MOLPRO 2002.6 software (Werner, Knowles, Schütz, Lindh, Celani, Korona, Rauhut, Manby, Amos, Bernhardsson, Berning, Cooper, Deegan, Dobbyn, Eckert, Hampel, Hetzer, Lloyd, McNicholas, Meyer, Mura, Nicklaß, Palmieri, Pitzer, Schumann, Stoll, Stone, Tarroni, and Thorsteinsson, 2002). The relevant details in computing the mixing angle and quasidiabatic potentials are described in the **chapters 4, 5 and 6**.

CHAPTER 3

THE TIME INDEPENDENT QUANTUM DYNAMICS

STUDY - THE VCC-RIOSAS SCHEME

In this chapter we briefly review the details of the full close-coupling method and the use of rotational infinite-order sudden approximation. The details of calculations of collision attributes in the quantum dynamics study is also discussed in brief followed by the application of VCC-RIOSAS scheme for the ion-molecule collision.

3.1 The full close-coupling method

In principle, one can study the quantum dynamics of the system in the time-independent formulation of scattering theory with full close-coupling approach. In particular, to describe the interaction between a diatomic molecule and an atom and the dynamics of the IVE and the VCT channels, the standard Jacobi coordinates are used as shown in Fig. 3.1, where \mathbf{r} is the vector joining the diatom BC and \mathbf{R} is the vector connecting the c.m of the diatomic molecule BC and the atom A and γ is the angle between the vectors \mathbf{R} and \mathbf{r} and the relationship among \mathbf{R} , \mathbf{r} and γ is $\gamma = \cos^{-1}(\mathbf{R} \cdot \mathbf{r})$.

The Schrödinger equation subjected to solve is

$$\hat{H}_{tot}\Psi(\mathbf{R}, \mathbf{r}, \mathbf{q}) = E\Psi(\mathbf{R}, \mathbf{r}, \mathbf{q}) \quad (3.1)$$

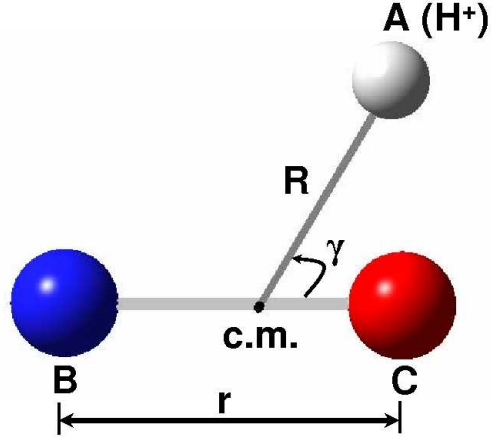


Figure 3.1: Jacobi coordinates

where

$$\hat{H}_{tot} = -\frac{\hbar^2}{2\mu_{ABC}R^2} \frac{\partial}{\partial R} \left(R^2 \frac{\partial}{\partial R} \right) + \frac{\mathbf{L}^2}{2\mu_{ABC}R^2} + V(R, r, \gamma, \mathbf{q}) + \hat{H}_{BC}^0(\mathbf{r}, \mathbf{q}) \quad (3.2)$$

where R , r and γ are the nuclear Jacobi coordinates, q is the electronic coordinate, $\Psi(\mathbf{R}, \mathbf{r}, \mathbf{q})$ is the total scattering wavefunction which is a function of nuclear and electronic coordinates, μ_{ABC} is the atom-molecule reduced mass

$$\mu_{ABC} = \frac{(m_B + m_C) m_A}{m_A + m_B + m_C} \quad (3.3)$$

\mathbf{L} is the orbital angular momentum of the atom relative to the molecule, and

$$\hat{\mathbf{L}}^2 |lm_l\rangle = l(l+1) \hbar^2 |lm_l\rangle \quad (3.4)$$

in which l is orbital angular momentum quantum number and m_l is the projection of \mathbf{L} onto the space fixed axes and $|lm_l\rangle$ are the eigen functions of $\hat{\mathbf{L}}^2$ operator. $V(R, r, \gamma, \mathbf{q})$ is the atom-molecule interaction potential, which vanishes at infinite separation R and $\hat{H}_{BC}^0(\mathbf{r}, \mathbf{q})$

is the unperturbed Hamiltonian for the diatomic molecule BC and is given by

$$\hat{H}_{BC}^0(\mathbf{r}, \mathbf{q}) = -\frac{\hbar^2}{2\mu_{BC}r^2} \frac{\partial}{\partial r} \left(r^2 \frac{\partial}{\partial r} \right) + \frac{\mathbf{I}^2}{2\mu_{BC}r^2} + \hat{H}_{BC}^e(\mathbf{r}, \mathbf{q}) \quad (3.5)$$

where \mathbf{I} is the rotational angular momentum of the diatom BC, and

$$\hat{\mathbf{I}}^2 |jm_j\rangle = j(j+1) \hbar^2 |jm_j\rangle \quad (3.6)$$

in which j is the rotational angular momentum quantum number and m_j is the projection of I onto the space-fixed axes, and $|jm_j\rangle$ are the eigen functions of $\hat{\mathbf{I}}^2$ operator. $\hat{H}_{BC}^e(r, q)$ is the electronic Hamiltonian of the diatom BC and depends on all the electronic coordinates \mathbf{q}

$$\hat{H}_{BC}^e(r, \mathbf{q}) = \hat{T}_e(\mathbf{q}) + \hat{V}_{en}(r, \mathbf{q}) + \hat{V}_{ee}(r, \mathbf{q}) \quad (3.7)$$

where $\hat{T}_e(\mathbf{q})$ is the kinetic energy operator of the electrons, $\hat{V}_{en}(r, \mathbf{q})$ is the electron-nuclei coulomb interaction potential operator, $\hat{V}_{ee}(r, \mathbf{q})$ is the electron-electron coulomb interaction potential operator. The eigenfunction of the $\hat{H}_{BC}^0(\mathbf{r}, \mathbf{q})$ can be represented as the direct products of electronic ($|n\rangle$), rotational ($|jm_j\rangle$) and vibrational ($|vj\rangle$) wavefunctions (Alexander, 1982; Hougen, 1970)

$$|n j v\rangle = |n\rangle |j m_j\rangle |v j\rangle \quad (3.8)$$

On substituting the Eq. (3.8) in Eq. (3.5) and solving for the vibrational part in each elec-

tronic state, we get

$$\begin{aligned}\hat{H}_{BC}^0(\mathbf{r}, \mathbf{q}) |vj\rangle &= \left(-\frac{\hbar^2}{2\mu_{BC}r^2} \frac{\partial}{\partial r} \left(r^2 \frac{\partial}{\partial r} \right) + \frac{j(j+1)\hbar^2}{2\mu_{BC}r^2} + V_{BC}^n(r) \right) |vj\rangle \\ &= \epsilon_{vj}^n |vj\rangle\end{aligned}\quad (3.9)$$

where ϵ_{vj}^n is the eigenvalue corresponding to the rovibrational energies and $V_{BC}^n(r)$ is the adiabatic potential energy curve for the diatom BC in its n^{th} electronic state.

The total angular momentum (\mathbf{J}) for the system is given as the sum of the orbital angular momentum (\mathbf{L}) and the rotational angular momentum (\mathbf{I})

$$\mathbf{J} = \mathbf{I} + \mathbf{L} \quad (3.10)$$

The eigenfunctions $|jlJM\rangle$ of the total angular momentum (\mathbf{J}) are obtained by the direct product of the rotational wavefunction of the diatomic molecule BC ($|jm_j\rangle$) which are the eigenfunctions of the $\hat{\mathbf{I}}^2$ operator and orbital wavefunction ($|lm_l\rangle$) which are the eigenfunctions of the $\hat{\mathbf{L}}^2$ operator. They are coupled by the Clebsch-Gordan coefficients and are represented as

$$|jlJM\rangle = \sum_{m_j} \sum_{m_l} c(jlJ; m_j m_l M) |lm_l\rangle |jm_j\rangle \quad (3.11)$$

where $c(jlJ; m_j m_l M)$ are the Clebsch-Gordan coefficients and M is the projection of \mathbf{J} onto space-fixed axes. It is convenient to expand the total scattering wavefunction $\Psi(\mathbf{R}, \mathbf{r}, \mathbf{q})$ in terms of product of the eigenfunctions $|jlJM\rangle$ of the total angular momentum (\mathbf{J}) and the vibrational wavefunction $|vj\rangle$ and the electronic wavefunction $|n\rangle$ of the diatomic molecule BC (Arthus and Dalgarno, 1960; Balint-Kurti, 1975; Alexander, 1982; Alexander and Corey,

1986)

$$\Psi(\mathbf{R}, \mathbf{r}, \mathbf{q}) = \sum_{J,M} \sum_{n,j,v,l} k_{n,v,j,l}^{J,M} \quad (3.12)$$

where

$$k_{n,v,j,l}^{J,M} = \frac{1}{R} \sum_{n'} \sum_{v',j',l'} f_{n'v'j'l'}^{J,nvjl}(R) |n'\rangle |v'j'\rangle |j'l'JM\rangle \quad (3.13)$$

Using Eq. (3.12) and Eq. (3.13) in Eq. (3.1) and on following the algebra leads to the full close-coupled equations for R-dependent coefficients $f_{n'v'j'l'}^{J,nvjl}(R)$ in which n, v, j and l represents the fixed asymptotic initial state and n', v', j' and l' represents the final state (Arthus and Dalgarno, 1960; Pack, 1974; Parker and Pack, 1978).

$$\begin{aligned} & \left(\frac{d^2}{dR^2} - \frac{l'(l'+1)}{R^2} + k_{n'v'j'l'}^2 \right) f_{n'v'j'l'}^{J,nvjl}(R) \\ &= \frac{2\mu_{ABC}}{\hbar^2} \sum_{n''} \sum_{v''j''l''} \langle j''l''JM | V_{n''v''j''n'v'j'}(R, \gamma) | j'l'JM \rangle f_{n''v''j''l''}^{J,nvjl}(R) \end{aligned} \quad (3.14)$$

where

$$V_{n''v''j''n'v'j'}(R, \gamma) = \langle v''j'' | V_{n'',n'}(R, r, \gamma) | v'j' \rangle \quad (3.15)$$

and

$$V_{n'',n'}(R, r, \gamma) = \langle n'' | \hat{V}(R, r, \gamma, \mathbf{q}) | n' \rangle \quad (3.16)$$

are the matrix elements of the interaction potential operator on the electronic wavefunction over all the electronic coordinates \mathbf{q} . The diagonal terms corresponds to the interaction PES of the electronic states involved, while the nondiagonal terms represent the diabatic coupling between them. The wave vector $k_{n'v'j'}^2$ is defined as

$$k_{n'v'j'}^2 = \frac{2\mu_{ABC}}{\hbar^2} \left(E - \epsilon_{v'j'}^{n'} \right) \quad (3.17)$$

where E is the collision energy and $\epsilon_{v'j'}^{n'}$ are the rotational-vibrational energies of the diatom BC in the n' electronic state and can be obtained from Eq. (3.9).

The close-coupled equations (Eq. (3.14)) are propagated into the asymptotic region where all the terms vanish except the centrifugal part of the potential $\frac{l'(l'+1)}{R^2}$. The close-coupled (Eq. (3.14)) are solved subjected to the boundary condition

$$\begin{aligned}
 f_{n'v'j'l'}^{J,nvj} (R) &\xrightarrow{R \rightarrow 0} 0 \\
 f_{n'v'j'l'}^{J,nvj} (R) &\xrightarrow{R \rightarrow \infty} (k_{n'v'j'})^{-\frac{1}{2}} \left\{ \delta_{nn'} \delta_{vv'} \delta_{jj'} \delta_{ll'} \exp \left[-i \left(k_{nvj} R - \frac{l\pi}{2} \right) \right] \right. \\
 &\quad \left. - S_{n'v'j'l' \leftarrow nvjl}^J \exp \left[i \left(k_{n'v'j'} R - \frac{l'\pi}{2} \right) \right] \right\}
 \end{aligned} \tag{3.18}$$

where $S_{n'v'j'l' \leftarrow nvjl}^J$ are the elements of scattering matrix (S-matrix) and are related to the transition matrix (T-matrix) by

$$T_{n'v'j'l' \leftarrow nvjl}^J = \delta_{nn'} \delta_{vv'} \delta_{jj'} \delta_{ll'} - S_{n'v'j'l' \leftarrow nvjl}^J \tag{3.19}$$

As the collision energy is increased, the size of the coupled equations increases very rapidly because of the $(2l+1)(2j+1)$ multiplicity in the asymptotic states. Therefore, it is important to make reasonable physically valid (sudden) approximation. The history of various quantum sudden approximation has been reviewed elsewhere (Arthus and Dalgarno, 1960; Khare, 1977; Parker and Pack, 1978; Schinke and McGuire, 1978*b*; Gianturco, 1979; Kouri, 1979). Therefore, we briefly summarize the working principles of the VCC-RIOSAs framework in the next section.

3.2 The infinite-order sudden approximation(IOSA)

Although the quantum dynamics of a system can be studied with full close-coupling approach, in principle, it still remains a prohibitive task computationally, particularly for the experimental (moderate and high) collision energy range, where the number of close-coupled equations becomes too large to solve. At a typical collision energy of 10 eV and considering the interaction potential to be short ranged ($\sim 100 a_o$), one estimates the collision time to be of the order of a few sub-femtoseconds which is almost three orders of magnitude less compared to a typical rotational period of a diatom, which is of the order of picoseconds. Thus at relatively high collision energies the rotational motion of the target diatom can be considered to be nearly frozen, that is, the projectile effectively sees a molecule with no rotational angular momentum. This physical situation allows the complete decoupling of rotational and orbital angular momenta resulting in enormous simplification in the coupled equations which is usually referred to as the sudden or the rotational "infinite-order-sudden" (RIOS) approximation.

If the rotational spacing in a molecule is small as compared to the collision energy, then change in the initial and final wavevectors (with respect to the rotational states) is negligible, that is,

$$k_{nvj'}^2 - k_{nvj}^2 = \frac{2\mu_{ABC}}{\hbar^2} (\epsilon_{vj}^n - \epsilon_{nj'}^n) \cong 0 \quad (3.20)$$

and

$$\epsilon_{vj}^n = \epsilon_v^n + B_v^n j(j+1) \hbar^2 \quad (3.21)$$

B_v^n is the rotational constant. Under this approximation one can replace j in Eq. (3.21) with an effective value \bar{j} . In that case, one has two choices for \bar{j} , that is, either $\bar{j} =$ (initial)

j or $\bar{j} = (\text{final}) j'$. One may choose $\bar{j} = j$ which assumes that the elastic component in each set of coupled equations has the correct energy. However, in the sudden approximation one replaces k_{nvj} with k_{nv} for all the rotational states. This assumption is called energy or centrifugal sudden. This implies that the rotational distortion can be (safely) neglected and vibrational-rotational wavefunction of the target molecule $|vj\rangle$ can be replaced by $|v\rangle$ which can be obtained by solving Eq. (3.9) with $j = 0$.

Furthermore, the centrifugal potential $\frac{l(l+1)}{R^2}$ is replaced by an effective centrifugal potential $\frac{\bar{l}(\bar{l}+1)}{R^2}$ for a given total angular momentum J . Here again, one has two reasonable choices for \bar{l} , that is, either $\bar{l} = (\text{initial}) l$ or $\bar{l} = (\text{final}) l'$. It has been shown that both the choices of \bar{l} lead to identical results for degeneracy-averaged cross sections (Khare, 1977; Parker and Pack, 1978; Schinke and McGuire, 1978a). Thus, with the combination of centrifugal sudden and infinite order sudden approximation, the close-coupling equations are modified. The coupled equations in the vibrational close-coupling rotational infinite order sudden approximation (VCC-RIOSAs) can be written as

$$\begin{aligned} & \left(\frac{d^2}{dR^2} - \frac{\bar{l}(\bar{l}+1)}{R^2} + k_{n'v'\bar{j}}^2 \right) f_{n'v'\bar{j}}^{nv\bar{l}}(R; \gamma) \\ &= \frac{2\mu_{ABC}}{\hbar^2} \sum_{n''} \sum_{v''} V_{n''v'',n'v'}(R, \gamma) f_{n''v''}^{nv\bar{l}}(R; \gamma) \end{aligned} \quad (3.22)$$

where the wavevector $k_{n'v'\bar{j}}^2$ is defined as

$$k_{n'v'\bar{j}}^2 = \frac{2\mu_{ABC}}{\hbar^2} \left(E - \epsilon_{v'\bar{j}}^{n'} \right) \quad (3.23)$$

The function $f_{n'v'\bar{j}}^{nv\bar{l}}(R; \gamma)$ depend on the γ angle only parametrically through the anisotropy of the potential matrix $V_{n''v'',n'v'}(R, \gamma)$, so that the Eq. (3.22) can be solved at fixed value

of γ . This yields the angle dependent S-matrix $S_{n'v' \leftarrow nv}^{\bar{j}\bar{l}}(\gamma)$ parameterized by the effective quantum numbers \bar{l}, \bar{j} and defined by the standard boundary conditions in Eq. (3.18). Hence, now the T-matrix elements takes the form

$$T_{n'v' \leftarrow nv}^{\bar{j}\bar{l}}(\gamma) = \delta_{nn'}\delta_{vv'} - S_{n'v' \leftarrow nv}^{\bar{j}\bar{l}}(\gamma) \quad (3.24)$$

Since the S-matrix elements in the ion-molecule systems are known to show a strong γ dependency because of anisotropy existing in the interaction potential, particularly at small \bar{l} , the T-matrix elements are normally expanded in terms of Legendre polynomials (Schinke and McGuire, 1978a) at each \bar{l} as

$$T_{n'v' \leftarrow nv}^{\bar{j}\bar{l}} = \sum_{\lambda} A_{\lambda}^{\bar{l}}(\bar{j}nv \rightarrow n'v') P_{\lambda}(\cos \gamma) \quad (3.25)$$

Using the orthogonality of the Legendre polynomials, it can be shown that the expansion coefficients $A_{\lambda}^{\bar{l}}$ would be determined by a set of linear equations

$$\sum_{\lambda=0}^{N^*} A_{\lambda}^{\bar{l}}(\bar{j}nv \rightarrow n'v') \sum_{i=1}^N P_{\lambda}(\cos \gamma_i) P_{\lambda'}(\cos \gamma_i) = \sum_{i=1}^N T_{n'v' \leftarrow nv}^{\bar{j}\bar{l}}(\gamma_i) P_{\lambda}(\cos \gamma_i) \quad (3.26)$$

where N is the total number of γ values considered and

$$\lambda, \lambda' = 0, 2, 4, \dots, N^*; N^* \leq 2(N - 1) \quad (3.27)$$

for the homonuclear system (B_2), and

$$\lambda, \lambda' = 0, 1, 2, 3, \dots, N - 1; N^* = N \quad (3.28)$$

for the heteronuclear systems (BC).

At higher collision energies vibrational excitations are expected to become the dominant processes in proton-molecule collisions. Rotational transition resolution in the H^+/H energy-loss spectroscopy still pose challenging problems. Therefore, comparison between the experiment and theory is often made for the cross-sections summed over the final rovibrational states. Therefore, we summarize below the working formulae for the degeneracy averaged rotationally-summed cross sections. For their detailed derivations see the reference (Parker and Pack, 1978; Schinke and McGuire, 1978a) and references therein. The rotationally-summed differential cross section are obtained as

$$\begin{aligned} \frac{d\sigma}{d\omega} (\bar{j}nv \rightarrow n'v') &= \sum_{\lambda} (2\lambda + 1)^{-1} \frac{d\sigma^{\lambda}}{d\omega} (\bar{j}nv \rightarrow n'v') \\ \frac{d\sigma^{\lambda}}{d\omega} (\bar{j}nv \rightarrow n'v') &= \frac{1}{4k_{n'v'\bar{j}}^2} \left| \sum_{\bar{l}} (2\bar{l} + 1) P_{\bar{l}}(\cos \theta_{c.m.}) A_{\lambda}^{\bar{l}} (\bar{j}nv \rightarrow n'v') \right|^2 \end{aligned} \quad (3.29)$$

Here $\theta_{c.m.}$ is the c.m scattering angle and $k_{n'v'\bar{j}}^2$ denotes the wavevector in Eq. (3.22). Note that the rotationally-summed cross sections depend on the initial rotational state \bar{j} ($= j$) through the wavenumber $k_{n'v'\bar{j}}$ only, and the dynamical information on the strength of a $j \rightarrow j'$ transition is transformed to the Clebsch-Gordon coefficients. The differential cross sections including the individual rotational transitions are given by

$$\frac{d\sigma}{d\omega} (jnv \rightarrow j'n'v') = \sum_{\lambda} (2\lambda + 1)^{-1} C^2(j\lambda j'; 000) \frac{d\sigma^{\lambda}}{d\omega} (\bar{j}nv \rightarrow n'v') \quad (3.30)$$

where $C^2(j\lambda j'; 000)$ are the Clebsch-Gordon coefficients and $\frac{d\sigma^\lambda}{d\omega}(\bar{j}nv \rightarrow n'v')$ is defined in Eq. (3.29). The calculations are generally performed with rotational quantum number $\bar{j} = 0$ of the target atom. The DCS for any $nvj \rightarrow n'v'j'$ can be performed from $j = 0, nv \rightarrow n'v'j'$ transition as

$$\begin{aligned} \frac{d\sigma}{d\omega}(jnv \rightarrow j'n'v') &= \left(\frac{k_{nv, j=0}}{k_{nvj'}} \right)^2 \sum_{j''} C^2(jj''j'; 000) \\ &\frac{d\sigma}{d\omega}(j = 0, nv \rightarrow j'n'v') \end{aligned} \quad (3.31)$$

Similarly, the rotationally-summed integral cross sections are obtained as

$$\begin{aligned} \sigma(\bar{j}nv \rightarrow n'v') &= \sum_{\lambda} (2\lambda + 1)^{-1} \sigma^\lambda(\bar{j}nv \rightarrow n'v') \\ \sigma^\lambda(\bar{j}nv \rightarrow n'v') &= \frac{\pi}{k_{n'v'\bar{j}}^2} \sum_{\bar{l}} (2\bar{l} + 1) \left| A_{\lambda}^{\bar{l}}(\bar{j}nv \rightarrow n'v') \right|^2 \end{aligned} \quad (3.32)$$

One can also obtain the orientation-dependent integral cross section as

$$\sigma(\bar{j}nv \rightarrow n'v'; \gamma) = \frac{\pi}{k_{n'v'\bar{j}}^2} \sum_{\bar{l}} (2\bar{l} + 1) \left| T_{nv \rightarrow n'v'}^{\bar{l}}(\gamma) \right|^2 \quad (3.33)$$

from which one further obtains a useful angle-dependent quantity called opacity function for each partial wavel \bar{l} as

$$\sigma^{\bar{l}}(\bar{j}nv \rightarrow n'v'; \gamma) = \frac{\pi}{k_{n'v'\bar{j}}^2} (2\bar{l} + 1) \left| T_{nv \rightarrow n'v'}^{\bar{l}}(\gamma) \right|^2 \quad (3.34)$$

All the above computed quantities are discussed in detail in the respective chapters.

3.3 Application of VCC-RIOSAs in ion(atom)-molecule collisions

The decoupling scheme discussed above and their possible failure because of strong dynamical mixing between rotational and vibrational excitation channels in the case of ion-molecule interaction with heavy ions have been extensively discussed by Gianturco (Gianturco, 1979). However, this scheme has been widely used to study a number of ion-molecule collision systems, and it has been shown to be reliable in most of the cases, particularly in the collision energy range 10 eV - 100 eV. Interestingly, the VCC-RIOSAs scheme has been reported to work well for energies as low as $E_{cm} = 3.7\text{eV}$ for the $\text{H}^+ + \text{H}_2$ system (McGuire, 1976; Schinke and McGuire, 1978*a*). It has been argued that the presence of interaction well in the system also helps in increasing the local velocity of the projectile (H^+) in the vicinity of the diatom.

At moderate collision energies in the range 10-30 eV, the dynamics study of proton collisions with H_2 (Schinke and McGuire, 1978*a*; Saieswari and Kumar, 2007*c,a*, 2008*c*), N_2 (Gianturco, Kumar, Ritschel, Vetter, and Zülicke, 1997; Gianturco, Kumar, and Schneider, 1996) and CO (Dhilip Kumar and Kumar, 2004) have been treated under the VCC-RIOSAs scheme yielding results in very good agreement with experiments. Dynamics studies on the $\text{H}^+ + \text{O}_2$ (Sidis, Grimbert, Sizun, and Baer, 1989; Gianturco, Palma, Semprini, Stefani, and Baer, 1990; Saieswari and Kumar, 2007*b*, 2008*a*) were also carried out under this scheme. Also, there are several other collision systems and their quantum dynamics studies have been studied under this scheme. For the reference of earlier studies, see (Parker and Pack, 1978). Other atom-molecule systems have been also studied, for example, the collision of H with D_2 (Zhang, Zhang, Kouri, and Baer, 1987), collision of O with HO_2 (Varandas and Szich-

man, 1998), collision of H with CO (Balakrishana, Yan, and Dalgarno, 2002) and collision of H with SiO (Derouich, 2006) have been studied under the VCC-RIOSAscheme.

CHAPTER 4

NONADIABATIC DYNAMICS ON THE TWO COUPLED ELECTRONIC PESs : THE $H^+ + CO$ SYSTEM

In this chapter, we study the dynamics of the IVE, $H^+ + CO (X^1\Sigma^+, v = 0) \longrightarrow H^+ + CO (X^1\Sigma^+, v')$, and the VCT, $H^+ + CO (X^1\Sigma^+, v = 0) \longrightarrow H ({}^2S) + CO^+ (X^2\Sigma^+, v'')$, processes. The experimental and theoretical data available on the $H^+ + CO$ collision system till date have been reviewed already in detail in **chapter 1**. Here, we focus on the present study by discussing the newly generated global *ab initio* PESs of the GS and the first ES and their topological characteristics. We also present briefly the details of the *ab initio* diabatization procedure used and the corresponding quasi-diabatic PESs computed in the present study. We have performed time-independent quantum dynamics study within the VCC-RIOSAs framework at the experimentally reported collision energies, $E_{cm} = 9.5$ eV and 28.96 eV and compared our results with those of experiments and the earlier theoretical studies. We also provide new complementary state-to-state theoretical data for the VCT channel at $E_{cm} = 9.5$ eV.

4.1 Present focus

Since there have not been any previous structural *ab initio* and quantum dynamics studies involving the GS PES and the first ES PES, we pay our attention to *ab initio* computations of these PESs as well as to their interaction properties such as mixing angle (α), coupling

potential (V_{12}^d) and nonadiabatic coupling matrix elements (NACME). We also examine the role of the other low-lying excited electronic states in influencing the overall collision dynamics of the system relevant to proton energy-loss experiments in the collision energy range $E_{cm} = 9.5-30$ eV, where the experiments (Krutein and Linder, 1979) reveal very little amount of inelastic vibrational excitations of CO as only the $v = 0 \rightarrow v' = 1$ excitation is observed along with very small amount of the $v = 0 \rightarrow v' = 2$ excitation. At these collision energies the involvement of the second and third ESs cannot be ruled out completely, and one also observes rich nonadiabatic interactions among the higher ESs particularly for closer approach of H^+ . However, in the present study, we assume that only the GS ($1^2A'$) and the first ES ($2^2A'$) PESs are primarily involved in the dynamics. Therefore, hereafter, in the present study, we refer to $2^2A'$ state as the first excited state.

As pointed out earlier in **chapter 3**, at these collision energies (9.5 - 30 eV) the collision time becomes much shorter than the rotational period of the diatom. Therefore, one can make physically valid assumption that the relative orientations of the diatom and the projectile are fixed. In such a situation, the nonadiabatic couplings arising from the radial (vibrational-translational) motions become important. Considering that the couplings arising from rotations would be small, the nonadiabatic couplings arising from the $\Sigma - \Pi$ interactions have not been considered in the present study, only the coupling arising from the radial (r, R in the Jacobi coordinates) motions are considered.

4.2 *Ab initio* adiabatic PESs

Ab initio calculations for the system have been carried out in the Jacobi coordinates (see Fig. 3.1 of **Chapter 3**) at the multireference internally contracted configuration interaction

(MRCI) level of accuracy (Werner and Knowles, 1988; Knowles and Werner, 1988, 1992) for the GS and the first ES. The MRCI calculations refer to only the single and double excitations in the configuration interaction calculations and they were carried out to obtain the three-dimensional PESs as a function of r , R and γ on the set of grid points. The grid for γ was kept at the interval of 15° , that is, $\gamma = 0^\circ - 180^\circ(15^\circ)$. The typical grid points for $\gamma = 0^\circ, 90^\circ$ and $\gamma = 180^\circ$ were set as follows

- for $\gamma = 0^\circ$, $R = 1.4 - 2.0(0.2), 2.1 - 4.2(0.1), 4.4 - 6.0(0.2), 7.0 - 10.0(1.0), 12.0 - 20.0(2.0)$
- for $\gamma = 90^\circ$, $R = 0.2 - 2.0(0.2), 2.1 - 4.2(0.1), 4.4 - 6.0(0.2), 7.0 - 10.0(1.0), 12.0 - 20.0(2.0)$
- for $\gamma = 180^\circ$, $R = 2.1 - 4.2(0.1), 4.4 - 6.0(0.2), 7.0 - 10.0(1.0), 12.0 - 20.0(2.0)$
- for each γ , $r = 1.5 - 3.2(0.1)$

The numbers in the parenthesis indicate the increments in the given intervals. $\gamma = 0^\circ$ and $\gamma = 180^\circ$ signify the approaches of H^+ towards the oxygen and the carbon atom of the CO molecule, respectively

We present now some of the computational details of *ab initio* calculations. At the Hartree-Fock (HF) level, the chosen basis set produced 74 contracted molecular orbitals (MO) and they were listed out as $33a_1, 17b_1, 17b_2, 7a_2$ in the C_{2v} point group and $50a', 24a''$ in the C_s point group. Note that for the collinear and the perpendicular ($\gamma = 0^\circ, 180^\circ$ and 90°) geometries the calculations were performed using the C_{2v} point group, and for all off-collinear geometries the calculations were done in the C_s point group for the singlet spin symmetry employing Dunning's *cc-pVTZ* basis set (Dunning, 1989) using the MOLPRO software (Werner, Knowles, Schütz, Lindh, Celani, Korona, Rauhut, Manby, Amos, Bernhardsson, Berning, Cooper, Deegan, Dobbyn, Eckert, Hampel, Hetzer, Lloyd, McNicholas, Meyer, Mura, Nickla β , Palmieri, Pitzer, Schumann, Stoll, Stone, Tarroni, and Thorsteinsson,

2002). The valence MOs in these point groups are $5a_1, 2b_1, 2b_2$ and $7a', 2a''$, respectively. The $1a_1, 2a_1$ MOs in the C_{2v} and $1a', 2a'$ MOs in the C_s are treated as core orbitals. At the HF level, the ground state electronic configurations are $5a_1, 1b_1, 1b_2$ and $6a', 1a''$ for the C_{2v} and the C_s geometries, respectively. Note that all the MOs are doubly occupied accounting for 14 electrons for the triatomic $[\text{HCO}]^+$ system. For the MRCI calculations (Werner and Knowles, 1988; Knowles and Werner, 1988, 1992) the two doubly occupied core orbitals were frozen, that is, they were excluded from the excitations. Thus, 4 core electrons were kept frozen and only the 10 valence electrons were considered in the single and the double excitations and we refer this to MRCI and, hereafter, we report only the MRCI values for the system. The number of active orbitals for the C_{2v} and the C_s point groups were $7a_1, 2b_1, 2b_2$ and $7a', 8a', 9', 2a''$, respectively. The number of external orbitals for the two symmetries were $63 : (25a_1 + 15b_1 + 15b_2 + 7a_2)$ for the C_{2v} and $(41a' + 22a'')$ for the C_s . The threshold value of energy was kept at 0.32×10^{-3} hartrees. The CI wavefunction consists of 520 CSFs in the reference space, 5292 CSFs in N electron internal space, 8292 CSFs in N-1 electron internal space and 8412 CSFs in N-2 electron internal space. The total number of contracted configurations is 223986, out of this internal configurations is 1436 singly external configurations is 137096 and doubly external configurations is 85454 and of uncontracted configurations is 4405136. These details are for the collinear geometry (C_{2v} point group). For off-collinear geometries (C_s point group), the CI wavefunction consists of 2744 CSFs in the reference space, 5292 CSFs in N electron internal space, 8820 CSFs in N-1 electron internal space, 12852 CSFs in N-2 electron internal space. The total number of contracted configurations is 448260, out of which, the number of internal configurations is 2744 and of the singly and the doubly external configuration are 279692 and 165824 and total number of uncontracted configuration are 4405136.

Before we present and discuss the results it would be worthwhile to compare the computed parameters for the diatoms CO(CO⁺) with those obtained from the experiments. The comparisons are reported for the CO and the CO⁺ molecules in Table 4.1. The various symbols used in these tables have been explained there. One can see that almost all the experimental data have been predicted quite well.

Table 4.1: Comparison of computed molecular properties of CO and CO⁺ with experiments. r_{eq} is equilibrium bond distance. D_0 is the dissociation energy in the GS. I.P is the ionization potential. $\Delta E_{rot}^{0 \rightarrow 1}$ is the energy of first rotational excitation, $j = 0 \rightarrow j = 1$ expressed in milli eV in the GS. $\Delta E_{vib}^{0 \rightarrow 1}$ is the energy of first vibrational excitation, $v = 0 \rightarrow v = 1$ in the GS. $\Delta E_{elec}^{0 \rightarrow 1}$ is the energy of first electronic excitation from $v = 0$ of the GS to $v' = 0$ of the first ES and D is the dipole moment for the GS expressed in atomic units.

	CO(¹ Σ ⁺)						
	r_{eq} (bohr)	D_0 (eV)	I.P(eV)	$\Delta E_{rot}^{0 \rightarrow 1}$ (meV)	$\Delta E_{vib}^{0 \rightarrow 1}$ (eV)	$\Delta E_{elec}^{0 \rightarrow 1}$ (eV)	D(a.u)
Present	2.147	10.825	13.68	0.39	0.2635	6.0457	0.07255
Mulliken and Ermler ^a	2.1357	11.09					
Mizushima ^b			14.0	0.48	0.266	5.898	
Hagstrum and Tate ^c		9.6	14.1				
Stogryn and Stogryn ^d							-0.044
Huber and Herzberg ^e	2.1325	11.108	14.0	0.48	0.2691		
	CO ⁺ (² Σ ⁺)						
Present	2.123	8.1665	27.1890	0.485	0.2677	2.574	-1.029
Huber and Herzberg ^e	2.1077	9.9	27.90	0.49	0.2745		
Reddy and Viswanath ^f		8.33					

^aExpt : Mulliken and Ermler (1977)

^bExpt : Mizushima (1975)

^cExpt : Hagstrum and Tate (1941)

^dExpt : Stogryn and Stogryn (1966)

^eExpt : Huber and Herzberg (1979)

^fExpt : Reddy and Viswanath (1990)

In order to further test the quality of the generated PESs, we compare the collinear equilibrium geometry properties of the bound molecular ions, HCO⁺ and HOC⁺, in terms of bond distances at their respective minima in the global GS PES in Table 4.2 along with the earlier theoretical and experimental values. The highest level of computations involve CCSD(T) calculations employing *cc-pVQZ* basis set (Martin, Taylor, and Lee, 1993; Mladenović and Schmatz, 1998). The latter authors generated the semi-global GS PES in order to

Table 4.2: Equilibrium geometry (collinear) data for the bound HCO^+ and HOC^+ ions. The bond distances are in \AA .

	$\text{HCO}^+ (\gamma = 180^\circ)$		$\text{HOC}^+ (\gamma = 0^\circ)$	
	r_{HC}	r_{CO}	r_{HO}	r_{CO}
Martin <i>et al.</i> (1993)	1.0930	1.1080	0.9900	1.1579
Mladenović and Schmatz (1998)	1.0935	1.1086	0.9904	1.1579
Grunenberg <i>et al.</i> (2003)	1.0912	1.1066	0.9891	1.1553
Dhilip Kumar and Kumar (2004)	1.0898	1.1056	0.9889	1.1563
Present	1.1018	1.1082	0.9882	1.1532
Woods (1988) (Expt)	1.0972	1.1047	0.9750	1.1570

characterize the potential wells corresponding to stable HCO^+ and HOC^+ isomers. More recent calculations have been done at $\text{CCSD(T)/aug-cc-pVQZ}$ and cc-pVTZ levels (Grunenberg, Streubel, Frantzius, and Marten, 2003; Dhilip Kumar and Kumar, 2004). It is gratifying to note that the present calculations predict the bond distances of these collinear isomers in good agreement with the existing theoretical and experimental data (data in the present work printed in bold in Table 4.2) thus lending credence and confidence to the present *ab initio* computations. We further compare our results with those of the theoretical results obtained by Bruna *et al.* (1975) in Table 4.3 in terms of the location of minima for collinear approaches of H^+ towards CO. Both results are matching very well.

Table 4.3: Calculated minimum energy geometries for $\text{H}^+ - \text{CO}$. r_m is the distance between the atoms of the diatom, R_m is the distance between the center of mass of the diatom and the proton, γ is the angle between r_m and R_m , ϵ is the well depth.

	$r_m(\text{\AA})$	$R_m(\text{\AA})$	$\gamma(\text{deg})$	$\epsilon(\text{eV})$
Bruna <i>et al.</i> (1975)	1.11	1.56	0	6.26
	1.17	1.47	180	5.46
Present	1.153	1.482	0	4.87
	1.108	1.735	180	6.56

We present the adiabatic PECs for the GS (red) and the first ES (blue) for three molecular orientations $\gamma = 0^\circ, 90^\circ, 180^\circ$ in Fig. 4.1 as a function of R at $r_{eq} = 2.13a_0$. The symmetry

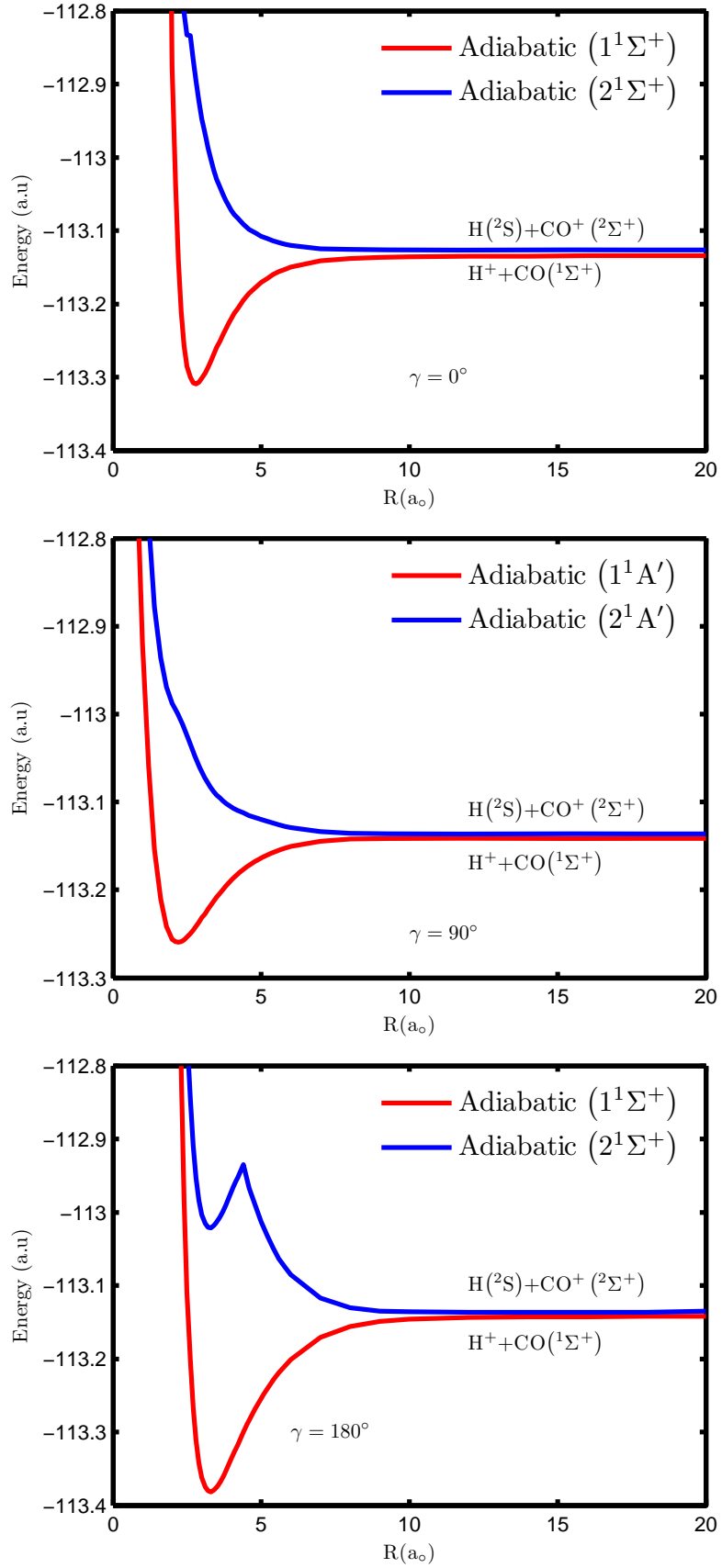
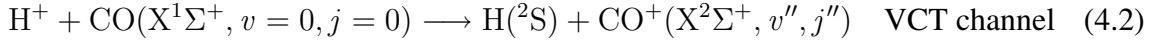


Figure 4.1: The adiabatic GS and first ES PECs for $\gamma = 0^\circ, 90^\circ$ and 180° as a function of R for $r = r_{eq} = 2.13a_0$.

designations of the GS and ES PECs are $1^1\Sigma^+$ and $2^1\Sigma^+$ for collinear orientations ($C_{\infty v}$) and $1^1A'$ and $2^1A'$ for off-collinear orientations (C_s), respectively. As one can see from Fig. 4.1, there is a hump at $R = 4.4a_0$ for $\gamma = 180^\circ$ which is missing in other two angles and also for $R > 10a_0$ both the GS and first ES PECs run parallel to each other with very small energy gap. In the asymptotic regions, the GS correlates with the $H^+ + CO(X^1\Sigma^+)$ while the first ES correlates with the $H(^2S) + CO^+(X^2\Sigma^+)$. Therefore, the IVE and the VCT channels for the system are :



Since the GS and the first ES lie very close to each other energetically for $R > 10a_0$ it suggests that the ES is accessible from the GS by Rosen-Zener-Demkov type of coupling (Demkov, 1964; Nakamura, 1996; Rosen and Zener, 1932). The experimentally reported (Niedner-Schatteburg and Toennies, 1992) value for the endoergicity of the two asymptotic channels is ~ 0.42 eV. We compare this value with those of experiment and earlier theoretical data in Table 4.4. The theoretical values are obtained for $R = 20a_0$, $r = r_{eq} = 2.13a_0$

Table 4.4: Comparison of endoergicity of VCT process relative to IVE process with experimental as well as theoretical data

	R (bohr)	r_{eq} (bohr)	γ (deg)	endoergicity(eV)
Expt ^a				0.42
Present	20	2.13	90°	0.1439
Kimura <i>et al.</i> (2000)	20	2.13	90°	0.14

^aNiedner-Schatteburg and Toennies (1992)

and $\gamma = 90^\circ$ and appears to be somewhat underestimating.

At short distances $R < 5a_0$ and at r_{eq} , there exists a coupling between the first ES and

second ES of Σ symmetry for $\gamma = 180^\circ$ but not for $\gamma = 0^\circ$ and $\gamma = 90^\circ$. The sharp peak visible in $\gamma = 180^\circ$ is due to an avoided crossing of the first ES with second ES. However, this coupling appears to be not present or negligible for other angles and becomes important for proton approaches towards the C-end of the CO molecules ($\gamma = 180^\circ$). We now show in Fig. 4.2 the adiabatic GS and the ES PECs for $\gamma = 0^\circ, 90^\circ, 180^\circ$ as a function of r for R fixed at $3a_0$ and $5a_0$. The symmetry designations remains the same as that of previous Fig. 4.1. The bottom figure is shown for $R = 5a_0$ so that the hump in the ES PEC can be highlighted. For $\gamma = 0^\circ$, the hump appears at shorter distance, ($R = 3a_0$). These humps again arise because of the avoided crossings of the first ES and the second ES. Interestingly, no such coupling appears to exist for $\gamma = 90^\circ$. The coupling between the GS and the first ES appears to be important either for small approaches of H^+ and mostly for larger values of r . This aspect will be further discussed a little later.

Kimura *et al.* (2000) had also computed the GS and the first ES of Σ or A' symmetries for these three molecular orientations using Dunning's *cc-pVTZ* (Dunning, 1989) basis set and MRDCI method (Kimura, Gu, Hirsch, Buenker, and Stancil, 2000). We compare our results with theirs in Fig. 4.3 and observe that both the results match rather closely except a few noticeable deviations as can be seen in Fig. 4.3. One among the reasons for this difference could be attributed to the difference in the selection of configurations or the difference in the optimization of orbitals in their computation. Another small deviation is that for $\gamma = 90^\circ$, the endoergicity computed in the present calculations appears to be slightly overestimating than that obtained by them. Their PECs for the first ES also show the sign of avoided crossing with the second ES as a function of R at $r = r_{eq}$.

The *ab initio* adiabatic PESs for the GS ($1^1\Sigma^+$) and the first ES ($2^1\Sigma^+$) for the system are

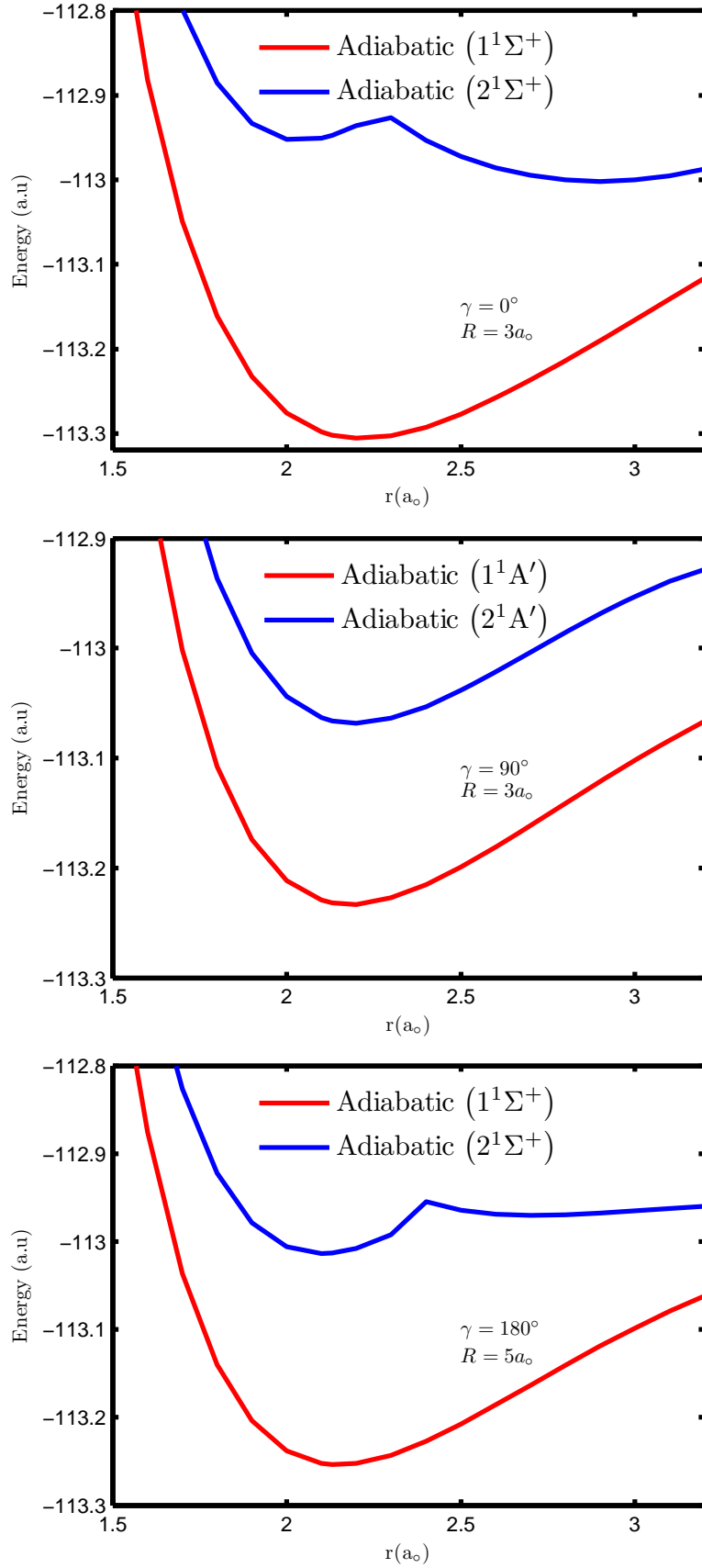


Figure 4.2: The adiabatic GS and first ES PECs for $\gamma = 0^\circ, 90^\circ$ and 180° as a function of r at R fixed at $3a_0$ and $5a_0$. The energy is in atomic units and r is in the units of bohr

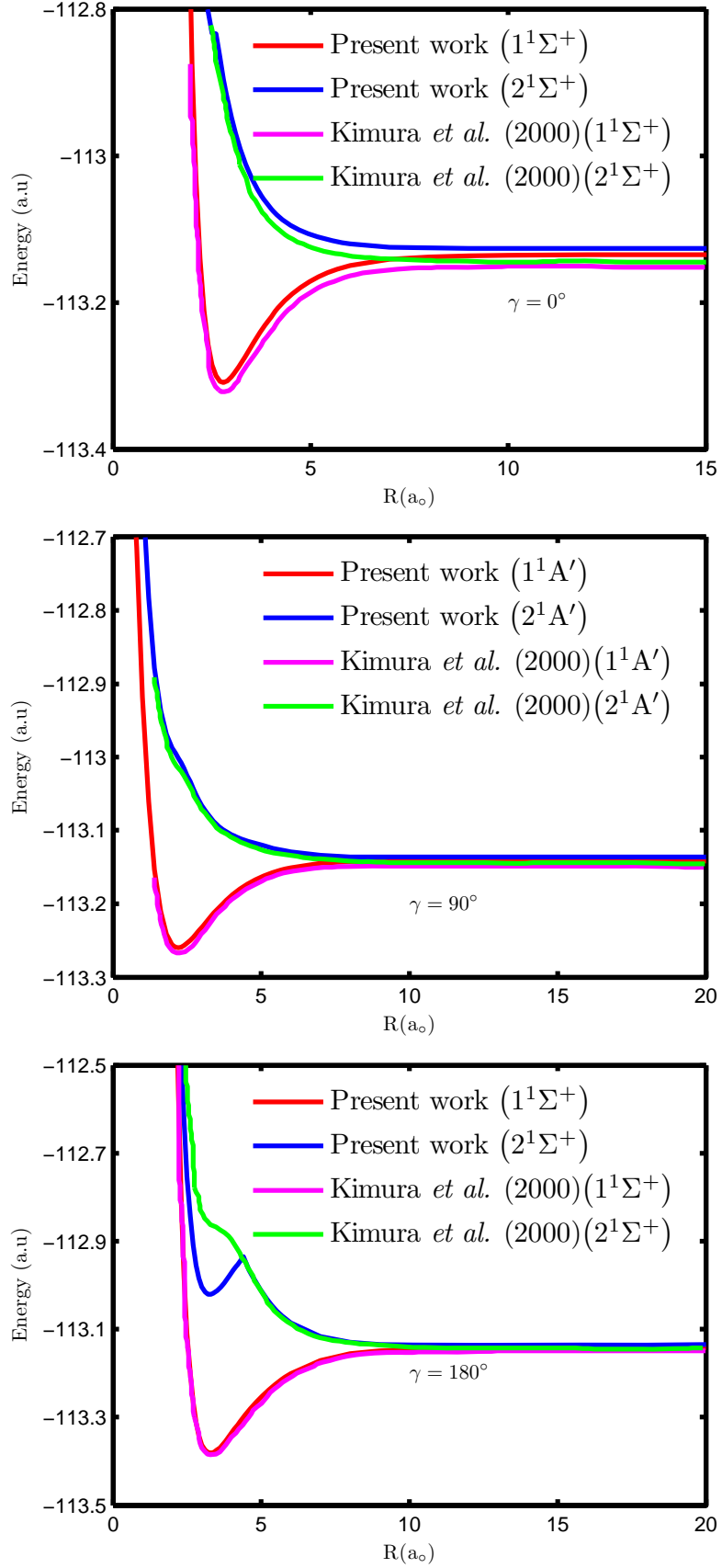


Figure 4.3: Comparison between our adiabatic GS and first ES PECs for $\gamma = 0^\circ, 90^\circ$ and 180° as a function of R at $r = r_{eq} = 2.13a_0$. The available PECs of Kimura *et al.* (2000) have also been reproduced.

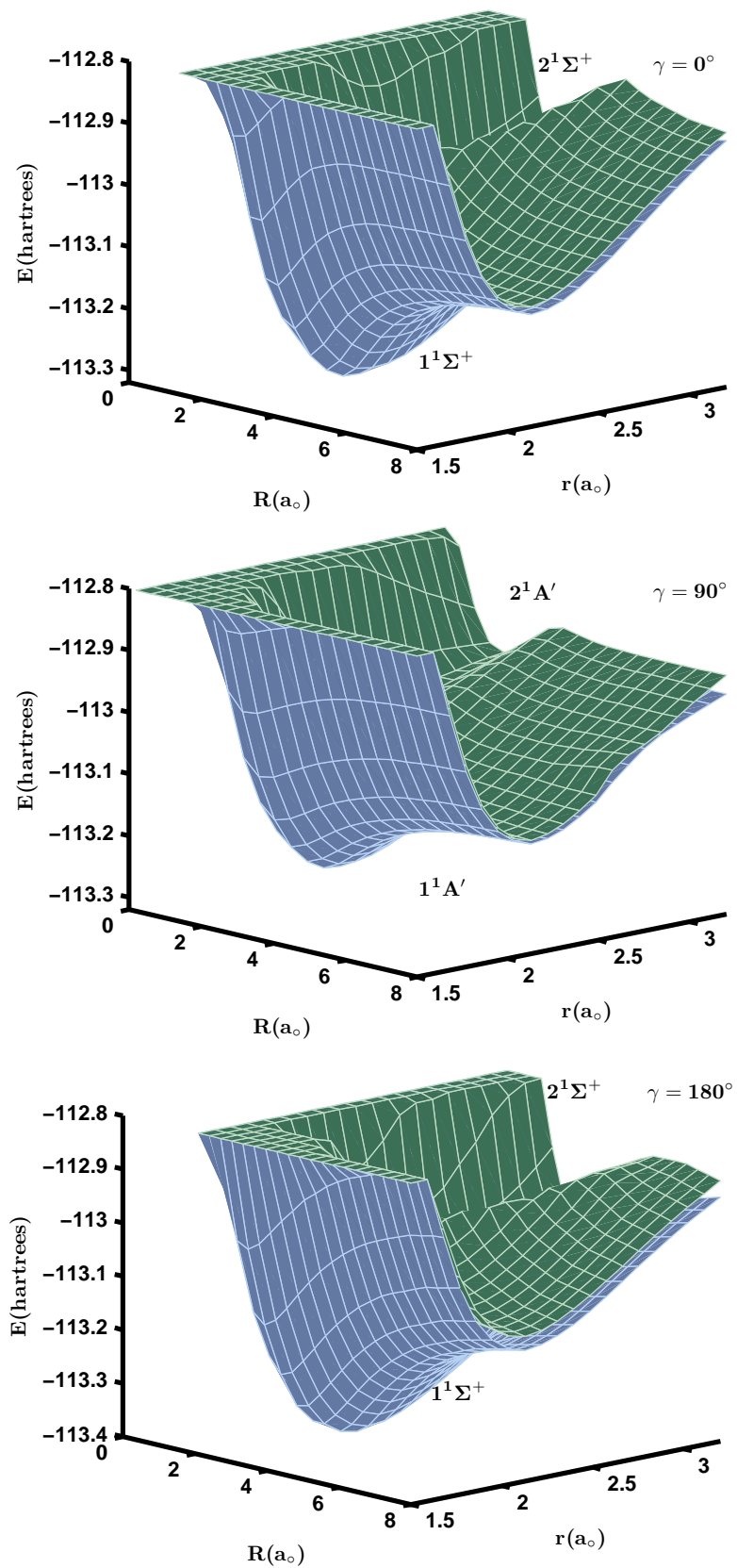


Figure 4.4: The adiabatic PESs as a function R and r for $\gamma = 0^\circ, 90^\circ$ and 180° for the GS and the first ES PESs. The distances are in bohr and energy in atomic units (hartrees)

shown in for $\gamma = 0^\circ, 90^\circ, 180^\circ$ in Fig. 4.4. Here we are able to get a full three-dimensional view of the PESs as a function of R and r for a fixed value of γ . The GS and the first ES asymptotically correlate to $\text{H}^+ + \text{CO}(X^1\Sigma^+)$ and $\text{H}(^2S) + \text{CO}^+(X^2\Sigma^+)$ channels, respectively. To further illustrate the characteristics of the PESs we have shown the corresponding contour plots in Fig. 4.5. The GS PES exhibits a deep interaction well for all γ values while the first ES PES shows mostly a repulsive behaviour with a ridge suggesting the existence of avoided crossing with the second ES ($3^1\Sigma^+$) PES. The two PESs have been again displayed

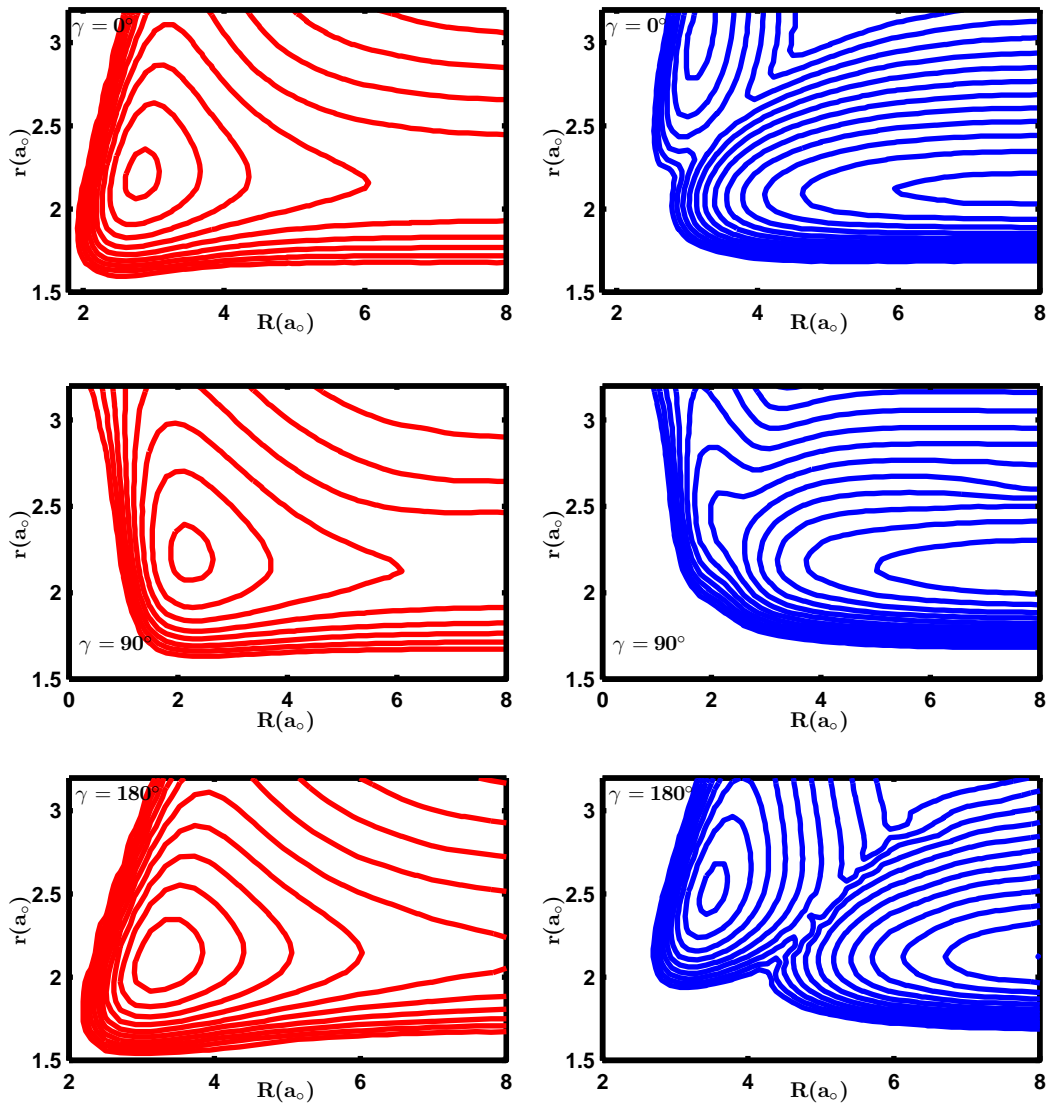


Figure 4.5: Contour diagrams of the GS (left) and ES (right) PESs of the $\text{H}^+ + \text{CO}$ system as a function of R and r for $\gamma = 0^\circ, 90^\circ, 180^\circ$

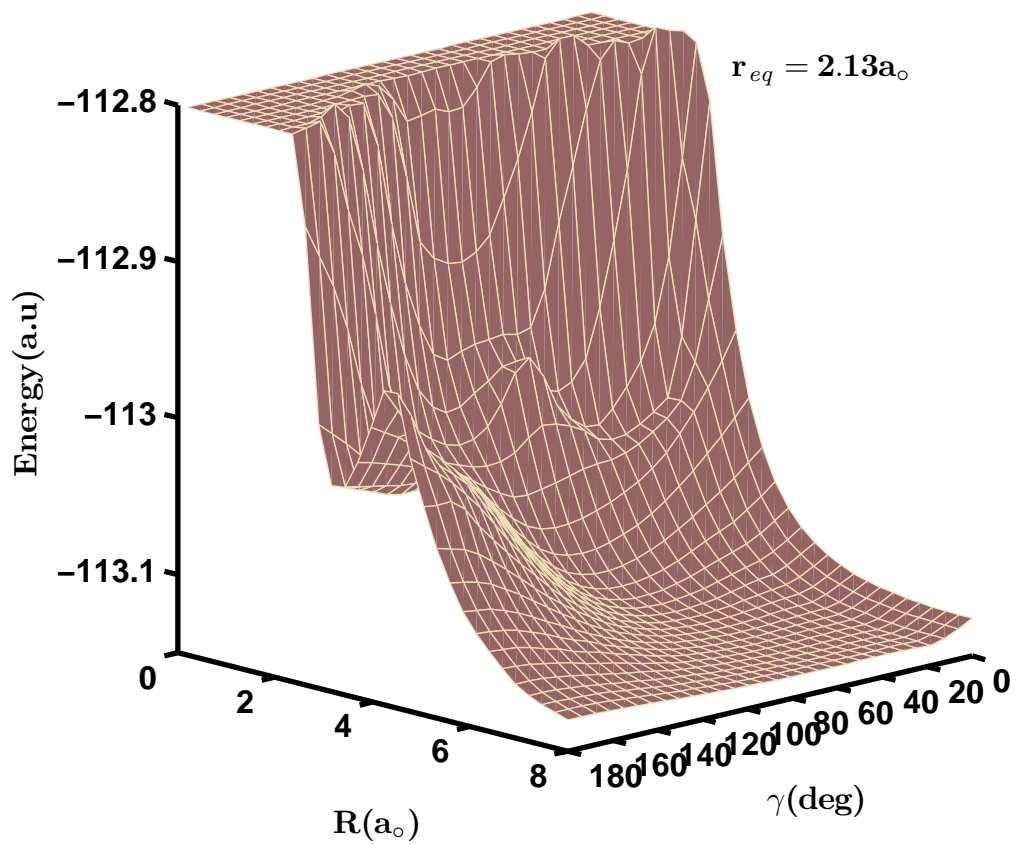
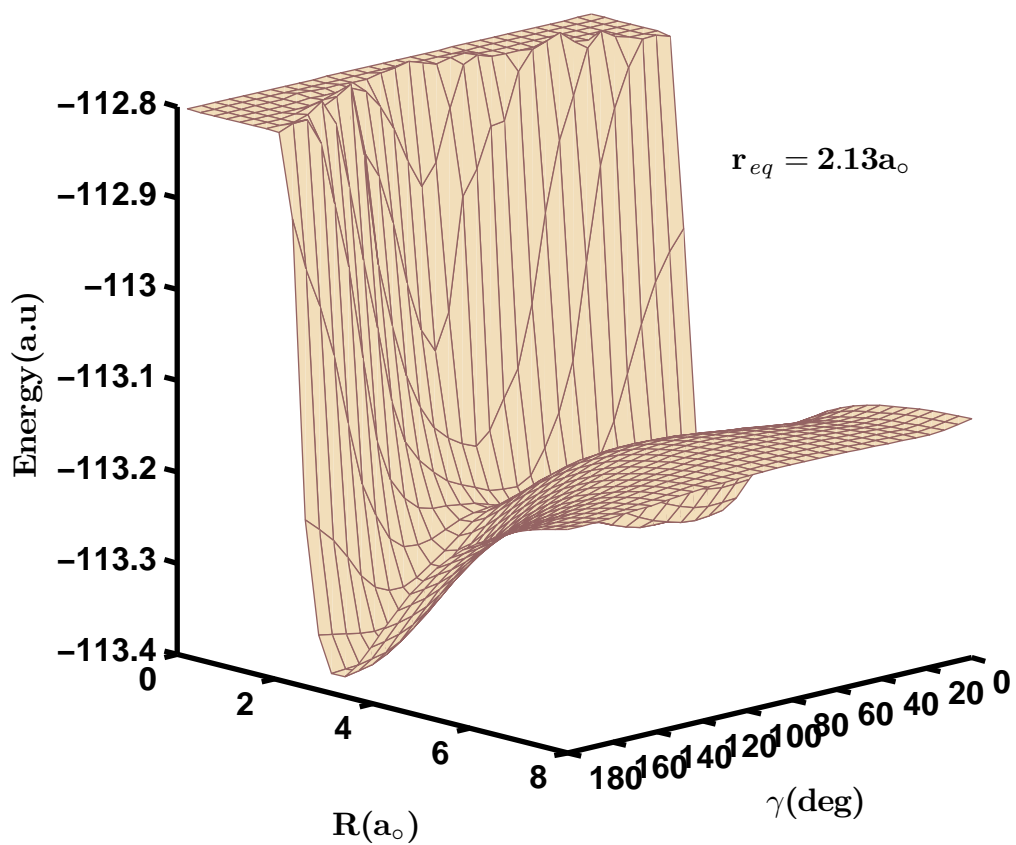


Figure 4.6: The adiabatic GS and ES PES as a function R and γ for fixed $r = r_{eq} = 2.13a_0$. The R is in bohr and γ is in degrees and energy in atomic units (hartrees)

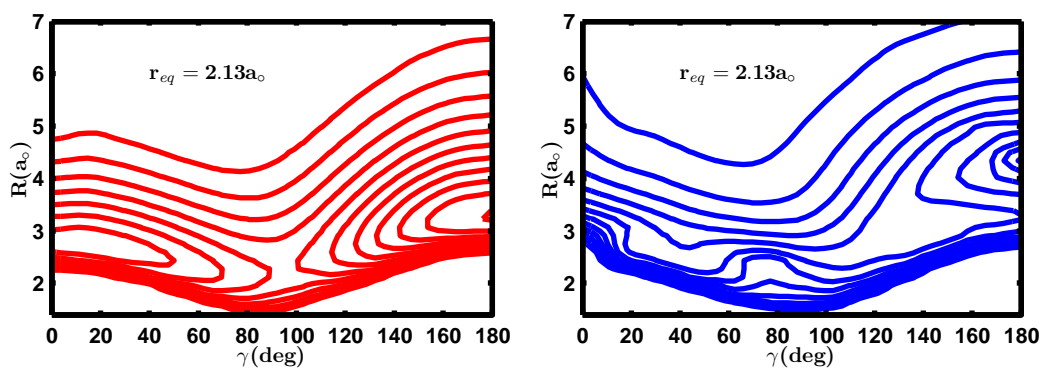


Figure 4.7: Contour diagrams of the GS (left) and ES (right) PES of HCO^+ system as a function of R and γ for fixed $r = r_{eq} = 2.13a_0$

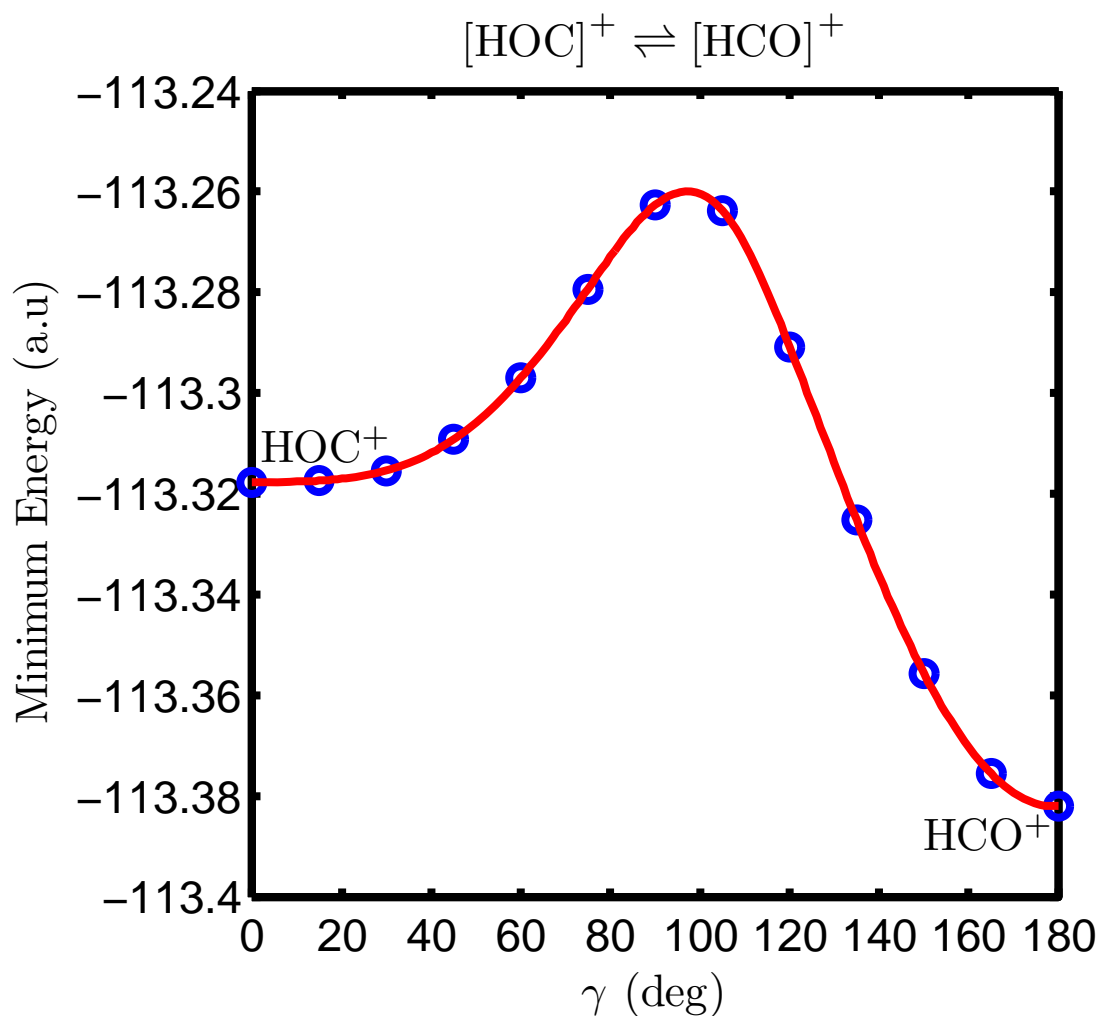


Figure 4.8: The splined minimum energy pathway of adiabatic GS showing minimum and maximum during the interconversion process, $\text{HOC}^+ \rightleftharpoons \text{HCO}^+$

Table 4.5: The local energy minima of the adiabatic GS PES and the well depth at each local minima relative to the asymptotic products is listed out as a function of Jacobi coordinates (R, r, γ) .

γ	r	R	Adiabatic GS Energy (a.u)	Well depth ^a (eV)
0°	2.2	2.8	-113.317665	4.788091185
15°	2.2	2.8	-113.317419	4.781397525
30°	2.2	2.6	-113.315359	4.725344925
45°	2.2	2.5	-113.309201	4.557785745
60°	2.2	2.3	-113.296959	4.224680925
75°	2.2	2.2	-113.279291	3.743934645
90°	2.2	2.2	-113.262659	3.291377925
105°	2.2	2.4	-113.263764	3.321444975
120°	2.13	2.7	-113.290738	4.055407515
135°	2.13	2.9	-113.325219	4.993635525
150°	2.1	3.1	-113.355590	5.820030435
165°	2.1	3.2	-113.375529	6.362570625
180°	2.1	3.3	-113.382035	6.539599429

^arelative to asymptotic energy limit, $E = -113.14169693$ a.u, corresponding to $\text{H}^+ + \text{CO}(X^1\Sigma^+, r = r_{eq})$ products.

in Fig. 4.6 but as a function of R and γ with r fixed at $r_{eq} = 2.13a_0$. The corresponding contour plots are shown in Fig. 4.7. From the adiabatic PESs, we tabulate local minima and their location as a function of γ in Table 4.5 and the minimum energy is plotted in Fig. 4.8 against γ . The well depth is relative to asymptotic product of the IVE channel. We can see that HCO^+ is the most stable isomer corresponding to $\gamma = 180^\circ$, followed by HOC^+ , corresponding to $\gamma = 0^\circ$ for the interconversion process. The transition state isomer of this process lies at $\gamma = 97.2^\circ$, possessing the electronic energy of -113.261 a.u and the energy difference between this least stable isomer and the most stable isomer is computed to be 3.29 eV.

4.3 Asymptotic interaction potential

The long range interaction potential V_{as} for the $\text{H}^+ + \text{CO}$ system is modelled and obtained in terms of multipolar expansion terms which is given below

$$V_{as}(R, r; \gamma) \sim \frac{\mu(r)}{R^2} P_1(\cos \gamma) + \frac{Q(r)}{R^3} P_2(\cos \gamma) - \frac{\alpha_0(r)}{2R^4} - \frac{\alpha_2(r)}{2R^4} P_2(\cos \gamma) \quad (4.3)$$

where V_{as} is the asymptotic potential, $\mu(r)$ is the dipole moment of CO, $Q(r)$ is the quadrupole moment of CO, $\alpha_0(r)$ and $\alpha_2(r)$ are the polarizability components of CO, P_1, P_2 are the Legendre polynomials. All the above mentioned properties are computed using MOLPRO (Werner, Knowles, Schütz, Lindh, Celani, Korona, Rauhut, Manby, Amos, Bernhardsson, Berning, Cooper, Deegan, Dobbyn, Eckert, Hampel, Hetzer, Lloyd, McNicholas, Meyer, Mura, Nicklaß, Palmieri, Pitzer, Schumann, Stoll, Stone, Tarroni, and Thorsteinsson, 2002) with *cc-pVTZ* basis set and MRCI level of theory as a function of bond distance (r) of CO and the computed values are fitted with a quartic polynomial given below

$$f(r) = a_0 + a_1(r - r_{eq}) + a_2(r - r_{eq})^2 + a_3(r - r_{eq})^3 + a_4(r - r_{eq})^4 \quad (4.4)$$

where $r_{eq} = 2.132a_0$ is the equilibrium bond distance of CO and a_0, a_1, a_2, a_3, a_4 are the unknown coefficients and are tabulated in the Table 4.6. For the VCT process, $\text{H}(^2\text{S}) + \text{CO}^+(1^2\Sigma^+)$, only the polarizability component of the H atom ($\alpha_0 = 2.7372922\text{a.u.}$) was used to generate asymptotic potentials. These are then matched with the respective *ab initio* electronic energy to get long range PESs which are subjected to the computation of vibrational coupling matrix elements.

Table 4.6: Values of coefficients (a.u) used in Eq. (4.4) for the prediction of μ , Q , α_0 and α_2 as a function of r

f	a_0	a_1	a_2	a_3	a_4
μ	0.057	-0.6636	0.0008	0.1337	-0.0054
Q	-1.46	1.03	0.40	-	-
α_0	13.19	5.52	1.74	-0.35	-0.33
α_2	3.66	8.28	3.32	-0.24	-0.42

4.4 *Ab initio* quasi-diabatic PESs

An adiabatic-to-diabatic transformation has been made for the sake of computational convenience for the dynamics study. In the diabatic representation the nuclear KE operator \hat{T} becomes diagonal and potential energy operator \hat{V} becomes nondiagonal which are nondiagonal and diagonal, respectively, in the adiabatic representation. The diabatization procedures, their exactness and their associated advantages for numerical computations have been discussed and documented in the literature in detail (Smith, 1969; Mead and Truhlar, 1982; Sidis, 1992; Pacher, Cederbaum, and Köppel, 1993; Adhikari and Billing, 2002; Baer, 2002*a,b*; Child, 2002; Worth and Robb, 2002; Jasper, Zhu, Nangia, and Truhlar, 2004; Köppel, 2004; Vertesi, Bene, Vibok, Halasz, and Baer, 2005). A general discussion on it has been recently published (General Discussion, 2004). The nonadiabatic coupling matrix elements (NACME) in the KE operator (\hat{T}) are of the form

$$\left\langle \phi_1^a \left| \frac{\partial^l}{\partial \mathbf{q}^l} \right| \phi_2^a \right\rangle \quad (4.5)$$

where $l = 1$ (first order NACME) or 2 (second order NACME). The kets $|\phi_1^a\rangle$ and $|\phi_2^a\rangle$ represent the real electronic wavefunctions of the two involved adiabatic electronic states and \mathbf{q} stands for the Jacobi coordinate as mentioned in Fig. 3.1 of **Chapter 3**. The terms

with $l = 2$ are mostly smaller in magnitude and are generally ignored in the dynamical calculations. In the present calculations they have been ignored.

For the two-state coupling, the transformation from an adiabatic representation with electronic wavefunctions $\phi_{1,2}^a$ to a diabatic representation characterized by the electronic wavefunctions $\phi_{1,2}^d$ is achieved by the unitary transformation,

$$\begin{pmatrix} \phi_1^d \\ \phi_2^d \end{pmatrix} = \begin{pmatrix} \cos \alpha & \sin \alpha \\ -\sin \alpha & \cos \alpha \end{pmatrix} \begin{pmatrix} \phi_1^a \\ \phi_2^a \end{pmatrix} \quad (4.6)$$

where α is the mixing angle describing the mixing between the two adiabatic electronic states and is a function of R , r and γ . Using Eq. (4.6), the matrix elements of \hat{H}_{el} in the diabatic representation are given by

$$\begin{aligned} V_{11}^d &= \langle \phi_1^d | \hat{H}_{el} | \phi_1^d \rangle = V_1^a \cos^2 \alpha + V_2^a \sin^2 \alpha \\ V_{22}^d &= \langle \phi_2^d | \hat{H}_{el} | \phi_2^d \rangle = V_1^a \sin^2 \alpha + V_2^a \cos^2 \alpha \\ V_{12}^d &= \langle \phi_1^d | \hat{H}_{el} | \phi_2^d \rangle = (V_1^a - V_2^a) \cos \alpha \sin \alpha \end{aligned} \quad (4.7)$$

where $\phi_{1,2}^d$ are the (real) electronic wavefunction of the two coupled states in the diabatic representation and their corresponding potential values are given by V_{11}^d and V_{22}^d . $V_{1,2}^a$ are the potential energy values in the adiabatic representation whose corresponding electronic wavefunctions are given by $\phi_{1,2}^a$. The coupling between the two states in the diabatic representation is given by V_{12}^d and $V_{12}^d = V_{21}^d$.

In the diabatic representation one sets the condition that the first order NACME, that is, assuming a one dimensional case, $\mathbf{q} = R$, $\langle \phi_1^d | \frac{d}{dR} | \phi_2^d \rangle = 0$ (or it becomes vanishingly small in case of quasidiabatic states). Therefore, using (4.6) one arrives at the following

relation:

$$\left\langle \phi_1^a \left| \frac{d}{dR} \right| \phi_2^a \right\rangle = \frac{d\alpha}{dR}. \quad (4.8)$$

The mixing angle α can be obtained by integration of first order NACME values

$$\alpha(R) = \alpha_{R_{ref}} + \int_{R_{ref}}^R \left\langle \phi_1^a \left| \frac{d}{dR'} \right| \phi_2^a \right\rangle dR' \quad (4.9)$$

where $\alpha_{R_{ref}}$ is chosen to be zero at $R = R_{ref}$, assuming that the adiabatic and diabatic representation become identical at R_{ref} . In the case of multidimensional problem the integration involves a contour integral over the coordinates.

Other approximate methods (see Simah, Hartke, and Werner (1999) and references therein) have also been suggested which avoid direct computation of NACME and where α is obtained from the CI coefficients of the electronic wavefunctions. An improvement has also been suggested in this scheme by determining the (quasi)diabatic wavefunctions (and the corresponding CI vectors) so that they vary as little as possible as a function of geometry. This condition is met by using the invariance of the MRCI energies with respect to unitary transformation among the active orbitals so that the geometry dependence of the orbitals is minimized. This is accomplished by maximizing the overlap for all the pairs of active orbitals at R_{ref} with those at neighbourhood geometry R' using the Jacobi rotation technique. In this paper, we adopt this procedure. We have used MOLPRO (version 2002.6) software (Werner, Knowles, Schütz, Lindh, Celani, Korona, Rauhut, Manby, Amos, Bernhardsson, Berning, Cooper, Deegan, Dobbyn, Eckert, Hampel, Hetzer, Lloyd, McNicholas, Meyer, Mura, Nicklaß, Palmieri, Pitzer, Schumann, Stoll, Stone, Tarroni, and Thorsteinsson, 2002) to compute α for the 2×2 case, involving the $1^1A'$ (GS) and the $2^1A'$ (ES) states with $R_{ref} = 16a_0$ (for a fixed γ) as a function of R and parametrically dependent on r .

First we analyse the nonadiabatic effects between the electronic states in terms of the nonadiabatic coupling matrix elements (NACME). Mathematically, it is denoted as $\left\langle \phi_1^a \left| \frac{\partial^l}{\partial \mathbf{q}^l} \right| \phi_2^a \right\rangle$ where the kets $|\phi_1^a\rangle$ and $|\phi_2^a\rangle$ represent the adiabatic electronic wavefunctions of the two involved electronic states, \mathbf{q} stands for the nuclear coordinates, that is, R and r and where $l = 1$ (first order NACME), and $l = 2$ (second order NACME). The second order NACMEs are generally very small in magnitude and are mostly ignored in the dynamics calculations. The first order NACME is computed between GS and ES by the numerical differentiation using the finite difference method, $\left\langle \phi_1^a \left| \frac{d}{dR} \right| \phi_2^a \right\rangle = \frac{1}{2\Delta R} \langle \phi_1^a (R_o + \Delta R) | \phi_2^a (R_o - \Delta R) \rangle$, where ΔR is the small increment, taken as $\Delta R = 0.0002a_o$ in our computation, as function of R , keeping r and γ fixed. Thus, we obtained the first order NACME as a function r and R for a fixed value of γ . As an illustration, we show the computed first order NACME as a function of R in Fig. 4.9 alone for a fixed $r = r_{eq} = 2.13a_o$ for those three molecular orientation. We also compare the computed NACME values with those of Kimura *et al.* (2000). Our first order NACME for 90° is actually little higher than those of Kimura *et al.* (2000) whereas for other two angles the difference is not so pronounced between present NACME values and that of Kimura *et al.* (2000). Overall, present work values are overestimated than that of Kimura *et al.* (2000) for all three orientations. Fig. 4.10, illustrates the variations of the NACME values as a function of r and R for $\gamma = 0^\circ, 90^\circ$ and 180° . They are high at small r values for 0° , and in the case of 90° , they are high at $r = 2.5a_o$ and roughly at $R \approx 6a_o$ and in 180° orientation, they are small everywhere between GS and first ES. For the entire r range, when R exceeds $10a_o$, the surface becomes flat and reaches the values of zero, indicating that both adiabatic and diabatic surfaces coincides in these regions.

It is important to note that the α can be obtained from the knowledge of NACME values ((4.9)). Alternatively, α can also be obtained using the *ab initio* procedure (Simah, Hartke,

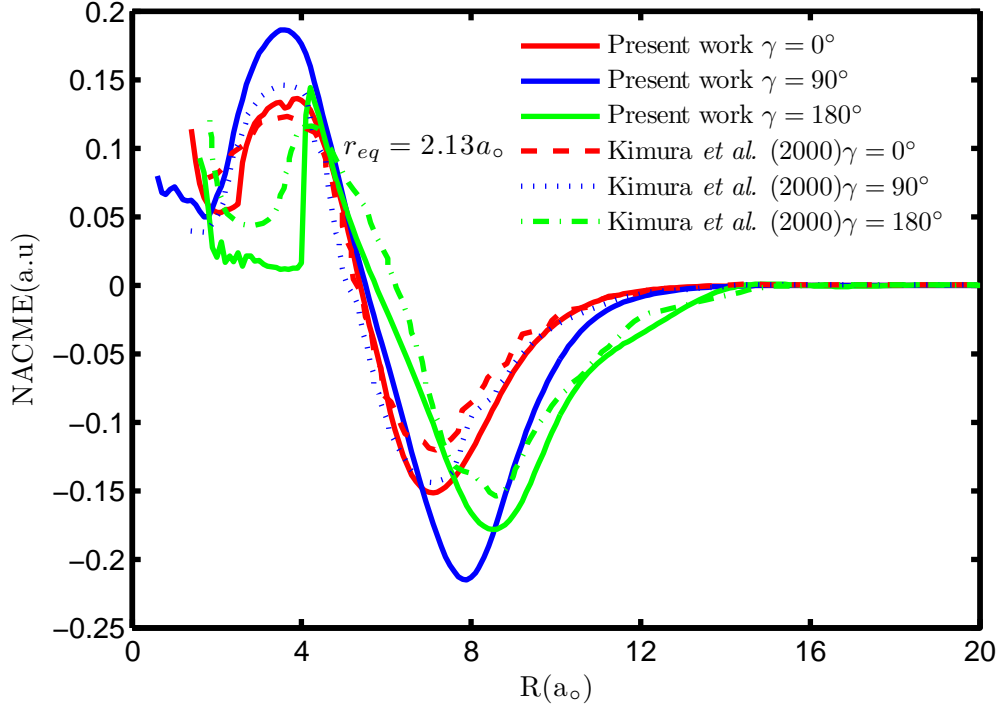


Figure 4.9: The first-order NACME as a function R for a fixed $r = r_{eq} = 2.13a_0$ for $\gamma = 0^\circ, 90^\circ$ and 180° orientations between GS and first ES PESs and compared with Kimura *et al.* (2000). The R are in bohr units and first order NACME $\langle \phi_1^a | \frac{d}{dR} | \phi_2^a \rangle$ in a.u.

and Werner, 1999). It is worthwhile to point out that both procedures gave almost identical results. The computed values of mixing angle using the *ab initio* procedure are displayed as a function of r and R for $\gamma = 0^\circ, 90^\circ$ and 180° in Fig. 4.11. The mixing angle surfaces show a gaussian type of shape reaching perfectly flat when $R > 10a_0$ for the entire range of r and the changes in α happen only when $R < 10a_0$. The region where α assumes the value of zero means that in those region, both adiabatic and diabatic PESs merge together. Hence, we can expect the difference in adiabatic and diabatic PECs below $R = 10a_0$.

Once α is known the corresponding (quasi) diabatic potential matrix can be obtained using Eq. (4.7). In Fig. 4.12, we show and compare the diabatic PECs with those of adiabatic PECs for the GS and the ES for r_{eq} for three molecular orientations as a function of R . The Fig. 4.12 shows that the diabatic curves are sandwiched between the two adiabatic

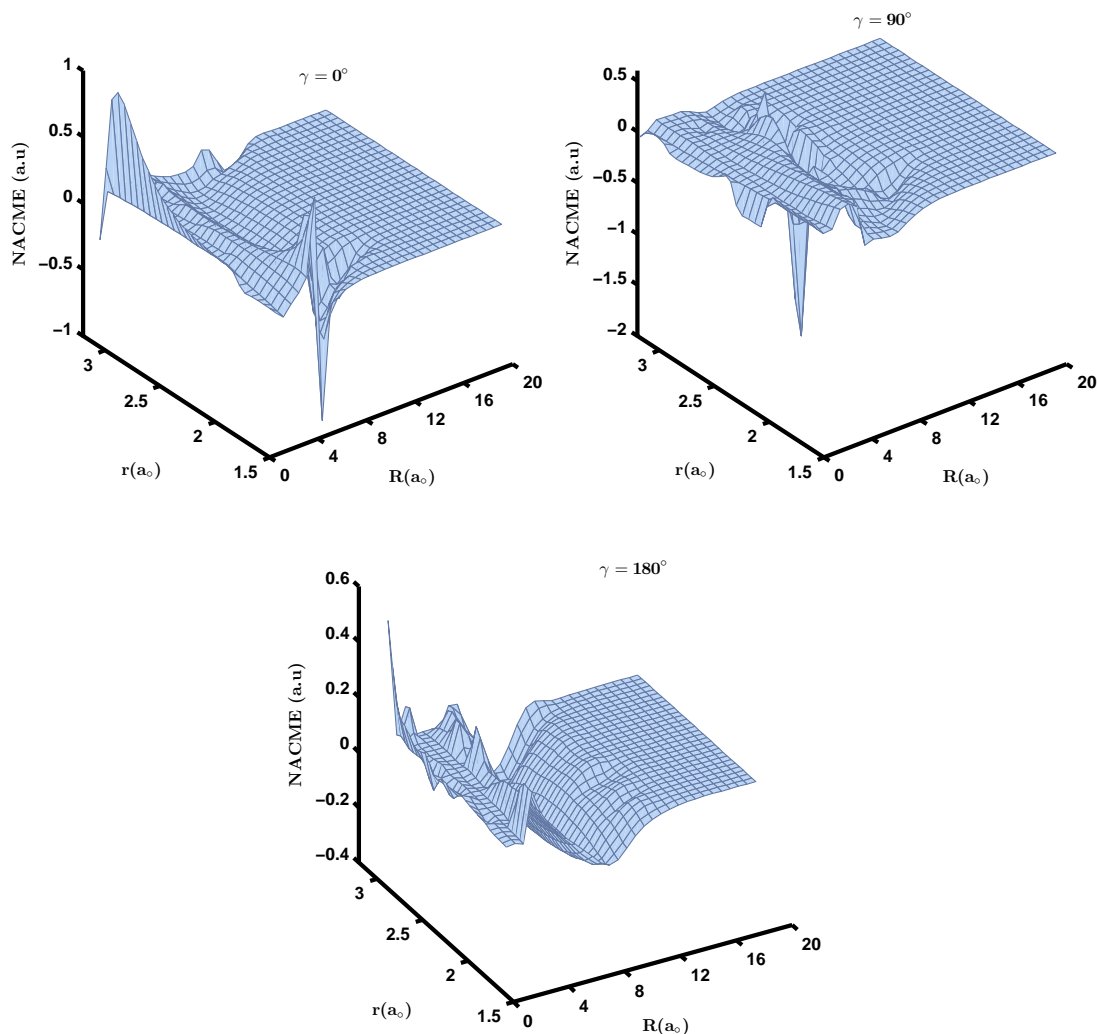


Figure 4.10: First-order NACME between the GS and the first ES PESs as a function R and r for $\gamma = 0^\circ, 90^\circ$ and 180° orientations. The R and r are in bohr units and the NACME values are in a.u.

curves in all three cases and as we move from 0° to 180° we can see the extent of deviation from the adiabatic curve and is largest in 180° . At long range of R , both adiabatic and diabatic energies become equal in all three cases.

After the detailed analysis of the diabatic PECs, it is time to take a look at the diabatic PESs for three cases and they are shown in Fig. 4.13. Both the adiabatic and quasidiabatic PESs look similar except the deviations in energies in certain regions. Also, there is no crossing between these two diabatic surfaces as it happened in their adiabatic counterpart in

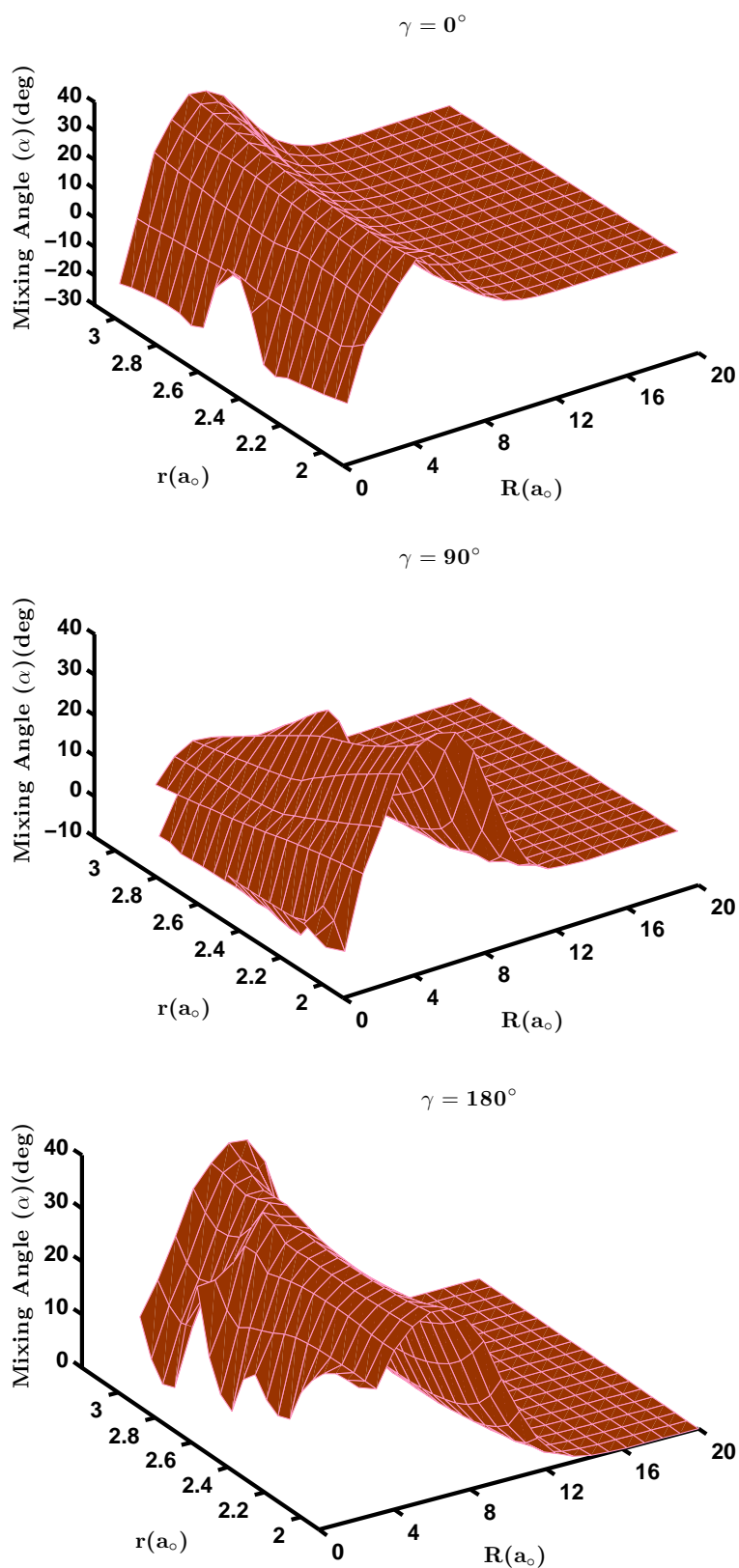


Figure 4.11: The mixing angle as a function R and r for $\gamma = 0^\circ, 90^\circ$ and 180° orientations between GS and first ES PESs. The R and r are in bohr units and mixing angle in degrees

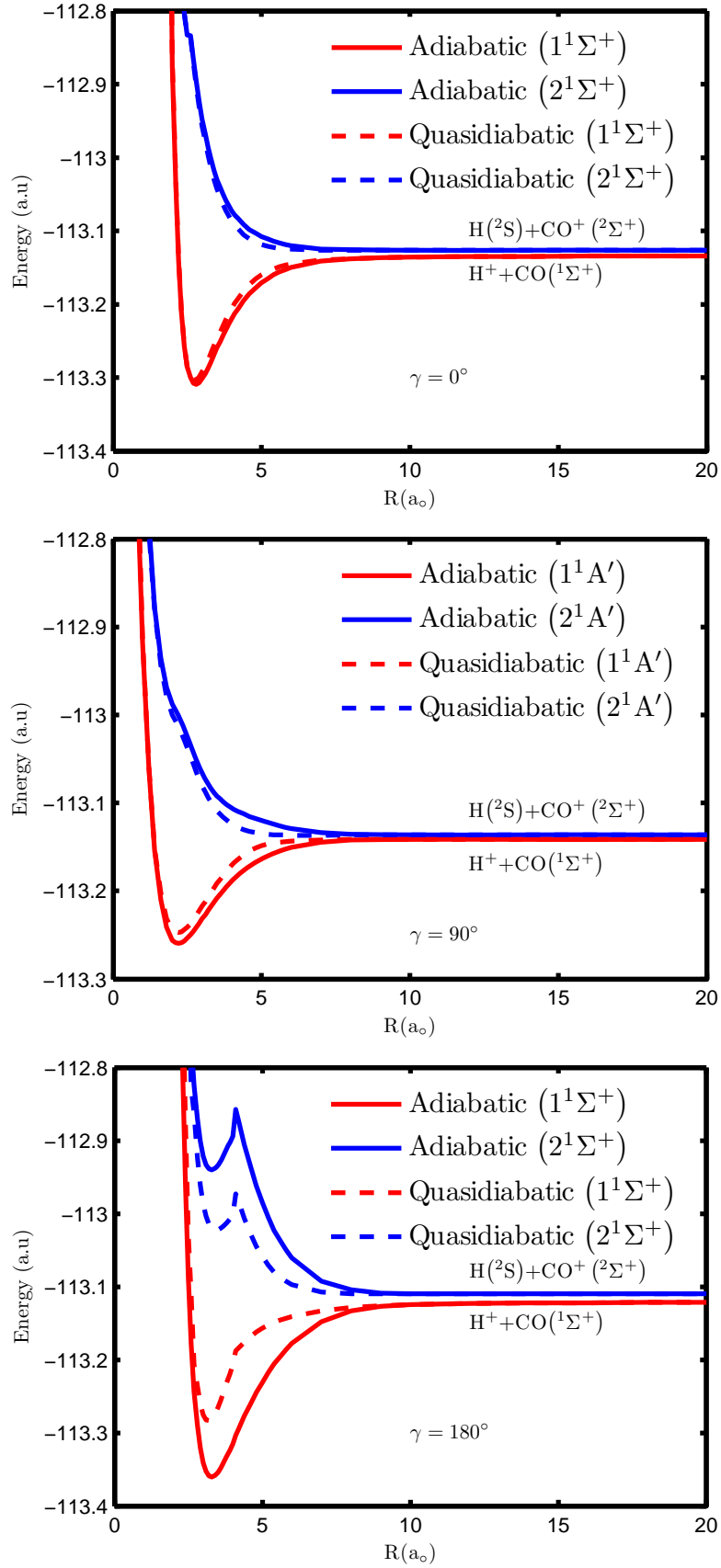


Figure 4.12: The quasidiabatic PECs as a function R (distance of H⁺ from the cm of CO) at $r_{eq} = 2.13a_0$ for $\gamma = 0^\circ, 90^\circ$ and 180° orientations for GS and first ES superposed with the corresponding adiabatic PECs for comparison

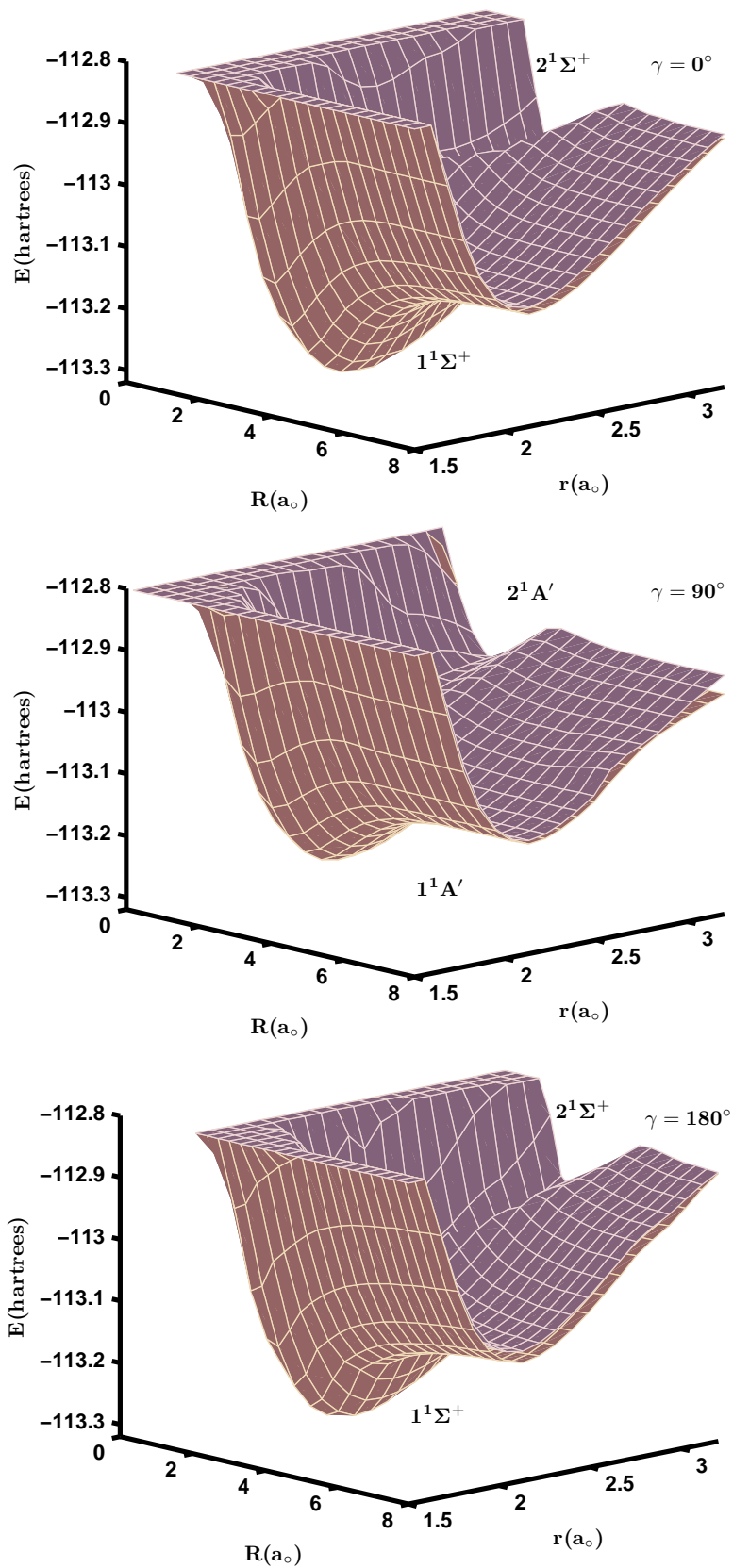


Figure 4.13: The diabatic PESs as a function R and r for $\gamma = 0^\circ, 90^\circ$ and 180° orientations for GS and first ES PESs. The lengths are in bohr and energy in atomic units (hartrees).

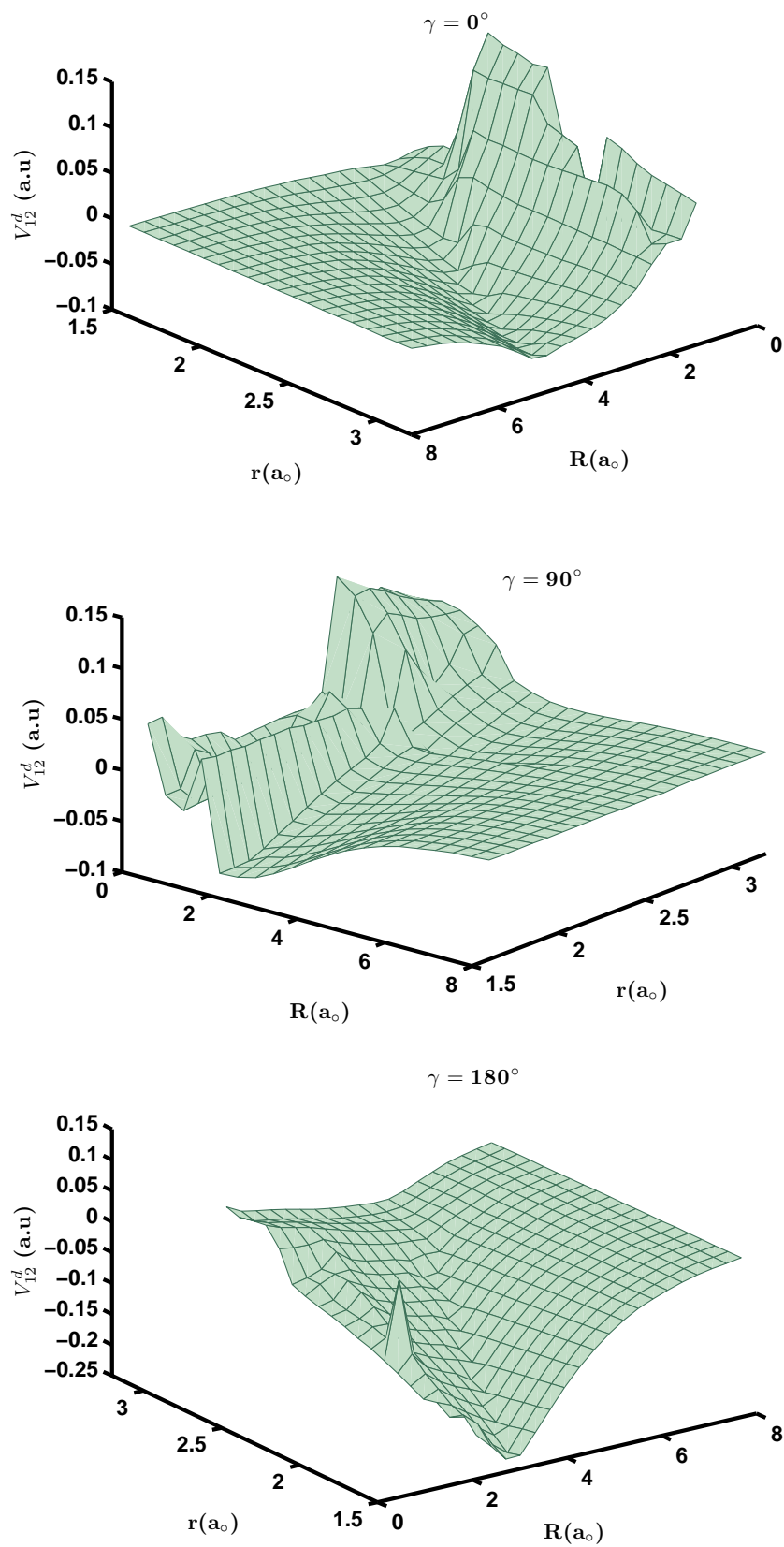


Figure 4.14: The coupling potential as a function R and r for $\gamma = 0^\circ, 90^\circ$ and 180° orientations between GS and first ES PESs. The R and r are in bohr units and coupling potential V_{12}^d in a.u.

the entire range of r and R for a fixed γ . In Eq. (4.7), $V_{12}^d = V_{21}^d$ is the coupling potential (off-diagonal elements in 2×2 potential energy matrix in the diabatic representation) between the GS PES and the ES PES. This coupling potential is a function of R and r , parametrically dependent on γ and is measure of influence of GS PES over the ES PES or vice versa. In Fig. 4.14, we show the coupling potential surfaces for $\gamma = 0^\circ, 90^\circ, 180^\circ$ as a function of r and R for a fixed value of γ . From the Fig. 4.14, it is found that coupling potential range for 180° in the z-axis is from 0.15a.u to -0.25a.u, unlike the other two cases wherein it is from 0.15a.u to -0.1a.u. This means that influence of GS PES over ES PES or vice versa is more in the case of 180° . Even though the magnitude of coupling potential is very small compared to the actual potential energy of individual electronic states, this can be taken as an evidence of existence of nonadiabatic effect between the two electronic states.

4.5 Vibrational coupling matrix elements ($V_{vv'/v''}(R; \gamma)$)

Before we present the results of quantum dynamics it would be desirable to analyse some of the computed vibrational coupling matrix elements (VCMs) which have strong bearing on both the IVE, $\text{H}^+ + \text{CO}(v = 0) \longrightarrow \text{H}^+ + \text{CO}(v')$ and the VCT, $\text{H}^+ + \text{CO}(v = 0) \longrightarrow \text{H}(^2\text{S}) + \text{CO}^+(v'')$ channels. They are defined as $V_{vv'/v''}(R; \gamma) = \langle \chi_v(r) | V^{in}(R, r, \gamma) | \chi_{v'/v''}(r) \rangle$ where $\chi_v(r)$ represents the initial vibrational wavefunction of the diatom CO/CO⁺, and $\chi_{v'/v''}(r)$ represent the final vibrational wavefunction of the diatom CO/CO⁺ respectively. v refers to the initial vibrational state of a diatom and v' and v'' refer to the final vibrational state of CO/CO⁺ respectively. $V^{in}(R, r, \gamma) = V(R, r, \gamma) - V(R = \infty, r, \gamma)$ and is 2×2 quasidiabatic potential matrix where the diagonal elements, V_{11}^d and V_{22}^d , stand for the interaction potential for the GS and the first ES, respectively and they tend to zero in

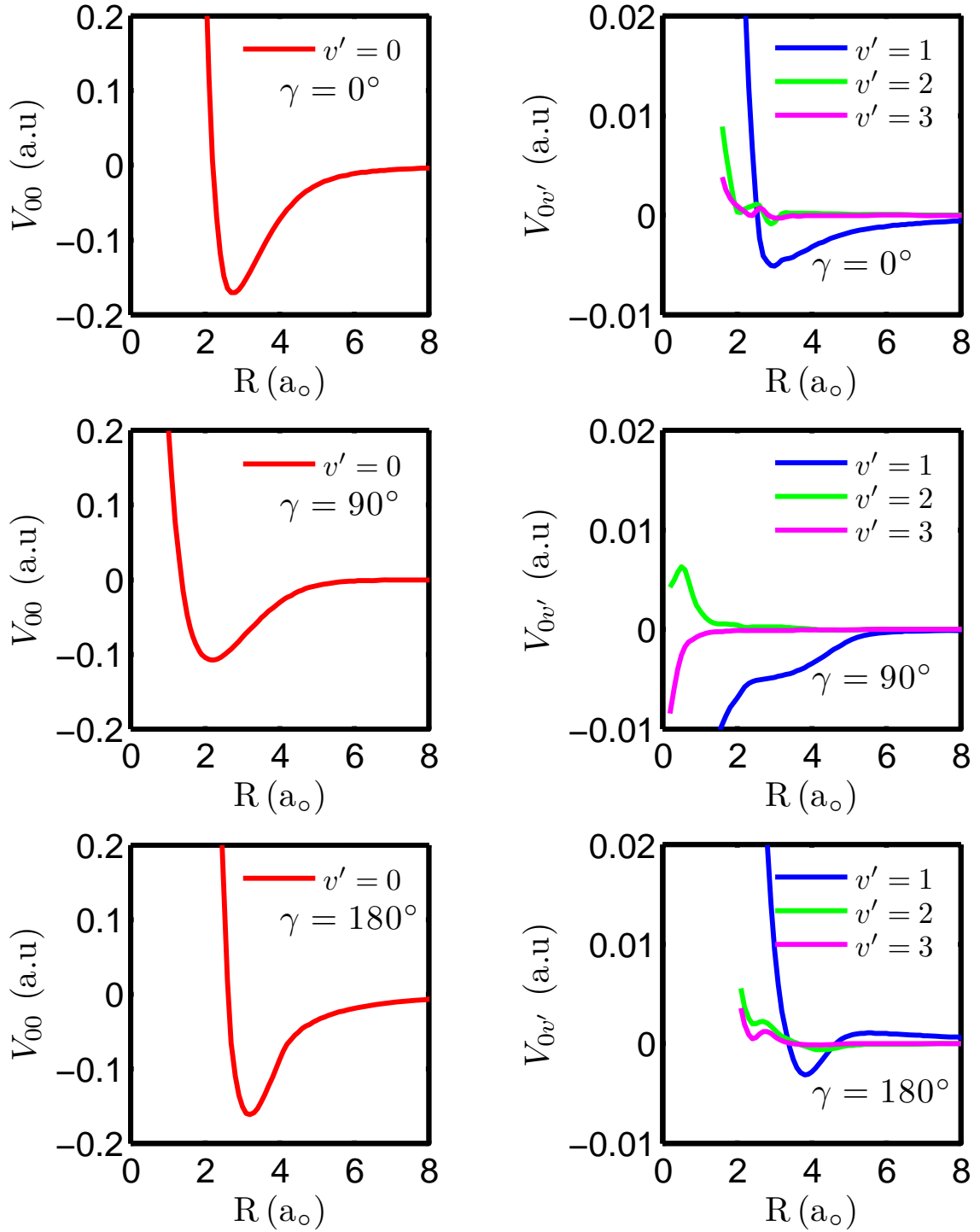


Figure 4.15: Vibrational coupling matrix elements ($V_{vv'}$) for the IVE channel, $\text{H}^+ + \text{CO}(v = 0) \rightarrow \text{H}^+ + \text{CO}(v')$, as a function of R for $\gamma = 0^\circ, 90^\circ, 180^\circ$. Elastic channel V_{00} (left panel) and Inelastic channel $V_{0v'}$ (right panel). See the text

the asymptotic limit. $V_{12}^d (= V_{21}^d)$ are the coupling potential which also tend to zero in the asymptotic limit.

In Fig. 4.15, we show the computed VCME as a function of R for $\gamma = 0^\circ, 90^\circ$ and 180° for both elastic (left panel) and inelastic (right panel) vibrational excitation channels. From the Fig. 4.15, we can easily see that the vibrational coupling matrix elements for elastic channels V_{00} (left panel) is relatively large, smooth and shows a deep attractive well when compared to that of inelastic channels $V_{0v'}$ (right panel). This means that the vibrationally elastic channel will be the strongest in the IVE process. The magnitude of VCMEs follow the order: $V_{01} > V_{02} > V_{03}$ and this trend is found for all angular approaches and the higher order inelastic channels such as V_{04}, V_{05}, V_{06} etc are so small that they are not included in the Fig. 4.15. The trend in $V_{vv'}$ shows that vibrational inelasticity in this system is rather small in accordance with the experimental observation of (Gianturco, Gierz, and Toennies, 1981; Krutein and Linder, 1979).

In Fig. 4.16, we show the computed VCMEs ($V_{vv''}$) for VCT channel as a function of R for $\gamma = 0^\circ, 90^\circ$ and 180° for the cases V_{00} (left) and $V_{0v''}$ (right). The VCT V_{00} channel shows stronger coupling with the translation motion of H^+ than those of VCT $V_{0v''}$ channels and it is almost of the same order of magnitude as that of the IVE V_{00} channel. Unlike in the case of IVE channel (see Fig. 4.15), the VCT V_{00} channel does not show any deep attractive well but rather a repulsive and an exponential decaying curve in $\gamma = 0^\circ$ and $\gamma = 90^\circ$ and a exponential decaying curve with a hump in-between for 180° . The VCT $V_{0v''}$ channel (right panel) show weak coupling with translational mode of H^+ as indicated by their small values which follows the trend $V_{01} > V_{02} > V_{03}$, indicating that the probability of coupling with ($v'' = 0$) level of CO^+ by H^+ from ($v = 0$) level of CO is the highest, followed by ($v'' = 1$) and ($v'' = 2$) and so on. The coupling strength is reduced from VCT V_{00} to VCT V_{01}, V_{02}, V_{03} by roughly 20 times and even more for higher order VCT channels which is highly insignificant. This trend is observed in all the angular approaches and higher order

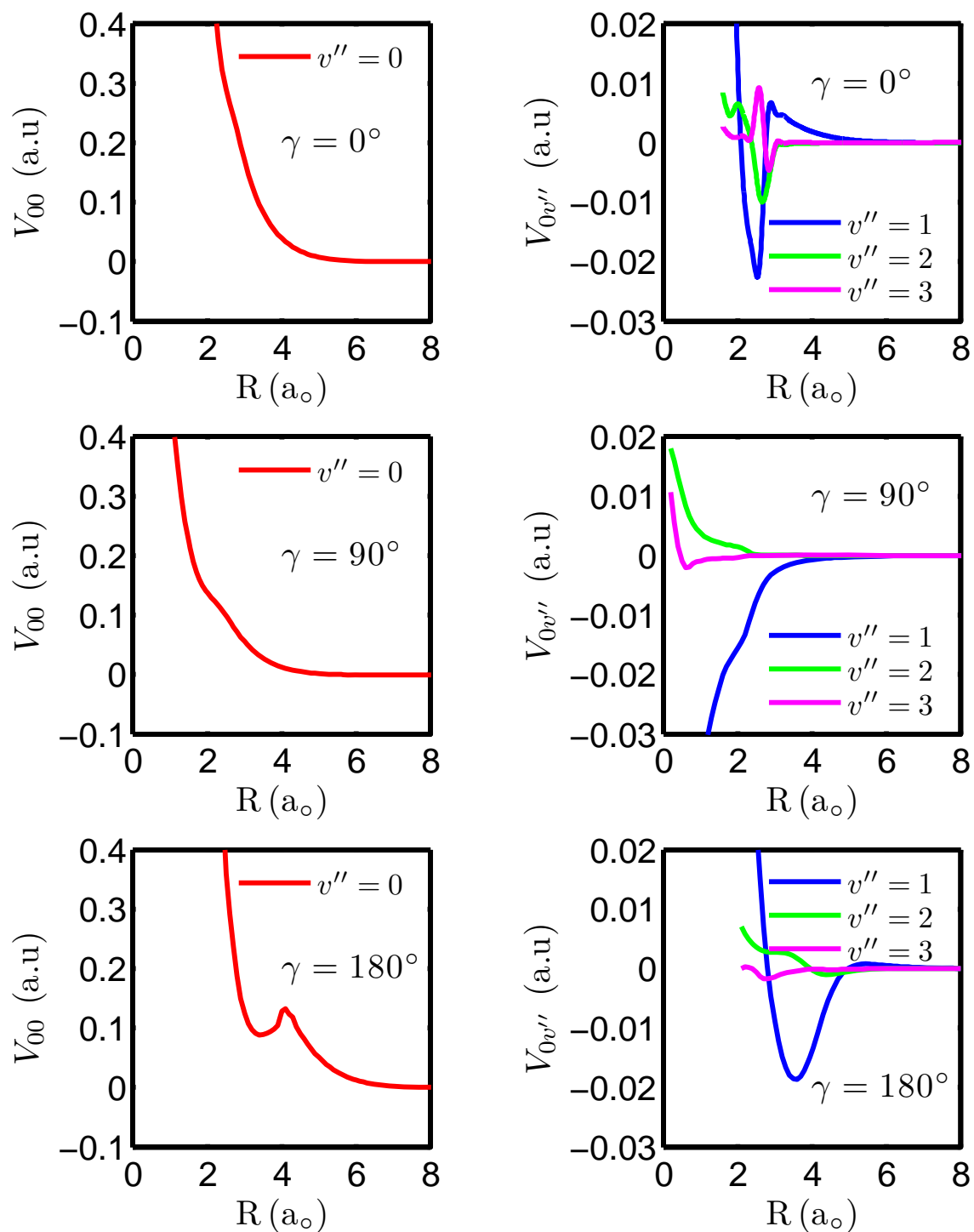


Figure 4.16: Vibrational coupling matrix elements ($V_{vv''}$) for the VCT channel, $\text{H}^+ + \text{CO}(v = 0) \rightarrow \text{H}(^2\text{S}) + \text{CO}^+(v'')$, as a function of R for $\gamma = 0^\circ, 90^\circ, 180^\circ$. VCT channel V_{00} (left panel) and VCT channel $V_{0v''}$ (right panel)

VCT channels such as V_{04}, V_{05}, V_{06} , etc. are so small that they are not included in the Fig.

4.16.

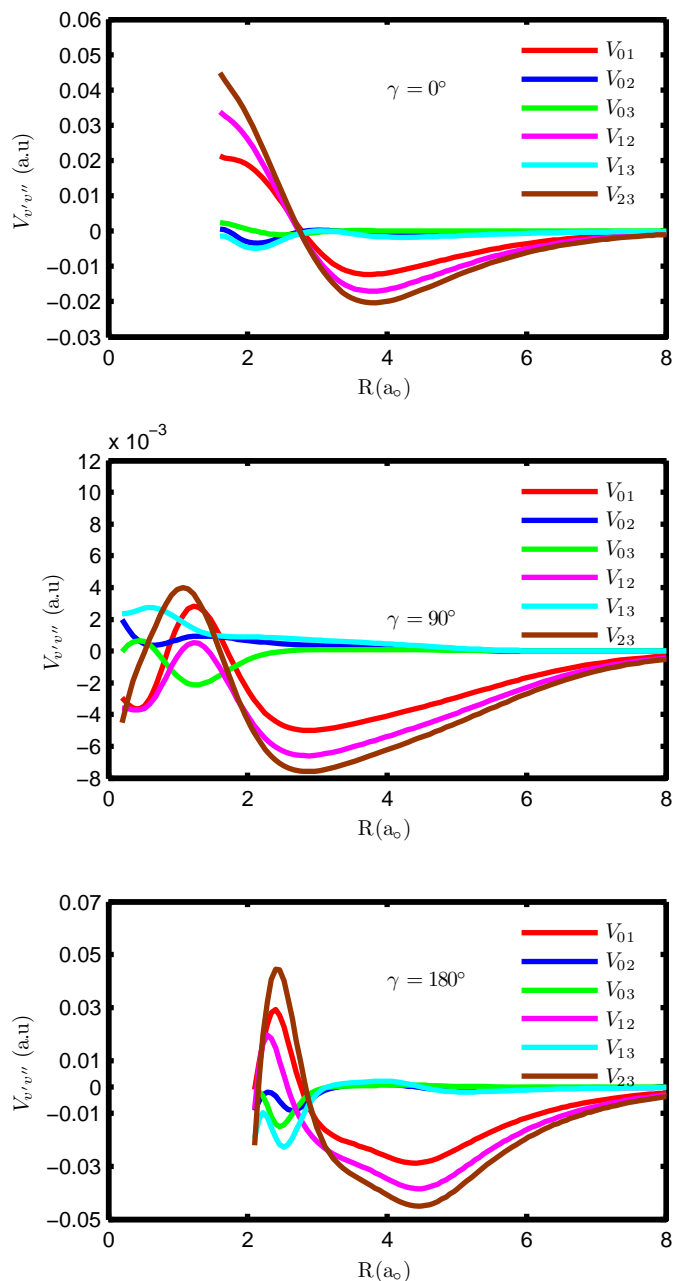


Figure 4.17: Vibrational coupling matrix elements ($V_{v'v''}$) in the vibrational manifold of charge transfer channel, $\text{H}^+ + \text{CO}(v') \rightleftharpoons \text{H}^{(2)\text{S}} + \text{CO}^+(v'')$, as a function of R for $\gamma = 0^\circ, 90^\circ, 180^\circ$. The reversible arrow denotes that process can occur in both directions

In Fig. 4.17, we show the computed VCMEs ($V_{v'v''}$) in the vibrational manifold of charge transfer channel as a function of R for $\gamma = 0^\circ, 90^\circ$ and 180° . We see larger magnitude for V_{23}, V_{12}, V_{01} with following order: $V_{23} > V_{12} > V_{01}$ and they survive upto a larger value of R for all three orientations. Also, we can see that VCMEs values are less for 90° by almost

10 times, when compared with other two collinear orientations, and they are still following the same order of magnitudes. This is because vertical impact of H^+ is not able to produce sufficient amount of vibrational excitation of CO when compared with sidewise impact. The order of magnitude means that relative populations of CO in $v = 2$ level is more than in $v = 1$ and $v = 0$ levels and excitation from $v = 2$ to $v = 3$ of CO^+ is more intense. In other words, the incoming H^+ couples strongly with CO in $v = 2$ level. Similarly, excitation from $v = 1$ and $v = 0$ of CO to $v = 2$ and $v = 1$ of CO^+ takes place. The VCMEs of other channels V_{02}, V_{03}, V_{13} are very weak in all three orientations, indicating that the excitations from heavily populated $v = 0$ and $v = 1$ levels of CO to $v = 2$ and $v = 3$ of CO^+ are relatively lower and it dies down immediately as a function of R . $V_{01}, V_{02}, V_{03}, V_{12}, V_{13}, V_{23}$ follows overall pattern found in the VCMEs in the vibrational manifold of the charge transfer channel and hence, higher order of channels such V_{04}, V_{14}, V_{24} etc. are not mentioned in the discussion either because they are too weak or they also follow the same order of VCMEs mentioned above. We must keep in mind that all VCMEs discussed here are much smaller than the VCMEs discussed in earlier cases, meaning that pure elastic, inelastic and VCT channels still couples strongly with the incoming H^+ .

4.6 Quantum dynamics within the VCC-RIOSAs approach

The details of the vibrational close-coupling rotational infinite-order sudden approximation has been discussed in detail in **chapter 3**. Here, we briefly present only the necessary equation. In the diabatic representation, the two coupled nuclear schrödinger equations in the Jacobi coordinates (defined in (see Fig. 3.1 of **Chapter 3**) for the $A^+(A) + BC(BC^+)$

system can be written as

$$\left[-\frac{\hbar^2}{2\mu_{ABC}} \frac{\partial^2}{\partial R^2} + \frac{\hbar^2}{2\mu_{ABC}} \frac{l(l+1)}{R^2} + V_{11}^d(R, r; \gamma) - \frac{\hbar^2}{2\mu_{BC}} \frac{\partial^2}{\partial r^2} + \frac{\hbar^2}{2\mu_{BC}} \frac{j(j+1)}{r^2} + V_{BC}(r) \right] \tilde{\psi}_1(R, r; \gamma) + V_{12}^d(R, r; \gamma) \tilde{\psi}_2(R, r; \gamma) = 0 \quad (4.10)$$

$$\left[-\frac{\hbar^2}{2\mu_{ABC}} \frac{\partial^2}{\partial R^2} + \frac{\hbar^2}{2\mu_{ABC}} \frac{l(l+1)}{R^2} + V_{22}^d(R, r; \gamma) - \frac{\hbar^2}{2\mu_{BC}} \frac{\partial^2}{\partial r^2} + \frac{\hbar^2}{2\mu_{BC}} \frac{j(j+1)}{r^2} + V_{BC^+}(r) \right] \tilde{\psi}_2(R, r; \gamma) + V_{21}^d(R, r; \gamma) \tilde{\psi}_1(R, r; \gamma) = 0 \quad (4.11)$$

where μ_{ABC} is the atom-molecule reduced mass, μ_{BC} is the reduced mass of the diatom, $l(l+1)\hbar^2$ is the orbital angular momentum of the atom $A^+(A)$ relative to the diatomic molecule $BC(BC^+)$, $j(j+1)$ is the rotational angular momentum of the diatom, V_{BC} and V_{BC^+} are the diatomic potentials of BC and BC^+ , respectively. when $\tilde{\psi}_1(R, r; \gamma)$ and $\tilde{\psi}_2(R, r; \gamma)$ are expanded in translational and vibrational functions for a fixed r , one finally arrives at the vibrational close-coupled equation (Eq. (3.22)) (within the VCC-RIOSAs framework) as described in **chapter 3**. Their numerical solutions with proper boundary conditions yield the required S-matrix and T-matrix elements which finally give the required dynamical quantities.

In order to have converged cross section in the range of experimental collision energy E_{cm} , 9.5 eV - 28.96 eV, 10 vibrational levels of the target diatom (CO) and CO^+ were included in the vibrational close-coupling equations. Since the experiments hint very low IVE and the VCT, only 10 vibrational levels for each CO and CO^+ were considered so as to achieve numerically converged results for atleast lower vibrational excitations of the diatoms. The coupled channel equations were solved by the sixth-order Numerov method

for thirteen equally spaced orientations with γ values between 0° and 180° for each partial wave (l). The maximum partial wave, l_{max} , for the most dominant vibrationally elastic excitations at $E_{cm} = 9.5$ eV and 28.96 eV was 600 and 1200, respectively.

4.6.1 Dynamics at $E_{cm}=9.5$ eV

In this section, we compare the computed dynamical quantities with those of the existing experiments (Gianturco, Gierz, and Toennies, 1981). The state-to-state experimental data are available only for the IVE process at collision energy $E_{cm} = 9.5$ eV. We have computed the various dynamical attributes at this energy and compared them with those available from experiments. There does not seem to be any earlier quantum dynamics study at this collision energy.

4.6.1.1 The orientation opacities

The VCC-RIOSAs coupling scheme provides an important insight into the dynamics through the angle-dependent opacities defined in Eq. (3.34). This will provide useful information about steric effect in relation to the potential interaction and dynamical coupling for both the IVE and the VCT channels. We show in Fig. 4.18 the angle-dependent opacity functions for the rotationally-summed vibrational excitations $v = 0 \rightarrow v' = 0, v = 0 \rightarrow v' = 1, v = 0 \rightarrow v' = 2$ for the IVE channel, $\text{H}^+ + \text{CO}(v = 0) \rightarrow \text{H}^+ + \text{CO}(v')$ (left column) and for the rotationally-summed vibrational excitations $v = 0 \rightarrow v'' = 0, v = 0 \rightarrow v'' = 1, v = 0 \rightarrow v'' = 2$ for the VCT channel, $\text{H}^+ + \text{CO}(v = 0) \rightarrow \text{H}(^2\text{S}) + \text{CO}^+(v'')$ (right column) as a function of contributing angular momenta (l) (in the units of \hbar) at the collision energy of $E_{cm} = 9.5$ eV. In the IVE channel, order of magnitude of opacity functions

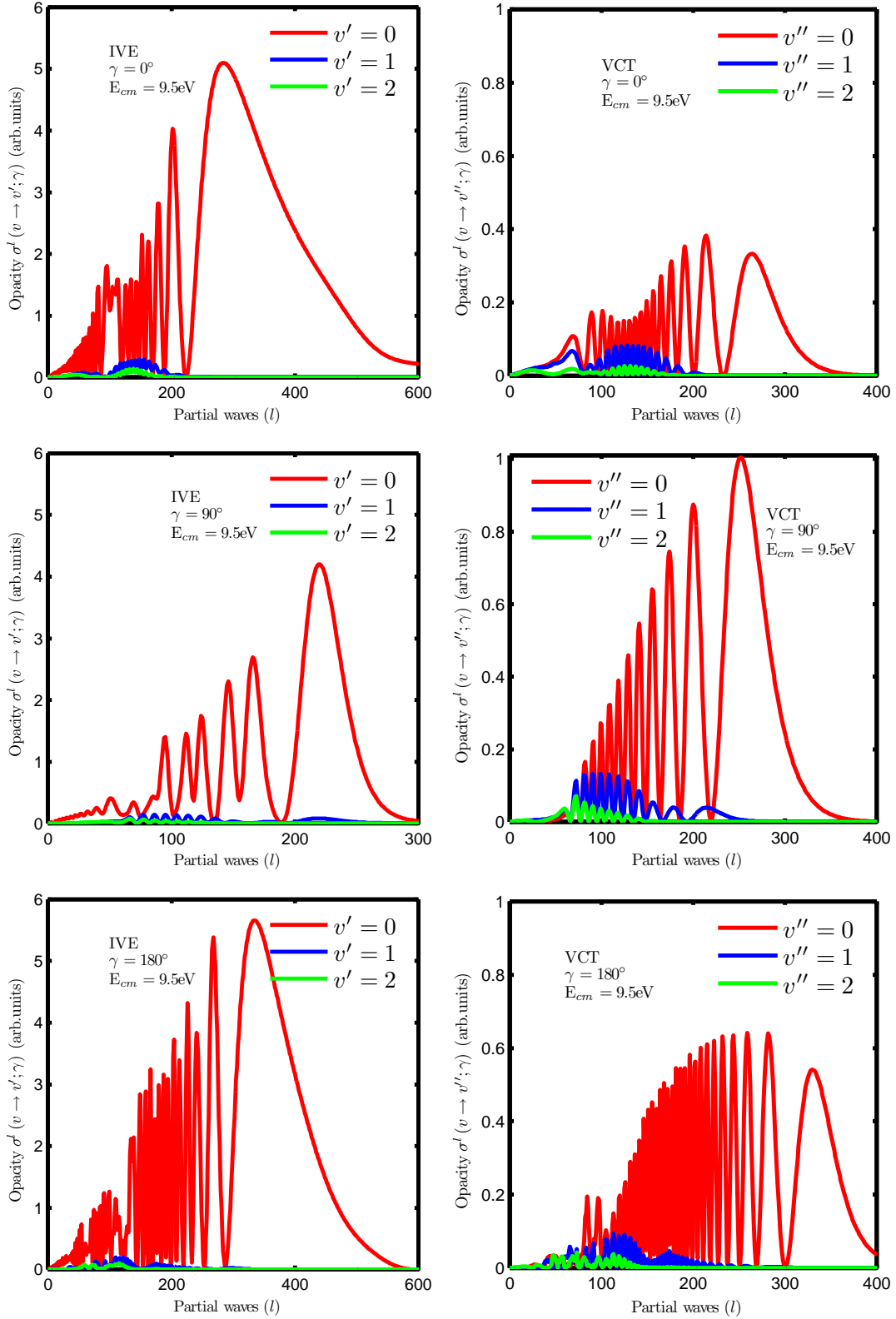


Figure 4.18: Opacity function (Eq. (3.34)) as a function of partial wave, l (in the units of \hbar) for three excitations, $v = 0 \rightarrow v' = 0, v = 0 \rightarrow v' = 1, v = 0 \rightarrow v' = 2$ for the IVE channel, $\text{H}^+ + \text{CO}(v = 0) \rightarrow \text{H}^+ + \text{CO}(v')$ (left panel) and for three excitations, $v = 0 \rightarrow v'' = 0, v = 0 \rightarrow v'' = 1, v = 0 \rightarrow v'' = 2$ for the VCT channel, $\text{H}^+ + \text{CO}(v = 0) \rightarrow \text{H}(2S) + \text{CO}^+(v'')$ (right panel) at the collision energy of $E_{cm} = 9.5 \text{ eV}$

follows $v = 0 \rightarrow v' = 0 > v = 0 \rightarrow v' = 1 > v = 0 \rightarrow v' = 2$ for all the three orientations and qualitatively follow the experimentally observed trend of vibrational inelasticity from the transition probability measurements $P_{0 \rightarrow v'}$ (Gianturco, Gierz, and Toennies, 1981). The magnitude of opacity function for 90° is less in comparison with that for 0° and 180° and survives only upto $l = 300$. The vibrational elasticity/inelasticity is highly favoured when H^+ approaches CO towards either C-end or O-end of CO and less favoured when H^+ approaches vertically towards the cm of CO molecule. In the VCT channel, the opacities are an order of magnitude less than those of the IVE channel and they follow the order : $v = 0 \rightarrow v'' = 0 > v = 0 \rightarrow v'' = 1 > v = 0 \rightarrow v'' = 2$ for all three molecular orientations and the magnitude in the case of 90° is higher when compared with 0° and 180° . The charge transfer processes are more favourable when H^+ approaches perpendicularly towards the center of mass of CO. Overall, the vibrational elasticity/inelasticity is highly favoured and charge transfer is less favoured for all approaches.

4.6.1.2 Rotationally-summed total differential cross section

In the scattering experiments, all the measurements were carried out in the laboratory frame of reference, while in the theory, the computation are performed in the center of mass frame of reference. Hence, to compare experimental data with the theory we have to convert experimental data available in laboratory frame to center of mass frame of reference using the relation given in Eq. (4.12)

$$\sin \theta_{c.m} = \frac{\sin \theta_{lab}}{m_2} \left(m_1 \cos \theta_{lab} + \sqrt{m_2^2 - m_1^2 \sin^2 \theta_{lab}} \right) \quad (4.12)$$

where m_1 is the mass of proton and m_2 is the mass of diatom. In the present case, $m_1 = 1.0$ a.m.u, $m_2 = 28$ a.m.u. In quantum calculations, scattering properties such as total differential cross section, state-selective differential cross section, transition probability etc. exhibit a lot of oscillatory structures as a function of θ_{cm} , which mostly arises from the constructive and destructive interferences of the partial waves l . Such undulatory structures could not be resolved in the experiments (Niedner, Noll, Toennies, and Schiler, 1987). Therefore, we smoothed our data for the sake of clarity by folding them with a Gaussian distribution (Eq. 4.13) in the same way as it was achieved in the earlier theoretical calculations of Baer *et al.* (Baer, Niedner-Schatterburg, and Toennies, 1989)

$$\frac{d\sigma}{d\omega}(\bar{\theta}) = \int_{\bar{\theta}-\Delta\theta}^{\bar{\theta}+\Delta\theta} \exp\left[-\frac{(\theta-\bar{\theta})^2}{2\sigma_\theta^2}\right] \frac{d\sigma^c}{d\omega}(\theta) d\theta \quad (4.13)$$

where $\Delta\theta = 1.0^\circ$, $\sigma_\theta = 0.33^\circ$, $\frac{d\sigma^c}{d\omega}$ is the calculated values of the TDCSs or DCSs. The assumed uncertainty in the related experiments was 0.5° , and it is the value at full width at half maximum (FWHM) in the energy-loss spectra (Noll and Toennies, 1986).

We show in Fig. 4.19 smoothed TDCS, computed by summing up rotationally-summed vibrational state-selective differential cross sections for the IVE, $\text{H}^+ + \text{CO}(v=0) \longrightarrow \text{H}^+ + \text{CO}(\Sigma v')$ and the VCT, $\text{H}^+ + \text{CO}(v=0) \longrightarrow \text{H}(^2\text{S}) + \text{CO}^+(\Sigma v'')$ channels at $E_{cm} = 9.5$ eV as a function of scattering angle θ_{cm} (deg). The TDCS is smoothed using Eq. 4.13 for both the channels with the parameters given above. The numbers on the ordinate in Eq. 4.13 is to be interpreted as powers of 10. The TDCS difference between the two channels is roughly estimated to be $0.27 \text{ \AA}^2/\text{sr}$ till θ_{cm} reaches 20° . The rainbow maximum occurs between the range $19^\circ - 20^\circ$ in both the IVE and the VCT channels. Unfortunately, we are not able to verify this through the comparison with experimental data as they are not available at this

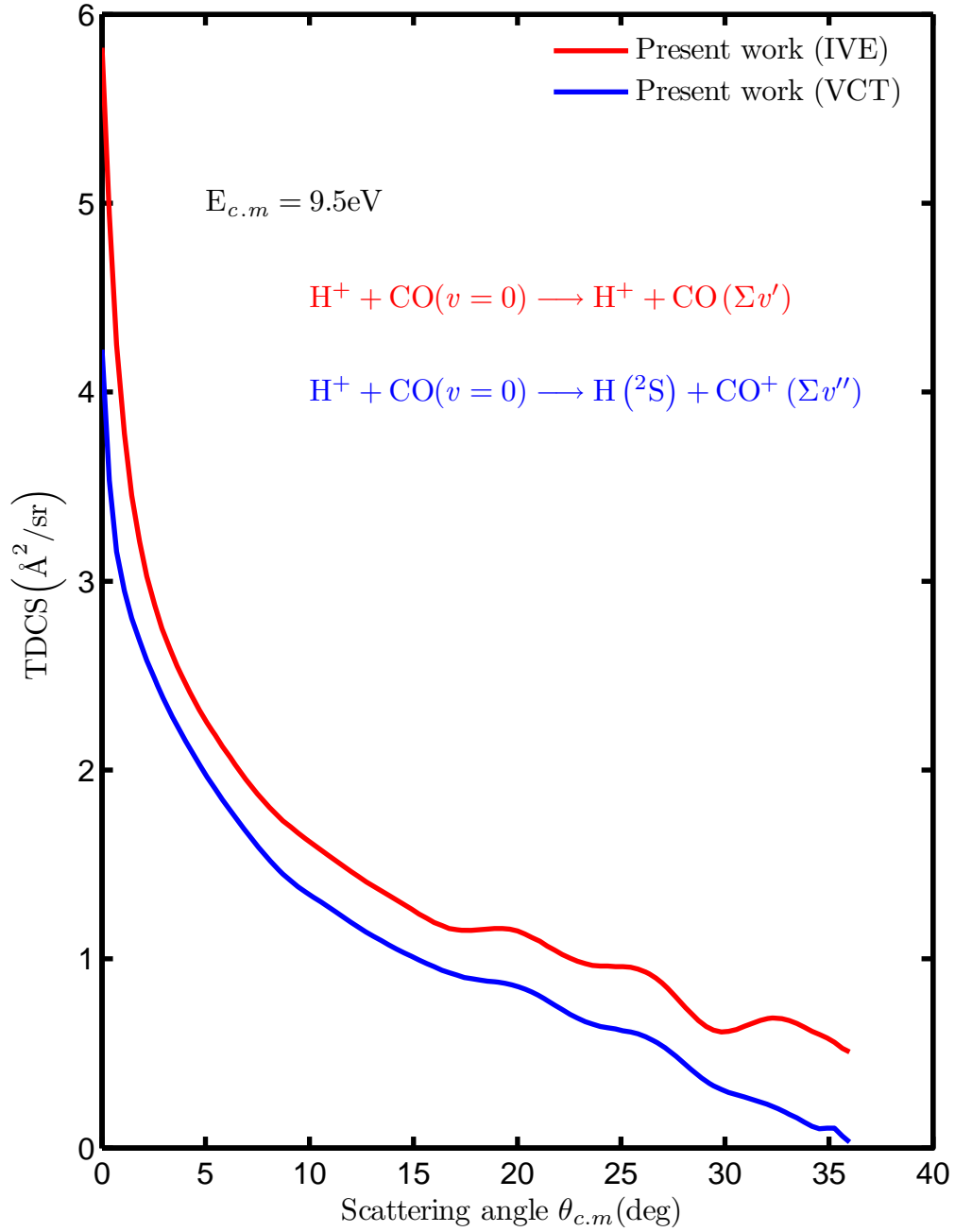


Figure 4.19: The computed TDCS for IVE and VCT channels at $E_{cm} = 9.5$ eV as a function of scattering angle θ_{cm} (deg). The numbers in the ordinate are the powers of 10. There is no experimental data available to compare with at this collision energy.

collision energy.

4.6.1.3 Rotationally-summed state-selective differential cross section (DCS)

Mathematically, rotationally summed DCS is defined in Eq. (3.29). The computed and smoothed (using Eq. 4.13) state-selected rotationally-summed DCS have been plotted in Fig. 4.20 for the IVE (right) and VCT (left) channel for the first six states as a function of scattering angle θ_{cm} . The numbers in the ordinate of Fig. 4.20 denote powers of 10. The elastic cross section (red), $v = 0 \rightarrow v' = 0$ and first charge transfer cross section (red), $v = 0 \rightarrow v'' = 0$ have been well separated from the rest of the cross sections in both the cases. Unfortunately again, there are no experimental data available for these to be compared with the present theoretical data. Still we can make out some judicious conclusion from the plots just by a close look at it. First of all, they are close spaced to each other as the vibrational state increases from 0 to 6 and the primary rainbow maximum below $\theta_{cm} = 20^\circ$ emerges to appear more and more strongly as we move from $v = 0 \rightarrow v = 6$. At large scattering angle, oscillation begin to appear because of the constructive and destructive interference of partial waves. In each case, the order of DCS from top to bottom exactly follows the pattern of increasing vibrational states and in VCT channel, DCS for $v'' = 4$ and $v'' = 5$ appear to cross each other at small θ_{cm} values. Note the enhancement of primary rainbow maxima in the VCT channel for $v = 0 \rightarrow v'' = 2, v = 0 \rightarrow v'' = 3, v = 0 \rightarrow v'' = 4, v = 0 \rightarrow v'' = 5$. This enhancement is also seen but to a lesser extent in IVE channel wherein the DCS for $v = 0 \rightarrow v' = 1$ transition remain almost flat, thus making it insensitive to the variation of scattering angle θ_{cm} in the range $10^\circ - 25^\circ$. The DCS in charge transfer channel decreases rapidly at larger scattering angle θ_{cm} than the inelastic channel where DCSs decrease slowly with the increase of scattering angle θ_{cm} .

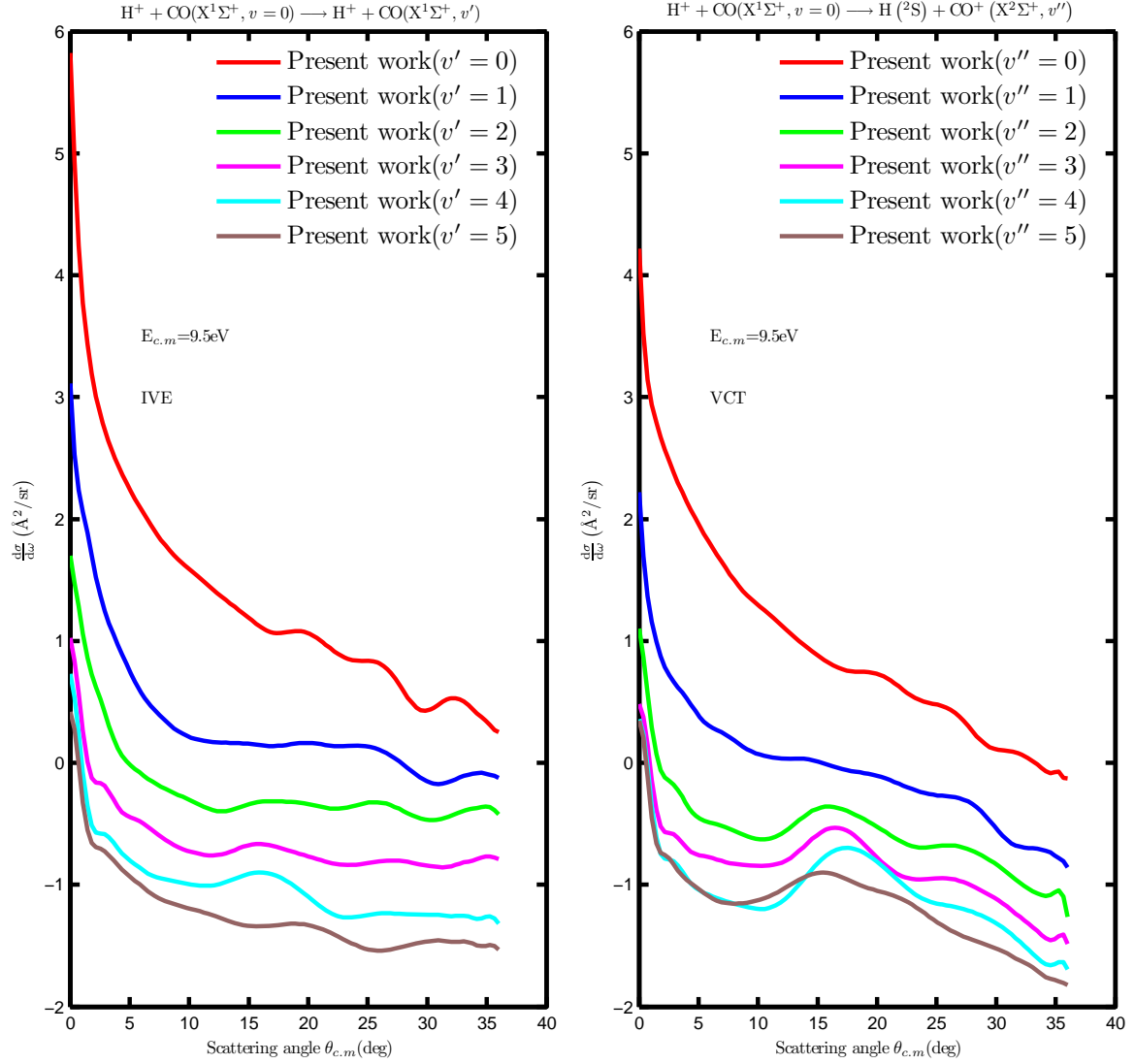


Figure 4.20: The computed state-selective rotationally summed DCS for IVE and VCT channels at $E_{cm} = 9.5$ eV as a function of scattering angle θ_{cm} (deg) for the first six states and the numbers in the ordinate are the powers of 10. There is no experimental data available to compare with at this collision energy

4.6.1.4 Transition Probability

Following the earlier theoretical calculations (Baer, Niedner-Schatteburg, and Toennies, 1989), the relative transition probabilities for the IVE processes were obtained from the

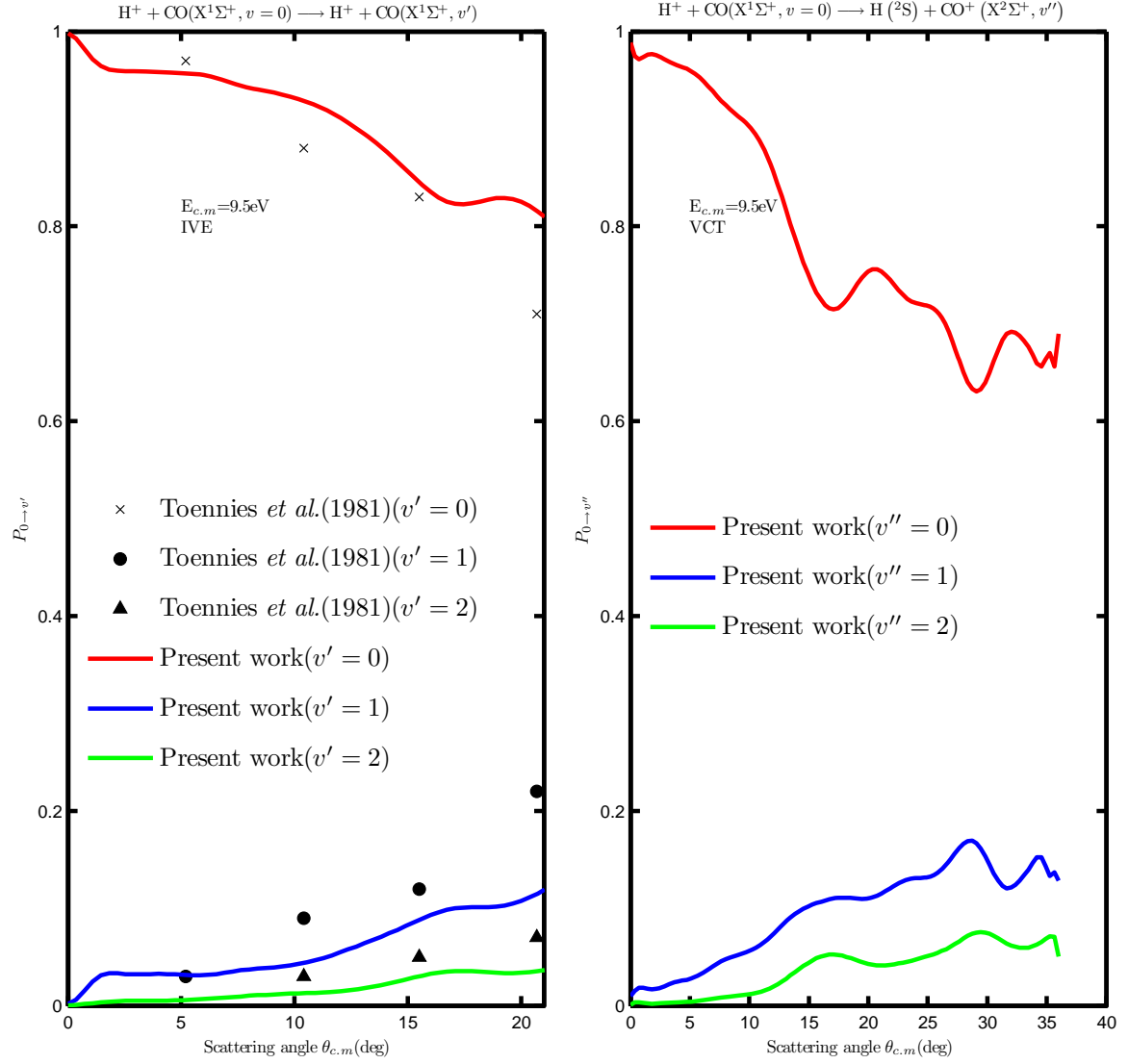


Figure 4.21: State-selective transition probability for IVE (left) for the first three states $v' = 0, v' = 1, v' = 2$ and VCT (right) for the first three states $v'' = 0, v'' = 1, v'' = 2$ as a function of scattering angle θ_{cm} at the collision energy $E_{cm} = 9.5 \text{ eV}$. The transition probability for IVE is compared with experimental data (Gianturco, Gierz, and Toennies, 1981). See the text.

rotationally-summed DCSs as

$$P_{0 \rightarrow v'}(\theta_{cm}) = \frac{\left. \frac{d\sigma}{d\omega}(0 \rightarrow v') \right|_{\theta_{cm}}}{\sum_{v'} \left. \frac{d\sigma}{d\omega}(0 \rightarrow v') \right|_{\theta_{cm}}} \quad (4.14)$$

and that for the VCT processes obtained as

$$P_{0 \rightarrow v''}(\theta_{cm}) = \frac{\left. \frac{d\sigma}{d\omega}(0 \rightarrow v'') \right|_{\theta_{cm}}}{\sum_{v''} \left. \frac{d\sigma}{d\omega}(0 \rightarrow v'') \right|_{\theta_{cm}}} \quad (4.15)$$

Note that in the above two formulae, the summation term in the denominator involves taking the sum of state-selected rotationally-summed DCSs upto the highest vibrational level and the numerator refers to the DCS for a particular vibrational state. The relative transition probability, $P_{0 \rightarrow v'}(\theta_{cm})$, for the IVE channel is shown in Fig. 4.21 (left) as a function of θ_{cm} for first three vibrational states $v = 0 \rightarrow v' = 0$, $v = 0 \rightarrow v' = 1$, $v = 0 \rightarrow v' = 2$ for which the experimental data are available upto $\theta_{cm} = 21^\circ$ (Gianturco, Gierz, and Toennies, 1981). The transition probability for elastic process $v = 0 \rightarrow v' = 0$ decays very quickly in this range and the theoretical values gives good agreement with the experiments. The two inelastic processes $v = 0 \rightarrow v' = 1$ and $v = 0 \rightarrow v' = 2$ begin from zero at $\theta_{cm} = 0^\circ$ and slowly rise up, reaching roughly 0.1 and 0.5 respectively. The magnitude for inelastic process is generally very small as compared to that of elastic processes as evident from the Fig. 4.21 (left). The Fig. 4.21 (right) shows the transition probability, $P_{0 \rightarrow v''}$, for the VCT channel as a function of θ_{cm} for first three vibrational states $v = 0 \rightarrow v'' = 0$, $v = 0 \rightarrow v'' = 1$, $v = 0 \rightarrow v'' = 2$ for which the experimental data are not available at this collision energy. The first VCT channel, $v = 0 \rightarrow v'' = 0$, is more probable when compared to the other two VCT channels, $v = 0 \rightarrow v'' = 1$ and $v = 0 \rightarrow v'' = 2$.

4.6.1.5 Average vibrational energy transfer

We analyze and compare the computed average vibrational energy transfer values $\overline{\Delta E_{vib}}$ (eV) as a function of θ_{cm} with those of experiments (Gianturco, Gierz, and Toennies, 1981)

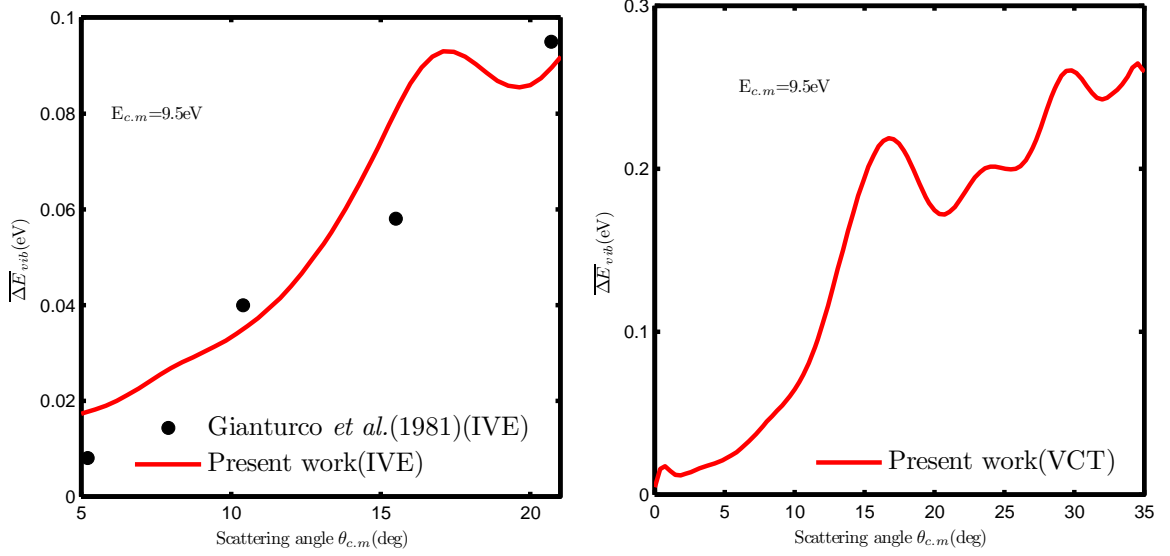


Figure 4.22: The computed average vibrational energy transfer $\overline{\Delta E}_{vib}$ (eV) for the IVE (left) and the VCT (right) as a function of scattering angle θ_{cm} at the collision energy $E_{cm} = 9.5$ eV. The theoretical values gives excellent agreement with the experiments (Gianturco, Gierz, and Toennies, 1981) for the IVE channel and no experimental data are available at this collision energy for VCT channel

in Fig. 4.22. The average vibrational energy transfer $\overline{\Delta E}_{vib}(\theta_{cm})$ for both IVE and VCT channels is computed using Eq. (4.16)

$$\begin{aligned}\overline{\Delta E}_{vib}(\theta_{cm}) &= \sum_{v'=0}^{\infty} P_{0 \rightarrow v'}(\theta_{cm}) \Delta E(0 \rightarrow v') \\ \overline{\Delta E}_{vib}(\theta_{cm}) &= \sum_{v''=0}^{\infty} P_{0 \rightarrow v''}(\theta_{cm}) \Delta E(0 \rightarrow v'')\end{aligned}\tag{4.16}$$

where $\Delta E(0 \rightarrow v')$ and $\Delta E(0 \rightarrow v'')$ are the energy differences of the vibrational levels of CO and CO^+ respectively. $P_{0 \rightarrow v'}(\theta_{cm})$ and $P_{0 \rightarrow v''}(\theta_{cm})$ are the rotationally-summed vibrational state-selected transition probabilities for the IVE and the VCT processes. In the IVE channel, the computed average vibrational energy transfer give excellent agreement with experimental data in Fig. 4.22 (left). In the case of the VCT channel, we show only our computed data points for $\Delta E(0 \rightarrow v'')$ in Fig. 4.22 (right) as there are no experimental data available for this channel at the collision energy of 9.5 eV.

4.6.1.6 Integral cross section

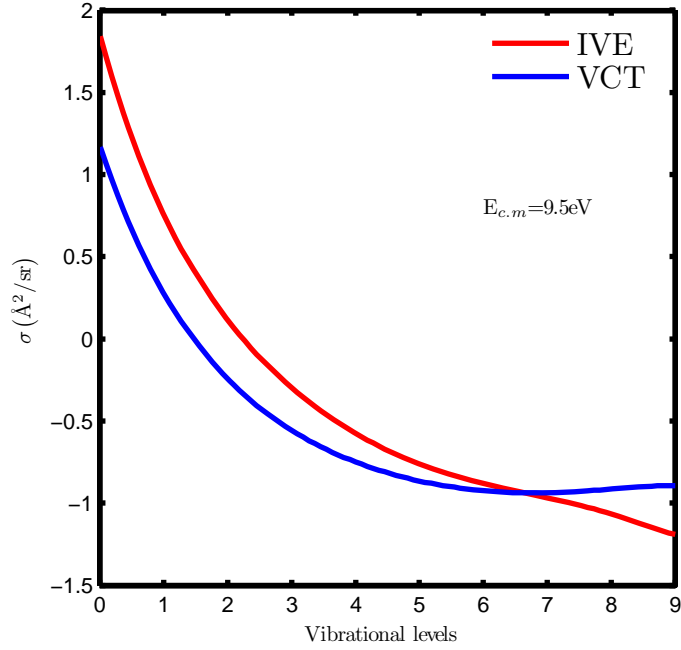


Figure 4.23: The computed integral cross section $\sigma(\text{\AA}^2/\text{sr})$ for the IVE and the VCT as a function of vibrational energy levels at the collision energy $E_{cm} = 9.5$ eV. The two curves run parallel to each other with a crossing at higher vibrational levels. The integral cross section for the IVE process is of higher magnitude than VCT process. Note that the numbers on the Y-axis indicate powers of 10.

Table 4.7: VCC-RIOSAs state-to-state integral cross section (absolute values) for the IVE channel, $\text{H}^+ + \text{CO}(v = 0) \rightarrow \text{H}^+ + \text{CO}(v')$ and the VCT channel, $\text{H}^+ + \text{CO}(v = 0) \rightarrow \text{H}^{(2)}\text{S} + \text{CO}^+(v'')$ at the $E_{cm} = 9.5$ eV.

$v'(v'')$	Integral cross section (\AA^2)	
	IVE	VCT
0	69.727	14.715
1	2.581	1.021
2	0.869	0.372
3	0.397	0.217
4	0.201	0.145
5	0.144	0.117
6	0.106	0.111
$\Sigma v'(v'')$	74.025	16.698

The state-to-state integral cross sections (ICS) for the IVE and the VCT channels at $E_{cm} = 9.5$ eV have been shown in Fig. 4.23. Note that the numbers on the ordinate indicate

powers of 10. Both the curve goes almost parallel to each other and at higher vibrational state, there is a crossing between the two. Note that the ics reduces drastically after the $v' = 0$ or $v'' = 0$ state as indicated in the Table 4.7 in which we list out vibrational statewise magnitude of integral cross section upto $v = 6$ for both the channels. The abnormally high value for $v = 0$ tell us that the the elastic collisions in the IVE channel and the first charge transfer collisions in the VCT channel dominate. For higher vibrational states the magnitudes of excitations for both the IVE ($0 \rightarrow v'$) and the VCT ($0 \rightarrow v''$) channels become very low and the $0 \rightarrow v'$ excitations become slightly more probable than $0 \rightarrow v''$ excitations.

4.6.2 Dynamics at $E_{cm}=28.96$ eV

In this section, we compare the computed dynamical quantities with those of the existing experiments (Niedner-Schatteburg and Toennies, 1992; Krutein and Linder, 1979). The state-to-state experimental data are available only for the IVE process at collision energy $E_{cm} = 28.96$ eV. We have computed the various dynamical attributes at this energy and compared them with those available from experiments. There does not seem to be any earlier quantum dynamics study at this collision energy.

4.6.2.1 The orientation opacities

The angle-dependent opacity function defined in Eq. (3.34) for both the IVE and the VCT channels have been shown in Fig. 4.24 at $E_{cm} = 28.96$ eV for the first three excitations, namely, $v = 0 \rightarrow v' = 0, v = 0 \rightarrow v' = 1, v = 0 \rightarrow v' = 2$ (IVE) and $v = 0 \rightarrow v'' = 0, v = 0 \rightarrow v'' = 1, v = 0 \rightarrow v'' = 2$ (VCT). The maximum value of l required for the

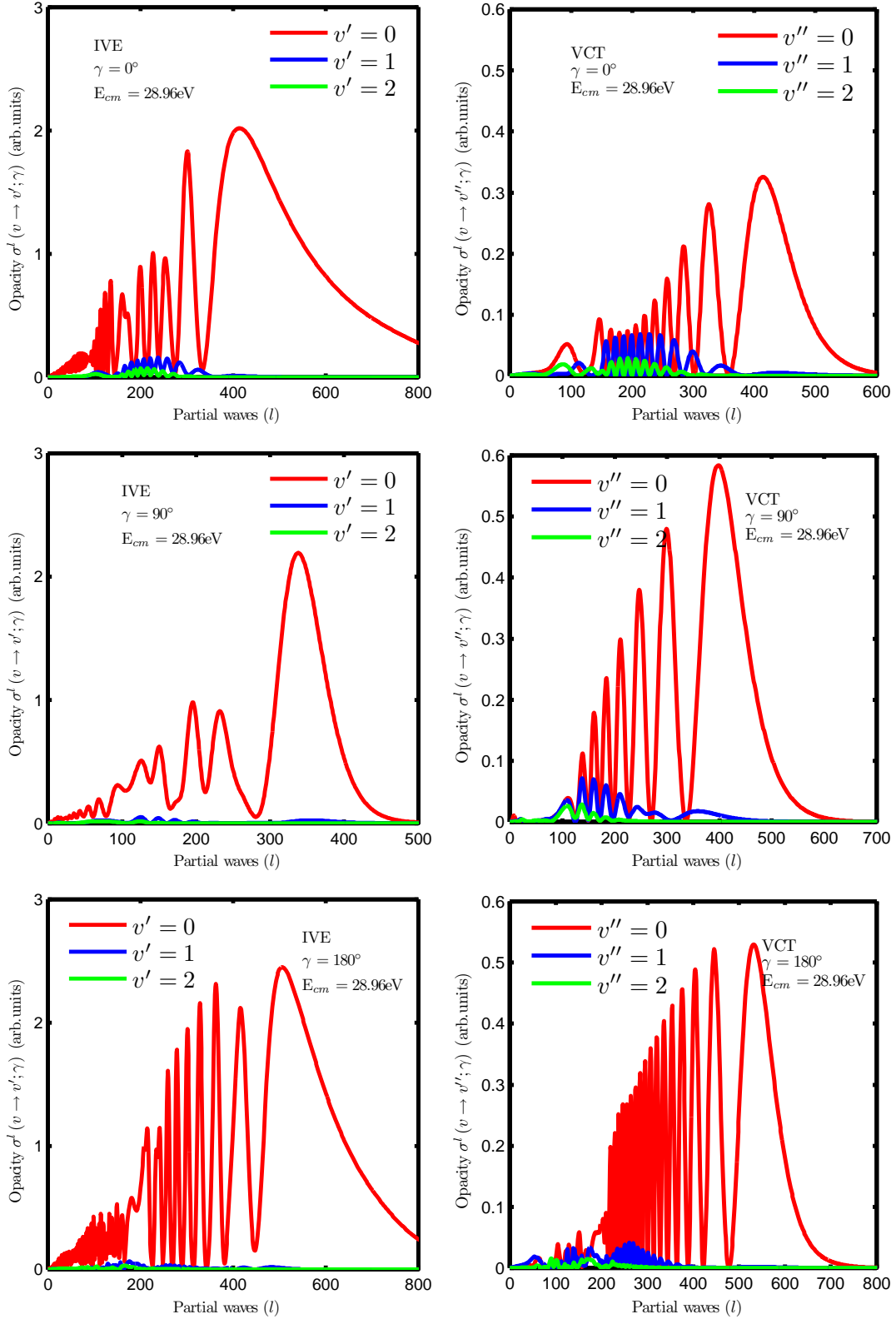


Figure 4.24: Opacity function (Eq. (3.34)) as a function of partial wave, l (in the units of \hbar) for three excitations, $v = 0 \rightarrow v' = 0, v = 0 \rightarrow v' = 1, v = 0 \rightarrow v' = 2$ for the IVE channel, $\text{H}^+ + \text{CO}(v = 0) \rightarrow \text{H}^+ + \text{CO}(v')$ (left column) and for three excitations, $v = 0 \rightarrow v'' = 0, v = 0 \rightarrow v'' = 1, v = 0 \rightarrow v'' = 2$ for the VCT channel, $\text{H}^+ + \text{CO}(v = 0) \rightarrow \text{H}(^2\text{S}) + \text{CO}^+(v'')$ (right column) at the collision energy of $E_{cm} = 28.96 \text{ eV}$

numerical convergence is $l_{max} = 800$ for $\gamma = 0^\circ, 180^\circ$ and $l_{max} = 500$ for $\gamma = 90^\circ$. The inelastic excitations, $v = 0 \rightarrow v' = 1$ and $v = 0 \rightarrow v' = 2$ are favoured in $\gamma = 0^\circ$ than $\gamma = 90^\circ, 180^\circ$ orientations. The charge transfer excitations, $v = 0 \rightarrow v'' = 1, v = 0 \rightarrow v'' = 2$ show almost equal probability in all three orientations but the opacities survive only for less number of partial waves.

4.6.2.2 Rotationally-summed total differential cross section

Based on the similar arguments given in subsection 4.6.1.2 on page 80, we retrieved experimental data (Niedner-Schatteburg and Toennies, 1992) available for forward scattering (below $\theta_{lab} < 20^\circ$) in the laboratory frame to center-of-mass frame using Eq. 4.12. We smoothed our total differential cross section data using (4.13) for both the IVE and the VCT processes, The total differential cross sections were computed by summing up the state-selected rotationally-summed differential cross sections for the transition from the lowest vibrational state ($v = 0$) to highest vibrational state (v') of CO or (v'') of CO^+ as a function of θ_{cm} . In order to avoid the undulatory oscillatory structures arising from the constructive and destructive interferences of large number of partial waves (l), We smoothed our total differential cross section data using (4.13) for both the IVE and the VCT processes In molecular beam experimental results, such oscillatory (noisy) behaviour as function of θ_{lab} was not resolved due to low resolving power of the apparatus and hence the experimental data appear as a smooth function of θ_{lab} . Since in experiments the state-to-state DCSs cannot be obtained on an absolute scale, they are reported on an arbitrary scale. In the calculations the DCSs values are obtained on an absolute scale. Therefore, the experimental data can be normalized with respect to the theoretical data. The experimental data for the IVE process were normalised with respect to the datum point at $\theta_{cm} = 9.3881^\circ$. In Fig. 4.25, we plot

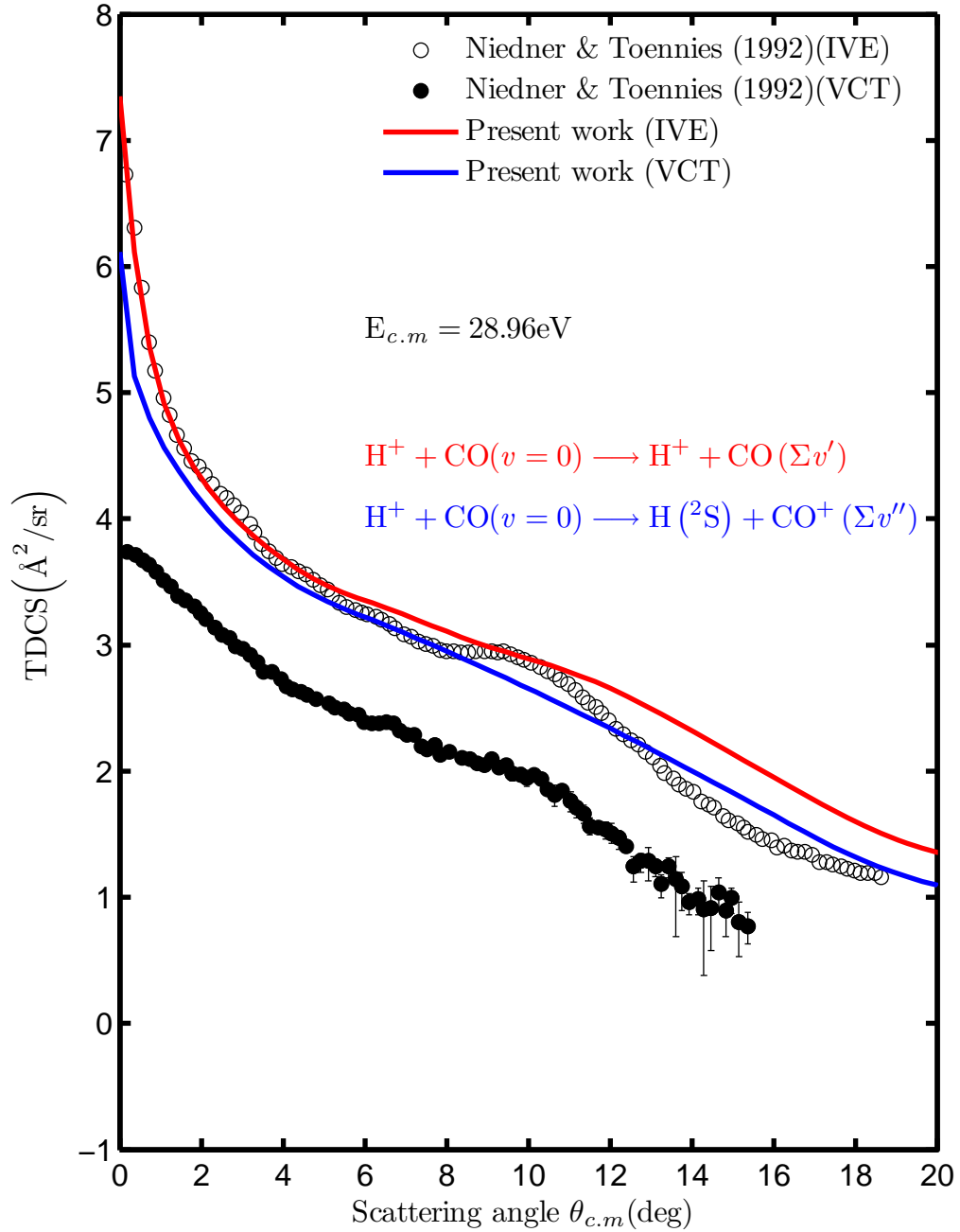


Figure 4.25: The computed TDCS for IVE, $\text{H}^+ + \text{CO}(v = 0) \longrightarrow \text{H}^+ + \text{CO}(\Sigma v')$, and VCT, $\text{H}^+ + \text{CO}(v = 0) \longrightarrow \text{H}(^2\text{S}) + \text{CO}^+(\Sigma v'')$, channels at $E_{cm} = 28.96$ eV as a function of scattering angle θ_{cm} (deg). The numbers in the ordinate are the powers of 10. The experimental data (Niedner-Schatteburg and Toennies, 1992) along with error bars for few points for charge transfer process is shown for IVE(\circ) and VCT(\bullet) at this collision energy. The experimental data were normalized at $\theta_{cm} = 9.3881^\circ$.

both the theoretical and the experimental data together at $E_{cm} = 28.96$ eV for both the IVE and the VCT channels. The numbers on the ordinate indicate the powers of 10. On an aver-

age, the theoretical data predict the observed behaviour of the TDCS for both the channels qualitatively well. However, there exist some noticeable discrepancies. One among them is that the rainbow maximum for the IVE channel. In theoretical data it lies slightly away from the experimental rainbow maximum located at $\theta_{cm} = 9.3881^\circ$ and appear less pronounced and weak than that of the experiment. For VCT channel, our theoretical values are overestimating the experimental data for entire scattering angle range. There is a weak rainbow maximum in the experimental data for the VCT channel roughly around $\theta_{cm} \approx 10^\circ$ which appear to be almost absent in the theoretical TDCSs curve. This clearly indicates that the modelling the dynamics as a two-state process is not sufficient and one must include the higher ESs in the calculations for better theoretical predictions of charge transfer process.

4.6.2.3 Rotationally-summed state-selected differential cross section (DCS)

The computed and smoothed (using Eq. 4.13) state-selected rotationally-summed DCSs have been plotted as a function of $\theta_{cm}(4^\circ - 16^\circ)$ in Fig. 4.26 (left) for the IVE channel at $E_{cm} = 28.96$ eV for the first six vibrational states, $v = 0 \rightarrow v' = 0, v = 0 \rightarrow v' = 1, v = 0 \rightarrow v' = 2, v = 0 \rightarrow v' = 3, v = 0 \rightarrow v' = 4, v = 0 \rightarrow v' = 5$. The experimental data (Krutein and Linder, 1979) are available for forward scattering only for $\theta_{lab} < 13^\circ$ for first three vibrational states, $v = 0 \rightarrow v' = 0(\times), v = 0 \rightarrow v' = 1(\bullet), v = 0 \rightarrow v' = 2(\blacktriangle)$ and they have been reproduced along with the theoretical data in Fig. 4.26 (left). The errorbars (uncertainty in experimental data) are also shown in three sets of data. The experimental data in θ_{lab} are converted into θ_{cm} using Eq. 4.12 and normalized with respect to the theoretical datum at $\theta_{cm} = 9.3881^\circ$. The rainbow maximum seen in the elastic excitation ($v = 0 \rightarrow v' = 0$) in the experimental data is pronounced. The theoretical curve (red) appears to predict the experimental data quite well. However, the

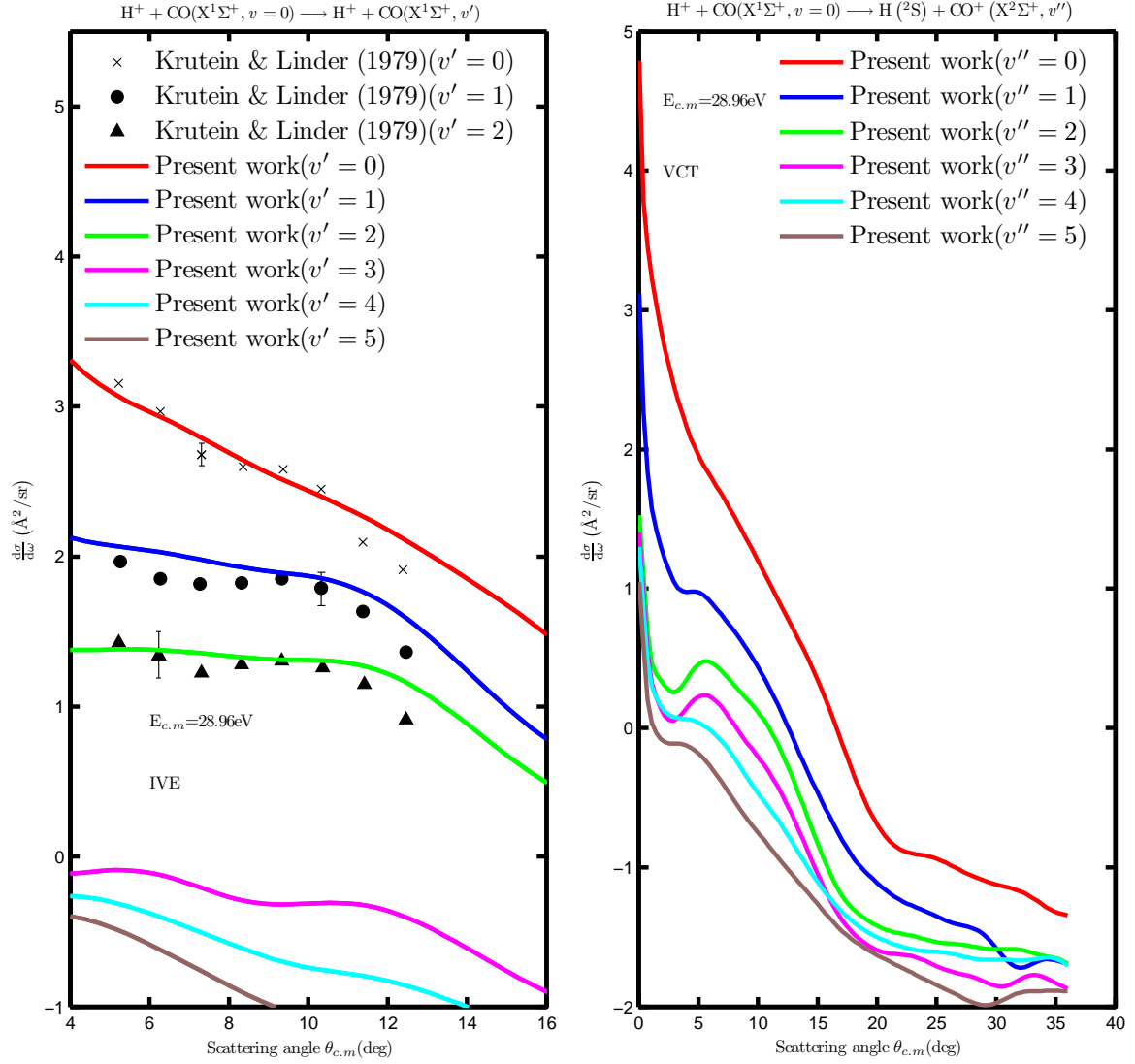


Figure 4.26: The computed state-selective rotationally summed DCS for IVE and VCT channels at $E_{cm} = 28.96$ eV as a function of scattering angle θ_{cm} (deg) for the first six states and the numbers in the ordinate are the powers of 10. The experimental data (Krutein and Linder, 1979) are available along with error bars for the IVE channel for first three states, $v = 0 \rightarrow v' = 0$ (\times), $v = 0 \rightarrow v' = 1$ (\bullet), $v = 0 \rightarrow v' = 2$ (\blacktriangle), and the experimental data are normalised at $\theta_{cm} = 9.3881^\circ$. There is no experimental data available for VCT channel $E_{cm} = 28.96$ eV.

rainbow maximum appears to be weakly predicted. As far as other two excitations are concerned, $v = 0 \rightarrow v' = 1$, $v = 0 \rightarrow v' = 2$, the present calculations predicts fairly well the experimental data points in the entire region of θ_{cm} . Interestingly, first three computed curves fall within the experimental bars shown on each of three sets of experimental data. The other excitations $v = 0 \rightarrow v' = 3$, $v = 0 \rightarrow v' = 4$, $v = 0 \rightarrow v' = 5$ for which no

experimental data points are available are also shown in Fig. 4.26(left). Their magnitudes are very low. The right panel of Fig. 4.26 shows the state-selected DCSs for for the first six excitations for the VCT processes : $v = 0 \rightarrow v'' = 0, v = 0 \rightarrow v'' = 1, v = 0 \rightarrow v'' = 2, v = 0 \rightarrow v'' = 3, v = 0 \rightarrow v'' = 4, v = 0 \rightarrow v'' = 5$. Unfortunately, there are no experimental data available for the VCT to compare with. There is a well marked developement of primary rainbow maxima in the lower order excitations between the range $\theta_{cm} = 5^\circ - 10^\circ$, namely, $v = 0 \rightarrow v'' = 2, v = 0 \rightarrow v'' = 3, v = 0 \rightarrow v'' = 4$.

4.6.2.4 Transition probability

The transition probabilities for IVE and VCT processes are computed using the rotationally summed state-selective DCSs using Eq. (4.14) and Eq. (4.15) on page 85 and page 86. In Fig. 4.27, we show the computed and experimental transition probability for IVE, $P_{0v'}$ and VCT, $P_{0v''}$, channel at $E_{cm} = 28.96$ eV as function $\theta_{cm}(\text{deg})$. The computed data are smoothed using Eq. 4.13 on page 81 and experimental data (Krutein and Linder, 1979) are expressed in center of mass frame of reference using the Eq. 4.12 on page 80 from the laboratory frame of reference. Surprisingly, our computed magnitudes of transition probability for IVE channel (Fig. 4.27(left)), $\text{H}^+ + \text{CO}(v = 0) \longrightarrow \text{H}^+ + \text{CO}(\Sigma v')$, agree very well with the experimental data for $v = 0 \rightarrow v' = 0(\times), v = 0 \rightarrow v' = 1(\bullet), v = 0 \rightarrow v' = 2(\blacktriangle)$ excitations. This can be judged from the fact that the computed values are lying within the limits of errorbars in all the three excitations. In the inelastic excitations the transition probability increases monotonically as a function of scattering angle θ_{cm} whereas, for elastic excitations it decreases steeply with θ_{cm} . A noted discrepancy arises beyond scattering angle $\theta_{cm} > 11^\circ$ where there is a slight mismatch between theory and experiment in all three excitations. In the case of VCT channel (Fig. 4.27(right)), $\text{H}^+ + \text{CO}(v = 0) \longrightarrow \text{H}(^2\text{S})$

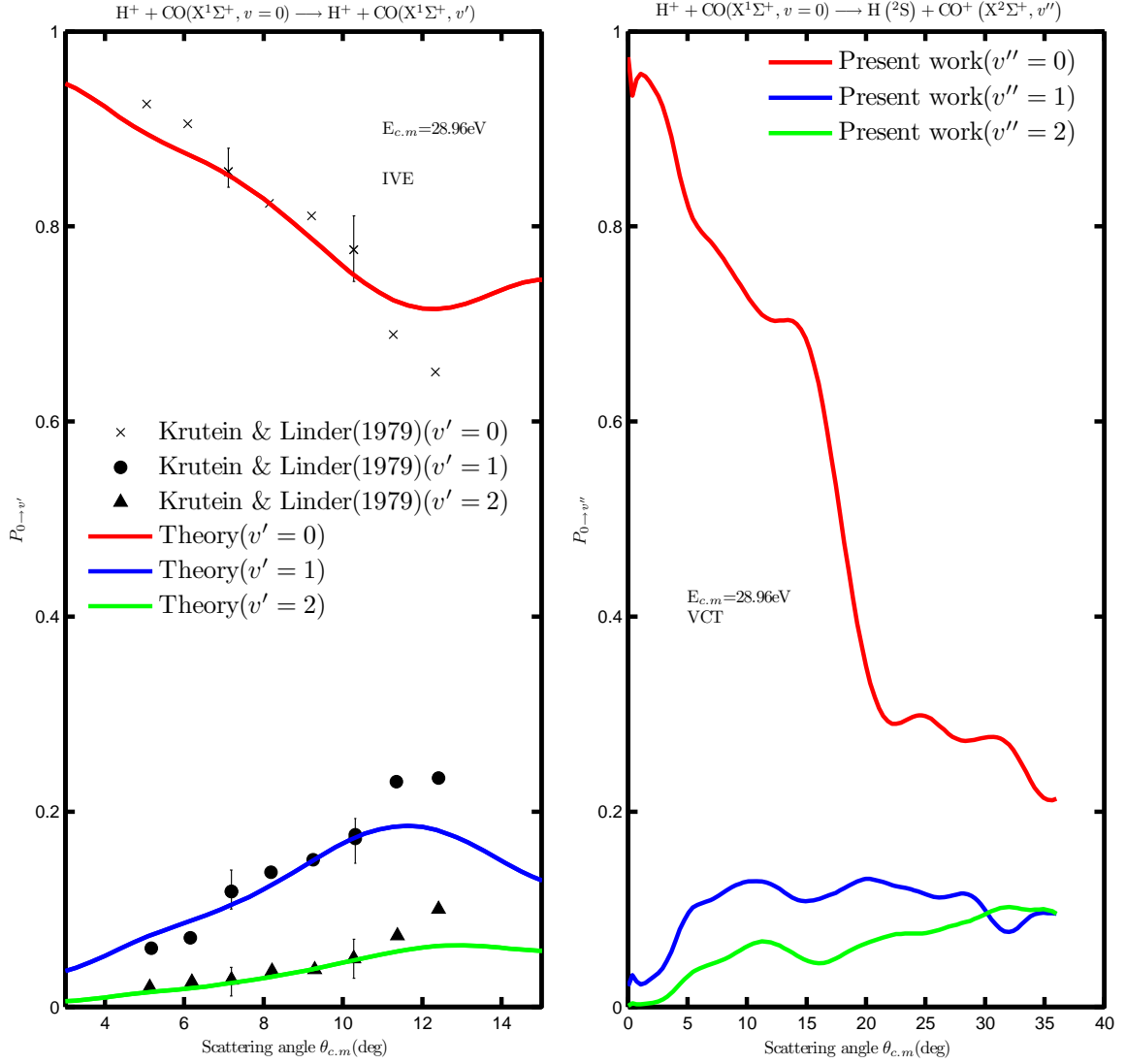


Figure 4.27: The computed transition probability $P_{0v'/v''}$ for IVE and VCT channels at $E_{cm} = 28.96$ eV as a function of scattering angle θ_{cm} (deg) for the first three states. The experimental data (Krutein and Linder, 1979) are available along with error bars for the IVE channel for first three excitations, $v = 0 \rightarrow v' = 0$ (\times), $v = 0 \rightarrow v' = 1$ (\bullet), $v = 0 \rightarrow v' = 2$ (\blacktriangle). There is no experimental data available for VCT channel and hence we show the plots in full range.

+ $CO^+(\Sigma v'')$, there is no experimental information available, hence we plot only our computed data alone with full range of scattering angle for first three excitations, $v = 0 \rightarrow v'' = 0$, $v = 0 \rightarrow v'' = 1$, $v = 0 \rightarrow v'' = 2$. The first charge transfer transition decreases monotonically rapidly as function of scattering angle whereas, second and third charge transfer excitations increase slowly and reaches a moderate values in transition probability $P_{0v''}$ at

very high scattering angle.

4.6.2.5 Average vibrational energy transfer

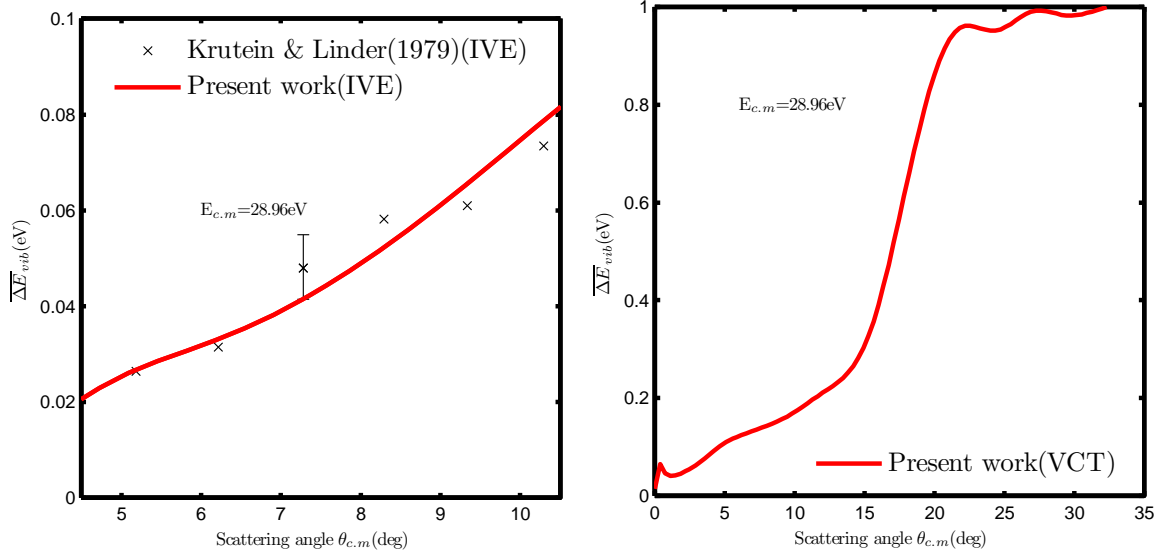


Figure 4.28: The computed average vibrational energy transfer $\overline{\Delta E}_{vib}$ (eV) for IVE (left) and VCT (right) as a function of scattering angle θ_{cm} at the collision energy $E_{cm} = 28.96$ eV. The theoretical values gives excellent agreement with the experimental data with error bars (Krutein and Linder, 1979) for the IVE channel and no experimental data are available at this collision energy for VCT channel

The average vibrational energy transfer $\overline{\Delta E}_{vib}(\theta_{cm})$ for both IVE and VCT channels is computed using Eq. (4.16) on page 87. The average vibrational energy transfer $\overline{\Delta E}_{vib}$ (eV) for both IVE and VCT channels have been shown in Fig. 4.28. The theoretical values and experimental values (Krutein and Linder, 1979) agree well within the experimental error as indicated by error bar in the case of elastic/inelastic channel Fig. 4.28(left). The average vibrational energy transfer increase almost linearly with scattering angle θ_{cm} in the plotted region and is of the order of milli electron volts. In the case of VCT channel, there is no experimental data available, hence we show only our computed results in Fig. 4.28(right), from which we can see that initially the mean vibrational energy transfer increases slowly

and at $\theta_{cm} \approx 15^\circ$, there is an abrupt increase of mean vibrational energy till $\theta_{cm} \approx 20^\circ$ and then it levels off after that. This kind of feature exists for the inelastic channel but is of less order of magnitude. This feature suggests that in certain range of scattering angle, energy transfer in the collision dynamics is quite strong, especially in the processes involving the electron transfer.

4.6.2.6 Intergral cross section

The rotationally summed state-to-state ICS is computed using Eq. (3.32) on page 41 and in Fig. 4.29, we show the computed ICS as a function of vibrational states for IVE and VCT channel at $E_{cm} = 28.96$ eV. The ICS values on the ordinate denotes the powers of 10. We can see IVE channel lying above the VCT channel and there is a flipping between IVE and VCT at slightly higher vibrational states. At $v = 0$, ICS is highest for both the channels, drastically reducing from $v = 1$ onwards and at higher v'/v'' states, ICS becomes too small (almost zero). This indicates that elastic and first charge transfer process have got maximum ICS, making them the dominant processes in any collisional events. The absolute values of

Table 4.8: VCC-RIOSAs state-to-state integral cross section (absolute values) for the IVE channel, $\text{H}^+ + \text{CO}(v = 0) \rightarrow \text{H}^+ + \text{CO}(v')$ and the VCT channel, $\text{H}^+ + \text{CO}(v = 0) \rightarrow \text{H}(^2\text{S}) + \text{CO}^+(v'')$ at the $E_{cm} = 28.96$ eV.

$v'(v'')$	Integral cross section (\AA^2)	
	IVE	VCT
0	48.609	14.871
1	1.967	1.068
2	0.528	0.384
3	0.224	0.240
4	0.147	0.162
5	0.088	0.119
6	0.096	0.123
7	0.076	0.096
$\Sigma v'(v'')$	51.735	17.062

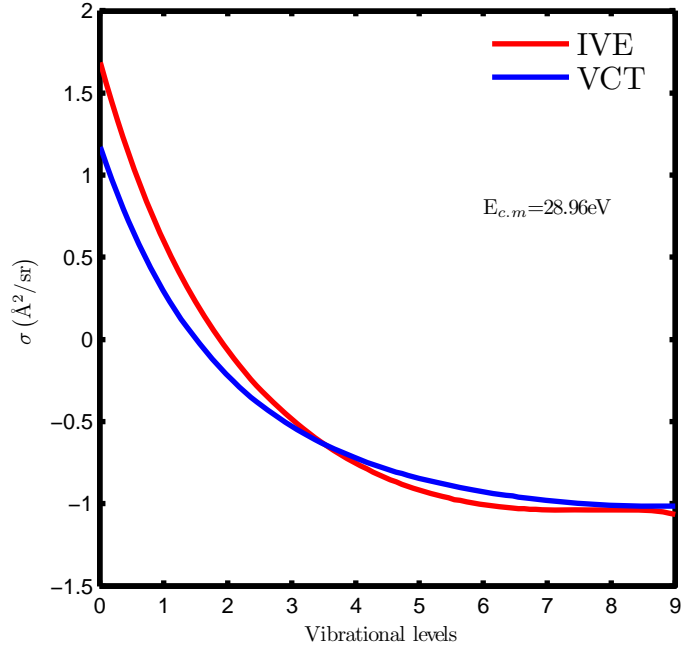


Figure 4.29: The computed integral cross section $\sigma(\text{\AA}^2/\text{sr})$ for IVE and VCT as a function of vibrational energy levels at the collision energy $E_{cm} = 28.96$ eV. The two curves run parallel to each other with a crossing at slightly higher vibrational levels and initially the integral cross section for IVE process is of higher magnitude than VCT process. Note that the numbers on the Y-axis indicate powers of 10.

ICS, obtained directly from the computation is tabulated in Table 4.8 for both the channels.

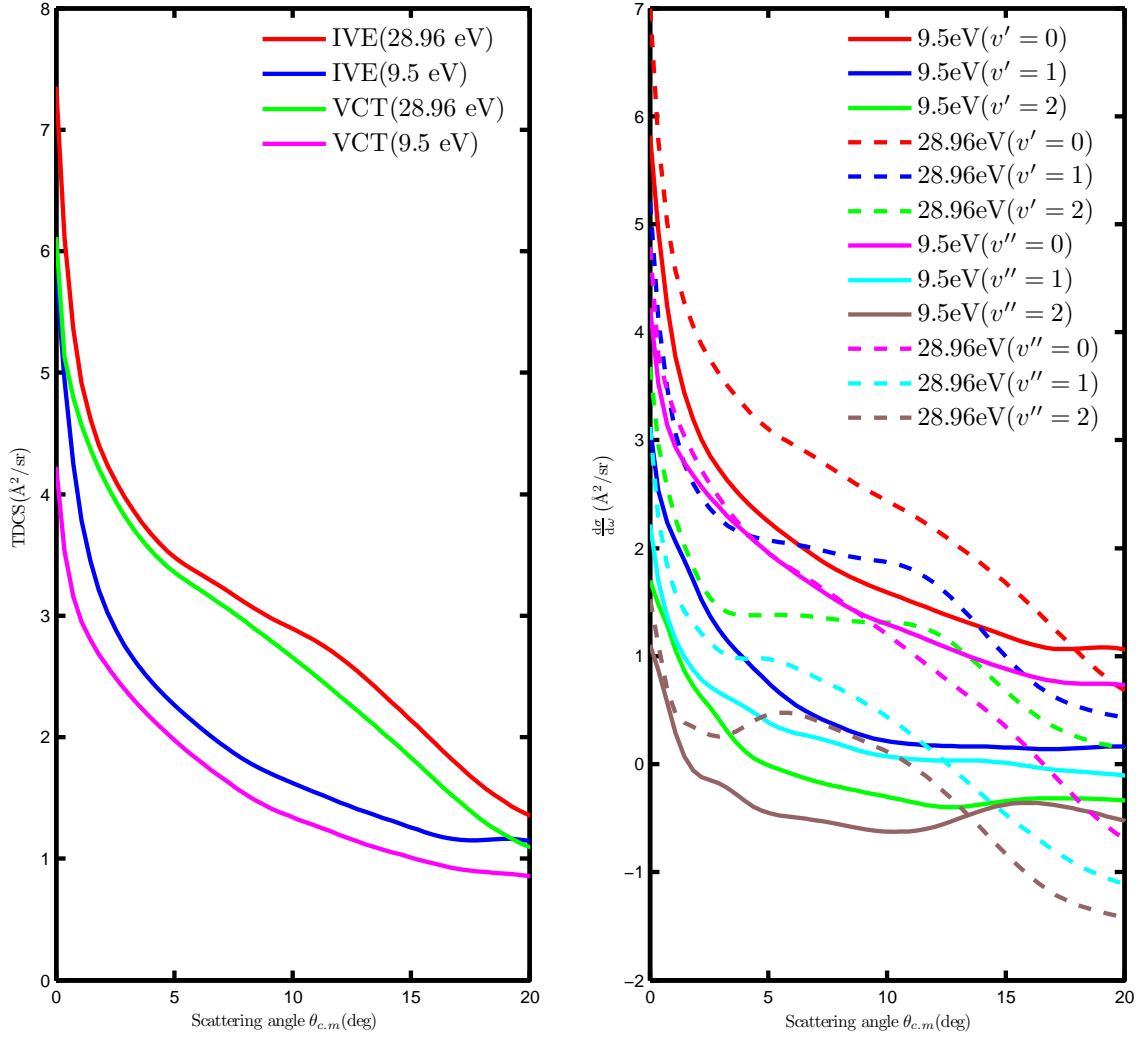
The last entry in the Table 4.8 denotes the sum of state-to-state ICS to give a single ICS for the entire process at the collision energy $E_{cm} = 28.96$ eV. They are estimated to be 51.735\AA^2 and 17.062\AA^2 for IVE and VCT channel respectively.

4.6.3 Dynamics : A comparison between 9.5eV and 28.96eV

We are going to discuss about how the scattering properties are influenced by the change of collision energy. Below we will compare one by one different scattering properties.

4.6.3.1 Rotationally-summed state-selective differential cross section (DCS)

Now that we have total differential cross sections and state-to-state differential cross section for two different collision energies we compare them in Fig. 4.30. In Fig. 4.30(a), we



(a) The computed TDCS for IVE, $\text{H}^+ + \text{CO}(v = 0) \longrightarrow \text{H}^+ + \text{CO}(\Sigma v')$, and VCT, $\text{H}^+ + \text{CO}(v = 0) \longrightarrow \text{H}(^2\text{S}) + \text{CO}^+(\Sigma v'')$, channels at $E_{cm} = 28.96$ eV and $E_{cm} = 9.5$ eV as a function of scattering angle θ_{cm} (deg).

(b) The computed rotationally summed state-to-state DCS for IVE, $\text{H}^+ + \text{CO}(v = 0) \longrightarrow \text{H}^+ + \text{CO}(\Sigma v')$, and VCT, $\text{H}^+ + \text{CO}(v = 0) \longrightarrow \text{H}(^2\text{S}) + \text{CO}^+(\Sigma v'')$, channels at $E_{cm} = 28.96$ eV and $E_{cm} = 9.5$ eV as a function of scattering angle θ_{cm} (deg).

Figure 4.30: A comparison between the TDCS and DCS at two different collision energies.

compare TDCS for $E_{cm} = 28.96$ eV and $E_{cm} = 9.5$ eV for IVE, $\text{H}^+ + \text{CO}(v = 0) \longrightarrow \text{H}^+ + \text{CO}(\Sigma v')$ and for VCT, $\text{H}^+ + \text{CO}(v = 0) \longrightarrow \text{H}(^2\text{S}) + \text{CO}^+(\Sigma v'')$, as a function of scattering angle θ_{cm} (deg). The Fig. 4.30(a) shows that the TDCS corresponding to $E_{cm} = 28.96$ eV is

characterized by the the presence of primary and secondary rainbow maxima even though their exact location differs from that predicted by the experiments (Niedner-Schatteburg and Toennies, 1992), but in the case of $E_{cm} = 9.5$ eV, this feature of primary and secondary rainbow maxima are absent in their corresponding TDCSs curves. Moreover, it shows that magnitudewise TDCS curves of $E_{cm} = 28.96$ eV lie above that of $E_{cm} = 9.5$ eV. The cross sectional difference between the IVE and VCT channel for $E_{cm} = 9.5$ eV is fairly constant as a function of scattering angle θ_{cm} (deg) whereas, for $E_{cm} = 28.96$ eV, it changes with θ_{cm} (deg) in the shown range of scattering angle from $\theta_{cm} = 0^\circ$ to $\theta_{cm} = 20^\circ$.

In Fig. 4.30(b), we compare rotationally summed stat-to-state differential cross sections for for $E_{cm} = 28.96$ eV and $E_{cm} = 9.5$ eV for IVE, $\text{H}^+ + \text{CO}(v = 0) \longrightarrow \text{H}^+ + \text{CO}(\Sigma v')$ and for VCT, $\text{H}^+ + \text{CO}(v = 0) \longrightarrow \text{H}(^2\text{S}) + \text{CO}^+(\Sigma v'')$, channels as a function of scattering angle θ_{cm} (deg) for the first three vibrational states in each case. The Fig. 4.30(b) shows that individual DCS for first three transition for IVE channel, $v = 0 \rightarrow v' = 0, v = 0 \rightarrow v' = 1, v = 0 \rightarrow v' = 2$, respectively for $E_{cm} = 28.96$ eV lie above that of $E_{cm} = 9.5$ eV. Similarly, the individual DCS for first three transition for VCT channel, $v = 0 \rightarrow v'' = 0, v = 0 \rightarrow v'' = 1, v = 0 \rightarrow v'' = 2$, respectively for $E_{cm} = 28.96$ eV lie above that of $E_{cm} = 9.5$ eV. The first charge transfer process $v = 0 \rightarrow v'' = 0$ in 9.5 eV and 28.96 eV lie very close to each other than any other processes below $\theta_{cm} = 10^\circ$ though if looked closely shows that 28.96 eV lies above 9.5 eV. A very weak rainbow maxima occurs in the state-to-state DCS for both IVE and VCT channels at $E_{cm} = 28.96$ eV (except in $v = 0 \rightarrow v'' = 2$ where it is strong) and is absent in both the channels at $E_{cm} = 9.5$ eV (except in $v = 0 \rightarrow v'' = 2$ where rainbow occurs at large θ_{cm}).The DCS for $E_{cm} = 28.96$ eV decays very quickly compared to 9.5 eV where it is almost flat at larger scattering angles.

4.6.3.2 Transition probability

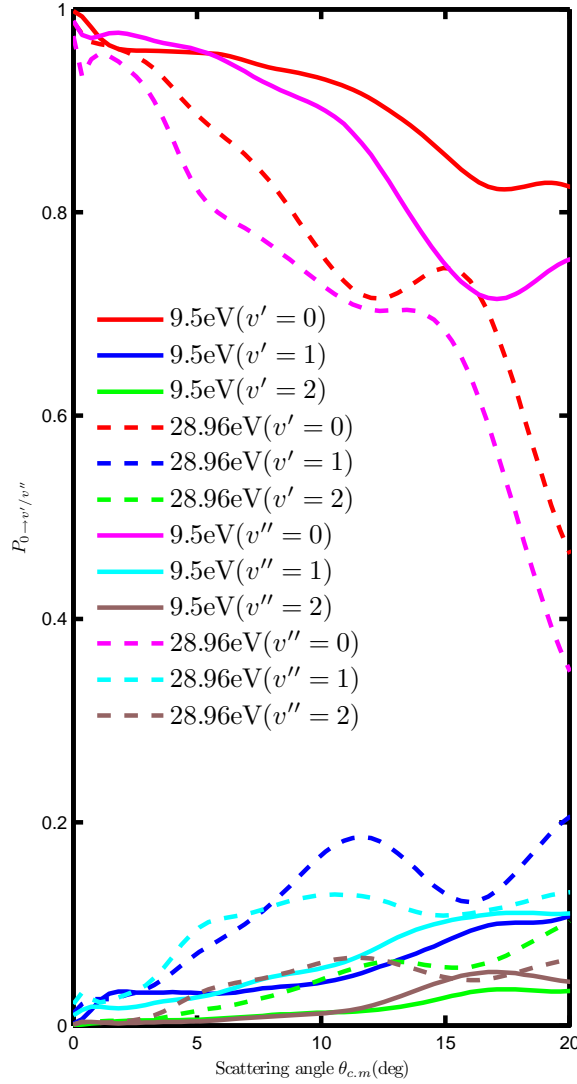


Figure 4.31: The computed transition probability $P_{0 \rightarrow v'/v''}$ for IVE channel, $\text{H}^+ + \text{CO}(v = 0) \rightarrow \text{H}^+ + \text{CO}(v')$ for the first three excitations, $v = 0 \rightarrow v' = 0, v = 0 \rightarrow v' = 1, v = 0 \rightarrow v' = 2$, and VCT channel, $\text{H}^+ + \text{CO}(v = 0) \rightarrow \text{H}(^2\text{S}) + \text{CO}^+(v'')$, for the first three excitations, $v = 0 \rightarrow v'' = 0, v = 0 \rightarrow v'' = 1, v = 0 \rightarrow v'' = 2$ at $E_{cm} = 28.96$ eV and $E_{cm} = 9.5$ eV as a function of scattering angle θ_{cm} (deg).

In Fig. 4.31, we compare the transition probability $P_{0 \rightarrow v'/v''}$ for IVE channel, $\text{H}^+ + \text{CO}(v = 0) \rightarrow \text{H}^+ + \text{CO}(v')$ for the first three excitations, $v = 0 \rightarrow v' = 0, v = 0 \rightarrow v' = 1, v = 0 \rightarrow v' = 2$, and VCT channel, $\text{H}^+ + \text{CO}(v = 0) \rightarrow \text{H}(^2\text{S}) + \text{CO}^+(v'')$, for the first three excitations, $v = 0 \rightarrow v'' = 0, v = 0 \rightarrow v'' = 1, v = 0 \rightarrow v'' = 2$

2 at $E_{cm} = 28.96$ eV and $E_{cm} = 9.5$ eV as a function of scattering angle θ_{cm} (deg). The transition probability $P_{0 \rightarrow v'}$ for the elastic channel and the same for the first charge transfer channel $P_{0 \rightarrow v''}$ keeps on decreasing at $E_{cm} = 28.96$ eV more than at $E_{cm} = 9.5$ eV as a function of scattering angle θ_{cm} . This suggests that at low energy collisions, elastic and first charge transfer process contribute more to the over all collisional events that at high energy collisions. The transition probability $P_{0 \rightarrow v'}$ of inelastic collisions and the same for the second and third CT channel $P_{0 \rightarrow v''}$ keeps on increasing at $E_{cm} = 28.96$ eV more than at $E_{cm} = 9.5$ eV as a function of scattering angle θ_{cm} . This suggests that at high collision energy, vibrational excitations and electron capture of higher order are more probable to occur than at low collision energy. Hence to obtain either higher order inelastic process or electron capture along with vibrational excitation in $H^+ + CO$ system one needs to increase the incident kinetic energy (KE) of H^+ and allow it to hit the target CO molecule at high θ_{cm} and whereas to obtain either elastic excitation alone or electron capture with no vibrational excitation, one needs to decrease the incident KE of H^+ and allow it to collide the target CO molecule at small θ_{cm} . For any given incident KE of H^+ , the probability of higher order excitation or electron capture will keep on decreasing as function of θ_{cm} .

4.6.3.3 Average vibrational energy transfer

In Fig. 4.32, we show average vibrational energy transfer $\overline{\Delta E_{vib}}$ (eV) for IVE channel, $H^+ + CO(v = 0) \longrightarrow H^+ + CO(v')$ and VCT channel, $H^+ + CO(v = 0) \longrightarrow H(^2S) + CO^+(v'')$, at $E_{cm} = 28.96$ eV and $E_{cm} = 9.5$ eV as a function of scattering angle θ_{cm} (deg). As previously mentioned the mean vibrational energy is computed by summing up product of all the state-to-state transition probabilities $P_{0 \rightarrow v'/v''}$ and change in energy of adjacent vibrational energy levels of CO and CO^+ . Hence the quantity as a function of scattering angle is suggestive of

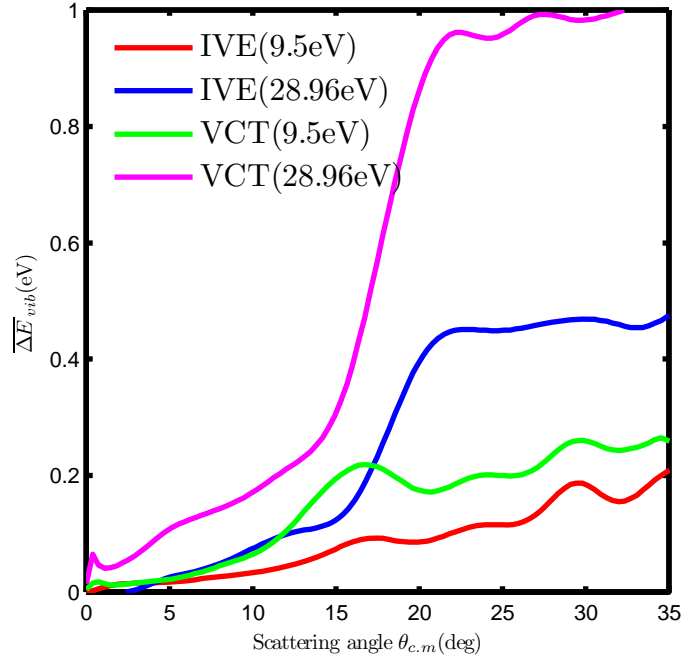


Figure 4.32: The computed average vibrational energy transfer $\overline{\Delta E}_{vib}$ (eV) for IVE channel, $H^+ + CO(v = 0) \rightarrow H^+ + CO(v')$ and VCT channel, $H^+ + CO(v = 0) \rightarrow H(^2S) + CO^+(v'')$, at $E_{cm} = 28.96$ eV and $E_{cm} = 9.5$ eV as a function of scattering angle θ_{cm} (deg). Note the jump in $E_{cm} = 28.96$ eV.

amount of energy transfer during the collision processes. The Fig. 4.32 explicitly shows that such energy transfer can be influenced by the incident collision energy of H^+ . At $E_{cm} = 28.96$ eV, there is quantum leap in the amount of energy transfer in both IVE and VCT processes in certain θ_{cm} range, as shown by vertical rise of curve between $\theta_{cm} = 15^\circ - 22^\circ$, even though the quantum leap in the case of VCT process is far higher than IVE process. This quantum leap actually comes from the incident KE of H^+ which is also higher. But in the case of $E_{cm} = 9.5$ eV collision, this kind of quantum leap in the energy transfer is about to develop but not developed enough to be recognized easily in both the channels even though both curve starts rising up as function of θ_{cm} . In 9.5 eV also, energy transfer involved is higher in the case of VCT rather than IVE channel. In summary, as a rule of thumb, we propose that as the incident collision energy increases the mean vibrational energy transfer also increases with VCT processes consuming higher proportion of incident KE than IVE

processes as suggested by Fig. 4.32.

4.6.3.4 Integral cross section

The rotationally summed state-to-state integral cross section (\AA^2) for both IVE and VCT channels at 9.5 eV and 28.96 eV have been shown in Fig. 4.33 as a function of vibrational quantum number of both CO and CO^+ . We can see quickly that the ICS for the VCT channel at $E_{cm} = 28.96$ eV and $E_{cm} = 9.5$ eV almost remain the same which gives us the impression that the change in collision energy does not affect the ICS values. But the change in collision energy E_{cm} indeed influence the magnitudes of IVE channel as can be verified from the Fig. 4.33 in which the ICS at $E_{cm} = 9.5$ eV is higher in magnitude than that at $E_{cm} = 28.96$ eV. This suggests that in the slow collision, H^+ comes into contact with the target molecule CO over a wide area for elastic/inelastic process, as reflected in the high value of ICS at $E_{cm} = 9.5$ eV. All this information have been summarized in the Table 4.9 which shows

Table 4.9: VCC-RIOSAs state-to-state integral cross section (absolute values) for the IVE channel, $\text{H}^+ + \text{CO}(v = 0) \rightarrow \text{H}^+ + \text{CO}(v')$ and the VCT channel, $\text{H}^+ + \text{CO}(v = 0) \rightarrow \text{H}^+(\text{2S}) + \text{CO}^+(v'')$ at the $E_{cm} = 28.96$ eV and $E_{cm} = 9.5$ eV.

$v'(v'')$	Integral cross section (\AA^2)			
	9.5 eV		28.96 eV	
	IVE	VCT	IVE	VCT
0	69.727	14.715	48.609	14.871
1	2.581	1.021	1.967	1.068
2	0.869	0.372	0.528	0.384
3	0.397	0.217	0.224	0.240
4	0.201	0.145	0.147	0.162
5	0.144	0.117	0.088	0.119
6	0.106	0.111	0.096	0.123
7	0.140	0.098	0.076	0.096
$\sum v'(v'')$	74.311	17.055	51.735	17.062

that elastic collision for IVE is highest at 9.5 eV and first charge transfer for VCT is almost

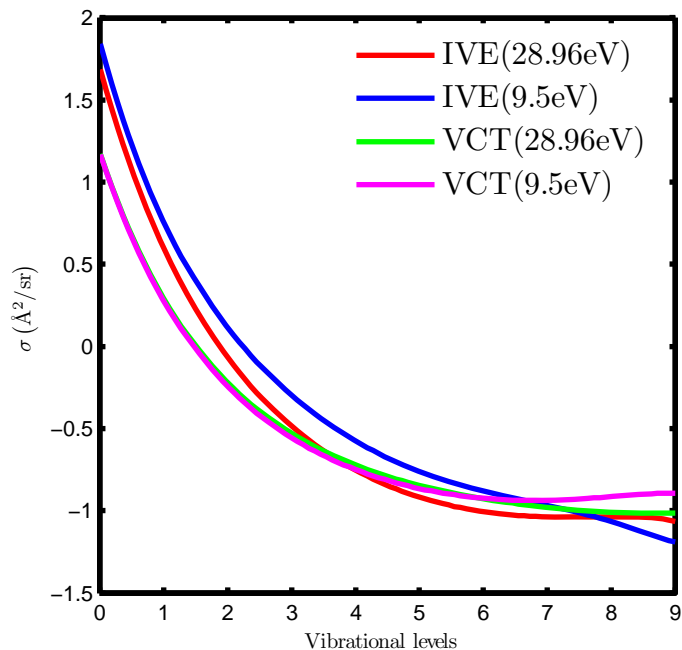


Figure 4.33: The computed VCC-RIOS state-to-state integral cross section $\sigma(\text{\AA}^2)$ for IVE channel, $\text{H}^+ + \text{CO}(v = 0) \longrightarrow \text{H}^+ + \text{CO}(v')$ and VCT channel, $\text{H}^+ + \text{CO}(v = 0) \longrightarrow \text{H}^{(2)\text{S}} + \text{CO}^+(v'')$, at $E_{cm} = 28.96$ eV and $E_{cm} = 9.5$ eV as a function of scattering angle $\theta_{cm}(\text{deg})$. Note that ICS for the VCT channel for 28.96 eV and 9.5 eV remains the same and Y-ordinates are powers of 10

the same at both collision energies. Numerically, ICS at 9.5 eV is at higher side for IVE channel than at 28.96 eV. If looked at total ICS given as the last entry, it suggests that ICS for IVE at 9.5 eV is higher than that at 28.96 eV and the same for VCT is almost the same sum at both collision energies, 17.055 and 17.062, respectively.

4.7 Summary

In the present study, we have generated new global *ab initio* adiabatic PESs for the GS and the first ES of the $\text{H}^+ + \text{CO}$ system using Dunning's *cc-pVTZ* basis set at the MRCI (with the single and double excitation) level of accuracy. Comparisons of various computed diatomic data for CO and CO^+ and the equilibrium data of the bound HCO^+ and HOC^+ ions

with those of experiments and high level *ab initio* calculations available for these ions lends credence to the accuracy of the present *ab initio* calculations. The various characteristics and topologies of the adiabatic PESs have been analysed in detail. The corresponding quasi-adiabatic PESs and the coupling between them are also obtained using the *ab initio* procedure at the same level of accuracy. The nonadiabatic interactions have been analysed in detail in terms of NACME and the coupling potentials.

We have analysed in detail the quantum dynamics of collision energy transfer processes in the $\text{H}^+ + \text{CO}$ collisions within the framework of the VCC-RIOSAs decoupling scheme. The quantum dynamics has been carried out at $E_{cm} = 9.5$ eV and at $E_{cm} = 28.96$ eV for which experimental data are available for the IVE channel. Only one data set is available from the experiment for the VCT channel at $E_{cm} = 28.96$ eV, and that is for the total DCS for the VCT channel. Modelling the dynamics as a two-state process at these energies we are able to predict almost all the experimental data for the IVE channel at these two collision energies quite accurately, except for some noticeable discrepancies. The predicted TDCS for the VCT channel overestimates the experimental values at $E_{cm} = 28.96$ eV.

We believe that the present *ab initio* and quantum dynamics study is perhaps the first study which reports the dynamics on the coupled PESs and the results for the various collision attributes and their comparisons with those of available experimental results. From the *ab initio* analysis of the nonadiabatic interactions it is suggested that at least two more low lying third and fourth ESs would also be involved in the collision dynamics. The second ES, which asymptotically correlates to the VCT channel, $\text{H}(^2\text{S}) + \text{CO}^+(\text{X}^2\Sigma^+)$, would be further coupled through nonadiabatic interactions to the third and the fourth ESs. Since the GS which asymptotically correlates to the IVE channel, $\text{H}^+ + \text{CO}(\text{X}^1\Sigma^+)$, lies quite

separated energetically with respect to the third and fourth ESs and its nonadiabatic coupling with them is expected to be less. Therefore, if the dynamics is carried out on 4×4 coupled electronic state we expect (a) the IVE attributes would be mostly be the same as it is observed for the present 2×2 coupled electronic state with minor variations and (b) that the flux entering into the first CT channel would be further partitioned effectively into the second and the third CT channels through their nonadiabatic coupling strengths; thus leaving reduced magnitudes for the first VCT collision attributes. Therefore, we believe that atleast 3×3 or 4×4 coupled electronic states quantum dynamics calculations would improve the theoretical results considerably in comparison with experiments.

CHAPTER 5

NONADIABATIC DYNAMICS ON THE TWO COUPLED ELECTRONIC PESs : THE $\text{H}^+ + \text{O}_2$ SYSTEM

In this chapter, we study the dynamics of the IVE, $\text{H}^+ + \text{O}_2(X^3\Sigma_g^-, v = 0) \longrightarrow \text{H}^+ + \text{O}_2(X^3\Sigma_g^-, v')$, and the VCT, $\text{H}^+ + \text{O}_2(X^3\Sigma_g^-, v = 0) \longrightarrow \text{H}(^2\text{S}) + \text{O}_2^+(X^2\Pi_g, v'')$, processes. A brief review on the experimental and the theoretical studies carried out on the $\text{H}^+ + \text{O}_2$ system till date has been given in **chapter 1**. In this chapter, we discuss the newly generated global *ab initio* potential energy surfaces of the GS and the next higher three ESs and their topological characteristics. We also present briefly the details of *ab initio* diabaticization procedure used and the corresponding quasi-diabatic PESs computed in the present study. We have performed a time-independent quantum dynamics study within the VCC-RIOSAs framework at the experimentally reported collision energies, $E_{cm} = 9.5$ eV and $E_{cm} = 23$ eV and compared the results with those of experiments as well as those of the earlier theoretical studies to test the suitability of the two-state diabatic PESs in explaining the experimental behaviour.

5.1 Present focus

Just recently, global *ab initio* adiabatic PESs for the GS and the first ES of the $\text{H}^+ + \text{O}_2$ system were reported (Saieswari and Kumar, 2007b, 2008a) along with the corresponding quasidiabatic PESs. The obtained NACME and the mixing angle values obtained using the

ab initio procedures showed quite an irregular behaviour in certain regions of the nuclear configurations. The irregular behaviour was indicative of existence of an avoided crossings with other low-lying (the third) ES with the second ES. However, in that study, it was assumed that only the GS and the first ES would be involved and the dynamics can be modelled mostly as a two-state process, and any further influence coming from the third ES would be rather small. This assumption was primarily based on the fact that the molecular beam experiments did not hint of any detection of electronically excited O_2^+ molecules. Therefore, the irregular behaviour (other than originating from the genuine interactions from the GS and the first ES) was smoothed and then the time-independent quantum dynamics was performed within the VCC-RIOSAs framework to study the IVE and the VCT channels. The obtained results were almost similar to the earlier theoretical results which were obtained using the semi-empirical PESs. Thus, using the smoothed two-state coupled *ab initio* PESs the improvement achieved in the quantum dynamics calculations was little. A preliminary analysis in terms of PECs as a function of R for a fixed value of $r = r_{eq}$ and γ showed that at least two more ESs (the third and the fourth ESs) could also be involved in influencing the dynamics of the IVE and the VCT channels at $E_{cm} = 23$ eV. However, their relative roles could not be ascertained. Also it was not clear whether the smoothing of the quasidiabatic PESs had the bearing on the dynamics outcome. Therefore, we have undertaken an extensive *ab initio* study to compute the adiabatic and the corresponding quasidiabatic PESs (with the coupling potential matrix) for the 4×4 coupled electronic state, that is, the GS and the three lowest lying ESs. First, we would like to test whether smoothing of PESs had any significant role and/or the 2×2 state coupling could largely represent the dynamics of the IVE and the VCT channels. Therefore, from the obtained 4×4 coupling potential matrix we just take out the 2×2 sub-matrix involving only the GS and the first ES and carry out the

quantum dynamics. In this chapter, we present the computational details of the 4×4 state *ab initio* calculations along with the some salient features of the GS and the first ES PESs and also analyse the quantum dynamics results obtained using the 2×2 potential matrix. The other characteristic details of the 4×4 potential matrix and the corresponding quantum dynamics are given and discussed in the following chapter (**chapter 6**).

5.2 *Ab initio* PECs

Ab initio computations have been performed in the Jacobi coordinates (see Fig. 3.1 of **Chapter 3**) for the triplet spin symmetry using the MOLPRO 2002.6 package (Werner, Knowles, Schütz, Lindh, Celani, Korona, Rauhut, Manby, Amos, Bernhardsson, Berning, Cooper, Deegan, Dobbyn, Eckert, Hampel, Hetzer, Lloyd, McNicholas, Meyer, Mura, Nicklaß, Palmieri, Pitzer, Schumann, Stoll, Stone, Tarroni, and Thorsteinsson, 2002). For the collinear ($\gamma = 0^\circ$) and the perpendicular ($\gamma = 90^\circ$) approaches the calculations were performed in the C_{2v} point groups while for off-collinear approaches they were carried out in the C_s point group. The computations were done for the four lowest electronic states with B_1 and A_2 (C_{2v}) and A'' (C_s) symmetries. Dunning's *cc-pVTZ* basis set (Dunning, 1989) was employed for the H and the two O atoms of the system resulting in 74 contracted wave functions (MOs). The break-ups were $(50a' + 24a'')$ for the C_s and $(33a_1 + 17b_1 + 17b_2 + 7a_2)$ for the C_{2v} (collinear case, $\gamma = 0^\circ$) and $(27a_1 + 13b_1 + 23b_2 + 11a_2)$ for C_{2v} (perpendicular case, $\gamma = 90^\circ$). The lowest two orbitals $1a', 2a'$ were treated as the core orbitals and next seven orbitals $3a' - 9a'$ and $1a'', 2a''$ were treated as the valence orbitals in the C_s . In the C_{2v} , $1a_1, 2a_1$ were the core orbitals and $5a_1 + 2b_1 + 2b_2 + 0a_2$ are the valence orbitals for $\gamma = 0^\circ$, and $1a_1$ and $1b_2$ were the core orbitals and $4a_1 + 1b_1 + 3b_2 + 1a_2$ were the valence

orbitals for $\gamma = 90^\circ$. The arrangement of the electrons in various orbitals at the reference geometry taken at $R = 16a_0$ for both the C_s and C_{2v} point group is tabulated in Table 5.1, with the number of electrons given in parenthesis. For $\gamma = 0^\circ$, the GS PES is of A_2 symmetry, corresponding to ${}^3\Sigma^-$ in the $C_{\infty v}$ group and the first ES PES of B_1 , corresponding to ${}^3\Pi$. For $\gamma = 90^\circ$, the GS PES is of B_1 symmetry and the first ES PES of A_2 symmetry. In the Multi-configuration self consistent field (MCSCF) computations (Werner and Knowles, 1985; Knowles and Werner, 1985) the $1a' - 2a'$ orbitals remained frozen with the four core electrons and $3a' - 9a'$ and $1a'' - 2a''$ remained active for the remaining 12 electrons for the C_s geometry. In the C_{2v} group, for $\gamma = 0^\circ$, the $1a_1 - 2a_1$ are the core orbitals and $3a_1 - 7a_1, 1b_1 - 2b_1, 1b_2 - 2b_2$ were the active orbitals for the remaining 12 electrons and for $\gamma = 90^\circ$, the $1a_1, 1b_2$ are the core orbitals and $2a_1 - 5a_1, 1b_1, 2b_2 - 4b_2, 1a_2$ were the valence orbitals for the 12 electrons for both the A_2 and the B_1 symmetries. Typically, the wavefunction consist of 1722 Configuration state functions (CSFs) with 2324 slater determinants for all the four electronic states with equal weightage of 0.25 for the C_s geometry. For the C_{2v} symmetry, roughly 858 CSFs with 1140 slater determinants for $\gamma = 0^\circ$, and 861 CSFs with 1162 slater determinants for $\gamma = 90^\circ$, were involved in the computation process at the MCSCF level. The convergence in MCSCF level is very sensitive to number of wavefunctions in the primary configuration space (p-space) and therefore, it was advisable to accomodate sufficient number of wavefunctions by increasing or decreasing the p-space. In the Multi-reference internally contracted configuration interaction (MRCI) calculations (Werner and Knowles, 1988; Knowles and Werner, 1992, 1988), which involved only the single and the double excitations, the wavefunctions in the reference space amounted to 686 configurations consisting of 1722 CSFs for the four states in the C_s ; Those in N electron internal space consisted of 1470 configurations with 3402 CSFs and N-1 and N-2 internal

Table 5.1: The symmetrywise arrangement of orbitals in eV at the SCF level at the reference geometry $R_{ref} = 16a_0$ of the $H^+ + O_2$ system. The occupational pattern of electrons is given in parenthesis.

C_s		$C_{\infty v}$						C_{2v}					
		$\gamma = 0^\circ$			$\gamma = 90^\circ$			$\gamma = 0^\circ$			$\gamma = 90^\circ$		
orbitals	A''	orbitals	A_2	orbitals	B_1	orbitals	A_2	orbitals	B_1	orbitals	A_2	orbitals	B_1
$1a'(2)$	-20.7951	$1a_1(2)$	-20.7966	$1a_1(2)$	-20.7760	$1a_1(2)$	-20.7711	$1a_1(2)$	-20.7924	$1a_1(2)$	-20.7711	$1a_1(2)$	-20.7924
$2a'(2)$	-20.7895	$2a_1(2)$	-20.7887	$2a_1(2)$	-20.7667	$2a_1(2)$	-1.6850	$2a_1(2)$	-1.7051	$2a_1(2)$	-1.6850	$2a_1(2)$	-1.7051
$3a'(2)$	-1.7054	$3a_1(2)$	-1.7056	$3a_1(2)$	-1.6853	$3a_1(2)$	-0.8164	$3a_1(2)$	-0.7935	$3a_1(2)$	-0.8164	$3a_1(2)$	-0.7935
$4a'(2)$	-1.1624	$4a_1(2)$	-1.1628	$4a_1(2)$	-1.1332	$4a_1(2)$	-0.8715	$4a_1(2)$	-0.7632	$4a_1(2)$	-0.8715	$4a_1(2)$	-0.7632
$5a'(2)$	-0.7941	$5a_1(2)$	-0.7946	$5a_1(1)$	-0.8726	$5a_1(1)$	-0.7561	$1b_1(2)$	-0.7630	$1b_1(2)$	-0.7561	$1b_1(2)$	-0.7630
$6a'(2)$	-0.7634	$1b_1(2)$	-0.7635	$1b_1(2)$	-0.7564	$1b_2(2)$	-20.7706	$1b_2(2)$	-20.7915	$1b_2(2)$	-20.7706	$1b_2(2)$	-20.7915
$7a'(1)$	-0.5947	$2b_1(1)$	-0.5951	$2b_1(1)$	-0.5947	$2b_2(2)$	-1.1324	$2b_2(2)$	-1.1619	$2b_2(2)$	-1.1324	$2b_2(2)$	-1.1619
$1a''(2)$	-0.7633	$1b_2(2)$	-0.7635	$1b_2(2)$	-0.8167	$3b_2(2)$	-0.5226	$3b_2(2)$	-0.5943	$3b_2(1)$	-0.5226	$3b_2(1)$	-0.5943
$2a''(1)$	-0.5946	$2b_2(1)$	-0.5951	$2b_2(2)$	-0.5231	$1a_2(1)$	-0.5933	$1a_2(1)$	-0.5942	$1a_2(1)$	-0.5933	$1a_2(1)$	-0.5942

space consisted of 2304 configuration with 9828 CSFs and 2550 configurations with 21306 CSFs, respectively. The total number of contracted configurations was 642952 which included total number of internal configurations, 1722, and total number of singly and double external configurations which were 309582 and 331648 respectively and total number of uncontracted configurations is 21477678. For the C_{2v} and for $\gamma = 0^\circ$, the reference space consisted of 382 configuration with 858 CSFs including 1470 N electron internal configuration with 3402 CSFs, 2304 N-1 electron internal configuration with 9828 CSFs and 2549 N-2 electron internal configurations with 21305 CSFs. The total number of contracted configurations was 326572 which included 858 internal configurations, 154806 singly external configurations and 170908 double external configurations and the total number of uncontracted configurations was 10744181 and for $\gamma = 90^\circ$, the reference space consisted of 343 configuration with 861 CSFs including 1470 N electron internal configuration with 3402 CSFs, 2304 N-1 electron internal configuration with 9828 CSFs and 2535 N-2 electron internal configurations with 21271 CSFs. The total number of contracted configurations was 322036 which includes 861 internal configurations, 154771 singly external configurations and 166404 double external configurations and the total number of uncontracted configurations was 10721927. The accuracy limit set for the convergence in MCSCF and MRCI level was 0.32×10^{-6} hartrees and the improvement of the computed values of energy from HF level to MRCI level for three orientations such as $\gamma = 0^\circ, 45^\circ, 90^\circ$ at r_{eq} is summarized in the Table 5.2. The energies computed with multi-reference configuration interaction including single and double excitations with the correction for higher order excitations in terms of Davidson's correction (Jenson, 1999) is referred to as MRDCI and it is also listed there. The convergence at the MRCI level is not as difficult as at the MCSCF level and can be achieved by simply increasing the number of iteration. If the convergence was achieved in the MC-

Table 5.2: Comparison of electronic energies for three molecular orientations at different levels of methodologies at r_e

	$\gamma = 0^\circ$	$\gamma = 45^\circ$	$\gamma = 90^\circ$
	$R = 3.0a_0$	$R = 2.6a_0$	$R = 2.0a_0$
HF	-149.65151103	-149.66013373	-149.46972008
MCSCF	-149.90909165	-149.95310848	-149.87223377
MRCI	-150.24093219	-150.28011292	-150.21297843
MRDCI	-150.26350817	-150.30212861	-150.23734711

SCF level then there was a greater likelihood that convergence would be reached smoothly in the MRCI level, too, though it was not always true in other cases as it had happened in the two-state diabatic PESs computation of the $H^+ + CO$ system for $\gamma = 180^\circ$ orientation because of the involvement of further low-lying excited states.

The *ab initio* MRCI computations involving the GS and the three lowest ESs of ($^3\Sigma^- / ^3\Pi$), ($^3B_1, ^3A_2$) and $^3A''$ electronic states were carried out on the following grid in the Jacobi coordinates (Fig. 3.1):

- for $\gamma = 0^\circ$, $R = 2.0 - 7.0(0.2)$, $8 - 15(1.0)$
- for $\gamma = 15^\circ$, $R = 1.2 - 7.0(0.2)$, $8 - 15(1.0)$
- for $\gamma = 45^\circ$, $R = 0.8 - 7.0(0.2)$, $8 - 15(1.0)$
- for $\gamma = 75^\circ$, $R = 0.2 - 7.0(0.2)$, $8 - 15(1.0)$
- for $\gamma = 90^\circ$, $R = 0.2 - 7.0(0.2)$, $8 - 15(1.0)$
- for each γ , $r = 1.5 - 3.5(0.1)$
- $\gamma = 0^\circ - 90^\circ(15^\circ)$

The numbers in the parenthesis are the increments in the given intervals and the distances are expressed in bohr. Before proceeding to describe the computation of the PECs for this system, O_2 was optimized at the MRCI level of theory using Dunning's *cc-pVTZ* basis set (Dunning, 1989) to give the best value for equilibrium bond length, $r_{eq} = 2.2934a_0$. and this

value is used throughout for r_{eq} . Some of the molecular properties of O_2 and O_2^+ relevant to this study have been summarized in the Table 5.3. All the computed properties agree quite well the available experimental values for the diatomic species.

Table 5.3: The computed molecular properties of O_2 and O_2^+ are compared with the experimental values. r_{eq} is the equilibrium bond length, E_{eq} is the electronic energy at equilibrium bond length, D_o is the dissociation energy, P.A is the proton affinity relative to asymptote $H^+ + O_2(X^3\Sigma_g^-)$, I.P is the ionization potential, $\Delta E_{rot}^{0\rightarrow 1}$ is the energy of first rotational excitation, $\Delta E_{vib}^{0\rightarrow 1}$ is the energy of first vibrational excitation and ΔE_{elec} is the energy of first electronic excitation, $O_2(^1\Delta_g \leftarrow ^3\Sigma_g^-)$, $O_2^+(^4\Pi_u \rightarrow ^2\Pi_g)$, $O_2^+(^2\Pi_u \rightarrow ^4\Pi_u)$ and $O_2^+(^4\Sigma_g^- \rightarrow ^4\Pi_u)$. All properties are computed using MRCI level of accuracy and *cc-pVTZ* basis set.

	$O_2(^3\Sigma_g^-)$		$O_2^+(^2\Pi_g)$		$O_2^+(^4\Pi_u)$		$O_2^+(^4\Sigma_g^-)$	
	Theory	Expt ^a	Theory	Expt ^b	Theory	Expt ^b	Theory	Expt ^b
$r_{eq}(\text{\AA})$	1.2132	1.21	1.1221	1.1227	1.39	1.38	1.29	1.28
$E_{eq}(\text{a.u.})$	-150.10		-149.68		-149.53		-149.45	
D_o (eV)	4.76	5.08	6.55	6.48	2.596		2.544	
I.P (eV)	11.58	12.6	23.69	24.2	19.74		17.59	
P.A (eV)	4.85	4.38 ^c						
$\Delta E_{rot}^{0\rightarrow 1}$ (meV)	0.35	0.36	0.41	0.42	0.269	0.274	0.312	0.319
$\Delta E_{vib}^{0\rightarrow 1}$ (eV)	0.191	0.193	0.23	0.233	0.125	0.128	0.142	0.148
ΔE_{elec} (eV)	0.99	0.98	3.95	4.08	0.975		2.15	2.066

^aGianturco, Gierz, and Toennies (1981)

^bHuber and Herzberg (1979)

^cBohme (1975)

The corresponding quasidiabatized PESs and the 4×4 coupling potential matrix using the *ab initio* procedures were obtained in the same manner as described in **chapter 2**. We used $R_{ref} = 16a_o$ at which both the adiabatic and quasidiabatic PESs become identical. For the construction of quasidiabatic PESs for a particular r , the diabatic PESs were obtained as a function of R for a fixed value of r . Although one obtains the quasidiabatic potential matrix directly from the *ab initio* computations and there is no need to compute for the NACMEs, yet we have computed them for the sake of understanding of the coupling dynamics. The NACME values were obtained in a similar manner using the same step-size as described in

chapter 4.

As mentioned above, we wish to carry out in this chapter quantum dynamics study using only the 2×2 coupled state. Therefore, we present and analyse only the GS and the first ES PESs and their couplings. It is important to note that this 2×2 coupled potential matrix is simply taken out from the 4×4 coupled potential matrix.

The adiabatic PECs for $\gamma = 0^\circ$ and $\gamma = 90^\circ$ as a function of R and r (in bohr units) have been shown in Fig. 5.1. As we can see, there is direct curve crossing between the GS and the first ES PECs for both the angles as a function of R (left panel, $r = r_{eq}$) and r (right panel, $R = 4a_0$) because they are of different symmetries. The GS PEC is $1^3\Sigma^-$ and the first ES PEC is $1^3\Pi$, for $\gamma = 0^\circ$ and GS PEC being 1^3B_1 and first ES PEC being 1^3A_2 , in the case of $\gamma = 90^\circ$. The asymptotic correlations of the GS and the first ES PECs are $H^+ + O_2(^3\Sigma_g^-)$ (the IVE channel) and $H(^2S) + O_2(^3\Pi_g)$ (the first VCT) respectively. From Fig. 5.1, it can be seen that the first charge transfer (electron capture) process is exoergic relative to the inelastic process. The computed value of exoergicity is 2.02 eV and agree fairly well with the experimental value $\Delta E = +1.52$ eV (Niedner-Schatteburg and Toennies, 1992). Since the charge transfer channel is highly exoergic it is expected to be probable.

Since the two states are of different symmetries there is no coupling between them along the radial coordinates (R, r) . These crossings turn into avoided crossings for off-collinear geometries (C_s point group) where the degeneracy of Π state is lifted into A' and A'' states, and the Σ^- state correlates to A'' state, making it as the GS with triplet spin symmetry. Again, there exists no coupling between the A' and the A'' along the radial coordinates (R, r) in the C_s geometry. Therefore, we show PECs of the A'' symmetry and show them for $\gamma = 15^\circ, \gamma = 45^\circ, \gamma = 75^\circ$ in Fig. 5.2. The adiabatic (solid) and quasidiabatic

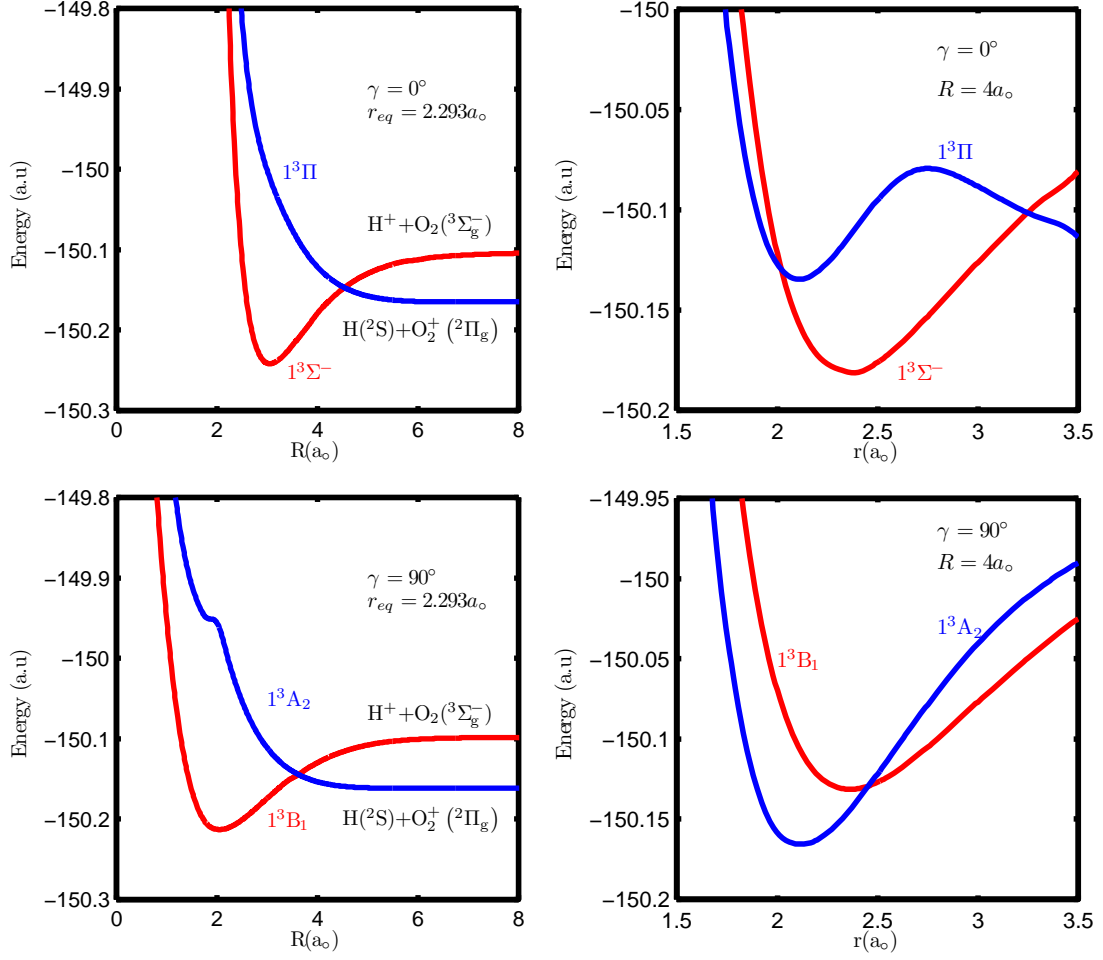


Figure 5.1: *Ab initio* adiabatic PECs of the GS and the first ES for $\gamma = 0^\circ$ and 90° orientations as a function of R for a fixed $r = r_{eq} = 2.293a_0$ (left panel) and as a function of r (right) for a fixed $R = 4.0a_0$ (right panel). Note the presence of crossings between the two electronic states of different symmetries in all four cases.

PECs (dashed) are shown as a function of R at $r = r_{eq} = 2.293a_0$ (left panel) and as a function of r at $R = 4.0a_0$ (right panel). It can be seen that both the adiabatic and diabatic curves tend to merge for $R > 6a_0$ implying that at large R the quasi-diabatic matrix becomes almost diagonalized. The hump seen in the upper adiabatic curve indicates that the $2^3A''$ state is involved in the Landau-Zener type of coupling (Landau, 1932; Zener, 1932) with the $3^3A''$ state, with the coupling being strengthened at $\gamma = 45^\circ$ orientation. The asymptotic correlations of the entrance channel is $H^+ + O_2(3\Sigma_g^-)$ and of the charge transfer is $H(2S) + O_2^+(2\Pi_g)$ for all the three orientations. The calculated energy differences between

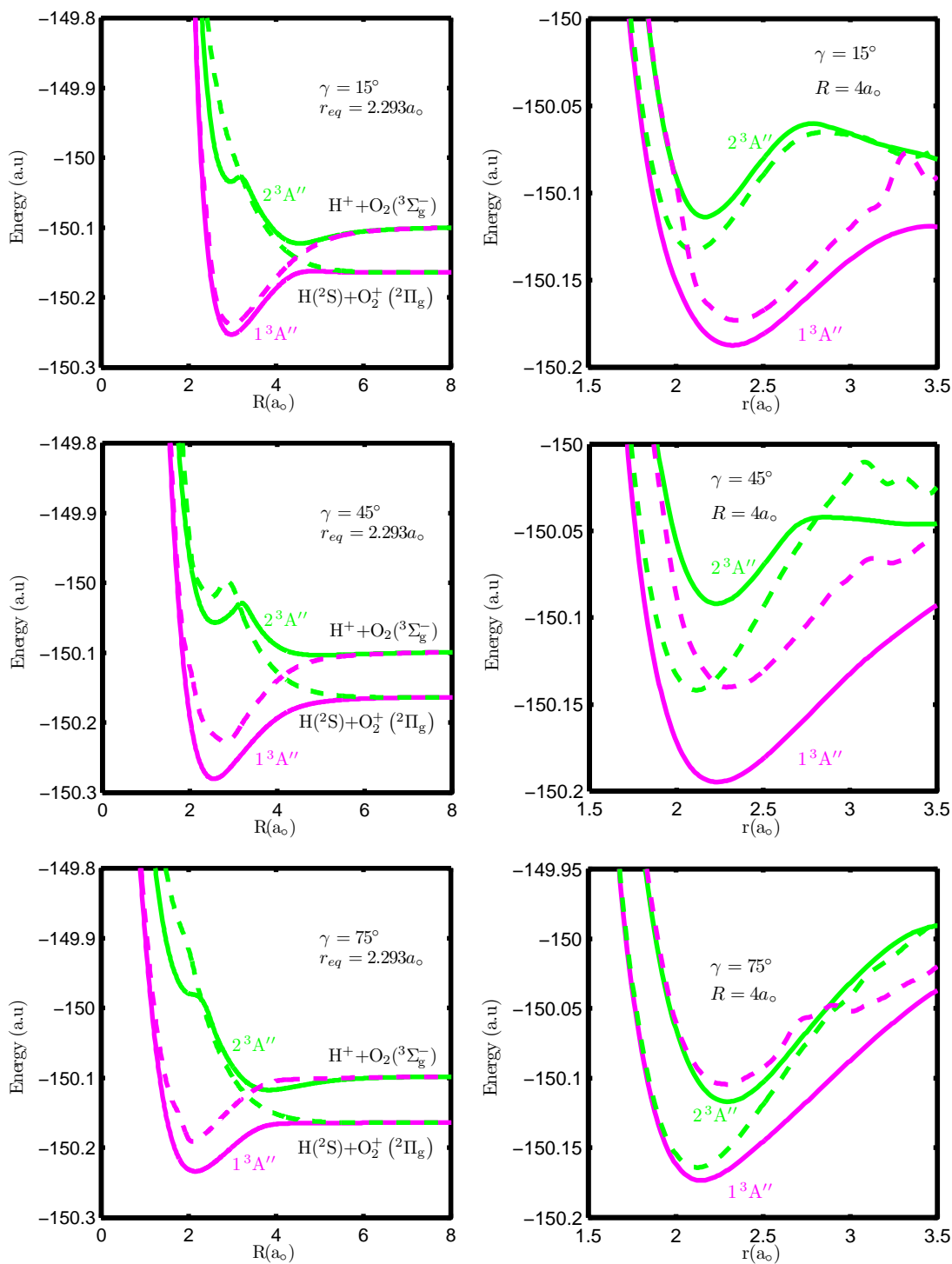


Figure 5.2: *Ab initio* adiabatic (solid) and diabatic (dashed) PECs of the GS and the first ES for $\gamma = 15^\circ, 45^\circ, 75^\circ$ as a function of R for a fixed $r = r_{eq} = 2.293a_0$ (left panel) and as a function of r for a fixed $R = 4.0a_0$ (right panel). Note the presence of avoided crossings in the adiabatic curves and crossings in the quasi-diabatic curves in both the right and the left panels and the asymptotic relationships at large R . A small shallow well is present in the upper adiabatic curves and is slightly seen for $\gamma = 75^\circ$.

Table 5.4: The calculated energy difference ΔE between the first H/O₂⁺ channel and the H⁺/O₂ channel at r_{eq} and at $R = 15a_o$ for various γ values.

γ	ΔE (eV)
0°	1.701
15°	1.788
30°	1.789
45°	1.790
60°	1.792
75°	1.793
90°	1.721

Table 5.5: The computed well depth (eV) present in first ES PEC at $r_{eq} = 2.293a_o$ at different γ for off-collinear geometries. The earlier reported computed values is about roughly 1 eV (Staemmler and Gianturco, 1985). R (bohr) is the location at which shallow well exists.

γ	R	Well depth
0°	6.8	0.01
15°	4.6	0.67
30°	4.8	0.27
45°	5.0	0.15
60°	4.6	0.20
75°	3.8	0.54
90°	5.8	0.02

the first VCT channel and the entrance channel at r_{eq} and at $R = 15a_o$ is given in Table 5.4 as a function of γ . This angular dependent energy differences at $R = 15a_o$ will become angular independent quantity at $R = \infty$ (exoergicity or endoergicity) and this turns out to be 2.02 eV as stated above. It is worth pointing out here that there exists a shallow well in the first ES adiabatic PEC that may support the charge transfer complex [O₂⁺ ... H]. The well depth and its location on the first ES PECs is summarized in the Table 5.5. The depth is the highest at 15°, followed by 75° and lowest at 0°.

5.3 *Ab initio* PESs

Now, we present the adiabatic and quasi-diabatic PESs for the two electronic states as a function of R, r, γ and analyse their characteristics.

The computation of PESs at extended or shortened r was a herculean task because of the convergence problems both at the MCSCF and the MRCI levels. They arose due to the involvement of further low lying excited states. These difficulties can be sorted out

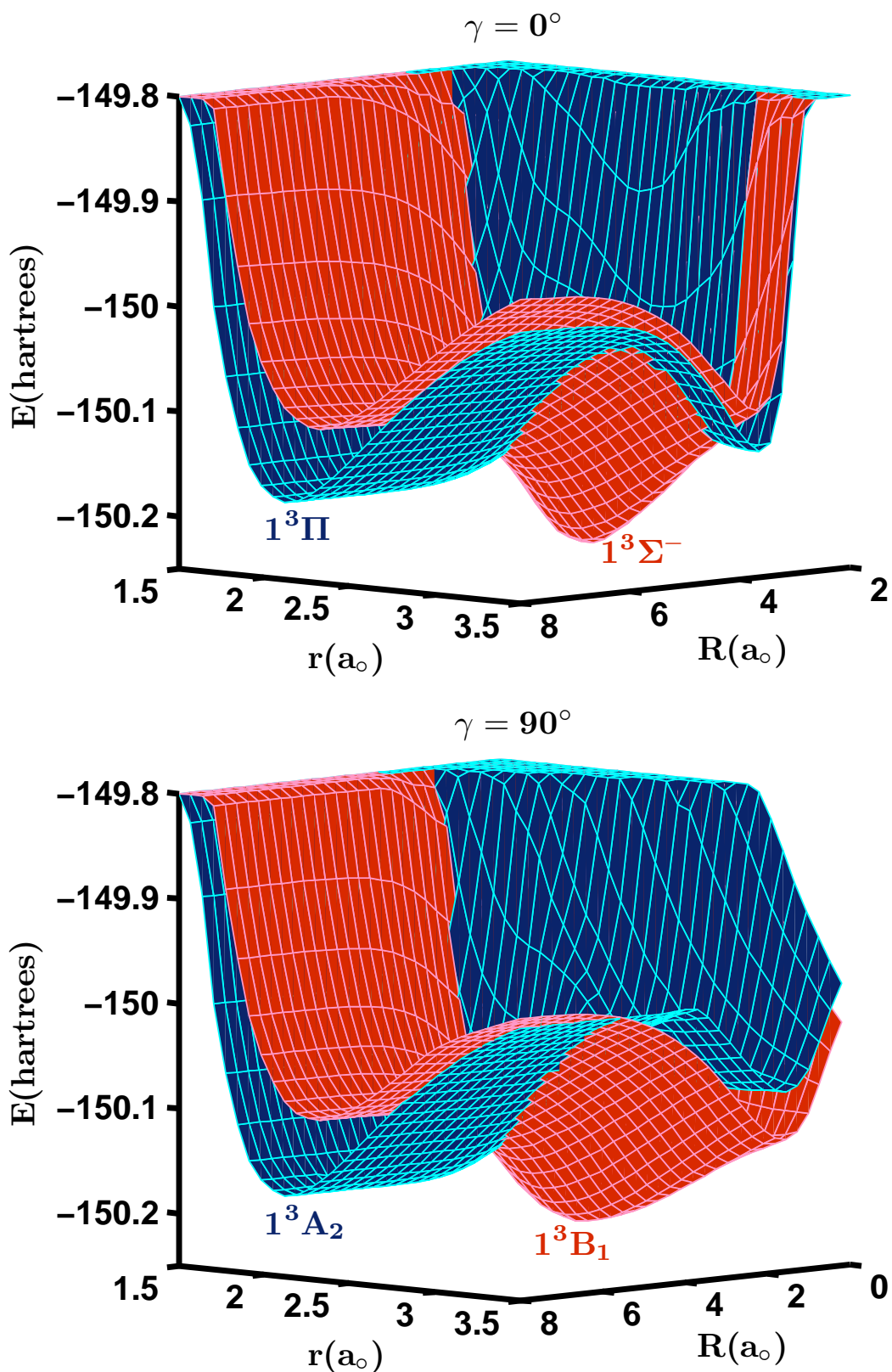


Figure 5.3: *Ab initio* smoothed adiabatic PESs of the GS ($1^3\Sigma^-/1^3B_1$) and the first ES ($1^3\Pi/1^3A_2$) for $\gamma = 0^\circ$ and 90° orientations as a function of R and r . Note the presence of crossings between the two electronic surfaces of different symmetries.

by using **p**-space, restrict, maxiti cards judiciously both in the reference geometry as well as in the displaced geometries. On an average, 870 *ab initio* points have been computed involving the lowest four electronic states. Table 5.6 lists the total number of *ab initio* data points calculated on the grid of R , r for a fixed γ . The grid details of PESs had already

Table 5.6: The number of *ab initio* points per electronic state for all γ values and the grand total computed using *cc-pVTZ* basis set and MRCI level of accuracy for the $\text{H} + \text{O}_2$ system.

γ	Points/surface
0°	748
15°	836
30°	836
45°	880
60°	946
75°	946
90°	946
Total	6138

been given in the **section 5.2**, yet we briefly mention those details here for the sake of convenience. The gridding along R coordinate depends upon the γ , and for example, for $\gamma = 90^\circ$, $R = 0.2 - 7.0(0.2), 8 - 15(1.0)$ and for a particular γ , $r = 1.5 - 3.5(0.1)$ and $\gamma = 0^\circ - 90^\circ(15^\circ)$. The numbers in the parenthesis denote the increments in bohr in the stated interval and γ is measured in degrees and R and r are measured in bohr.

We show the adiabatic GS and the first ES PESs for $\gamma = 0^\circ$ (collinear geometry) and $\gamma = 90^\circ$ (perpendicular geometry) in Fig. 5.3. Since there exists no radial coupling between the GS ($1^3\Sigma^-/1^3B_1$) and the first ES ($1^3\Pi/1^3A_2$) there is no quasidiabatization, and therefore no quasidiabatic PESs are shown here. There exists direct surface crossing in both the orientations. The asymptotic correlations along R coordinate for the GS and the first ES are $\text{H}^+ + \text{O}_2(^3\Sigma_g^-)$ (IVE channel) and $\text{H}(^2S) + \text{O}_2(^3\Pi_g)$ (VCT channel), respectively.

Now, we present the adiabatic PESs for the GS and the first ES for $\gamma = 15^\circ, 45^\circ, 75^\circ$

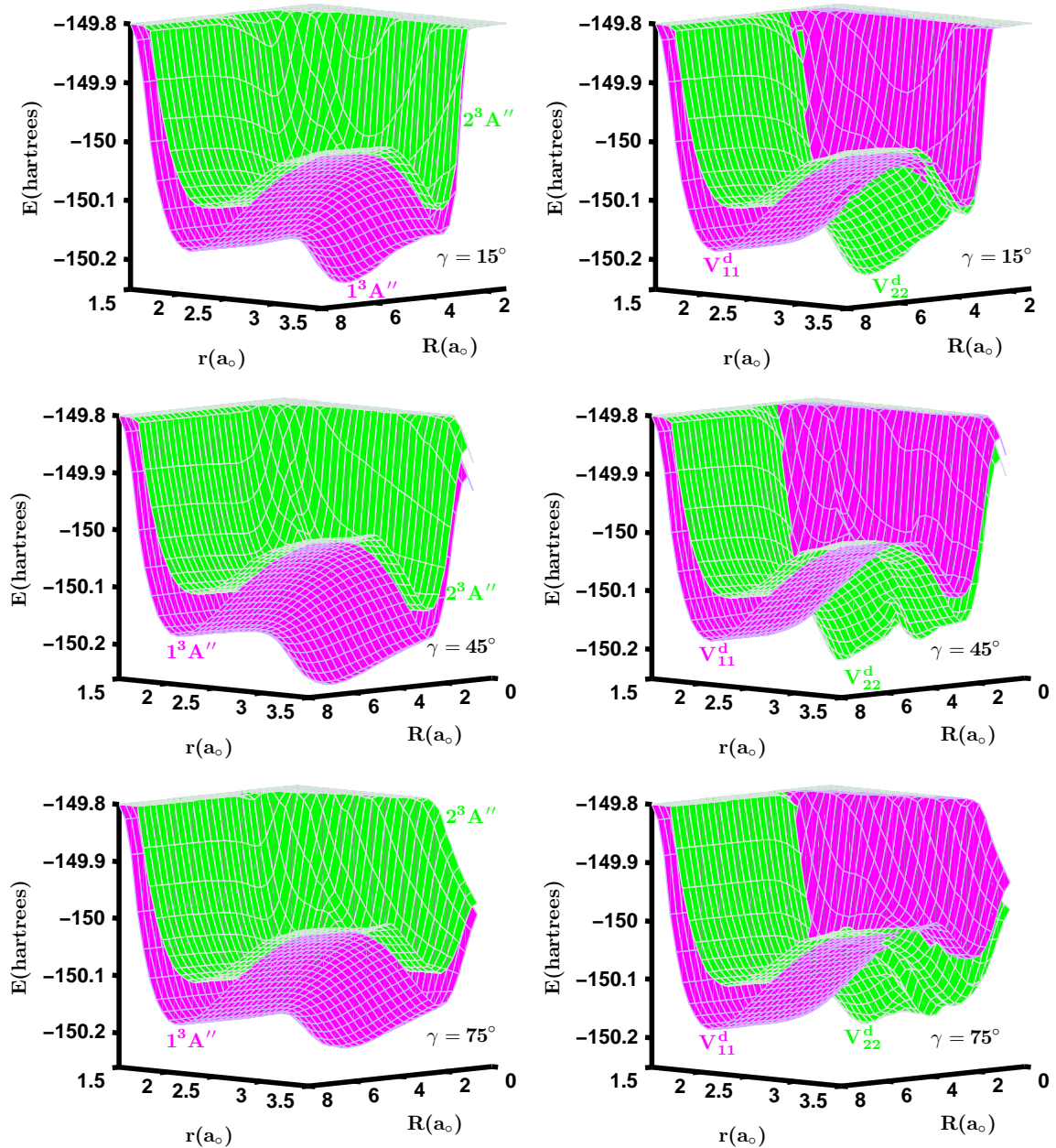


Figure 5.4: *Ab initio* adiabatic (left panel) and the corresponding quasi-diabatic (right panel) as a function of R and r for $\gamma = 15^\circ, \gamma = 45^\circ$ and $\gamma = 75^\circ$. Note that there exists avoided crossings in the adiabatic PESs (left panel) which are replaced by direct surface crossings in the diabatic PESs (right panel).

in Fig. 5.4 (left panel) along with the corresponding quasi-diabatic PESs in Fig. 5.4 (right panel). Since these orientations belong to the C_s point group, the spectroscopic term symbols for the adiabatic GS PES and first ES PES are $1^3A''$ and $2^3A''$, respectively. For each γ , we denote the corresponding quasi-diabatic PESs by V_{11}^d and V_{22}^d (where d stands for dia-

batic). There is a direct surface crossing giving rise to ambiguity in determining the GS PES and first ES PES. The suffix 11 and 22 denote the index in the diabatic matrix. The asymptotic correlations along R coordinate for the GS PES and first ES PES are $\text{H}^+ + \text{O}_2(^3\Sigma_g^-)$ (IVE channel) and $\text{H}(^2\text{S}) + \text{O}_2(^2\Pi_g)$ (VCT channel). The electron capture channel (VCT) is highly exoergic with respect to the entrance channel (IVE).

Fig. 5.5 shows the adiabatic GS and the first ES PES as a function of R and γ but for $r = r_{eq}$. There is a minimum in the GS PES around $\gamma = 45^\circ$. The first ES PES are mostly repulsive exhibiting a shallow well at far extended r and it is responsible for promoting the charge transfer process over inelastic process. After $R = 8a_o$, both surfaces remain flat and the asymptotic correlations also remain the same. The energy gap at the asymptotic region remain fairly constant as a function of γ at $r = r_{eq} = 2.293a_o$.

So far we have discussed adiabatic and quasi-diabatic PESs as function of R , r and γ and analysed their various characteristics. Now we analyse the locations of local minimum of energy in the GS PES as a function of γ . The details are summarized in Table 5.7 along with the well depths at each location relative to asymptotically separated products. Table 5.7 shows that the local minimum in the collinear approach of H^+ occurs when bond length of O_2 is at equilibrium distance and when the approach moves from the collinear to off-collinear and finally to perpendicular, the local minimum occurs at stretched bond distance and shorter R . From the Table 5.7, it is clear that the global minimum in the GS PES as a function of R , r and γ would be located around $\gamma = 45^\circ$. In other words, we fitted the adiabatic GS energy tabular data corresponding to the minimum as a function of γ and from the cubic splined curve obtained the value of γ for which the global minimum was predicted. In other words, the minimum energy path was fitted as a function of γ and the

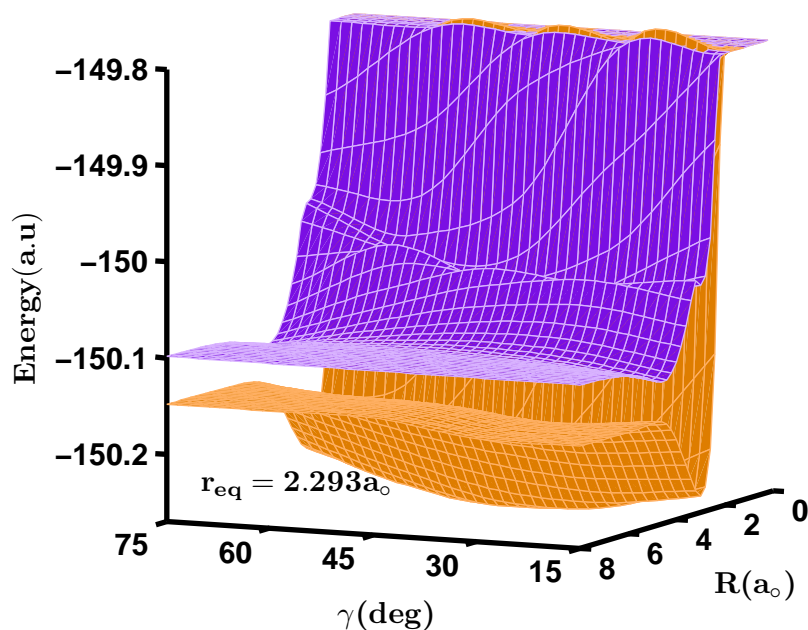


Figure 5.5: *Ab initio* adiabatic GS and the first ES PESs as a function of γ and R at $r = r_{eq} = 2.293a_0$.

result is shown in Fig. 5.6. Note that the potential is symmetric about $\gamma = 90^\circ$ and the data points for $90^\circ \leq \gamma \leq 180^\circ$ are obtained by symmetry in Fig. 5.6. From the fitting we obtained the equilibrium geometric configurations of $[\text{HO}_2]^+$ molecule in the GS PES and the results are summarized in Table 5.8 along with earlier theoretical results. We get the following equilibrium geometries : $r = 2.4a_0$, $R = 2.6a_0$ and $\gamma = 42.7^\circ$. We would like to highlight three sets of earlier *ab initio* calculations which were focussed purely on the equilibrium geometry of the $[\text{HO}_2]^+$. These calculations reported the equilibrium structure data in the valence coordinate. Therefore, we also converted our data in the Jacobi coordinates to the valence coordinates. Raine and Schaefer III (1984) carried out systematic study with extended basis set calculations and we have listed their data obtained with their "Ext III" calculations. Further high level *ab initio* calculations were carried out by Robbe *et al.* (2000) to describe the potential well using quartic force field. They also computed various spectroscopic constants along with the equilibrium structure parameters. It is also worth pointing

out here that ultra refined *ab initio* calculations around the equilibrium geometry have been reported recently by Huang and Lee (2008) predicting fundamental vibrational frequencies and spectroscopic constants. This set of data obtained using "TQ5+rel+ACPF/QZ" calculations is also listed in the Table 5.8. It is gratifying to note that the equilibrium geometry parameters obtained in the present study are in very good agreement with the high level calculations. This lends credence to our *ab initio* computations and to the quality of *ab initio* PESs. Robbe *et al.* (2000) had found a barrier for the proton migration for isomerization ($[\text{O}\cdots\text{O}\cdots\text{H}]^+ \longleftrightarrow [\text{H}\cdots\text{O}\cdots\text{O}]^+$) in a T-shaped structure. This is also seen in the

Table 5.7: The local energy minima of the adiabatic GS PES and the well depth at each local minima relative to the asymptotic products is listed out as a function of Jacobi coordinates (R, r, γ).

γ	r	R	Adiabatic GS Energy (a.u)	Well depth ^a (eV)
0°	2.293	3.0	-150.241483	3.783106977
15°	2.293	3.0	-150.253092	4.098987867
30°	2.3	2.8	-150.273583	4.656547977
45°	2.4	2.6	-150.280342	4.840460367
60°	2.4	2.4	-150.266552	4.465234467
75°	2.4	2.2	-150.237020	3.661668747
90°	2.4	2.0	-150.218255	3.151073097

^arelative to asymptotic energy limit, $E = -150.1024493$ a.u, corresponding to $\text{H}^+ + \text{O}_2(X^3\Sigma_g^-, r = r_{eq})$ products.

Table 5.8: Computed equilibrium geometry parameters in the valence coordinates of the $[\text{HO}_2]^+$ ion in the GS ($1^3A''$).

Theory	$r(\text{O} - \text{O})/(\text{\AA})$	$r(\text{O} - \text{H})/(\text{\AA})$	$\alpha(\text{O} - \text{O} - \text{H})/(\text{deg})$
This work	1.269	1.009	113.24
Earlier work ^a	1.22	0.995	111.54
Earlier work ^b	1.215	0.985	111.0
Earlier work ^c	1.237	1.007	118.8
Earlier work ^d	1.237	1.024	112.695
Earlier work ^e	1.24	1.005	111.39

^avan Lenthe and Ruttink (1978)

^bRaine and Schaefer III (1984)

^cRobbe, Monnerville, Chambaud, Rosmus, and Knowles (2000)

^dHuang and Lee (2008)

^eSaieswari and Kumar (2008a)

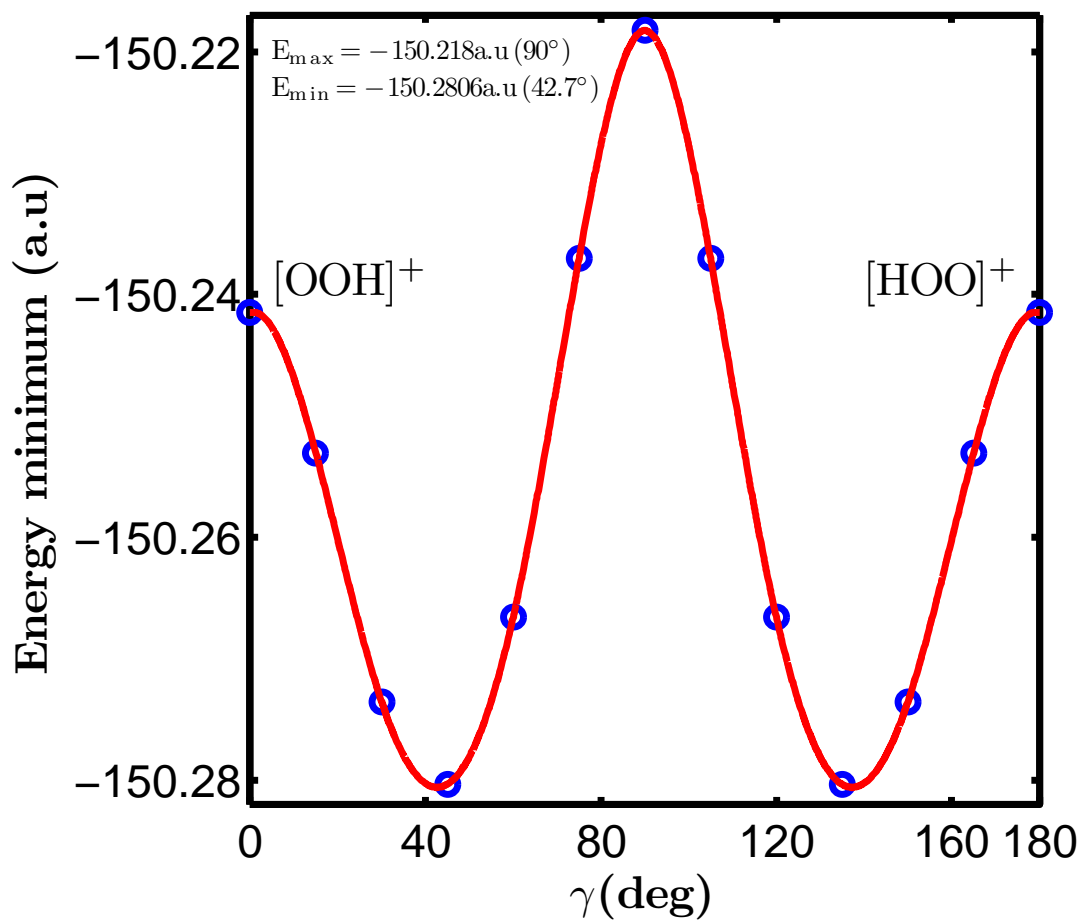


Figure 5.6: The splined minimum energy pathway of adiabatic GS showing minimum and maximum peaks during the interconversion process, $\text{HOO}^+ \rightleftharpoons \text{OOH}^+$

present calculations in Fig. 5.6. Since we are primarily interested in the dynamics we do not analyse these details any further.

5.4 Coupling PESs and NACME

We now analyse NACMEs and the 2×2 coupling potential which has been just taken out from the 4×4 coupled potential matrix. We show the coupling potential (left panel) and the corresponding NACMEs (right panel) as a function of nuclear coordinates, R and r , for $\gamma = 15^\circ$, $\gamma = 45^\circ$ and $\gamma = 75^\circ$ in Fig. 5.7. The NACME values were obtained in the same

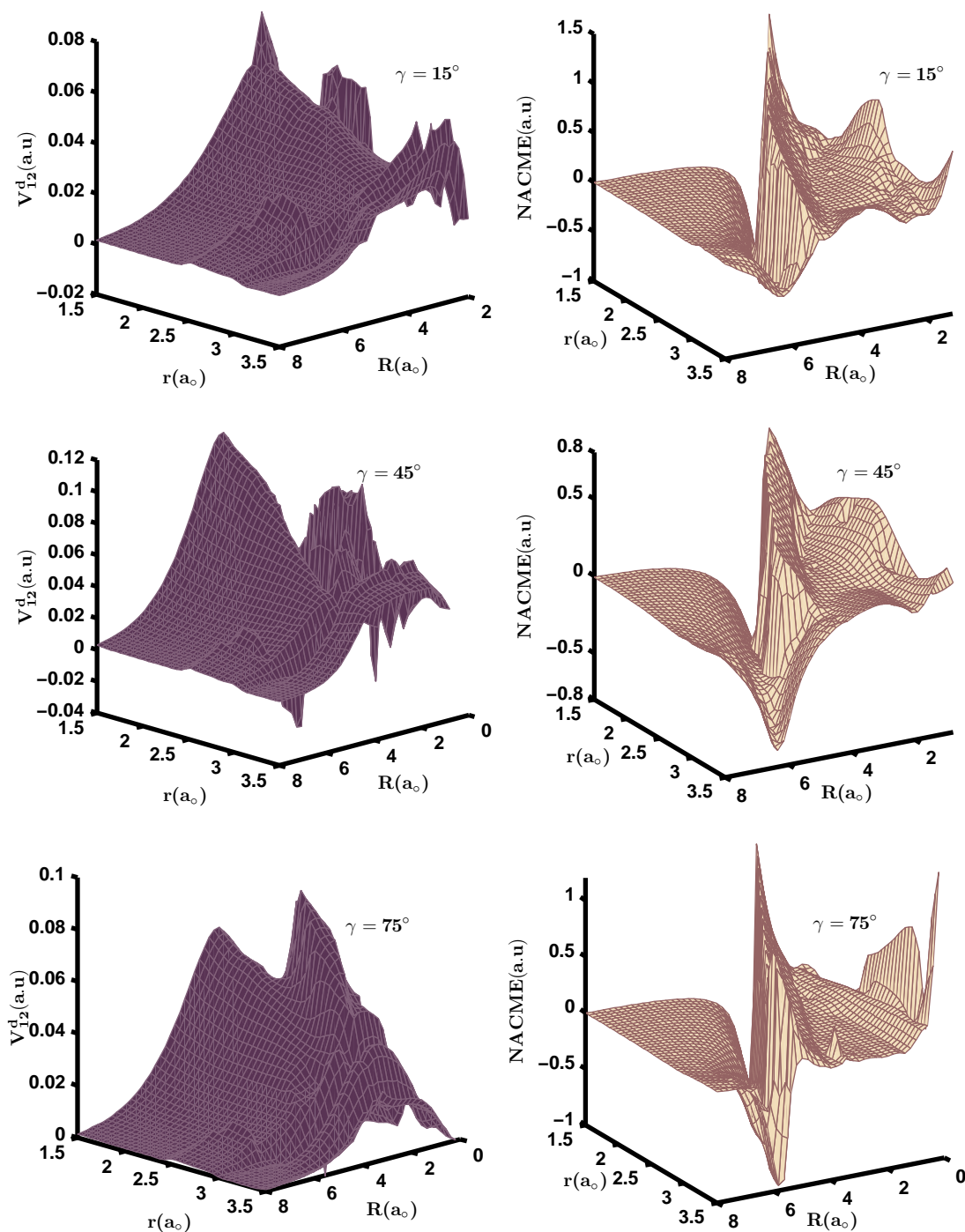


Figure 5.7: Coupling PESs (right panel) and NACME (left panel) as a function of R and r for a fixed γ . Since there is no radial couplings for the collinear and perpendicular geometries, coupling potential and NACME are not applicable to these orientations.

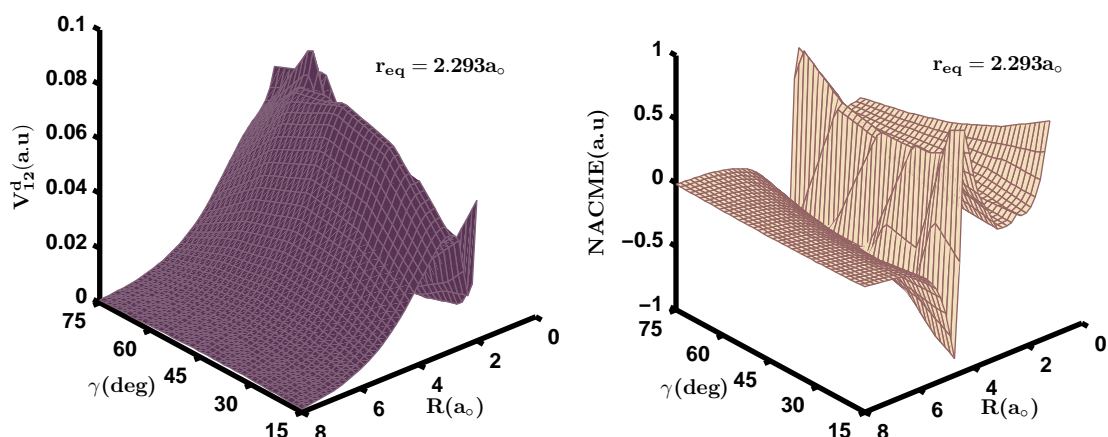


Figure 5.8: Coupling potential and NACME as a function of γ and R at $r = r_{eq} = 2.293a_0$. The γ range begins with 15° and ends with 75° because there is no radial couplings for 0° and 90° .

manner as described earlier in **section 4.4** of **chapter 4**. The coupling potential, $V_{12}^d = V_{21}^d$ shows a lot of irregularity in the smaller R regions because of the involvement of second and third excited states in the four-state computations. One can see that for $\gamma = 15^\circ$ and 45° there is higher degree of irregularity for small R values as a function of γ , as with respect to what is seen for $\gamma = 75^\circ$. This suggests that the nonadiabaticity is larger for small γ values or when the proton approaches towards the collinear geometries. One common feature found in all three cases is that coupling potential surfaces are smooth and reach almost zero for $R > 6a_0$ where the adiabatic and quasi-diabatic PESs merge together. This behaviour is also reflected in the NACME values (right panel) for all angles. Fig. 5.8 shows another view of the coupling potential (left) and the NACME (right) as a function of γ and R but at $r = r_{eq} = 2.293a_0$. The NACME values (right panel) in Fig. 5.7 as a function of R and r and in Fig. 5.8 as a function of γ and R at $r = r_{eq} = 2.293a_0$ show sharp changes at some R and r values across the (R, r) and the (γ, R) plane. The values range from -1 a.u to -1.5 a.u in all the three cases. There are sharp variations at places where the NACME change

from negative to positive values or vice versa. Such places are avoided crossings between the GS and the first ES. Other variations particularly for further small R values indicate the nonadiabatic interactions arising from the third and the fourth ES.

5.5 Asymptotic interaction potential

The long range interaction potential V_{as} for the $H^+ + O_2$ system is modelled and obtained in terms of multipolar expansion terms which are given below

$$V_{as}(R, r; \gamma) \sim \frac{Q(r)}{R^3} P_2(\cos \gamma) - \frac{\alpha_0(r)}{2R^4} - \frac{\alpha_2(r)}{2R^4} P_2(\cos \gamma) \quad (5.1)$$

where V_{as} is the asymptotic long range potential, $Q(r)$ is the quadrupole moment, $\alpha_0(r)$ and $\alpha_2(r)$ are the dipole polarizability components and the P_i 's are Legendre polynomials. In order to model the long range asymptotic interactions for quantum dynamics calculations we have computed the $Q(r)$, $\alpha_0(r)$ and $\alpha_2(r)$ as a function of internuclear distance (r) of $O_2(X^3\Sigma_g^-)$ and fitted them with the following functional form in Eq. (5.2)

$$x(r) = \sum_{i=0}^N C_x(i) \left(\frac{1}{r}\right)^i \quad (5.2)$$

where x stands for $Q(r)$ or $\alpha_0(r)$ or $\alpha_2(r)$. C_x are the coefficients used in the fitting and are listed out in the Table 5.9. These coefficients are used to generate asymptotic PESs correlating to the IVE channel, $H^+ + O_2(X^3\Sigma_g^-)$. For the VCT channels, $H(^2S) + O_2^+(X^2\Pi_g)$, $H(^2S) + O_2^+(X^4\Pi_u)$ and $H(^2S) + O_2^+(X^4\Sigma_g^-)$ the polarizability components of the H-atom ($\alpha_0 = 2.7372922$ a.u) are used to generate the asymptotic potentials. These computed asymptotic potentials have been connected smoothly to the respective interaction potentials

Table 5.9: Values of coefficients (in a.u) used in Eq. (5.2) for the generation of Q, α_0 and α_2 as a function of r of O_2 .

$C(i)$	Q	α_0	α_2
$C(0)$	0.95×10^2	0.71×10^2	0.63×10^2
$C(1)$	-0.20×10^4	-0.37×10^3	-0.48×10^3
$C(2)$	0.18×10^5	0.80×10^3	0.12×10^4
$C(3)$	-0.88×10^5	-0.95×10^3	-0.16×10^4
$C(4)$	0.26×10^6	0.70×10^3	0.12×10^4
$C(5)$	-0.47×10^6	-0.33×10^3	-0.60×10^3
$C(6)$	0.53×10^6	1.00×10^2	0.18×10^3
$C(7)$	-0.33×10^6	-0.19×10^2	-0.35×10^2
$C(8)$	0.88×10^5	1.00×10^1	0.38×10^1
$C(9)$		-0.91×10^{-1}	-0.18

in order to obtaine the global PESs for all γ . The coupling PESs become zero for all r for $R > 15a_0$.

5.6 Vibrational coupling matrix elements $(V_{vv'/v''}(R; \gamma))$

The definition of VCMEs is given in **chapter 4**. The angle dependent VCMEs for the IVE channel, $H^+ + O_2(v = 0) \longrightarrow H^+ + O_2(v')$ and the VCT channel, $H^+ + O_2(v = 0) \longrightarrow H(^2S) + O_2^+(v'')$ were computed as a function of R for all γ values. In order to get numerically converged results for the vibrational excitations upto $v'(v'') = 10$ of $O_2(X^3\Sigma_g^-)/O_2^+(X^2\Pi_g)$, 20 vibrational wavefunctions were included for both the diatoms. The *ab initio* PESs points were spline interpolated over a fine meshgrid in the two dimensional plane of (R, r) for a fixed γ . Essentially, the strength of the VCMEs indicate the extent of coupling of vibrational states within an electronic state or vibrational states of different electronic states with the incoming translational mode of the projectile $H^+(H)$.

The computed VCMEs are shown in Fig. 5.9 for both the channels as function of R for

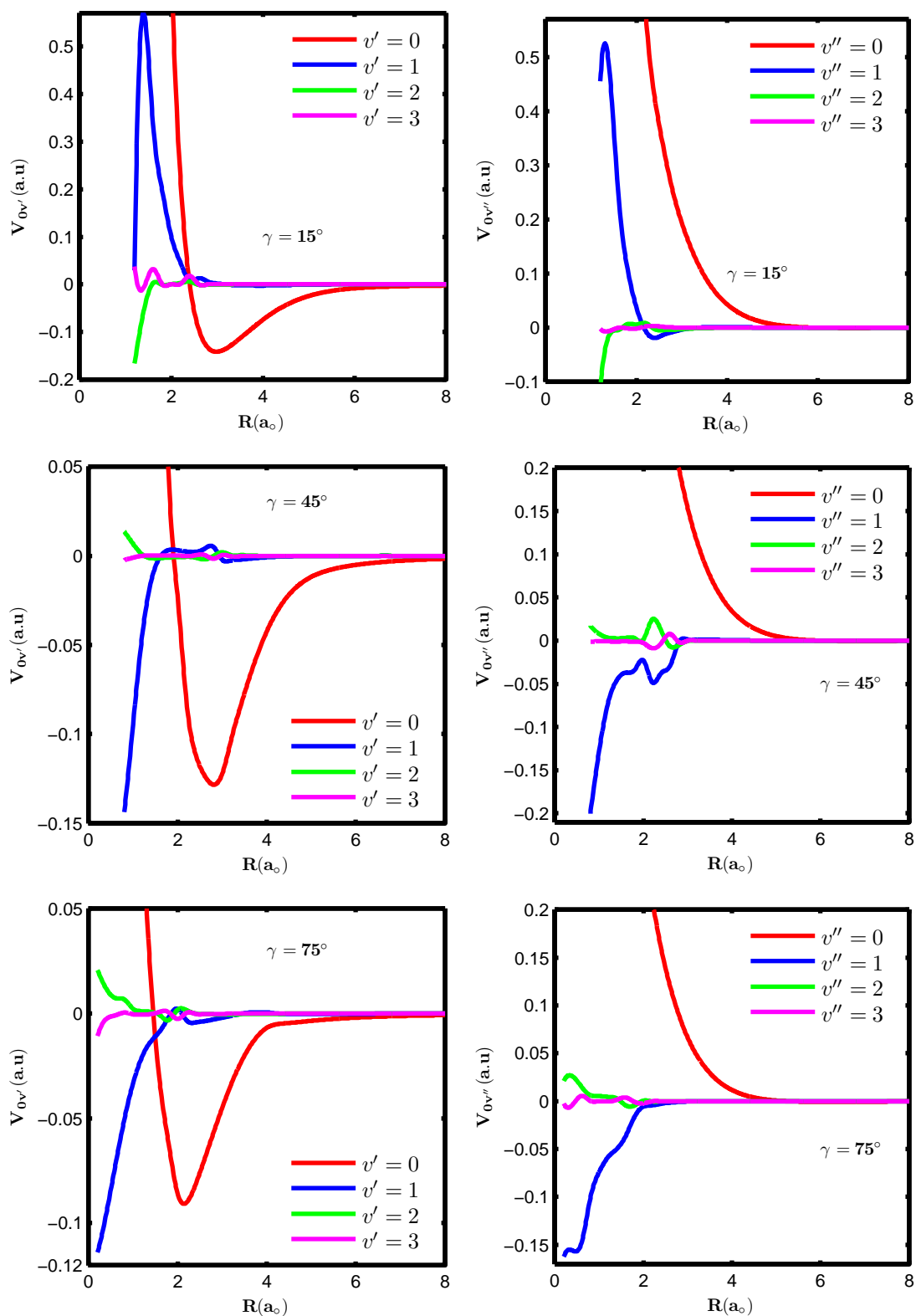


Figure 5.9: Vibrational coupling matrix elements (VCME) as a function of R for $\gamma = 15^\circ, \gamma = 45^\circ$ and $\gamma = 75^\circ$ for the IVE ($V_{0v'}$) channel $\text{H}^+ + \text{O}_2(v = 0) \rightarrow \text{H}^+ + \text{O}_2(v')$ (left panel) and the VCT ($V_{0v''}$) channel $\text{H}^+ + \text{O}_2(v = 0) \rightarrow \text{H}^{(2)}\text{S} + \text{O}_2^+(v'')$ (right panel).

different γ . Before we make comparison with the experimental results it would be desirable to analyse some of the computed VCMEs which have strong bearing on both the processes. Since the experiments were performed with O_2 in its ground vibrational state we show the $V_{vv'(v'')}$ with $v = 0$ where v' and v'' refer to the vibrational states of O_2 and $O_2^+(X^2\Pi_g)$. For the IVE channel (left panel) the coupling for the vibrationally elastic channel, V_{00} , that is, for $O_2(v = 0) \rightarrow O_2(v' = 0)$, is the largest and shows a deep attractive well before becoming repulsive at smaller R values. All other excitations remain mostly much smaller comparatively and they show their strengths again for small R following the order : $V_{00} > V_{01} > V_{02} > V_{03} \dots$. The existence of attractive well makes the H^+ to approach much smaller R values thereby making the IVE process quite effective following the said order above. On the contrary V_{00} in the VCT channel shows purely a repulsive behaviour. In this channel also the $V_{0v''}$ follows the order : $V_{00} > V_{01} > V_{02} > V_{03} \dots$ suggesting the same order for VCT. In fact, this qualitative ordering is seen in the experiments at $E_{cm} = 23$ eV (Niedner-Schatteburg and Toennies, 1992).

The VCMEs for the mixed channels, for the VCT, $H^+ + O_2(v') \rightarrow H(^2S) + O_2^+(v'')$ are shown in Fig. 5.10 for the three molecular orientations as a function of R . It is evident from the magnitudes of $V_{v'v''}$ that they follow the order : $V_{00} > V_{01} > V_{02} > V_{13} > V_{03} > V_{12} > V_{23}$ for all three orientations. Interestingly, the coupling with first excited state of O_2 and third excited state of O_2^+ is stronger than that with first excited state of O_2 and second excited state of O_2^+ . The magnitude of $V_{v'v''}$ for $\gamma = 45^\circ$ is little higher than the other two orientations.

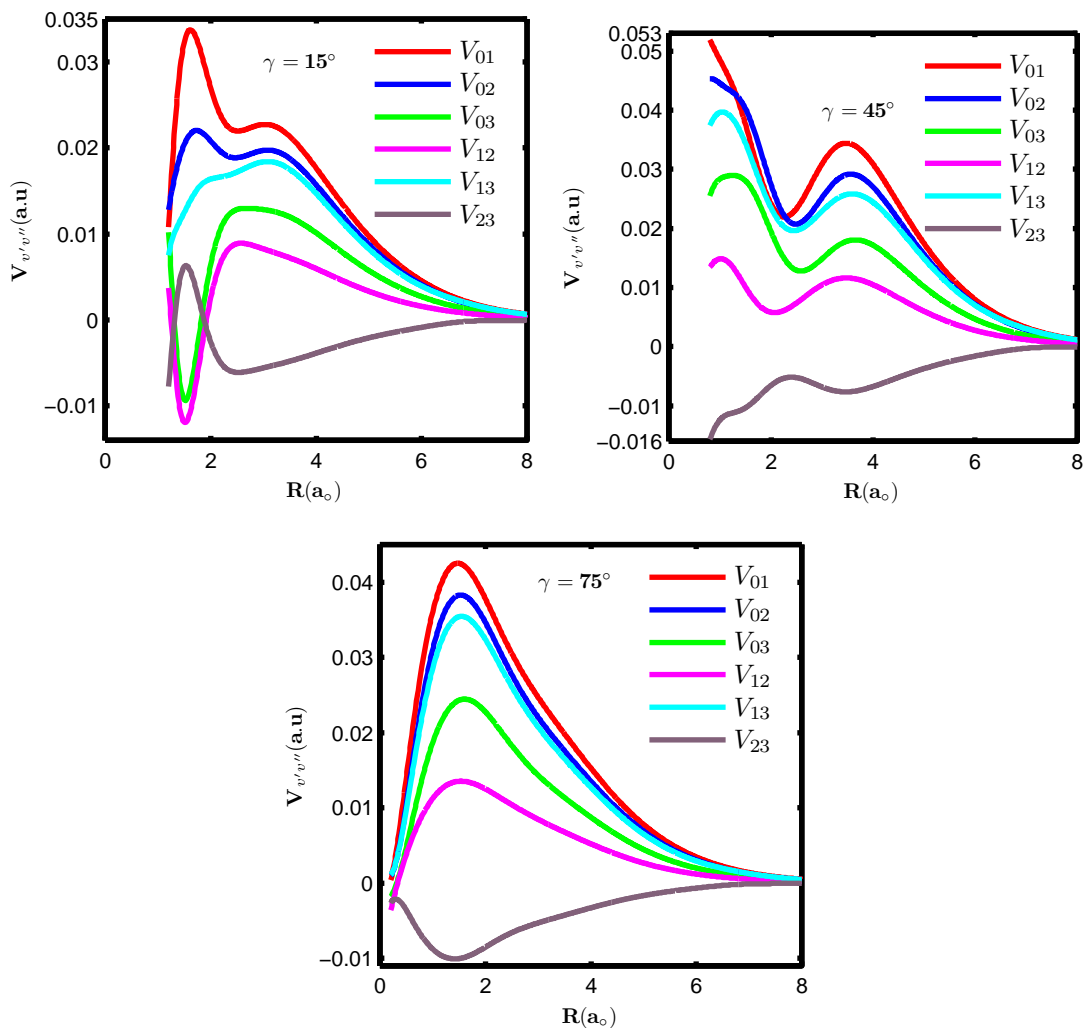


Figure 5.10: The vibrational coupling matrix elements ($V_{v'v''}$) for the VCT as a function of R for $\gamma = 15^\circ, 45^\circ$ and 75° orientations for the mixed channels, $\text{H}^+ + \text{O}_2(v') \longrightarrow \text{H}(^2\text{S}) + \text{O}_2^+(v'')$.

5.7 Quantum Dynamics

The quantum dynamics was performed within the VCC-RIOSAs framework, which appears to be quite valid for collision energies in the range $E_{cm} = 9.5 - 23$ eV. The details of the VCC-RIOSAs framework are given in **chapter 3** and **chapter 4**. Here we briefly provide the computation details of the dynamics. In order to have converged cross sections in the range of experimental collision energies $E_{cm} = 9.5 - 23$ eV, 20 vibrational levels of $\text{O}_2(X^3\Sigma_g^-)$ and 20 vibrational levels of $\text{O}_2^+(X^2\Pi_g)$ were included in the vibrational close-coupling (VCC)

equations. They were solved by the sixth-order Numerov method for 7 equally spaced orientations with γ values between 0° and 90° for each partial wave (l). The maximum partial waves l_{max} for the vibrationally elastic channel at $E_{cm} = 9.5$ eV and at $E_{cm} = 23$ eV was 600 and 900, respectively.

5.7.1 Dynamics at $E_{cm}=9.5$ eV

In this section, we compare the computed dynamical quantities with those of the experimental results (Gianturco, Gierz, and Toennies, 1981). The state-to-state experimental data are available only for the IVE process at the collision energy $E_{cm} = 9.5$ eV. We have computed the various dynamical properties at this energy using the 2×2 coupled-state potential matrix which have been taken out from the 4×4 coupled state potential matrix and compared them with those available from the experiments. There does not seem to be any quantum dynamical study at this collision energy using either the 2×2 or the 4×4 coupled electronic states.

5.7.1.1 The orientation opacities

The VCC-RIOSAs angle-dependent opacity function as defined in Eq. (3.34) in **chapter 3** is shown in Fig. 5.11 as a function of partial waves (l) (in the units of \hbar) for the IVE channel, $\text{H}^+ + \text{O}_2(v = 0) \longrightarrow \text{H}^+ + \text{O}_2(v')$ for $\gamma = 0^\circ$, $\gamma = 45^\circ$ and $\gamma = 90^\circ$ collisions (left panel) and the VCT channel (right panel), $\text{H}^+ + \text{O}_2(v = 0) \longrightarrow \text{H}(^2\text{S}) + \text{O}_2^+(v'')$. Note that for $\gamma = 0^\circ$ (collinear) and $\gamma = 90^\circ$ (perpendicular) (right panel) collisions. Since no radial coupling exists between two electronic states for $\gamma = 0^\circ$ and $\gamma = 90^\circ$, the GS and the first ES remain uncoupled. The IVE is totally governed by the dynamics on the GS

only. The angle (steric) dependent opacity function speaks about the amount of excitation of different vibrational states of O_2 and O_2^+ molecules during the collisions. The formula for opacity function, Eq. (3.34), involves the modulus square of the steric dependent T-matrix. From Fig. 5.11, it is easy to conclude that the amount of vibrational excitation differs greatly from the IVE channel to the VCT channel, with former being 1000 times higher than the latter, especially for $\gamma = 45^\circ$ and $\gamma = 75^\circ$ orientations. For the IVE channel, only elastic collisions ($v = 0 \rightarrow v' = 0$) remains the most dominant of all the collisions for all the three approaches. Considering the magnitudes of the opacity functions, the order of vibrational excitations for the IVE channel is as follows : $v = 0 \rightarrow v' = 0 > v = 0 \rightarrow v' = 1 > v = 0 \rightarrow v' = 2 > v = 0 \rightarrow v' = 3$. The amount of elastic excitation decreases from $\gamma = 0^\circ$ to $\gamma = 90^\circ$ with collinear approach of H^+ ion favouring the elastic excitation more than the off-collinear approaches. The opacity function is converged only when the contributing number of partial waves (l) reaches 500 while for the VCT channel this value is just around $l \approx 200$. Roughly, the order of vibrational excitations follow the order : $v = 0 \rightarrow v'' = 1 > v = 0 \rightarrow v'' = 2 > v = 0 \rightarrow v'' = 0 > v = 0 \rightarrow v'' = 3$. In Fig. 5.12, we show the comparison of opacity function of elastic transition in the IVE channel (left) and of first VCT process, $v = 0 \rightarrow v'' = 0$ (right) for all orientations. It is readily seen that the opacity for the elastic process decreases gradually from $\gamma = 0^\circ$ to $\gamma = 90^\circ$ and vanishes to zero at about 600 partial waves, whereas, the same for first VCT process $v = 0 \rightarrow v'' = 0$ is relatively very high for $\gamma = 15^\circ$ and less for other orientations and vanishes to zero at about 200 partial waves. The magnitudes of opacities are higher in the case of the IVE process than those of the VCT process.

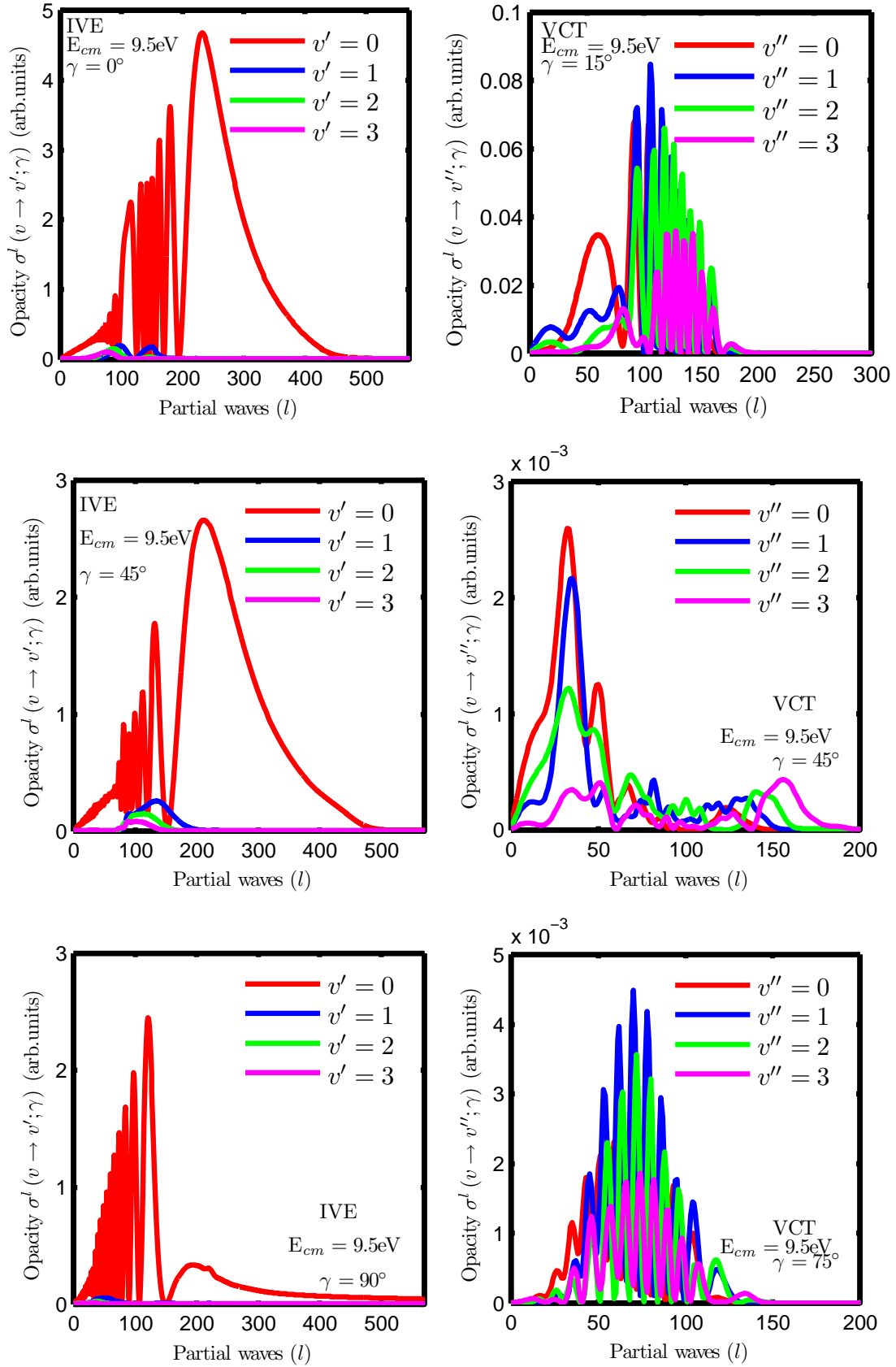


Figure 5.11: The opacity function as a function of partial waves (l , in the units of \hbar) for $\gamma = 0^\circ, \gamma = 45^\circ$ and $\gamma = 90^\circ$ for the IVE channel, $\text{H}^+ + \text{O}_2(v = 0) \longrightarrow \text{H}^+ + \text{O}_2(v')$ (left panel) and for $\gamma = 15^\circ, \gamma = 45^\circ$ and $\gamma = 75^\circ$ for the VCT channel $\text{H}^+ + \text{O}_2(v = 0) \longrightarrow \text{H}^{(2)\text{S}} + \text{O}_2^+(v'')$ (right panel).

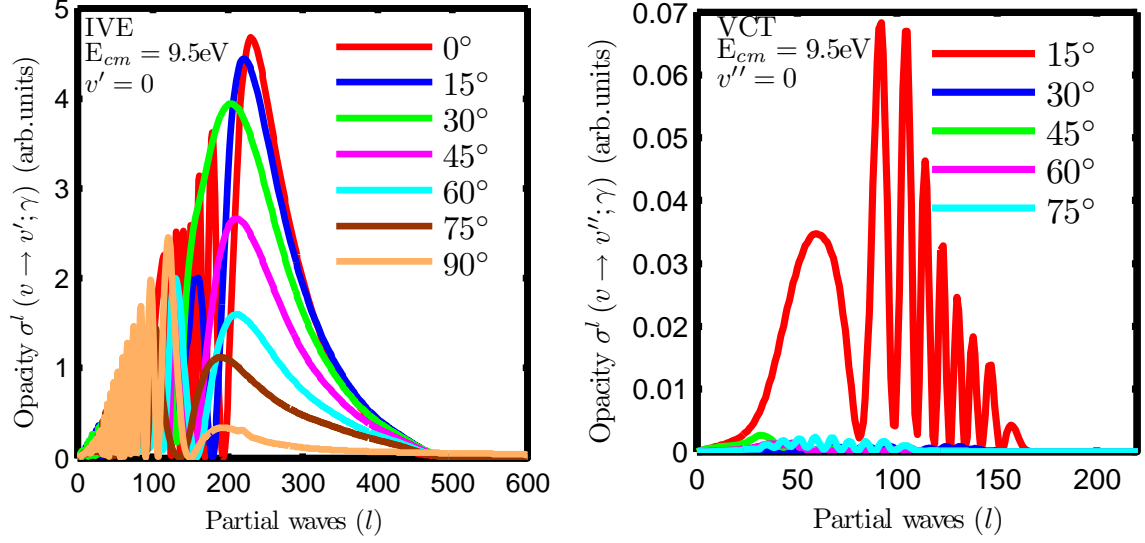


Figure 5.12: Opacity function for all γ values for the elastic collisions for IVE channel $\text{H}^+ + \text{O}_2(v = 0) \longrightarrow \text{H}^+ + \text{O}_2(v')$ (left) and for first charge transfer collisions for VCT channel $\text{H}^+ + \text{O}_2(v = 0) \longrightarrow \text{H}(^2\text{S}) + \text{O}_2^+(v'')$ (right).

5.7.1.2 Rotationally-summed state-selective differential cross section (DCS)

The rotationally-summed total differential cross section (TDCS) and rotationally-summed state-selective differential cross sections (DCS) have been computed and are shown in Fig. 5.13 as a function of scattering angle θ_{cm} at $E_{cm} = 9.5$ eV, for the IVE channel $\text{H}^+ + \text{O}_2(v = 0) \longrightarrow \text{H}^+ + \text{O}_2(v')$ (left) and the VCT channel $\text{H}^+ + \text{O}_2(v = 0) \longrightarrow \text{H}(^2\text{S}) + \text{O}_2^+(v'')$ (right). The computed TDCS and state-to-state DCSs showed a lot of oscillations as a function of θ_{cm} which arose mostly from the constructive and destructive interferences of contributing partial waves. Such undulatory structures could not be resolved in the experiments. Therefore, we smoothed our data for the sake of clarity by folding them with a Gaussian distribution $\frac{d\sigma}{d\omega}(\bar{\theta}) = \int_{\bar{\theta}-\Delta\theta}^{\bar{\theta}+\Delta\theta} \exp\left[-\frac{(\theta-\bar{\theta})^2}{2\sigma_\theta^2}\right] \frac{d\sigma^c}{d\omega}(\theta) d\theta$ with $\delta\theta = 1.0^\circ$, $\sigma_\theta = 0.33^\circ$ in the same way as it was achieved in the earlier theoretical calculations (Gianturco, Palma, Semprini, Stefani, and Baer, 1990) considering the experimental resolution. We report only such smoothed TDCS and state-selective DCS in Fig. 5.13 upto $v'(v'') = 5$ states for

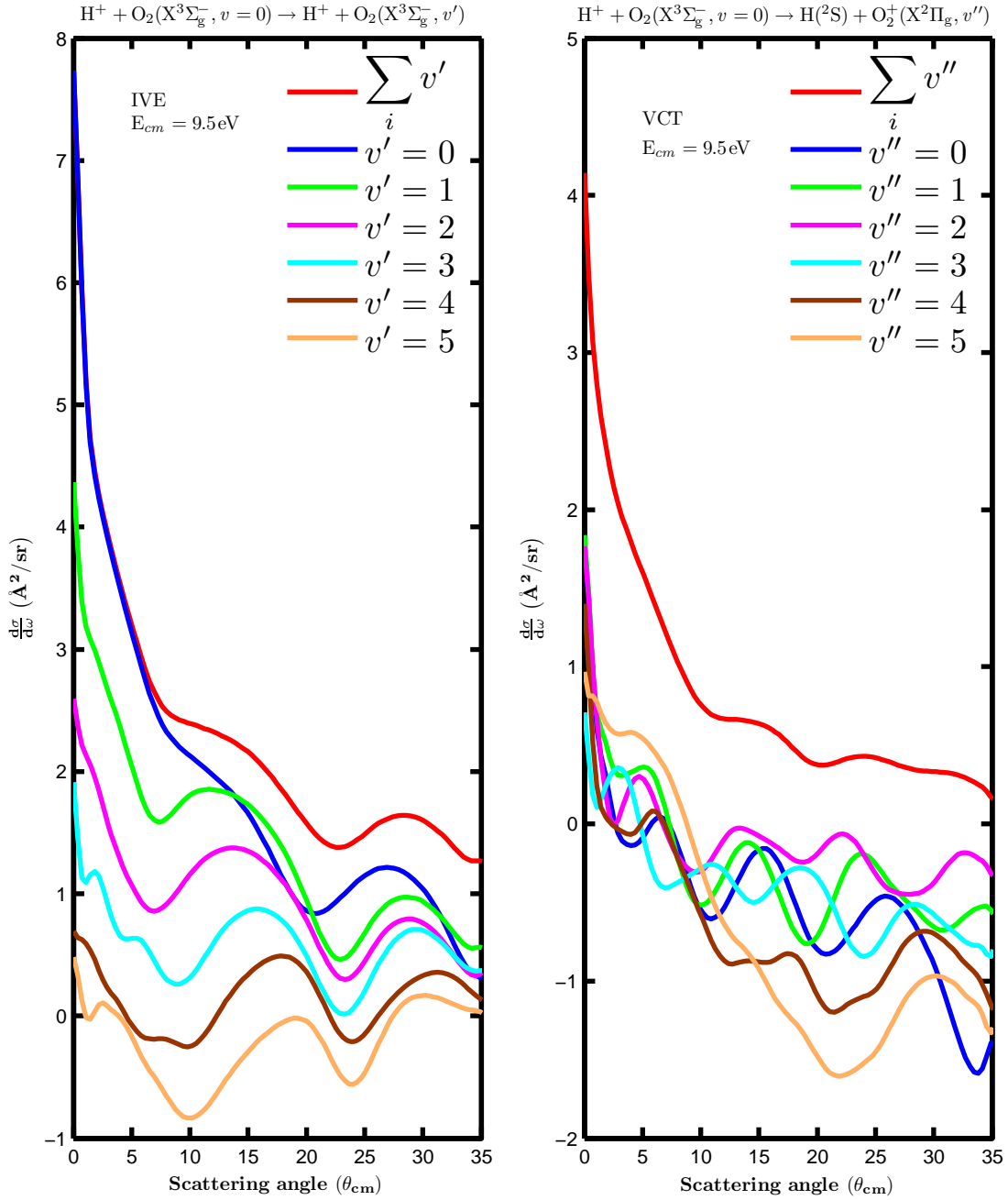


Figure 5.13: Rotationally-summed total differential cross section (TDCS) and rotationally-summed state-to-state DCS as function of θ_{cm} for the IVE channel $\text{H}^+ + \text{O}_2(v=0) \rightarrow \text{H}^+ + \text{O}_2(v')$ (left) and for the VCT channel $\text{H}^+ + \text{O}_2(v=0) \rightarrow \text{H}(^2\text{S}) + \text{O}_2^+(v'')$ (right) at $E_{cm} = 9.5$ eV. The number in the ordinate indicate the powers of 10. There are no experimental data available to compare with theoretical results at this collision energy.

$\theta_{cm} = 0^\circ - 35^\circ$. Unfortunately, there are no experimental data available for the TDCS and for the state-to-state DCSs to be compared with the theoretical results at this collision energy. The TDCS computed by summing up the state-to-state DCS upto 20 vibrational

states of O_2 for the IVE and 20 vibrational states of O_2^+ for the VCT from $v = 0$ of O_2 have been shown (red). In the IVE channel, the TDCS and DCS for $v' = 0$ state (blue) runs almost parallel to each other upto $\theta_{cm} \approx 7^\circ$ while in the VCT case, the former is largely separated from the later throughout the entire range of θ_{cm} . A primary rainbow maximum appears at $\theta_{cm} \approx 12^\circ$ in the IVE channel while the same appears at $\theta_{cm} \approx 14.5^\circ$ in the VCT channel. There are also rainbow structures in both the IVE and the VCT channels at far end of scattering angle region. In the IVE channel, all the DCS curves show monotonic decrease with scattering angle which is rather steep in the region upto $\theta_{cm} \approx 8^\circ$ and somewhat flatter at higher scattering angles. The individual DCS curves in the VCT channel are jumbled together.

5.7.1.3 Transition Probability

The relative state-to-state transition probability for IVE process, $P_{0 \rightarrow v'}(\theta_{cm})$ and for VCT process, $P_{0 \rightarrow v''}(\theta_{cm})$ have been computed as a function of scattering angle (θ_{cm}) from their respective state-to-state DCS values using the set of formulas given in Eq. (5.3).

$$P_{0 \rightarrow v'}(\theta_{cm}) = \frac{\left. \frac{d\sigma}{d\omega}(0 \rightarrow v') \right|_{\theta_{cm}}}{\sum_{v'=0}^{v_{max}} \left. \frac{d\sigma}{d\omega}(0 \rightarrow v') \right|_{\theta_{cm}}} \quad (5.3)$$

$$P_{0 \rightarrow v''}(\theta_{cm}) = \frac{\left. \frac{d\sigma}{d\omega}(0 \rightarrow v'') \right|_{\theta_{cm}}}{\sum_{v''=0}^{v_{max}} \left. \frac{d\sigma}{d\omega}(0 \rightarrow v'') \right|_{\theta_{cm}}}$$

The denominator involves the summation over state-to-state DCS upto 20 vibrational states of O_2 and O_2^+ molecules and the numerator involves the state-to-state DCS as a function of θ_{cm} for a specific vibrational state and the division between the two gives us the relative

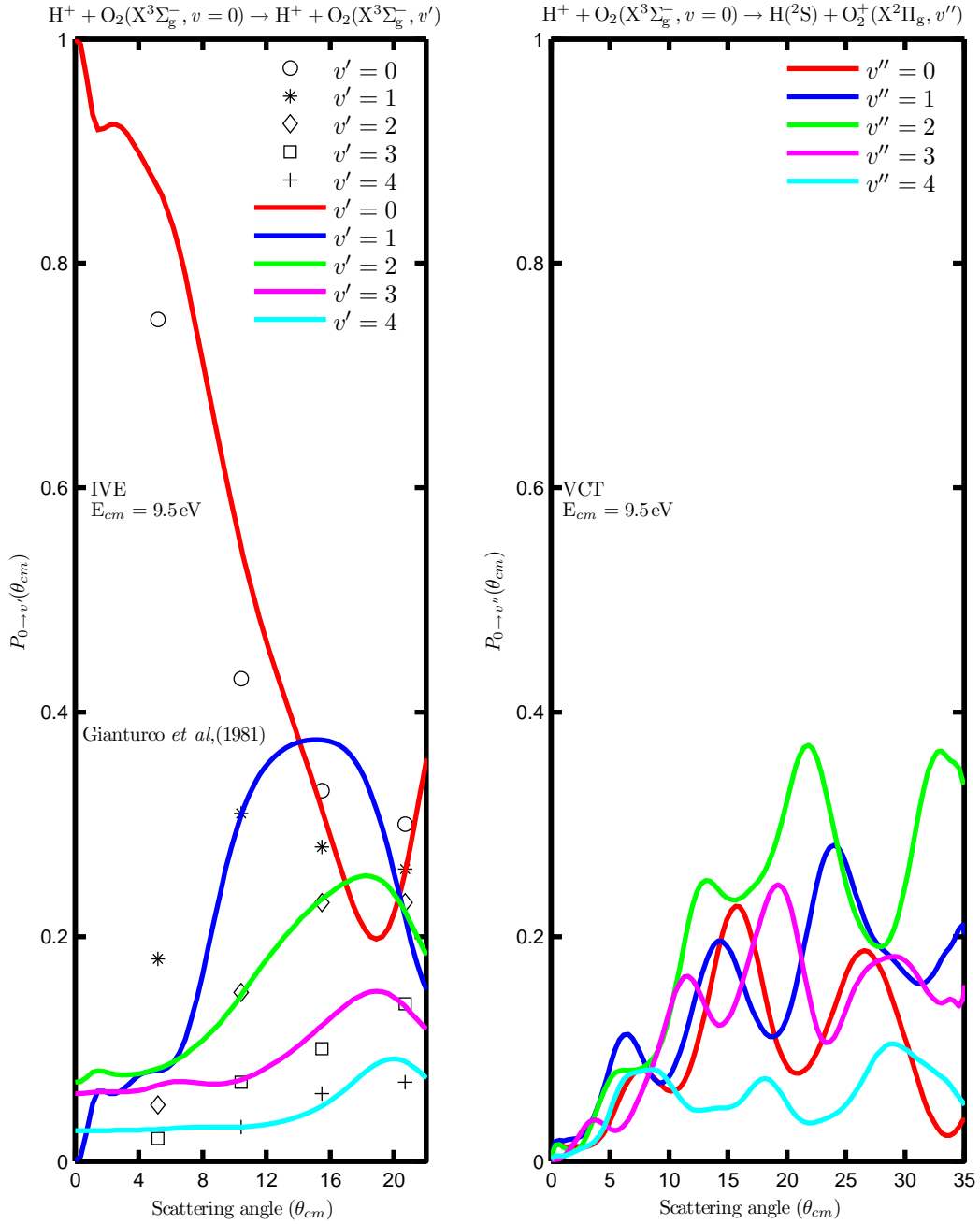


Figure 5.14: The transition probability for the IVE channel $P_{0 \rightarrow v'}(\theta_{cm})$, $H^+ + O_2(v = 0) \rightarrow H^+ + O_2(v')$, (left) and for the VCT channel $P_{0 \rightarrow v''}(\theta_{cm})$, $H^+ + O_2(v = 0) \rightarrow H(^2S) + O_2^+(v'')$ (right) at $E_{cm} = 9.5\text{ eV}$ as a function of θ_{cm} . Theory and experiments are compared only for the IVE channel (Gianturco, Gierz, and Toennies, 1981). No experimental data are available for the VCT channel.

state-to-state transition probability for the IVE and the first VCT channel. The transition probability for both the two channels have been shown in Fig. 5.14 for the first five vibrational states along with the experimental data (Gianturco, Gierz, and Toennies, 1981) for

the IVE channel alone. The agreement between theory and experiment is quite good for the excitation to higher vibrational states of O₂ such as $v = 0 \rightarrow v' = 2, v = 0 \rightarrow v' = 3, v = 0 \rightarrow v' = 4$ whereas some discrepancies exist for the excitation to states such as $v = 0 \rightarrow v' = 0, v = 0 \rightarrow v' = 1$ and the reason for such discrepancies may be probably due to the fact that the computation have been performed on the 2×2 coupled diabatic PESs, picked out from 4×4 coupled diabatic PESs, and hence we expect an improvement in the agreement between theory and experiment once all the four coupled PESs have been included in the computation. In the VCT channel (right) where there is no experimental data available to compare with the theory, $P_{0 \rightarrow v''}(\theta_{cm})$ for the entire range of scattering angle for all vibrational excitations does not exceed the values of 0.4. The magnitude of $P_{0 \rightarrow v''}$ follows the following order : $v = 0 \rightarrow v'' = 2 > v = 0 \rightarrow v'' = 1 > v = 0 \rightarrow v'' = 0 > v = 0 \rightarrow v'' = 3 > v = 0 \rightarrow v'' = 4$ and the most dominant excitation is found to be $v = 0 \rightarrow v'' = 2$, contrary to our expectations $v = 0 \rightarrow v'' = 0$.

5.7.1.4 Average vibrational energy transfer

The average vibrational energy transfer $\overline{\Delta E}_{vib}(\theta_{cm})$ (in eV) is computed for the IVE and the VCT processes using Eq. (5.4) given below at the collision energy of $E_{cm} = 9.5$ eV. It is just the sum over the product of transition probability at specific vibrational state, and the corresponding vibrational energy of either O₂(v') or O₂⁺(v'') as the case may be, as a function of θ_{cm} . The number of vibrational levels of the diatoms included in the computation is 20. The computed average vibrational energy transfer $\overline{\Delta E}_{vib}(\theta_{cm})$ for both type of processes have been shown in Fig. 5.15. The results for the IVE channel is compared with the available data from the experiments upto $\theta_{cm} = 20^\circ$. The results for VCT channel have been displayed

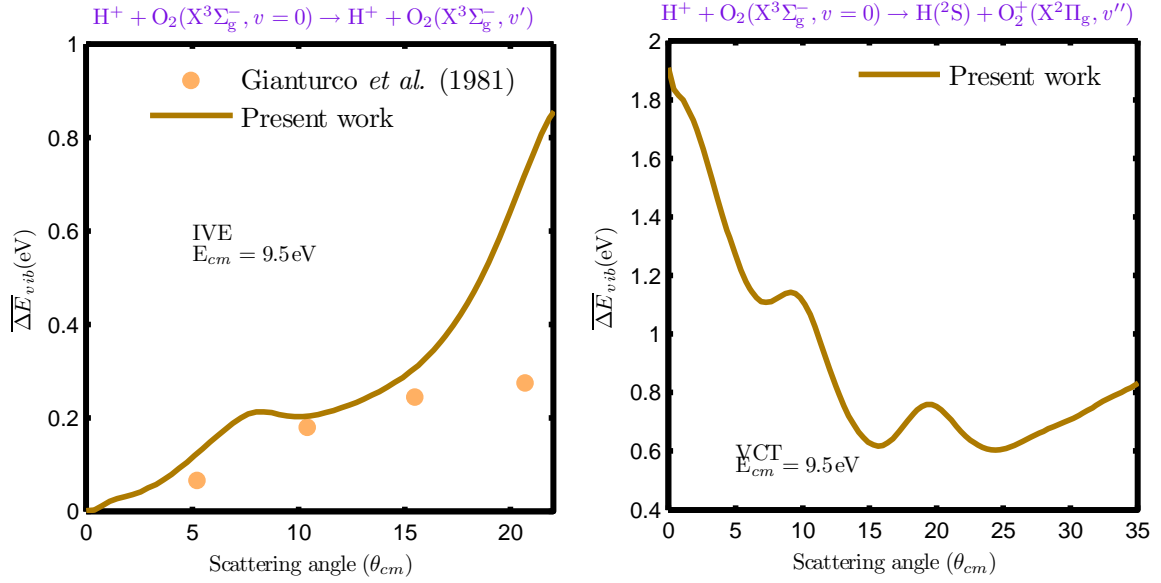


Figure 5.15: Average vibrational energy transfer $\overline{\Delta E}_{vib}(\theta_{cm})$ (in eV) as a function of scattering angle θ_{cm} for the IVE (left) and the VCT (right) channels at $E_{cm} = 9.5$ eV. Theory and experiment (Gianturco, Gierz, and Toennies, 1981) are compared for the IVE channel.

in full range of θ_{cm} without any experimental data.

$$\begin{aligned}\overline{\Delta E}_{vib}(\theta_{cm}) &= \sum_{v'=0}^{\infty} P_{0 \rightarrow v'}(\theta_{cm}) \Delta E(0 \rightarrow v') \\ \overline{\Delta E}_{vib}(\theta_{cm}) &= \sum_{v''=0}^{\infty} P_{0 \rightarrow v''}(\theta_{cm}) \Delta E(0 \rightarrow v'')\end{aligned}\tag{5.4}$$

The agreement between theory and experiment is fairly good even though there is a large deviation near $\theta_{cm} \approx 20^\circ$. In the VCT channel, $\overline{\Delta E}_{vib}(\theta_{cm})$ decreases sharply followed by slight increase as a function of θ_{cm} .

5.7.1.5 Integral cross section

The rotationally-summed state-to-state integral cross section (ICS) is computed using Eq. (3.32) and is shown in Fig. 5.16 as a function of vibrational quantum number of $O_2(v')$ for IVE channel (left) and as a function of vibrational quantum number of $O_2^+(v'')$ for VCT

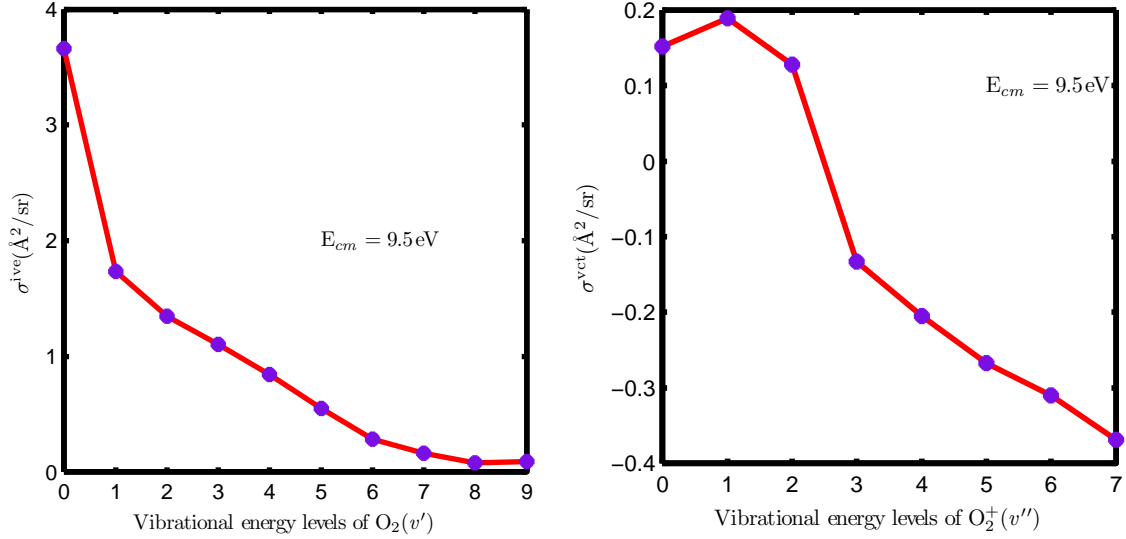


Figure 5.16: Rotationally-summed state-to-state integral cross section (σ) for the IVE (left) and the VCT (right) processes as a function of final vibrational energy levels of O_2 and O_2^+ , respectively at $E_{cm} = 9.5$ eV. Note that the ground vibrational state of $\text{O}_2(X^3\Sigma_g^-)$ is the initial state. The numbers in the ordinate indicate powers of 10.

Figure 5.17: The VCC-RIOSAs absolute rotationally-summed state-to-state integral cross section (σ) for the IVE channel, $\text{H}^+ + \text{O}_2(v = 0) \rightarrow \text{H}^+ + \text{O}_2(v')$, and the VCT channel, $\text{H}^+ + \text{O}_2(v = 0) \rightarrow \text{H}(^2\text{S}) + \text{O}_2^+(v'')$ at the $E_{cm} = 9.5$ eV for different vibrational states of $\text{O}_2(v')$ and $\text{O}_2^+(v'')$.

Integral cross section(\AA^2)		
$v'(v'')$	IVE	VCT
0	4381.07	1.42
1	49.95	1.55
2	20.99	1.34
3	11.13	0.74
4	6.11	0.62
5	3.18	0.54
6	1.80	0.49
7	1.38	0.42
8	1.11	
9	1.12	
$\sum v'(v'')$	4477.84	7.12

channel (right) at the collision energy of $E_{cm} = 9.5$ eV. Note that all the excitations refer to the excitations from the initial ground vibrational state of $\text{O}_2(X^3\Sigma_g^-)$. The numbers in the ordinate denote the power of 10. They have also been tabulated in Table 5.17. It shows that there is a huge difference in the magnitudes of the ICSs between $v' = 0$ and $v' = 1$

in the IVE channel. The maximum in ICS occurs for the $v' = 0$ (elastic) excitation in the IVE channel and for the $v'' = 1$ excitation in the VCT channel. The vibrationally elastic collisions are the dominant processes in the former while the collisions corresponding to $v = 0 \rightarrow v'' = 1$ excitation are dominant in the latter process. ICS shows an exponential decrease for the IVE and it passes through a maximum followed by a gradual decrease for the VCT.

5.7.2 Dynamics at $E_{cm}=23$ eV

In this section, like the previous section, we will show and compare all the computed scattering properties at $E_{cm} = 23$ eV with experiments (Noll and Toennies, 1986) and also with other theoretical studies performed earlier (Sidis, Grimbert, Sizun, and Baer, 1989; Gianturco, Palma, Semprini, Stefani, and Baer, 1990) along with the possible interpretations concerning the agreement between theory and experiment.

5.7.2.1 The orientation opacities

The VCC-RIOSAs angle-dependent opacity function as defined in Eq. (3.34) in **chapter 3** is shown in Fig. 5.18 as a function of partial waves (l) (in the units of \hbar) for the IVE channel (left panel), $\text{H}^+ + \text{O}_2(v = 0) \longrightarrow \text{H}^+ + \text{O}_2(v')$ for $\gamma = 0^\circ, 45^\circ$ and 90° and the VCT channel (right panel), $\text{H}^+ + \text{O}_2(v = 0) \longrightarrow \text{H}(^2\text{S}) + \text{O}_2^+(v'')$ for $\gamma = 15^\circ, 45^\circ$ and 75° orientations at $E_{cm} = 23$ eV. The magnitudes of opacities are less as compared with those at $E_{cm} = 9.5$ eV for the IVE channel while the opposite is true in the VCT channel. Nevertheless, at $E_{cm} = 23$ eV, more partial waves (l) are required for the convergence of the opacity than at $E_{cm} = 9.5$ eV. In the IVE channel, the opacity follows the following order

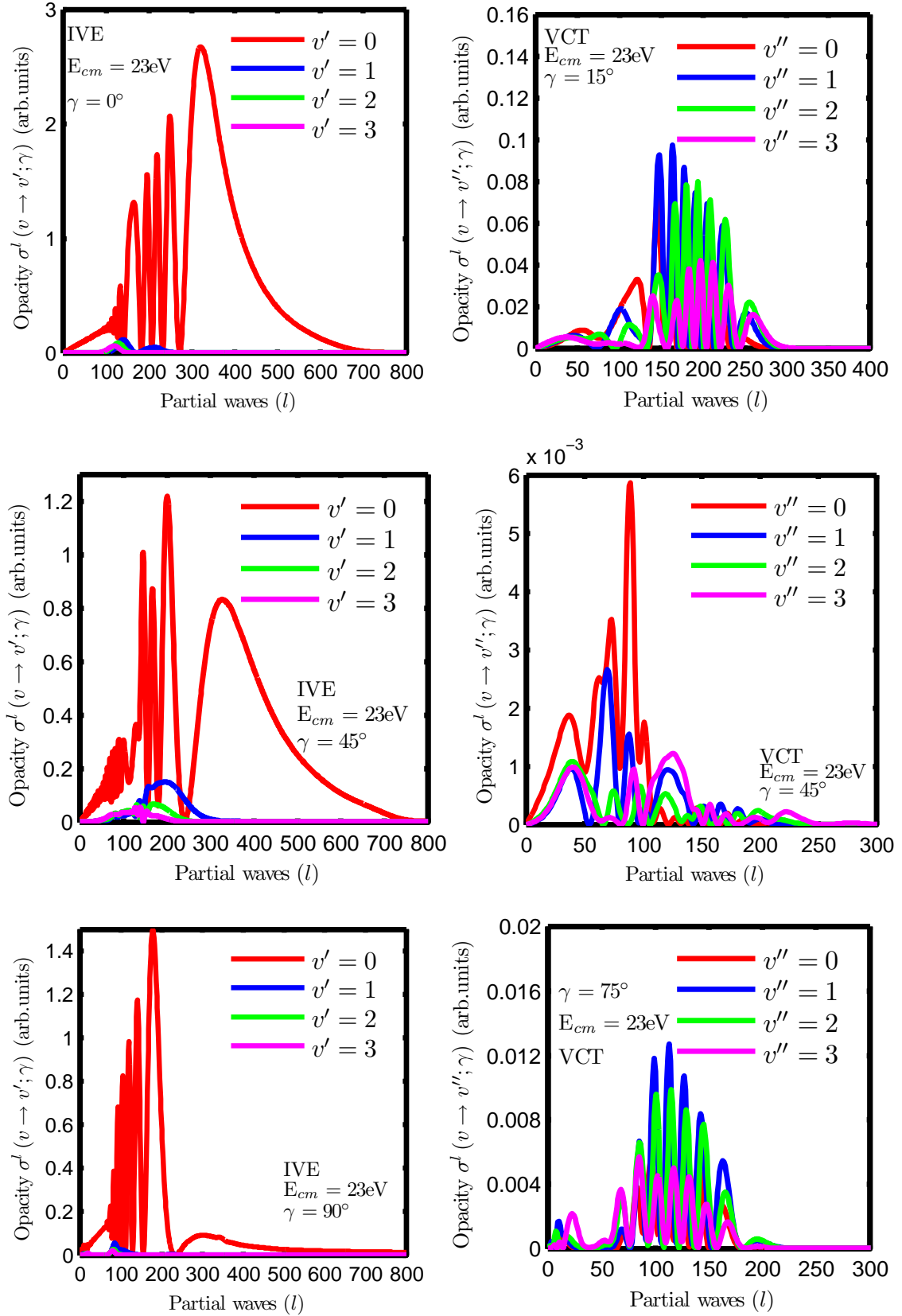


Figure 5.18: Opacity function as a function of partial waves (l , in the unit of \hbar) at $E_{cm} = 23$ eV for $\gamma = 0^\circ, \gamma = 45^\circ$ and $\gamma = 90^\circ$ for the IVE channel $\text{H}^+ + \text{O}_2(X^3\Sigma_g^-, v = 0) \rightarrow \text{H}^+ + \text{O}_2(X^3\Sigma_g^-, v')$ (left panel), and orientations for the VCT channel $\text{H}^+ + \text{O}_2(X^3\Sigma_g^-, v = 0) \rightarrow \text{H}(^2\text{S}) + \text{O}_2^+(X^2\Pi_g, v'')$ (right panel).

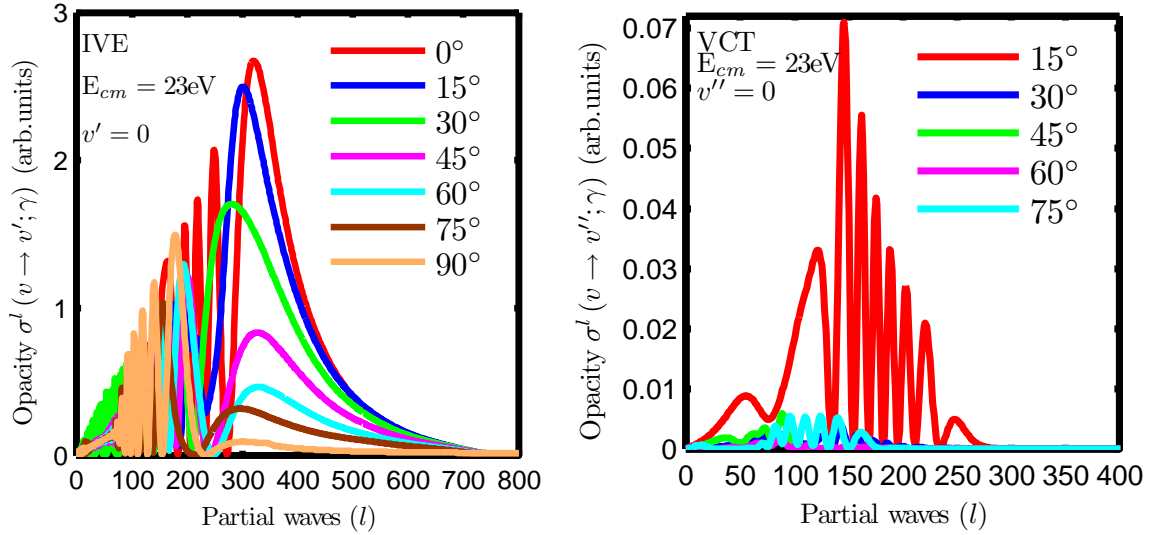


Figure 5.19: Opacity functions for all γ values at $E_{cm} = 23$ eV for the elastic collisions in the IVE channel $\text{H}^+ + \text{O}_2(v = 0) \rightarrow \text{H}^+ + \text{O}_2(v' = 0)$ (left) and for first charge transfer collisions in the VCT channel $\text{H}^+ + \text{O}_2(v = 0) \rightarrow \text{H}(^2\text{S}) + \text{O}_2^+(v'' = 0)$ (right).

of excitation : $v = 0 \rightarrow v' = 0 > v = 0 \rightarrow v' = 1 > v = 0 \rightarrow v' = 2 > v = 0 \rightarrow v' = 3$.

This suggests the dominance of elastic collisions over inelastic collisions, as it was also the case at $E_{cm} = 9.5$ eV. The opacity in the VCT channel follows a different order as compared to that of the IVE channel for $\gamma = 15^\circ$ and $\gamma = 75^\circ$ orientations, $v = 0 \rightarrow v'' = 1 > v = 0 \rightarrow v'' = 2 > v = 0 \rightarrow v'' = 0 > v = 0 \rightarrow v'' = 3$, and follows a similar order as observed for the IVE channel for $\gamma = 45^\circ$, $v = 0 \rightarrow v'' = 0 > v = 0 \rightarrow v'' = 1 > v = 0 \rightarrow v'' = 2 > v = 0 \rightarrow v'' = 3$. We compare in Fig. 5.19 the opacity functions for elastic (left) and zeroth order charge transfer (right) collision for all the molecular orientations and the magnitude of opacity decreases with γ , with 0° being the highest and 90° being the lowest for the elastic collisions ($v = 0 \rightarrow v' = 0$). The magnitude follows the order : $0^\circ > 15^\circ > 30^\circ > 45^\circ > 60^\circ > 75^\circ > 90^\circ$ and suggests that collinear approach promote elastic process very much. The magnitude for $v = 0 \rightarrow v'' = 0$ charge transfer collisions follows the order : $15^\circ > 75^\circ > 30^\circ > 45^\circ > 60^\circ$ and suggest that 15° orientation promote the charge transfer ($v = 0 \rightarrow v'' = 0$) collisions very much.

5.7.2.2 Rotationally-summed state-selective differential cross section (DCS)

The rotationally-summed total differential cross section (TDCS) and rotationally-summed state-selective differential cross sections (DCS) have been computed as a function of θ_{cm} $E_{cm} = 23$ eV for the IVE channel, $\text{H}^+ + \text{O}_2(v = 0) \longrightarrow \text{H}^+ + \text{O}_2(v')$ and the VCT channel, $\text{H}^+ + \text{O}_2(v = 0) \longrightarrow \text{H}(^2\text{S}) + \text{O}_2^+(v'')$. As discussed earlier (see **subsection 5.7.1**) we show here in Fig. 5.20(b) only the smoothed data along with earlier theoretical results in Fig. 5.20(c) (Gianturco, Palma, Semprini, Stefani, and Baer, 1990) and in Fig. 5.20(d) (Sidis, Grimbert, Sizun, and Baer, 1989). Note that in these theoretical calculations the same smoothing procedure was adopted. The experimental data (Noll and Toennies, 1986) are shown in Fig. 5.20(a). The earlier theoretical and experimental results have been reproduced from the mentioned references. Note that the earlier theoretical calculations were done on the 2×2 coupled electronic PESs which were obtained using semiempirical methods. Since experimental resolution was not sufficient to resolve the rotational excitations it would be proper to compare the rotationally-summed state-to-state DCS with that of the experimental state-to-state DCS. The earlier theoretical results also reported only the rotationally-summed DCS. All the theoretical values are plotted on absolute scale and no normalization was done. All the three sets of theoretical calculations yield different sizes of DCSs. In the experiments the measurements of DCSs could be reported only on relative scale. Therefore, we normalized the experimental data with the present theoretical values with respect to the theoretical datum value taken at $\theta_{cm} = 11.72^\circ$ (Experimental rainbow maximum for the TDCS). The existence of the rainbow maximum in the TDCS observed in the experiments is almost missing in the present calculations and predictions for the individual stat-to-state DCS appear to closely follow the experimental trend. The results of Gianturco *et al.* (1990)

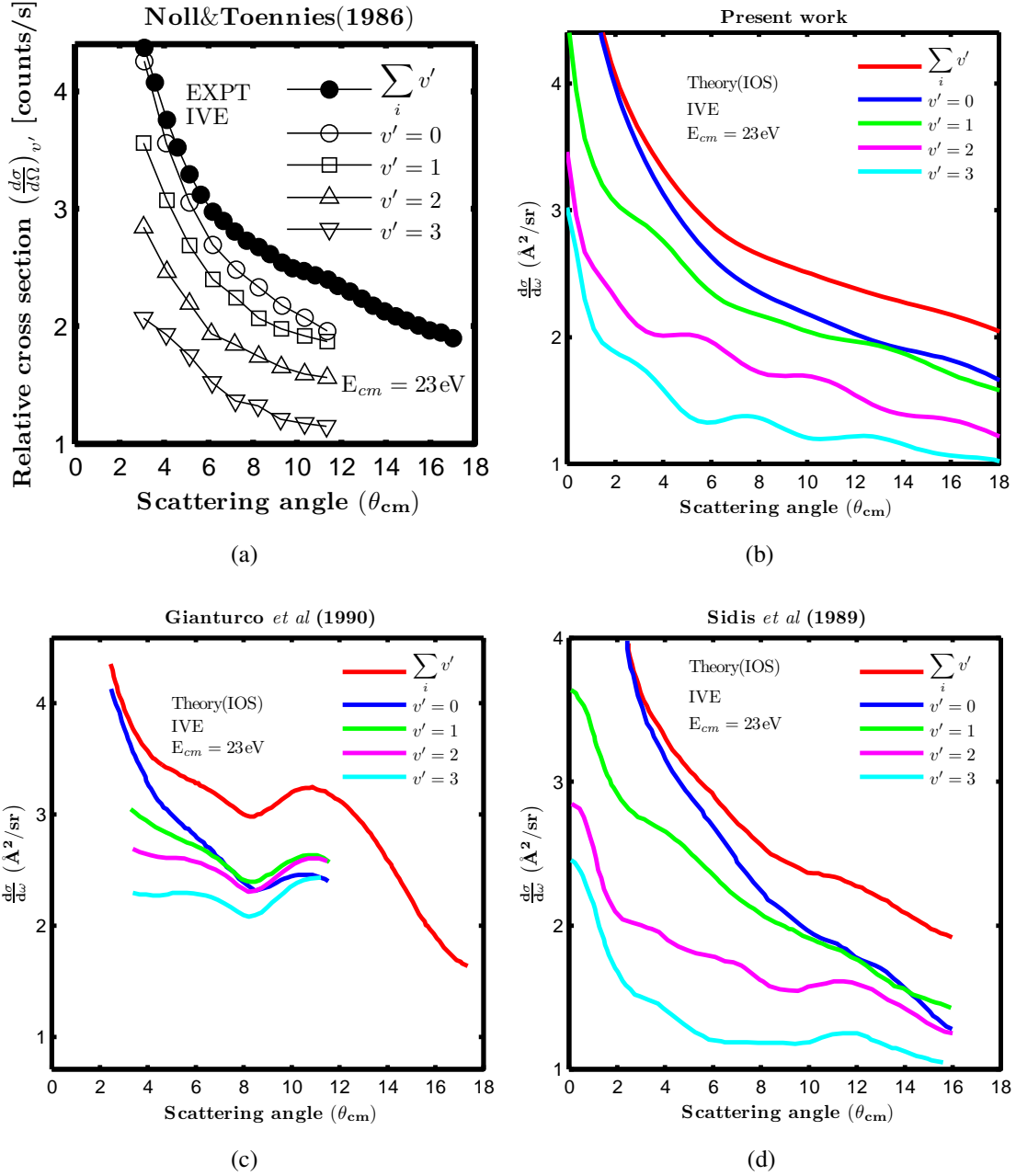


Figure 5.20: Rotationally-summed total differential cross section (TDCS) and rotationally-summed state-to-state DCS as function of θ_{cm} for IVE channel $H^+ + O_2(v = 0) \rightarrow H^+ + O_2(v')$ at $E_{cm} = 23$ eV along with experimental results (Noll and Toennies, 1986) and other two earlier theoretical works (Sidis, Grimbert, Sizun, and Baer, 1989; Gianturco, Palma, Semprini, Stefani, and Baer, 1990). The numbers in the ordinate denote powers of 10. See the text.

predict a rather strong rainbow maximum; The state-to-state DCSs are jumbled together showing also the existence of the rainbow maximum in the individual curves. The results of Sidis *et al.* (1989) appear to be in better agreement with those of experiments. Except for

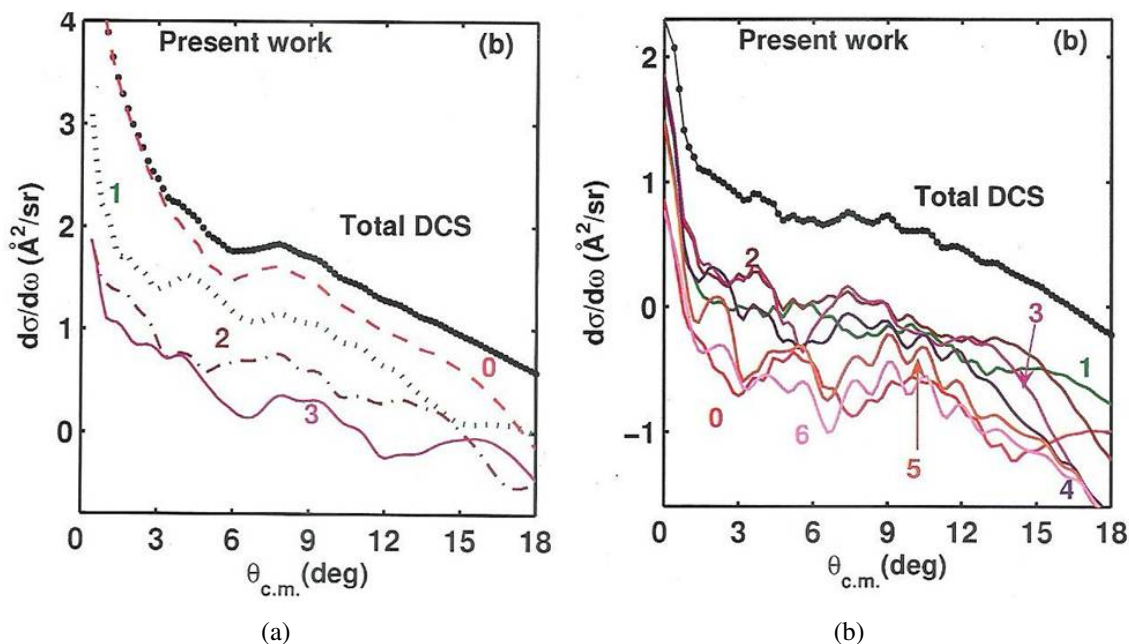


Figure 5.21: Rotationally-summed total differential cross section (TDCS) and rotationally-summed state-to-state DCS as function of θ_{cm} for the IVE channel $H^+ + O_2(v = 0) \rightarrow H^+ + O_2(v')$ and the VCT channel $H^+ + O_2(v = 0) \rightarrow H(^2S) + O_2^+(v'' = 0)$ at $E_{cm} = 23$ eV. These results have been reproduced from the earlier theoretical study (Saieswari and Kumar, 2007b, 2008a, 2009). The numbers in the ordinate denote powers of 10.

the rainbow maximum in the TDCS the present results appear to be mostly similar to those of Sidis *et al.*. For the sake of comparison we have reproduced the results of Saieswari and Kumar (2007b, 2008a, 2009) in Fig. 5.21(a) which were obtained using the 2×2 state smoothed coupled PESs (already discussed earlier in **section 5.3**). Their results show a pronounced rainbow maximum for the TDCS located at smaller θ_{cm} values as compared to that of a experiments. The existence of rainbow is also seen in the state-to-state DCSs which are absent in the experiments. The DCSs also appear to be "wavy" in nature. and present relatively a poor comparison against experiments.

The experimental results for the rotationally-summed TDCS and the rotationally-summed state-to-state DCSs for the VCT channel are shown in Fig. 5.22(a). The present smoothed theoretical results are shown in Fig. 5.22(b) and the earlier theoretical results are shown

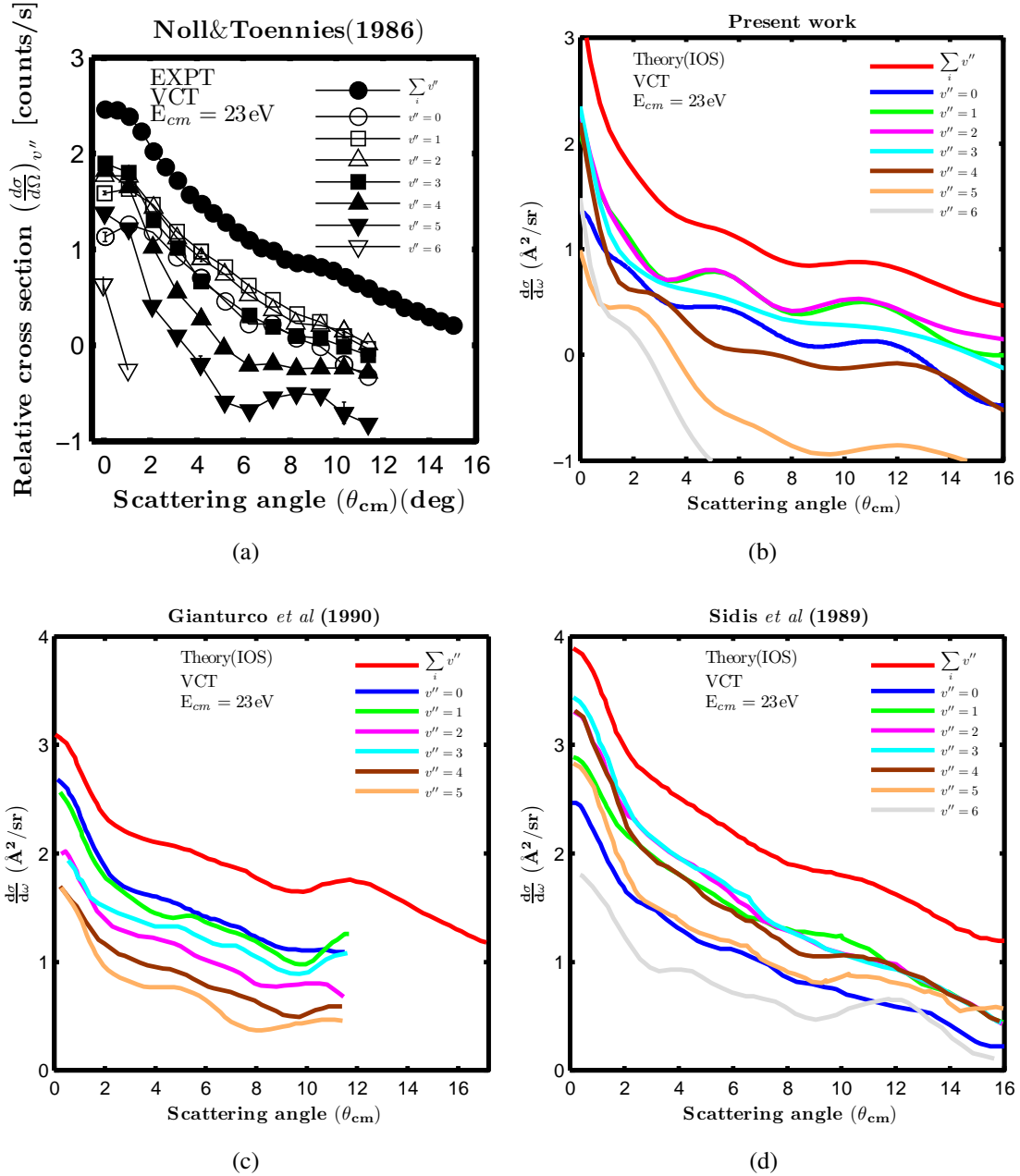


Figure 5.22: Rotationally-summed total differential cross section (TDCS) and rotationally-summed state-to-state DCS as function of θ_{cm} for the VCT channel $\text{H}^+ + \text{O}_2(v = 0) \rightarrow \text{H}(^2\text{S}) + \text{O}_2^+(v'' = 0)$ at $E_{cm} = 23 \text{ eV}$ along with experimental results (Noll and Toennies, 1986) and other two earlier theoretical results (Sidis, Grimbert, Sizun, and Baer, 1989; Gianturco, Palma, Semprini, Stefani, and Baer, 1990). The numbers in the ordinate denote powers of 10. See the text.

in Fig. 5.22(c) (Gianturco, Palma, Semprini, Stefani, and Baer, 1990) and in Fig. 5.22(d) (Sidis, Grimbert, Sizun, and Baer, 1989). All the theoretical results show smoothed data, and as discussed earlier, in this case also, the experimental data have been normalised with re-

spect to the present theoretical datum value of the TDCS at $\theta_{cm} = 9.027^\circ$ (the experimental rainbow maximum in the TDCS). Here, we see a rainbow maximum in the present calculations for the TDCS, which is however located at slightly larger θ_{cm} values ($\theta_{cm} \sim 11^\circ$). Interestingly, there appears to be another rainbow maximum at lower θ_{cm} ($\sim 5^\circ$). Such a rainbow is not seen neither in the experiment nor in earlier theoretical calculations. The results of Gianturco *et al.* show a pronounced rainbow maximum. The results of Sidis *et al.* appears to be able to predict the experimental curve of the TDCS quite satisfactorily. The trends for the state-to-state DCSs are more or less similar in all the theoretical sets and none of them appear to predict them well in comparison with those of experiment. However, the results of Sidis *et al.* appear to predict the results relatively better. The results of earlier calculations for the VCT (Saieswari and Kumar, 2007b, 2008a, 2009) obtained from the smoothed 2×2 coupled PESs have been reproduced in Fig. 5.21(b). Interestingly, one sees a broad rainbow maximum centered around $\theta_{cm} \sim 8^\circ$, close to the experimental rainbow maximum. However, the DCSs appears to be jumbled together and their behaviour does not appear to be satisfactory.

5.7.2.3 Transition Probability

The detailed behaviour of the state-to-state transition probability for different processes as a function of θ_{cm} is a good tool to determine the quality of theoretical calculations. The present computed and the experimental (Noll and Toennies, 1986) state-to-state transition probabilities are shown in Fig. 5.23 for the IVE channel, $\text{H}^+ + \text{O}_2(v = 0) \longrightarrow \text{H}^+ + \text{O}_2(v')$ (upper left) as well as the VCT channel $\text{H}^+ + \text{O}_2(v = 0) \longrightarrow \text{H}(^2\text{S}) + \text{O}_2^+(v'')$ (upper right) at $E_{cm} = 23$ eV, along with those of earlier theoretical results (Sidis, Grimbert, Sizun, and Baer, 1989; Gianturco, Palma, Semprini, Stefani, and Baer, 1990). We have also enlisted

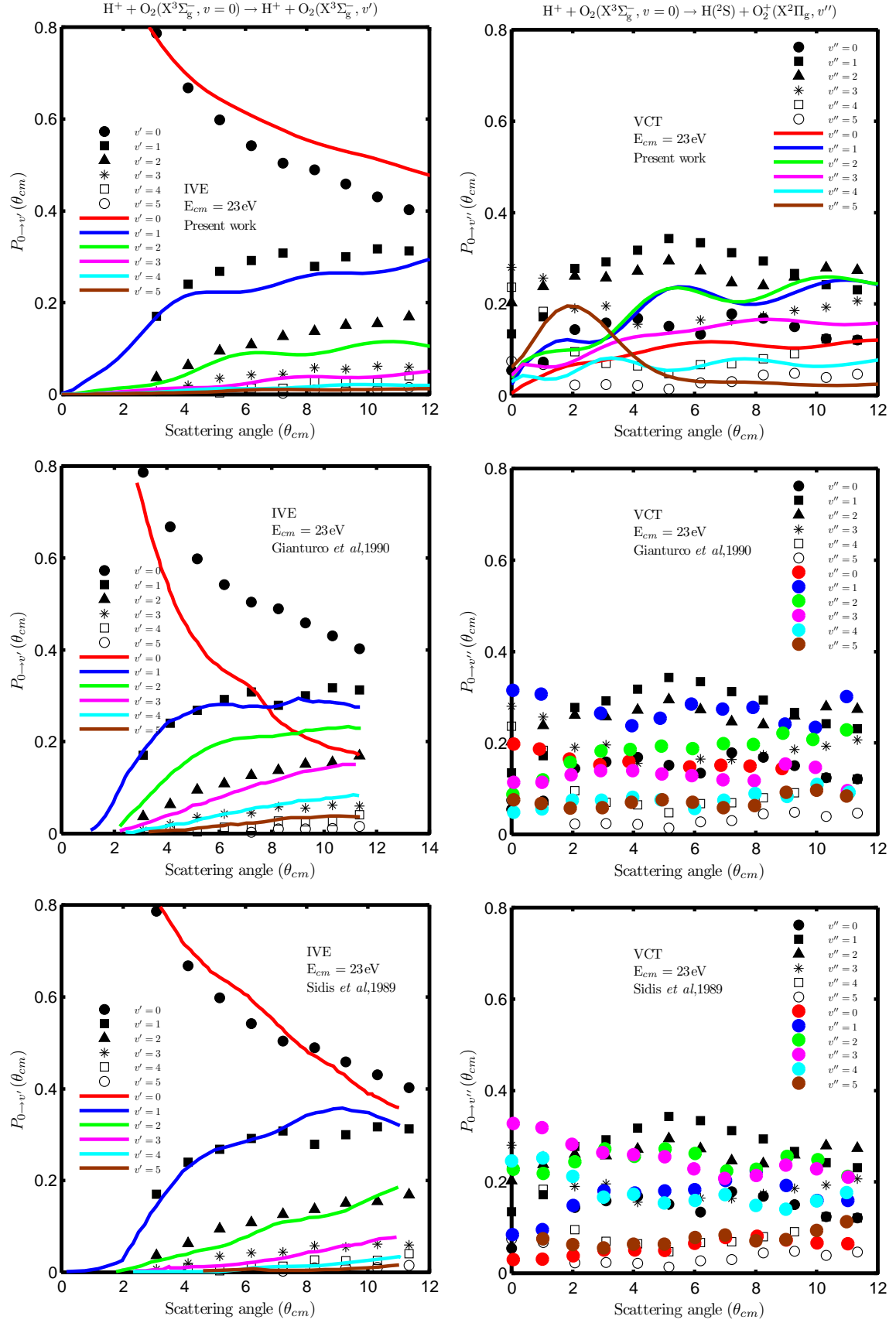


Figure 5.23: The transition probability, $P_{0 \rightarrow v'}(\theta_{cm})$, for IVE (left) and VCT (right) channel compared with experiment (Noll and Toennies, 1986) along with earlier theoretical works (Staemmler and Gianturco, 1985; Gianturco, Palma, Semprini, Stefani, and Baer, 1990).

Table 5.10: Measured relative transition probabilities (Noll and Toennies, 1986) for vibrational excitation of O₂ by proton impact at E_{lab} = 23.7 eV for various scattering angles compared with our computed values for the inelastic channel, H⁺ + O₂(v = 0) → H⁺ + O₂(v′) upto v′ = 5 levels.

θ _{cm} (deg)	Expt(IVE)						Theory(IVE)					
	P(0 → v′)						P(0 → v′)					
	v′ = 0	1	2	3	4	5	v′ = 0	1	2	3	4	5
3.09	0.786	0.170	0.037	0.007			0.776	0.169	0.023	0.012	0.009	0.003
4.12	0.668	0.240	0.063	0.020	0.009		0.693	0.216	0.045	0.014	0.012	0.004
5.15	0.598	0.268	0.095	0.035	0.004		0.643	0.223	0.075	0.016	0.012	0.006
6.18	0.542	0.292	0.109	0.043	0.014		0.607	0.225	0.091	0.025	0.012	0.009
7.21	0.504	0.308	0.127	0.044	0.014	0.003	0.575	0.244	0.088	0.036	0.013	0.010
8.24	0.489	0.279	0.138	0.058	0.027	0.010	0.548	0.261	0.088	0.039	0.017	0.010
9.28	0.458	0.300	0.151	0.055	0.025	0.010	0.529	0.264	0.102	0.037	0.021	0.010
10.31	0.430	0.317	0.155	0.062	0.026	0.011	0.512	0.265	0.114	0.038	0.021	0.011
11.34	0.402	0.313	0.169	0.060	0.041	0.015	0.490	0.280	0.112	0.046	0.019	0.012

Table 5.11: The computed vibrational transition probabilities for the charge transfer process $\text{H}^+ + \text{O}_2(v=0) \longrightarrow \text{H}(^2\text{S}) + \text{O}_2^+(v'')$ at $E_{cm} = 23$ eV compared with the experimental values (Noll and Toennies, 1986) for the scattering angle $\theta_{cm} = 0^\circ - 11^\circ$.

θ_{cm} (deg)	Expt(VCT)						Theory(VCT)							
	$P(0 \rightarrow v'')$						$P(0 \rightarrow v'')$							
	$v'' = 0$	1	2	3	4	5	6	$v'' = 0$	1	2	3	4	5	6
0.00	0.055	0.135	0.203	0.280	0.237	0.075	0.015	0.004	0.024	0.038	0.044	0.030	0.006	0.000
1.03	0.073	0.172	0.238	0.257	0.184	0.067	0.009	0.044	0.104	0.093	0.062	0.036	0.045	0.001
2.06	0.144	0.278	0.261	0.190	0.096	0.023	0.010	0.067	0.120	0.099	0.075	0.052	0.110	0.001
3.09	0.158	0.292	0.258	0.196	0.070	0.024		0.077	0.123	0.126	0.110	0.081	0.122	0.002
4.12	0.168	0.318	0.272	0.156	0.065	0.022		0.093	0.184	0.194	0.129	0.070	0.078	0.003
5.15	0.151	0.343	0.295	0.149	0.047	0.014		0.110	0.233	0.234	0.136	0.055	0.045	0.004
6.18	0.134	0.334	0.273	0.165	0.067	0.027		0.120	0.230	0.224	0.150	0.064	0.040	0.005
7.21	0.178	0.312	0.247	0.164	0.069	0.030		0.116	0.210	0.210	0.160	0.080	0.040	0.007
8.24	0.168	0.294	0.240	0.174	0.080	0.045		0.110	0.201	0.220	0.170	0.078	0.034	0.007
9.28	0.150	0.267	0.259	0.186	0.091	0.048		0.104	0.225	0.245	0.163	0.067	0.030	0.008
10.31	0.124	0.242	0.279	0.193	0.124	0.039		0.110	0.248	0.260	0.156	0.064	0.031	0.008
11.34	0.121	0.231	0.274	0.207	0.121	0.046		0.120	0.250	0.251	0.155	0.070	0.036	0.008

our present theoretical data for the same in Table 5.10 and in Table 5.11, respectively. For the IVE channel the experimental data are well predicted by the present and earlier calculations of Sidis *et al.* in comparison with those of Gianturco *et al.*. However, for the VCT channels, none of the theoretical calculations appear to predict the experimental data well in the entire region of θ_{cm} . It turns out that while one set of theoretical data predicts the experimental data well in certain region of θ_{cm} it fails to do so in another region of θ_{cm} .

5.7.2.4 Average vibrational energy transfer

Now, we analyse and compare the average vibrational energy transfer $\overline{\Delta E}_{vib}$ as a function of θ_{cm} for both the IVE and the VCT channels with that obtained from the experiments and earlier theoretical results. The expression for $\overline{\Delta E}_{vib}$ is defined earlier in Eq. (5.4). Here, we just mention that for both the IVE channel, $H^+ + O_2(v = 0) \longrightarrow H^+ + O_2(v')$ and the VCT channel, $H^+ + O_2(v = 0) \longrightarrow H(^2S) + O_2^+(v'')$, the number of vibrational energy levels in the summation was 20, that is, from $v = 0$ to $v'(v'') = 20$.

We can observe the general trend of the average vibrational energy transfer increasing with the increase of scattering angle and extrapolating to a finite value as $\theta \sim 0^\circ$ in Fig. 5.24 (top) for the IVE channel. This shows that for the forward scattering ($\theta_{cm} \sim 0^\circ$) the vibrationally elastic channel is the most dominant processes. The computed values in the present work lie closer to the experimental values than the values obtained by Gianturco *et al.*. The trend observed in the VCT channel is different from that in the IVE channel in Fig. 5.24 (bottom). Eventhough we observe the trend to be the same as that of experiment at least for $\theta_{cm} = 6^\circ - 12^\circ$. it is largely overestimated for small θ_{cm} . The theoretical data of Gianturco *et al.* (1990) were reported with the scaling factor of 0.66 while comparing their

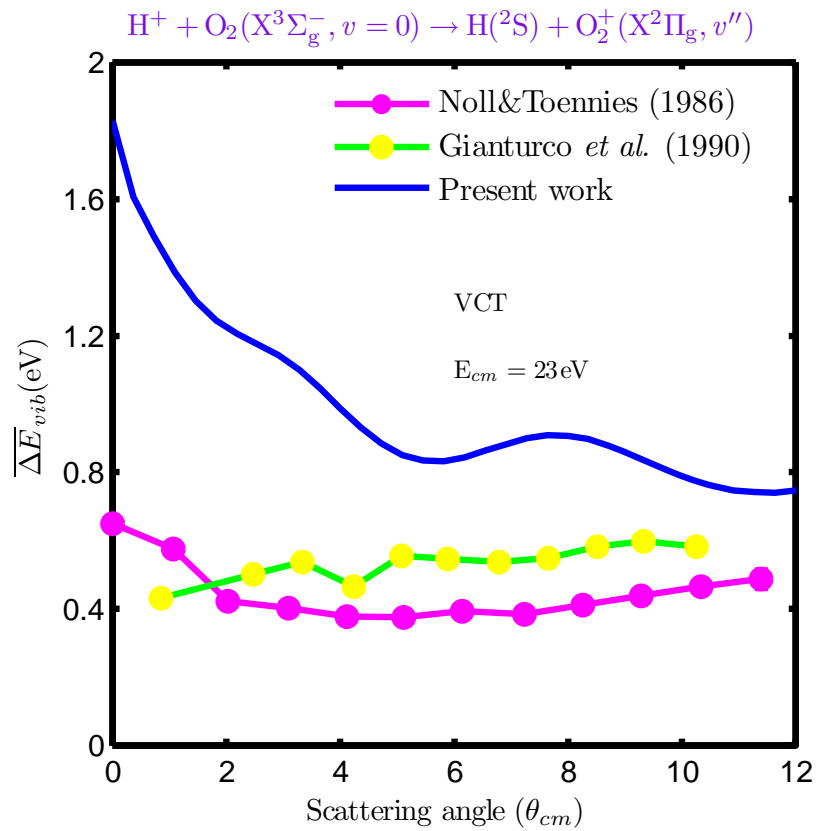
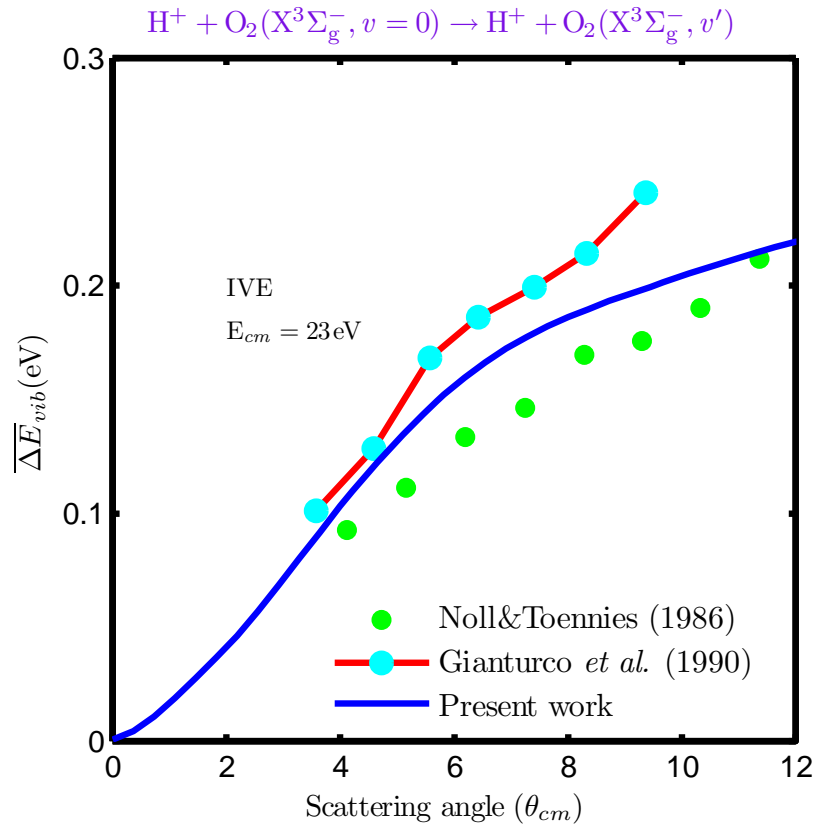


Figure 5.24: Average vibrational energy transfer $\overline{\Delta E}_{vib}$ (in eV) as a function of θ_{cm} at $E_{cm} = 23$ eV for the IVE (top) and the VCT (bottom) channels along with experimental data (Noll and Toennies, 1986) as well as earlier theoretical results (Gianturco, Palma, Semprini, Stefani, and Baer, 1990). Note the scaling factor ($\times 0.66$) in the data of Gianturco *et al.*. See the text.

values with those of experiments. We have just reproduced them from the above reference and in Fig. 5.24(bottom) they stand scaled by the factor 0.66. Interestingly, if we also scale our theoretical data by the same scale then the comparison would look almost similar against the experiments.

5.7.2.5 Integral cross section

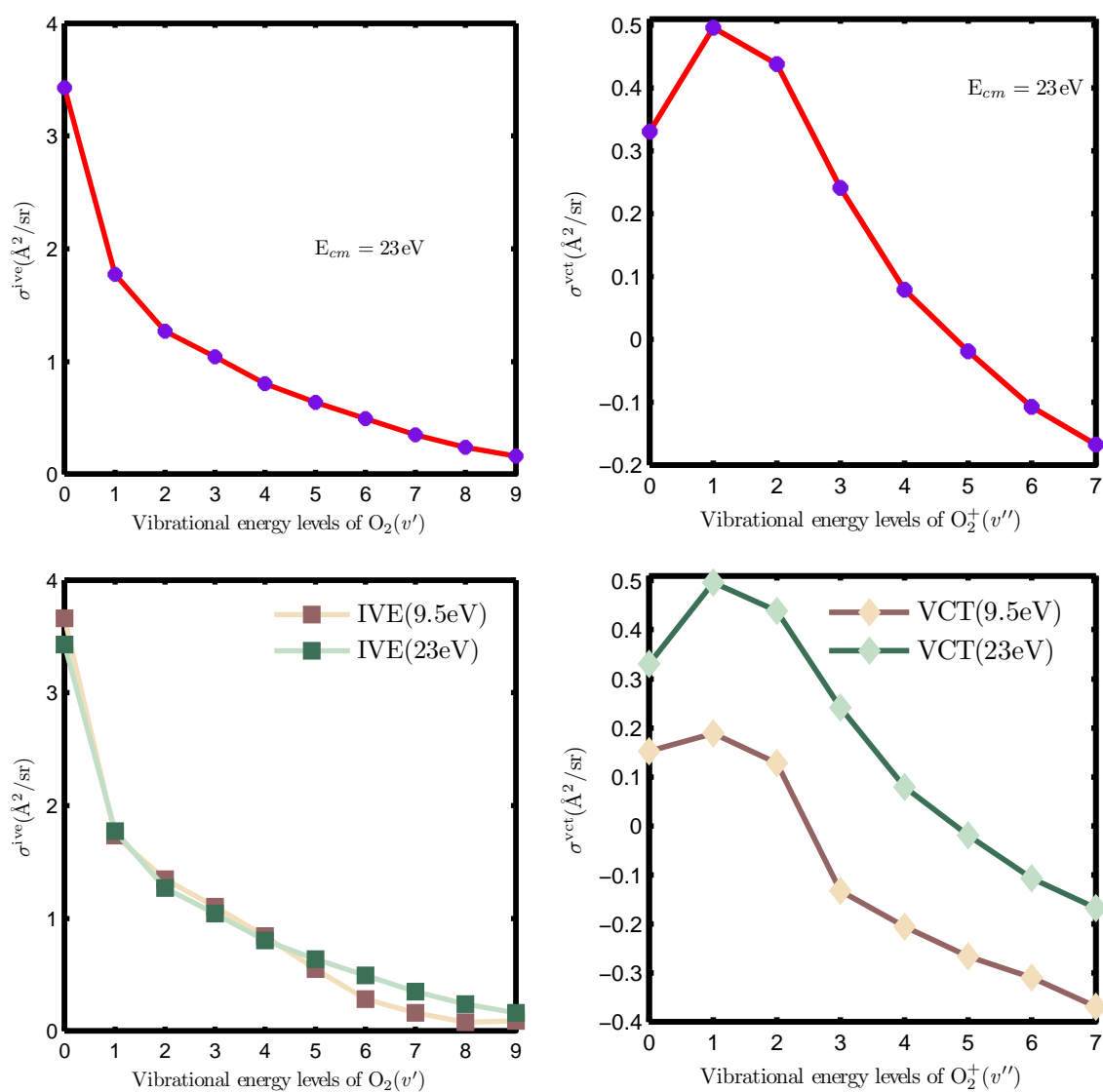


Figure 5.25: Rotationally-summed integral cross section (σ) for the IVE (top left) and VCT (top right) processes as a function of vibrational energy levels of O_2 and O_2^+ respectively at $E_{cm} = 23$ eV and comparison at two collision energies (bottom row). The numbers in the ordinate indicate powers of 10.

Rotationally-summed state-to-state integral cross section (ICS) for both IVE and the VCT channels are reported in Fig. 5.25 as a function of vibrational levels of target diatomic molecules O_2 and O_2^+ at $E_{cm} = 23$ eV (top row). The magnitudes of the computed ICS are compared at $E_{cm} = 9.5$ eV and at $E_{cm} = 23$ eV for both the processes (bottom row). There are no previously theoretical and experimental results for the ICS to be compared with. The ICS for the IVE channel decreases exponentially whereas that of VCT channel passes through a maximum at $v'' = 1$ followed by exponential decay with the magnitude of IVE process being higher than the VCT process. Also the comparison of the ICSs at $E_{cm} = 9.5$ eV and at $E_{cm} = 23$ eV shows that ICSs remains almost the same for both of these energies in the IVE channel whereas they differ widely in VCT channel, We also tabulate the absolute values of ICS at the two collision energies in the Table 5.12. We can conclude that the extent of the VCT is higher at $E_{cm} = 23$ eV than that at $E_{cm} = 9.5$ eV.

Table 5.12: The VCC-RIOSAs absolute state-to-state integral cross section (σ) for the IVE channel, $H^+ + O_2(v = 0) \rightarrow H^+ + O_2(v')$ and the VCT channel, $H^+ + O_2(v = 0) \rightarrow H(^2S) + O_2^+(v'')$ at $E_{cm} = 9.5$ eV and $E_{cm} = 23$ eV.

$v'(v'')$	Integral cross section (\AA^2)			
	9.5 eV		23 eV	
	IVE	VCT	IVE	VCT
0	4381.07	1.42	2671.78	2.14
1	49.95	1.55	59.05	3.14
2	20.99	1.34	18.52	2.75
3	11.13	0.74	10.96	1.74
4	6.11	0.62	6.31	1.20
5	3.18	0.54	4.32	0.96
6	1.80	0.49	3.13	0.78
7	1.38	0.42	2.24	0.68
8	1.11		1.73	
9	1.12		1.45	
$\sum v'(v'')$	4477.84	7.12	2779.511	13.39

5.8 Summary

A new set of global *ab initio* adiabatic and quasi-diabatic PESs for the lowest four electronics states of the $\text{H}^+ + \text{O}_2$ system have been obtained at the MRCI level of accuracy employing the Dunning's *cc-pVTZ* basis set in the Jacobi coordinates. The corresponding quasidiabatic PESs have also been computed at the same level of accuracy employing the *ab initio* procedure. The non-adiabatic interactions have been analysed in terms of the magnitudes of NACMEs and the coupling potential matrix elements.

We determined the equilibrium geometrical properties of bound triatomic $[\text{HO}_2^+]$ ion in the GS and compared them with the earlier theoretical results. Our results are found to be in excellent agreement with those obtained from earlier high level *ab initio* calculations which focussed on the description of the potential well of the GS PES, thus lending credence to our *ab initio* calculations.

We have taken out the 2×2 quasidiabatic potential matrix (describing the GS and the first ES and their coupling) out of the 4×4 quasidiabatic potential matrix. We have modelled the experimentally observed IVE and VCT processes as a two-state process and carried out quantum dynamics.

We performed quantum dynamics at two different collision energies such as $E_{cm} = 9.5$ eV and $E_{cm} = 23$ eV using only the coupled GS and first ES PESs along with the associated coupling potentials within the VCC-RIOSAs framework to obtain the five different scattering properties, namely, Opacity function, Differential cross sections, Transition probability, Average vibrational energy transfer, Integral cross section. We observe that there is an improvement in the computed collision attributes as compared with those of earlier reported results (Saieswari and Kumar, 2008a, 2007b, 2009) using "smoothed" *ab initio* quasidia-

batic coupled PESs. The improvement is much better for the IVE channel as compared to the VCT channel where the predictions for the former is in good agreement with the experimental results. However, serious discrepancies still exist between theory and experiment for the VCT channel where none of the theoretical results (the present and the earlier two results) are able to predict the experimental observation quite reliably. It turns out that if a particular set of theoretical data is in good agreement in certain range of θ_{cm} then it fails to do so in other range of θ_{cm} . It is hoped that discrepancies between theory and experiment that are found occasionally will be improved upon by the inclusion of two more ES PESs in the quantum dynamical calculations. In subsequent chapter, we take up the quantum dynamics on the 4×4 coupled quasidiabatic potential matrix.

CHAPTER 6

NONADIABATIC DYNAMICS ON THE FOUR

COUPLED ELECTRONIC PESs : THE $\text{H}^+ + \text{O}_2$ SYSTEM

In this chapter, we study the dynamics of the IVE, $\text{H}^+ + \text{O}_2(X^3\Sigma_g^-, v = 0) \longrightarrow \text{H}^+ + \text{O}_2(X^3\Sigma_g^-, v')$, and the three VCT, $\text{H}^+ + \text{O}_2(X^3\Sigma_g^-, v = 0) \longrightarrow \text{H}(^2\text{S}) + \text{O}_2^+(X^2\Pi_g, v'')$, $\text{H}^+ + \text{O}_2(X^3\Sigma_g^-, v = 0) \longrightarrow \text{H}(^2\text{S}) + \text{O}_2^+(X^4\Pi_u, v''')$ and $\text{H}^+ + \text{O}_2(X^3\Sigma_g^-, v = 0) \longrightarrow \text{H}(^2\text{S}) + \text{O}_2^+(X^4\Sigma_g^-, v''')$ processes. We present all four adiabatic and quasi-diabatic *ab initio* PESs and their associated NACMEs and Coupling potentials. We have performed a time-independent quantum dynamics study within the VCC-RIOSAs framework at the experimentally reported collision energies, $E_{cm} = 9.5$ eV and $E_{cm} = 23$ eV using these four coupled PESs and compared the results with those of experiments as well as those of the earlier theoretical studies, followed by a comparative study at these two collision energies.

6.1 Present focus

In the preceding chapter, we have discussed the details of the quantum dynamics carried out on the two-state (2×2) coupled surfaces (the GS and the first ES). This 2×2 coupling matrix was taken out from the 4×4 coupling matrix which involved *ab initio* computations of the GS and the three lowest ESs. The various characteristics of the GS and the first ES adiabatic as well as the quasi-diabatic PESs have been already analysed in detail in the **chapter 5**. The vibrational coupling matrix elements for these two surfaces have also been analysed there.

As noticed, there is a marked improvement in the quantum calculations as compared to those of earlier quantum calculations which were obtained by using the smoothened 2×2 coupled PESs. However, yet discrepancies exist. Therefore, in this chapter we present a thorough analysis of the characteristics of the involved four electronic states and present and discuss the quantum dynamics results involving the 4×4 coupled PESs along with the experimental and earlier theoretical results.

6.2 *Ab initio* PECs

The details of *ab initio* computations involving the 4×4 coupled electronic PECs have been given in **chapter 5** and hence we present and discuss the characteristics of GS, the first, the second and the third ESs together at $r = r_{eq}$ as a function of R for various γ values.

In Fig. 6.1, we show *ab initio* adiabatic PECs of GS, the first, the second and the third ESs for collinear ($\gamma = 0^\circ$, $C_{\infty v}$ group) and perpendicular approaches ($\gamma = 90^\circ$, C_{2v} group) of incoming H^+ as a function of R with r fixed at $r_{eq} = 2.293a_o$ (left panel) and as a function of r at $R = 4a_o$ (right panel). The spectroscopic designation of the four electronic states in $C_{\infty v}$ group is $1^3\Sigma^-$, $1^3\Pi$, $2^3\Pi$ and $3^3\Pi$ respectively in order of increasing energy at $r = r_{eq}$ and $R \approx 3a_o$, respectively and is 1^3B_1 , 1^3A_2 , 2^3B_1 and 3^3B_1 respectively in C_{2v} group. The GS PEC correlates to the IVE channel $H^+ + O_2(^3\Sigma_g^-)$ and the first ES PEC correlates to the first vibrational charge transfer channel (VCT) $H(^2S) + O_2(^2\Pi_g)$. The second and third ES PECs correlates to the second charge transfer channel $H(^2S) + O_2(^4\Pi_u)$ and the third charge transfer channel $H(^2S) + O_2(^4\Sigma_g^-)$, respectively.

A summary of essential molecular properties of O_2 and O_2^+ of different electronic states

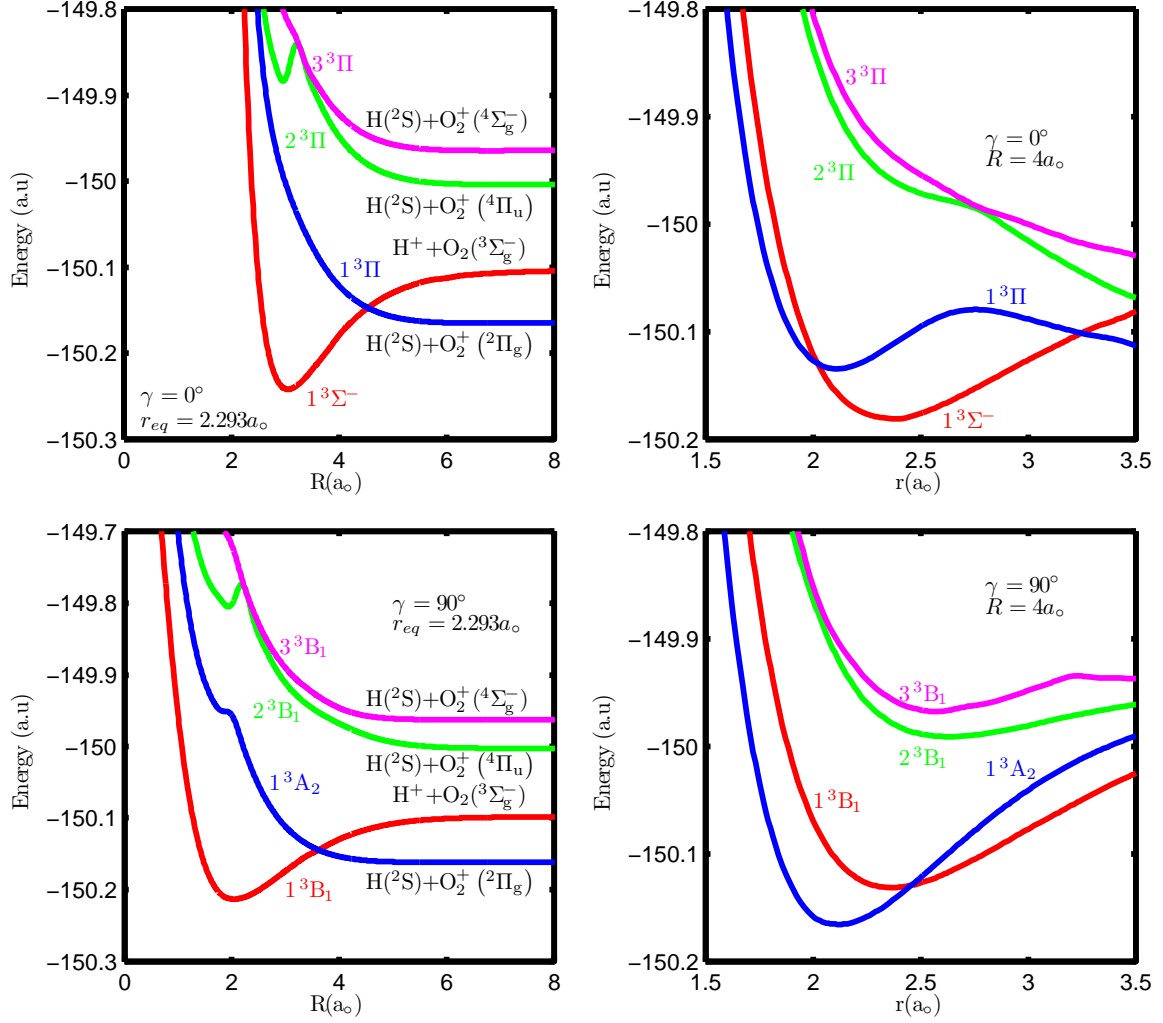


Figure 6.1: *Ab initio* adiabatic PECs of GS, the first, the second and the third ESs for $\gamma = 0^\circ$ and 90° as a function of R for a fixed $r = r_{eq} = 2.293a_0$ (left panel) and as a function of r for a fixed $R = 4.0a_0$ (right panel). Note the presence of crossings between the lowest two electronic states of different symmetries.

was already given in Table 5.3. In addition, we present in Table 6.1 vibrational energy level spacings of $O_2(^3\Sigma_g^-)$, $O_2^+(^2\Pi_g)$, $O_2^+(^4\Pi_u)$ and $O_2^+(^4\Sigma_g^-)$ which are used in the quantum dynamical computations involving four-states.

Note the presence of crossings between the lowest two electronic states of different symmetries. Also, the second and third ES PECs exhibit a long-range shallow well for $R > 5a_0$ even though not seen in Fig. 6.1(left panel). In Fig. 6.1(right panel), there appears crossings between PECs of symmetries $1^3\Sigma^-$ and $1^3\Pi$ at two places, one at around $r = 2a_0$ and

Table 6.1: The computed vibrational energy level spacing $\Delta E_{vib}^{v+1 \rightarrow v}$ (eV) of $O_2(^3\Sigma_g^-)$, $O_2^+(^2\Pi_g)$, $O_2^+(^4\Pi_u)$ and $O_2^+(^4\Sigma_g^-)$ from their corresponding PECs for first 20 states and $\Delta E_{vib}^{1 \rightarrow 0}$ transition have been given in bold

$\Delta E_{vib}^{v+1 \rightarrow v}$ (eV)	$O_2(^3\Sigma_g^-)$	$O_2^+(^2\Pi_g)$	$O_2^+(^4\Pi_u)$	$O_2^+(^4\Sigma_g^-)$
1 \rightarrow 0	0.1913	0.2300	0.1248	0.1420
2 \rightarrow 1	0.1884	0.2259	0.1224	0.1382
3 \rightarrow 2	0.1855	0.2218	0.1200	0.1343
4 \rightarrow 3	0.1827	0.2177	0.1175	0.1304
5 \rightarrow 4	0.1799	0.2137	0.1150	0.1266
6 \rightarrow 5	0.1771	0.2097	0.1123	0.1227
7 \rightarrow 6	0.1743	0.2056	0.1099	0.1188
8 \rightarrow 7	0.1715	0.2016	0.1074	0.1154
9 \rightarrow 8	0.1687	0.1976	0.1047	0.1131
10 \rightarrow 9	0.1659	0.1936	0.1020	0.1100
11 \rightarrow 10	0.1630	0.1895	0.0993	0.1045
12 \rightarrow 11	0.1602	0.1855	0.0965	0.0921
13 \rightarrow 12	0.1573	0.1815	0.0936	0.0137
14 \rightarrow 13	0.1544	0.1774	0.0906	0.0542
15 \rightarrow 14	0.1515	0.1734	0.0876	0.0505
16 \rightarrow 15	0.1485	0.1693	0.0844	0.0381
17 \rightarrow 16	0.1455	0.1652	0.0812	0.0496
18 \rightarrow 17	0.1424	0.1611	0.0778	0.0410
19 \rightarrow 18	0.1392	0.1569	0.0743	0.0441
20 \rightarrow 19	0.1359	0.1528	0.0707	0.0454

another in the range $3a_o - 3.5a_o$ and an avoided crossing between the PECs of symmetries $2^3\Pi$ and $3^3\Pi$ in the range $2.5a_o - 3.0a_o$ for $\gamma = 0^\circ$ at $R = 4a_o$.

The *ab initio* adiabatic (solid line) and the corresponding quasi-diabatic (dashed line) PECs of the GS, the first, the second and the third ESs for the three off-collinear orientations (C_s point group) such as $\gamma = 15^\circ$, $\gamma = 45^\circ$, $\gamma = 75^\circ$, have been shown as a function of R for a fixed $r = r_{eq} = 2.293a_o$ (left panel) and as a function of r for a fixed $R = 4.0a_o$ (right panel) in Fig. 6.2. The spectroscopic designations of the four electronic states in this C_s point group are $1^3A''$, $2^3A''$, $3^3A''$ and $4^3A''$ respectively in the increasing order of energy at $R \approx 3a_o$ and at $R = 4.0a_o$. Note that for $R > 8a_o$, the asymptotic correlations of the adiabatic PECs differ from that of $\gamma = 0^\circ$ and 90° orientations in Fig. 6.2 (right panel).

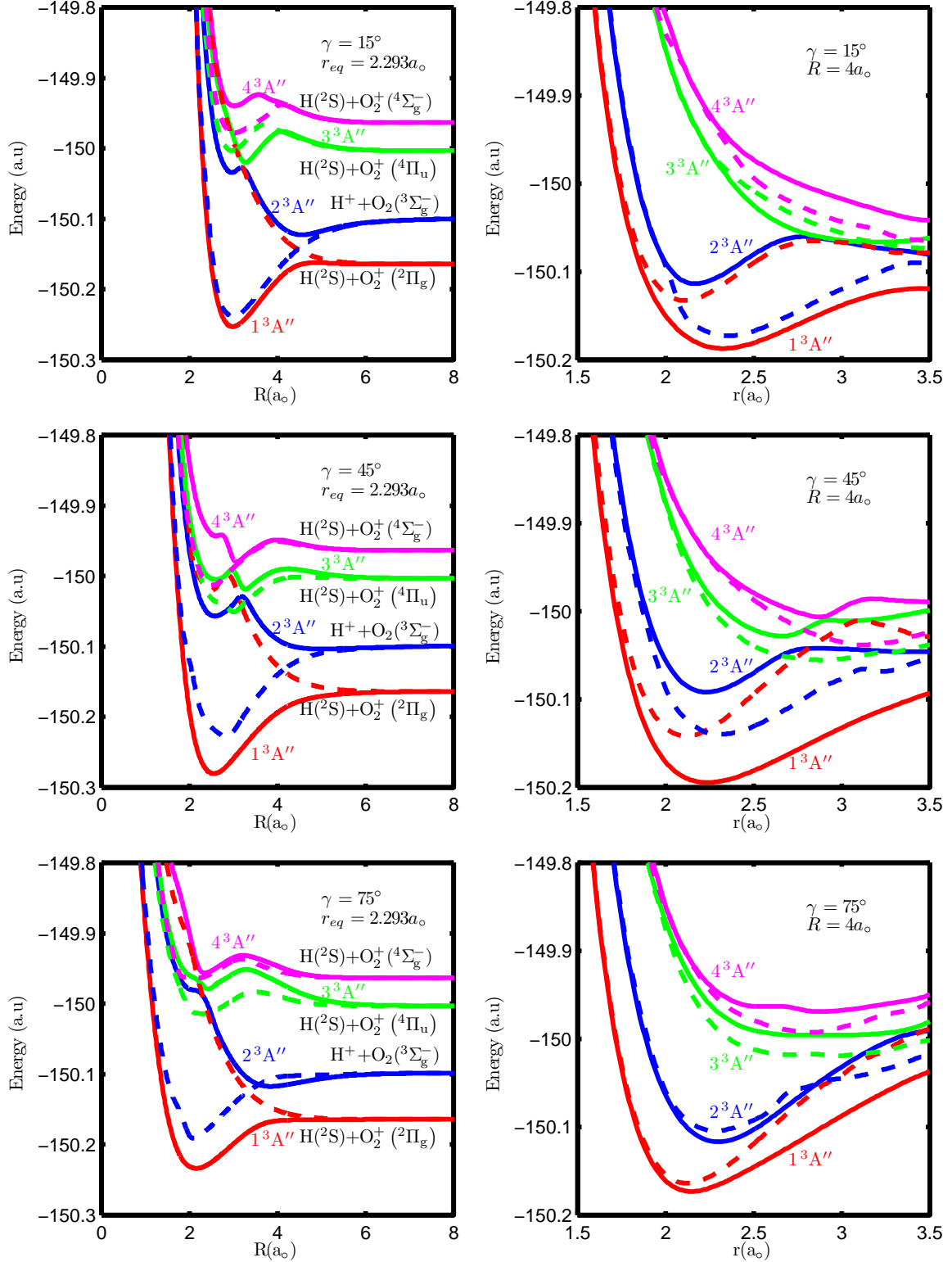


Figure 6.2: *Ab initio* adiabatic (solid line) and quasi-diabatic (dashed line) PECs of GS, first ES, second ES and third ES for $\gamma = 15^\circ, 45^\circ$ and 75° orientations as a function of R (left panel) for a fixed $r = r_{eq} = 2.293a_0$ and as a function of r (right panel) for a fixed $R = 4.0a_0$. Note the presence of various crossings and avoided crossings between the PECs of symmetry ${}^3A''$. The presence of shallow well in the second and third ES PECs as function of R lends support to the second and third charge transfer processes. See text.

The GS PEC correlates to the first VCT channel $H(^2S) + O_2^+(^2\Pi_g)$ and the first ES PEC correlates to the IVE channel, $H^+ + O_2(^3\Sigma_g^-)$. The second and the third ES PECs correlate to second charge transfer channel $H(^2S) + O_2^+(^4\Pi_u)$ and the third charge transfer channel $H(^2S) + O_2^+(^4\Sigma_g^-)$ respectively. In short, in the collinear and perpendicular approach, GS PEC correlates to the IVE channel and in the off-collinear approach of H^+ , it correlates to the first VCT channel. Unlike the collinear and the perpendicular geometries, the four state PECs belonging to off-collinear geometries of $^3A''$ symmetry show Landau-Zener type of coupling (Landau, 1932; Zener, 1932) at lower R values and Rosen-Zener-Demkov type of coupling (Demkov, 1964; Nakamura, 1996; Rosen and Zener, 1932) at higher R values where all PECs run parallel to each other. The Landau-Zener coupling appears to be stronger for $\gamma = 45^\circ$ orientation and occurs around $R = 3.2a_0$ between the first ES and the second ES and at $R = 3.0a_0$ between the second ES and the third ES as a function of R and at $r = 2.7a_0$ between the first ES and the second ES and at $r = 2.9a_0$ between the second ES and the third ES as a function of r . It is shifted to a smaller R and to a higher r for higher γ values, with decreasing coupling strength. In quasi-diabatic PECs of Fig. 6.2 (represented as dashed lines) there are direct curve crossings between the electronic states. All the three ES PECs exhibit long-range shallow well at extended R regions and their depths relative to asymptotic products are summarized in Table 6.2 different γ values. The probability of various processes depend on the depth of these shallow wells which is highest at $\gamma = 15^\circ$ and lowest at both $\gamma = 0^\circ$ and $\gamma = 90^\circ$. The location of well for second VCT process occurs at higher R than that of other two processes. As stated in preceding chapter, first VCT channel is exoergic than the IVE channel by **2.04 eV** and is the most probable VCT channel among all. The second and third VCT channels are endoergic relative to IVE channel by **1.96 eV** and **4.10 eV** respectively. Eventhough endoergic, it still occurs because of the presence of

Table 6.2: The computed well depth and its location in terms of R coordinate for first VCT, $\text{H}^+ + \text{O}_2(\text{X } ^3\Sigma_g^-, v = 0) \longrightarrow \text{H}(^2\text{S}) + \text{O}_2^+(\text{X } ^2\Pi_g, v'')$, second VCT, $\text{H}^+ + \text{O}_2(\text{X } ^3\Sigma_g^-, v = 0) \longrightarrow \text{H}(^2\text{S}) + \text{O}_2^+(\text{X } ^4\Pi_u, v''')$ and third VCT, $\text{H}^+ + \text{O}_2(\text{X } ^3\Sigma_g^-, v = 0) \longrightarrow \text{H}(^2\text{S}) + \text{O}_2^+(\text{X } ^4\Sigma_g^-, v''''')$ process given at $r = r_{eq} = 2.293a_o$ as a function of γ with the data under titles $\text{O}_2^+(^2\Pi_g)$, $\text{O}_2^+(^4\Pi_u)$ and $\text{O}_2^+(^4\Sigma_g^-)$ denoting the well depth in eV. The maximum well depth, its location and the mean well depth for each process is indicated in bold font.

γ	$R(a_o)$	$\text{O}_2^+(^2\Pi_g)$	$R(a_o)$	$\text{O}_2^+(^4\Pi_u)$	$R(a_o)$	$\text{O}_2^+(^4\Sigma_g^-)$
0°	6.8	0.0148	7.00	0.0097	6.80	0.0136
15°	4.6	0.6753	7.07	0.0105	6.70	0.0144
30°	4.8	0.2756	7.15	0.0090	6.68	0.0131
45°	5.0	0.1465	7.33	0.0073	6.58	0.0122
60°	4.6	0.1994	7.51	0.0061	6.45	0.0121
75°	3.8	0.5390	7.62	0.0055	6.33	0.0124
90°	5.8	0.0186	8.00	0.0050	6.20	0.0128
Mean	5.06	0.2670	7.38	0.0076	6.53	0.0129

shallow well in the corresponding PECs.

6.3 *Ab initio* PESs

We present now *ab initio* adiabatic PESs for the four electronic states as function of R and r for the collinear, $\gamma = 0^\circ$ and the perpendicular, $\gamma = 90^\circ$ orientations in Fig. 6.3. As noted above, these two geometries belong to $\text{C}_{\infty v}$ and C_{2v} point groups and hence the spectroscopic designations of the respective electronic states in order of increasing energy will be $1^3\Sigma^-$, $1^3\Pi$, $2^3\Pi$ and $3^3\Pi$ for the $\text{C}_{\infty v}$ and 1^3B_1 , 1^3A_2 , 2^3B_1 and 3^3B_1 in the C_{2v} group at $R \approx 3a_o$. The symmetry labellings can flip as function of R . For example, as seen in Fig. 6.3 at $R = 8a_o$, the order will be $1^3\Pi$, $1^3\Sigma^-$, $2^3\Pi$ and $3^3\Pi$ and 1^3A_2 , 1^3B_1 , 2^3B_1 and 3^3B_1 , respectively. The GS PES correlates to inelastic channel (IVE), $\text{H}^+ + \text{O}_2(\text{X } ^3\Sigma_g^-, v = 0) \longrightarrow \text{H}^+ + \text{O}_2(\text{X } ^3\Sigma_g^-, v')$, and the first ES PES correlates to the first vibrational charge transfer channel (VCT), $\text{H}^+ + \text{O}_2(\text{X } ^3\Sigma_g^-, v = 0) \longrightarrow \text{H}(^2\text{S}) +$

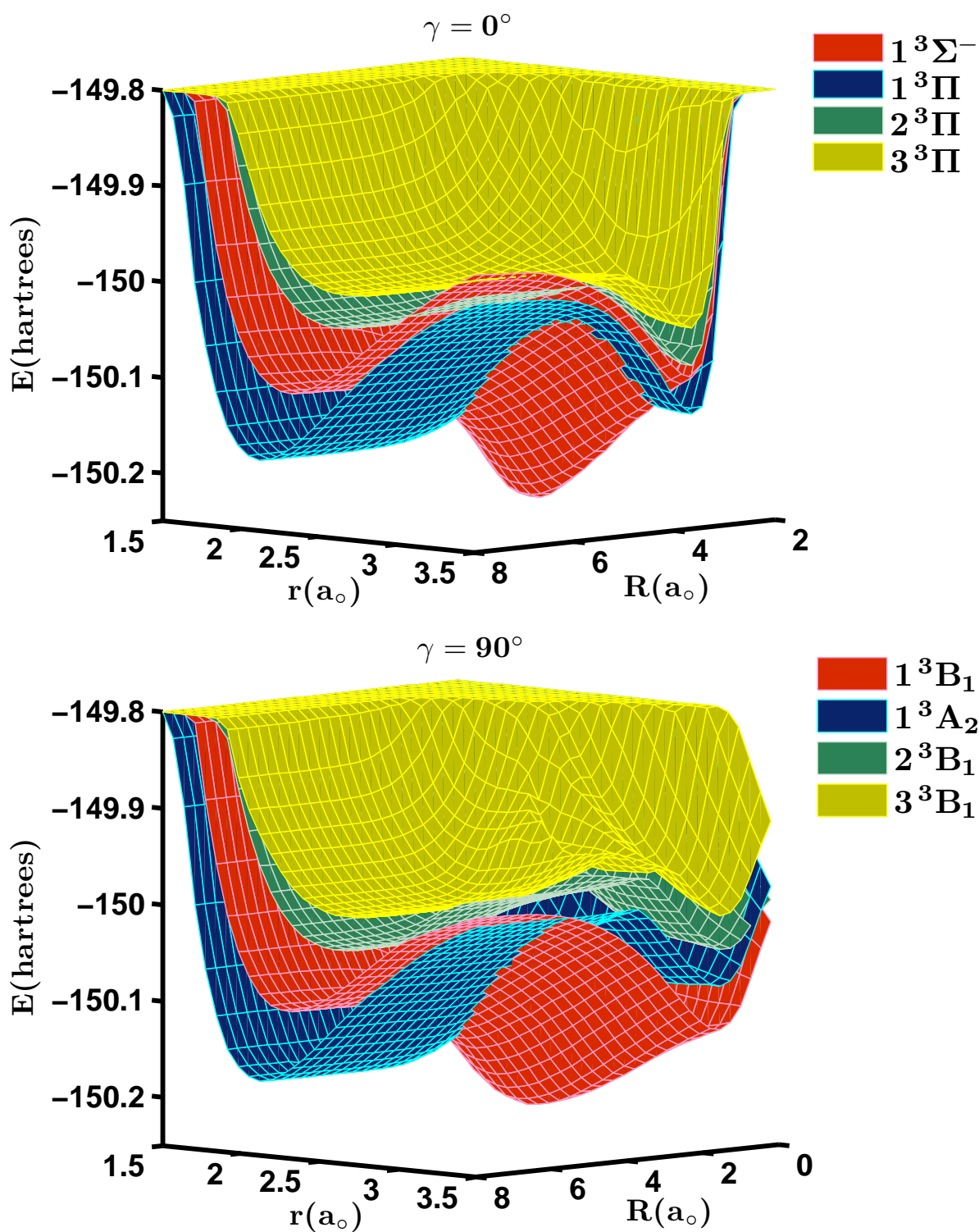


Figure 6.3: *Ab initio* adiabatic PESs for $\gamma = 0^\circ$ and $\gamma = 90^\circ$ as a function of r and R . The symmetry labelling differs due to the point group difference, $C_{\infty v}$ and C_{2v} , respectively. Note that there is direct surface crossing between the GS PES and first ES PES which are of different symmetry in both cases.

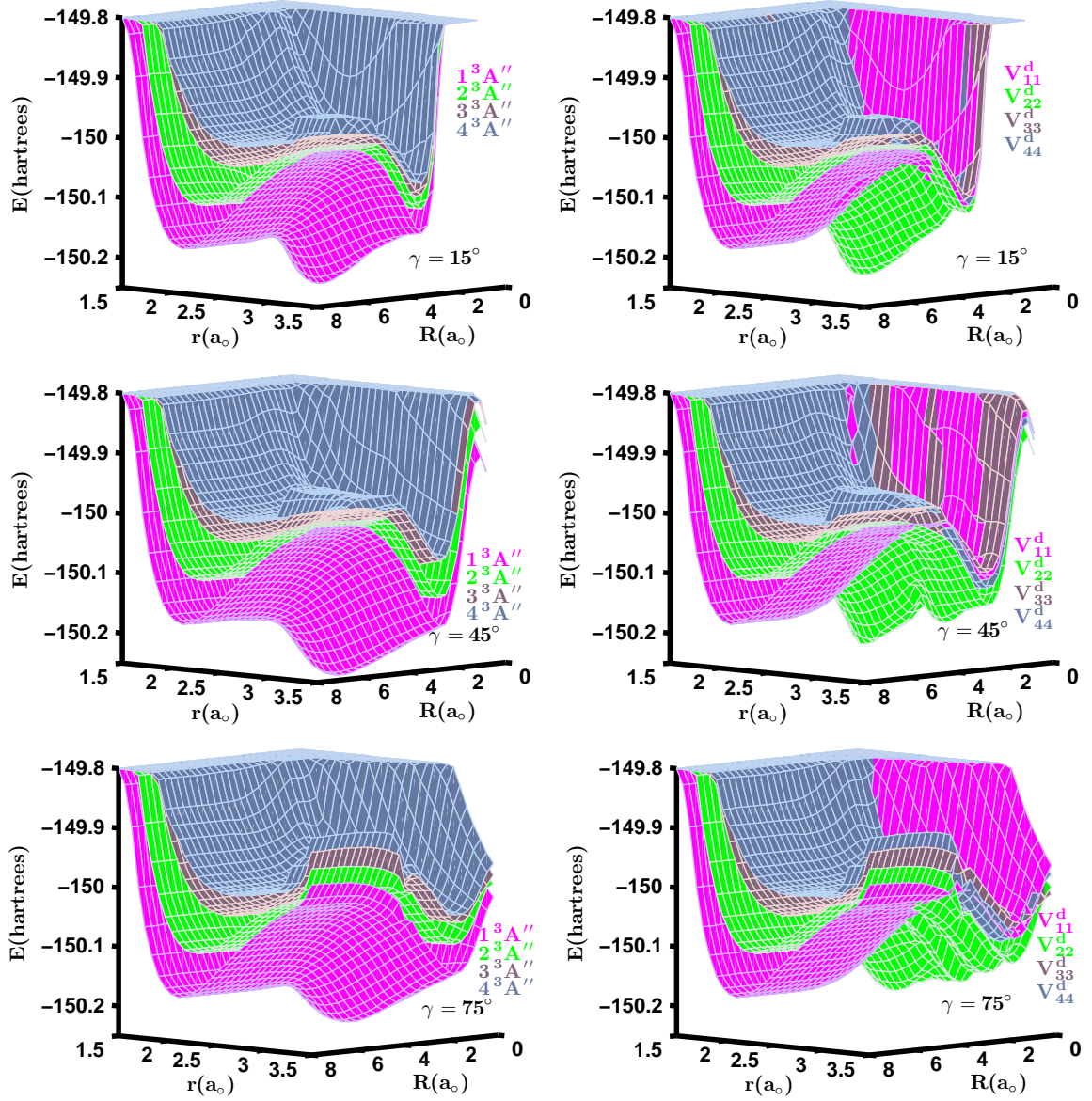


Figure 6.4: *Ab initio* adiabatic (left panel) and quasi-diabatic (right panel) PESs for $\gamma = 15^\circ, 45^\circ, 75^\circ$ as a function of r and R for four low lying electronic states of symmetries, $1^3A'', 2^3A'', 3^3A''$ and $4^3A''$ respectively. Note that there is a direct crossing of two low lying surfaces of same symmetry, $3^3A''$.

$O_2^+(X^2\Pi_g, v'')$. The second and third ES PESs correlates to second charge transfer channel, $H^+ + O_2(X^3\Sigma_g^-, v = 0) \longrightarrow H(^2S) + O_2^+(X^4\Pi_u, v''')$ and third charge transfer channel, $H^+ + O_2(X^3\Sigma_g^-, v = 0) \longrightarrow H(^2S) + O_2^+(X^4\Sigma_g^-, v''''')$ respectively.

For the off-collinear geometries (C_s point group) such as $\gamma = 15^\circ, 30^\circ, 45^\circ, 60^\circ, 75^\circ$, the symmetry labels for the four electronic states at $R \approx 3a_0$ are $1^3A'', 2^3A'', 3^3A''$ and

$4^3A''$, and they are shown in Fig. 6.4 as a function of R and r for $\gamma = 15^\circ$, $\gamma = 45^\circ$ and $\gamma = 75^\circ$. Asymptotic correlation remain the same here as for the collinear and perpendicular

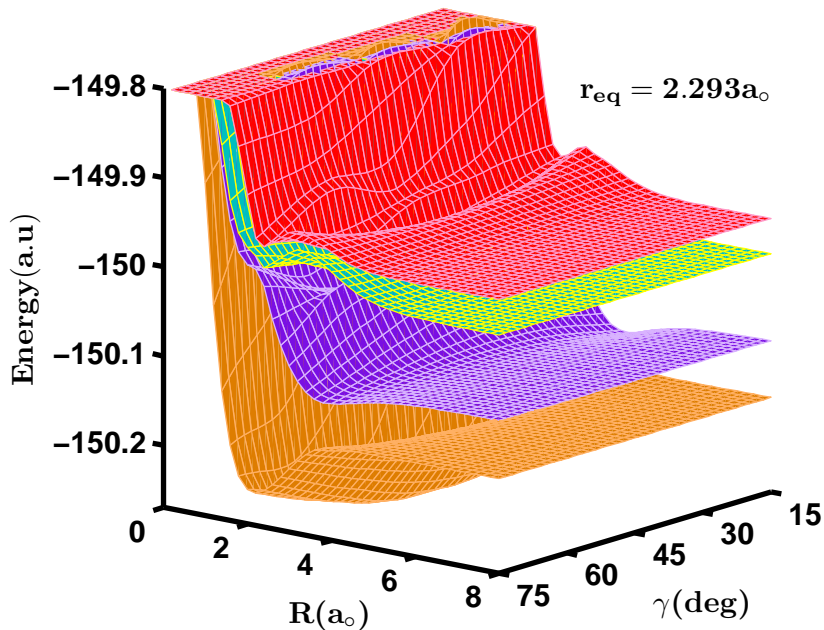


Figure 6.5: *Ab initio* adiabatic GS, first ES PES, second ES PES and third ES PES as a function of γ and R at $r = r_{eq} = 2.293a_0$. Note the large energy gap between the first ES and second ES PES.

approaches, with each state correlating to either ground or excited states of O_2 and O_2^+ . Note that in Fig. 6.4, the adiabatic PESs are shown in the left panel while those of the quasi-diabatic PESs are displayed in the right panel. There is an avoided crossing in the adiabatic GS PES and first ES PES in all the three orientations which turn into direct surface crossing in the quasi-diabatic case as is visible from the Fig.6.4 (right panel). The extent of interaction can be judged from the study of properties such as coupling potential and NACME etc. which will be discussed in the following section.

In Fig. 6.5, *ab initio* adiabatic GS, first ES, second ES and third ES PESs as a function of γ and R at $r = r_{eq} = 2.293a_0$ are shown. Except GS PES, first, second and third ES PES are repulsive in nature and kind of interaction among them is clearly visible from the

small hump like structure existing at smaller R values. At large R , all the four PESs remain almost flat. One last feature worth mentioning is that generally ES PESs quickly falls off and become flat in Jacobi plane (R, r) than the GS PES because the GS PES has been separated far away from the ES PESs energetically.

6.4 Coupling PESs and NACME

Now we present the coupling potentials (V_{mn}^d) (d stands for the diabatic (potential) and m and n denote the different or same electronic states) and the NACME values as a function of R and r for $\gamma = 15^\circ, 45^\circ$ and 75° . The coupling potentials and the NACME values for the GS and the first ES have already been discussed in the preceding chapter. Here, we first present the coupling potential between the GS and the second ES (V_{13}^d) and the same between the GS and the third ES (V_{14}^d) in Fig. 6.6. For the coupling of the GS with the first, the second and third ESs we can make the following observation that, barring the regions of very small R with highly compressed or enlarged r , their magnitudes generally follow the following trend : $V_{12}^d > V_{13}^d > V_{14}^d$. V_{12}^d is displayed in Fig. 5.7. This suggests that the effect of the second and third ESs coupling with GS would be comparatively small. Similarly, from Fig. 6.7, we observe that in general, $V_{23}^d > V_{24}^d$. V_{34}^d is displayed in Fig. 6.8(left panel) and as an illustration we have also shown the corresponding NACME in Fig. 6.8(right panel). In Fig. 6.9, the same has been plotted as a function of R and r at $r = r_{eq}$. Interestingly, the magnitudes of V_{34}^d are relatively smaller implying that the coupling between second and third ESs is comparatively smaller.

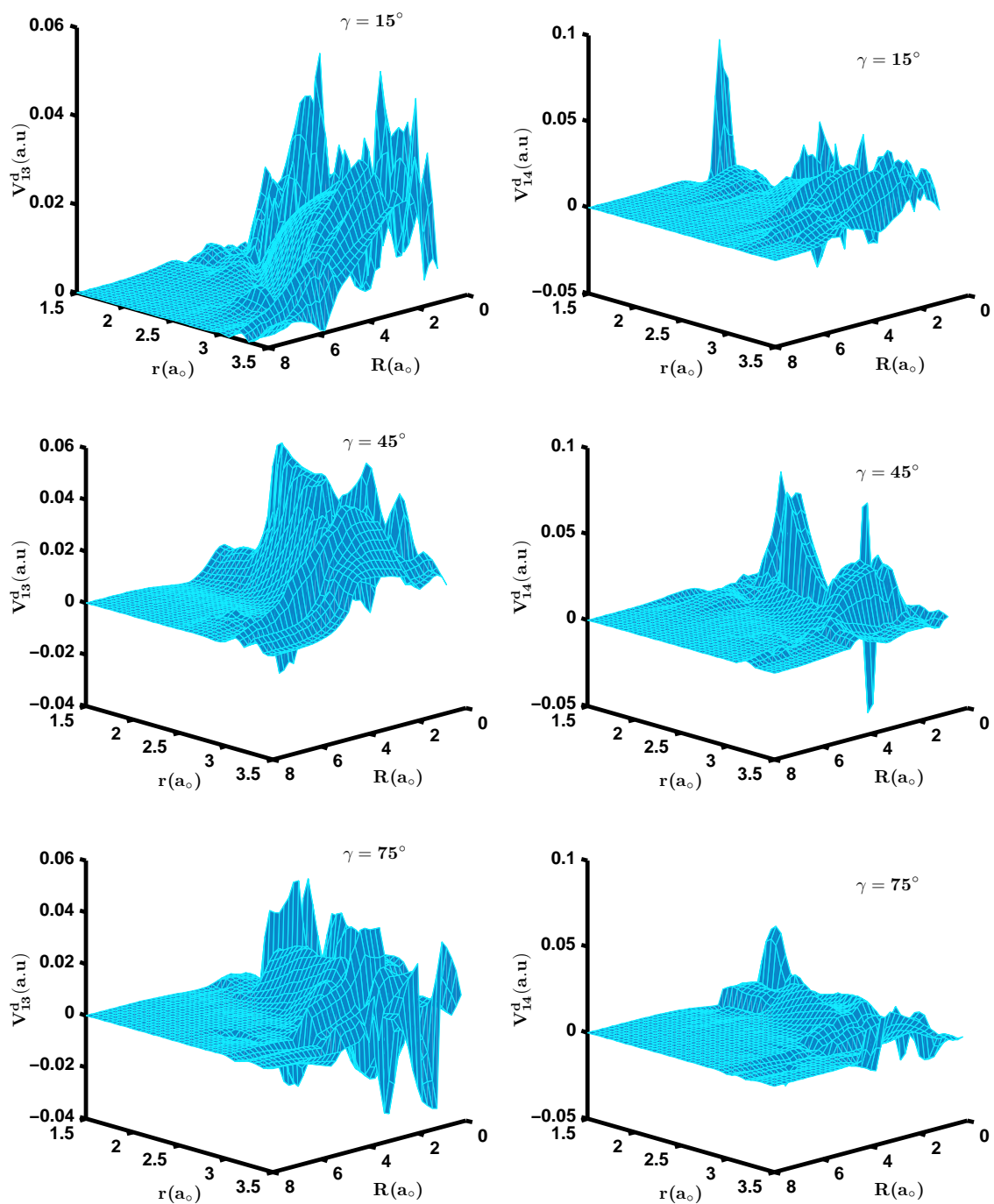


Figure 6.6: Coupling between GS and second ES PESs (left panel) and coupling between GS and third ES PESs (right panel) as a function of R and r for $\gamma = 15^\circ, 45^\circ, 75^\circ$.

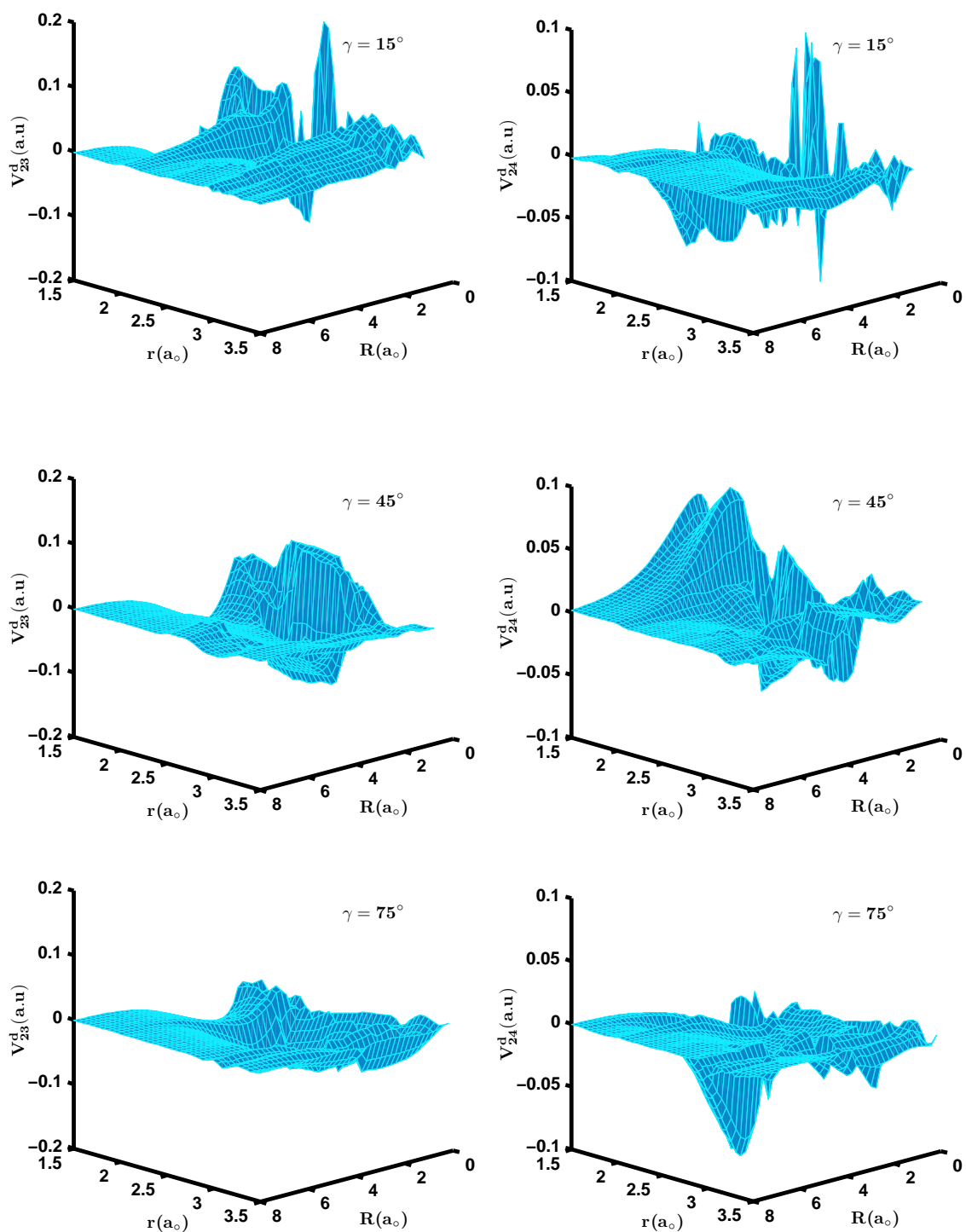


Figure 6.7: Coupling between first ES and second ES PESs (left panel) and coupling between first ES and third ES PESs (right panel) as a function of R and r for $\gamma = 15^\circ, 45^\circ, 75^\circ$.

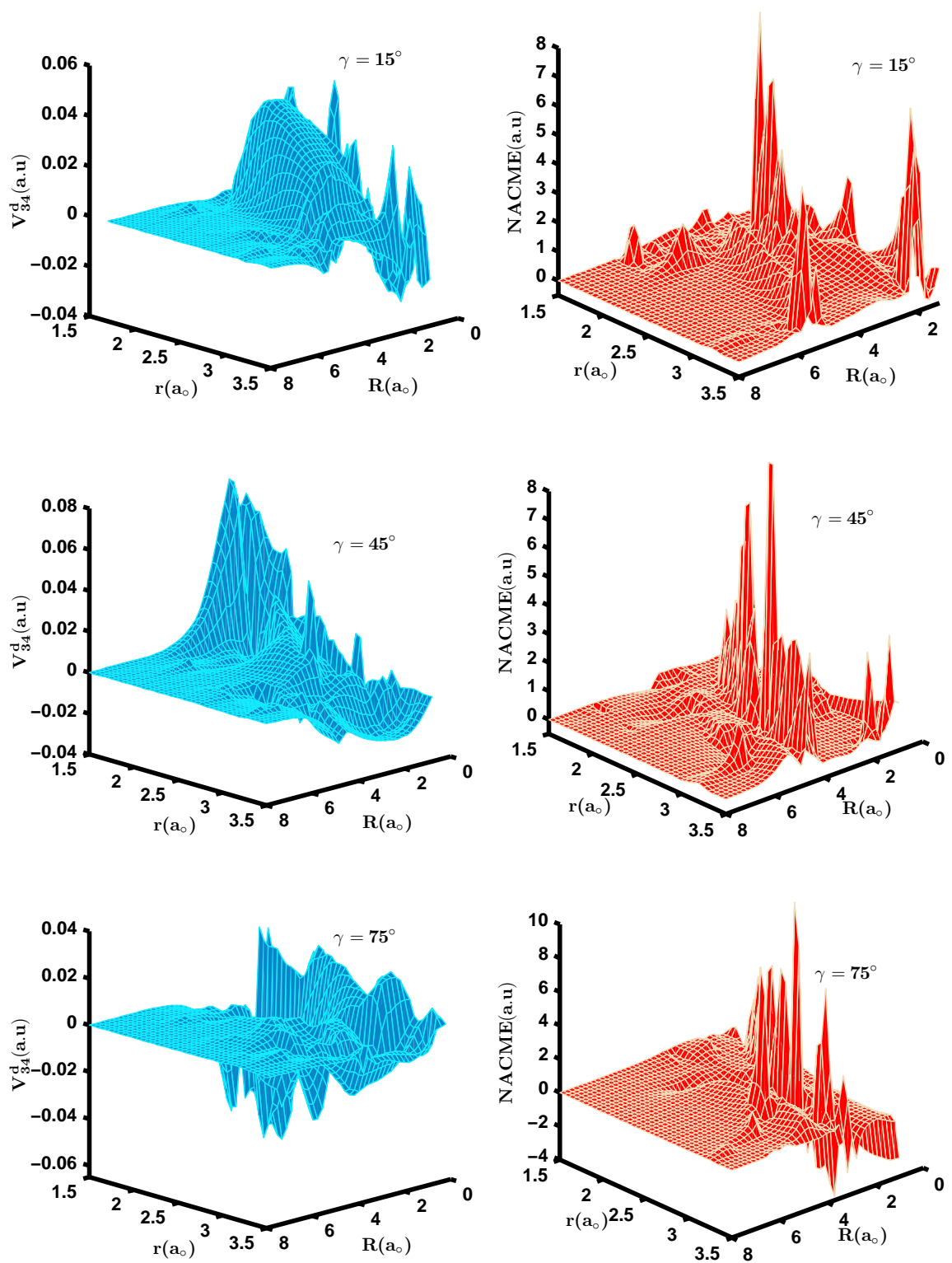


Figure 6.8: Coupling between second and third ES PESs (left panel) and NACME between second and third ES PESs (right panel) as a function of R and r for $\gamma = 15^\circ, 45^\circ, 75^\circ$.

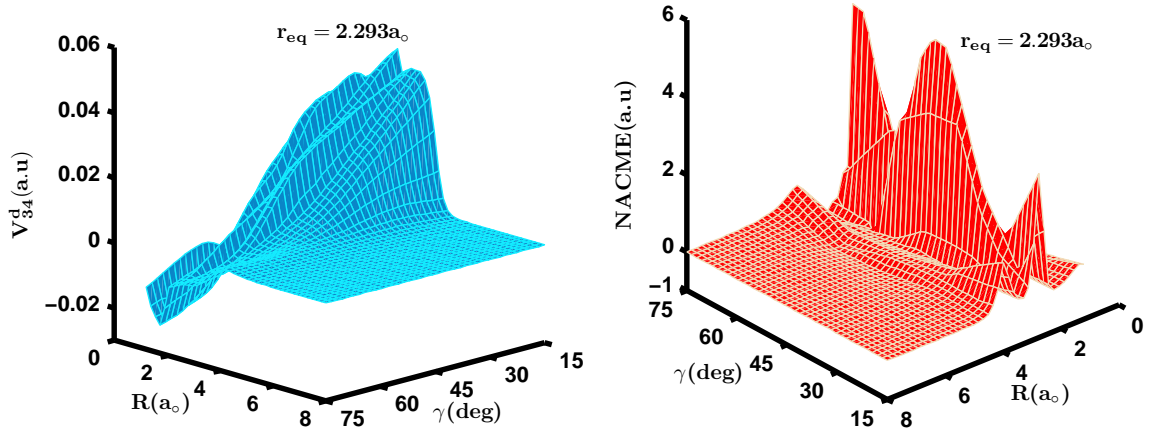


Figure 6.9: Coupling between second and third ES PESs (left) and NACME between second and third ES PESs (right) as a function of R and γ for $r = r_{eq} = 2.293a_0$.

6.5 Vibrational coupling matrix elements ($V_{v'v''}/v''''(R; \gamma)$)

The angular dependent vibrational coupling matrix elements (VCME) for second VCT channel ($V_{0v''''}$) (left panel) $\text{H}^+ + \text{O}_2(\text{X } ^3\Sigma_g^-, v = 0) \longrightarrow \text{H}(^2\text{S}) + \text{O}_2^+(\text{X } ^4\Pi_u, v''')$ and the third VCT ($V_{0v''''}$) channel (right panel) $\text{H}^+ + \text{O}_2(\text{X } ^3\Sigma_g^-, v = 0) \longrightarrow \text{H}(^2\text{S}) + \text{O}_2^+(\text{X } ^4\Sigma_g^-, v''''')$ are presented in Fig.6.10 as a function of R computed using asymptotically extended *ab initio* PESs upto $R = 50a_0$, *ab initio* PECs and vibrational energy level (lowest 20 levels) of diatomic molecules $\text{O}_2(^3\Sigma_g^-)$, $\text{O}_2^+(^2\Pi_g)$, $\text{O}_2^+(^4\Pi_u)$ and $\text{O}_2^+(^4\Sigma_g^-)$. Actually, it is the coupling of vibrational mode of the incoming H^+ along the reaction coordinate with the vibrational mode of O_2 and is defined as $V_{v'v''}/v''''(R; \gamma) = \langle \chi_{v'}(r) | V^{in}(R, r, \gamma) | \chi_{v''}/v''''(r) \rangle$, where $V^{in}(R, r, \gamma) = V(R, r, \gamma) - V(R = \infty, r, \gamma)$ with the superscript *in* meant for interaction potential and $\chi_{v'}(r)$ and $\chi_{v''}/v''''(r)$ are the wavefunction of diatoms of $\text{O}_2(^3\Sigma_g^-)$, $\text{O}_2^+(^2\Pi_g)$, $\text{O}_2^+(^4\Pi_u)$ and $\text{O}_2^+(^4\Sigma_g^-)$ as a function of r and is computed for each value of γ over a fine mesh of r . The matrix containing VCMEs for different vibrational states is

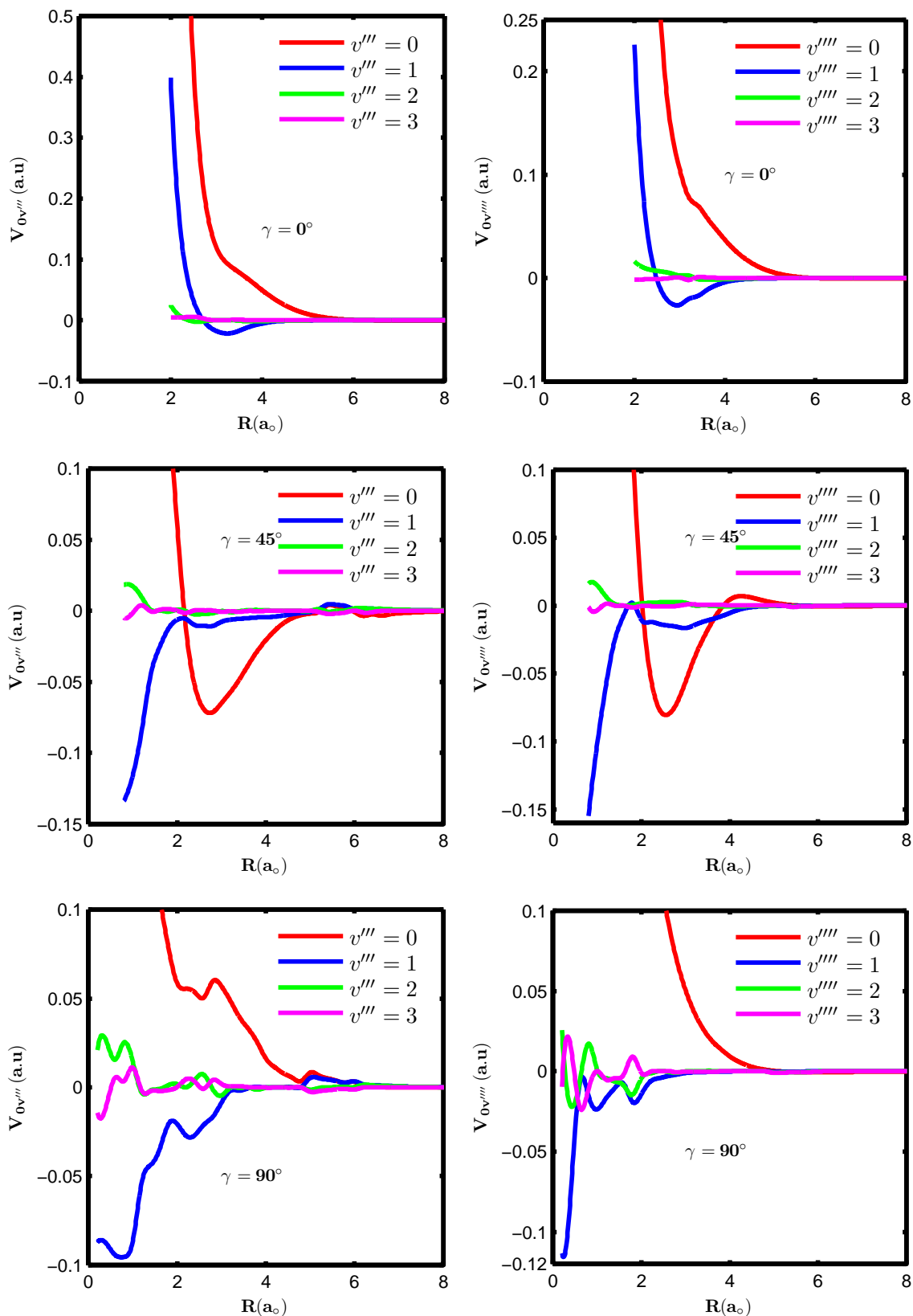


Figure 6.10: The vibrational coupling matrix elements as a function of R for $\gamma = 0^\circ, \gamma = 45^\circ$ and $\gamma = 90^\circ$ orientations for the second VCT ($V_{0v'''}(a.u.)$) channel $H^+ + O_2(X^3\Sigma_g^-, v = 0) \rightarrow H(2S) + O_2^+(X^4\Pi_u, v''')$ (left panel) and the third VCT ($V_{0v'''}(a.u.)$) channel $H^+ + O_2(X^3\Sigma_g^-, v = 0) \rightarrow H(2S) + O_2^+(X^4\Sigma_g^-, v''')$ (right panel).

symmetric matrix and size is 20×20 and it is R dependent. We will concentrate on the magnitude of these matrix elements as a function of R for different γ and is presented in Fig.6.10. The magnitudes of second and third VCT processes are always lesser than first VCT process, $\text{H}^+ + \text{O}_2(\text{X}^3\Sigma_g^-, v = 0) \longrightarrow \text{H}(^2\text{S}) + \text{O}_2^+(\text{X}^2\Pi_g, v'')$, and hence incoming H^+ couples more strongly with the first VCT process rather than second or third VCT process. The order of coupling with different vibrational energy levels of O_2^+ species remain independent of angular approach of projectile H^+ and follows $v'''/v'''' = 0 > 1 > 2 > 3$. In the collinear approach the coupling is the strongest and is reduced to about 50% from second VCT to third VCT and for off-collinear and perpendicular approach the magnitudes are similar in both the cases. This suggests that collinear geometry is most favoured geometry for second and third VCT processes compared to the other two geometries. It is zero for all practical purposes for all γ after $R = 8a_0$. The VCMEs for $v'''/v'''' = 2, 3$ goes to zero very quickly at about $R \approx 3a_0$ than $v'''/v'''' = 0, 1$ which falls to zero at around $R \approx 6a_0$. The $v'''/v'''' = 0$ coupling in each case tends to a high value as R decrease relative to other coupling $v'''/v'''' = 1, 2, 3 \dots$

6.6 Quantum dynamics

The quantum dynamics was performed under the VCC-RIOSAs approach at $E_{cm} = 9.5$ eV and at $E_{cm} = 23$. 20 vibrational levels each of $\text{O}_2(\text{X}^3\Sigma_g^-)$, $\text{O}_2^+(\text{X}^2\Pi_g)$, $\text{O}_2^+(\text{X}^4\Pi_u)$, and $\text{O}_2^+(\text{X}^4\Sigma_g^-)$ species were included in the vibrational close-coupling equations which were solved (with $\mathbf{J} = 0$) by the sixth-order Numerov method for 7 equally spaced γ values between 0° and 90° for each partial wave (l) to obtain the scattering properties at these two collision energies. We focus only on the IVE and first VCT channel even though second

and third VCT channels can be studied which we do not due to the absence of experimental information.

6.6.1 Dynamics at $E_{cm}=9.5$ eV

In this section, we compare the computed dynamical quantities with those of the experimental results (Gianturco, Gierz, and Toennies, 1981). The state-to-state experimental data are available only for the IVE process at collision energy $E_{cm} = 9.5$ eV. We have computed the various dynamical properties at this energy using the 4×4 coupled PESs and compared them with those available from the experiments. There does not seem to be any quantum dynamical study at this collision energy.

6.6.1.1 The orientation opacities

The VCC-RIOSAs angle-dependent opacity function as defined in Eq. (3.34) in **chapter 3** is shown in Fig. 6.11 as a function of partial waves (l) (in the units of \hbar). For the IVE channel (left panel), $H^+ + O_2(v = 0) \longrightarrow H^+ + O_2(v')$ they have been shown for $\gamma = 0^\circ$, $\gamma = 45^\circ$ and $\gamma = 90^\circ$. For $\gamma = 0^\circ$ and $\gamma = 90^\circ$, there is no radial coupling between the IVE and the VCT channels, and therefore, there are no VCT excitations. The opacities are shown for the first VCT channel, $H^+ + O_2(v = 0) \longrightarrow H(^2S) + O_2^+(v'')$ for $\gamma = 15^\circ$, $\gamma = 45^\circ$ and $\gamma = 75^\circ$ orientations (right panel). The steric dependent opacity function speaks about the amount of excitation of different vibrational states of O_2 and O_2^+ target molecules during the collisions as the formula for opacity function, Eq. (3.34), involves the squaring of the steric dependent T-matrix elements. By just looking at Fig. 6.11, it is easy to conclude that the amount of vibrational excitation differs greatly from the IVE channel to the first VCT

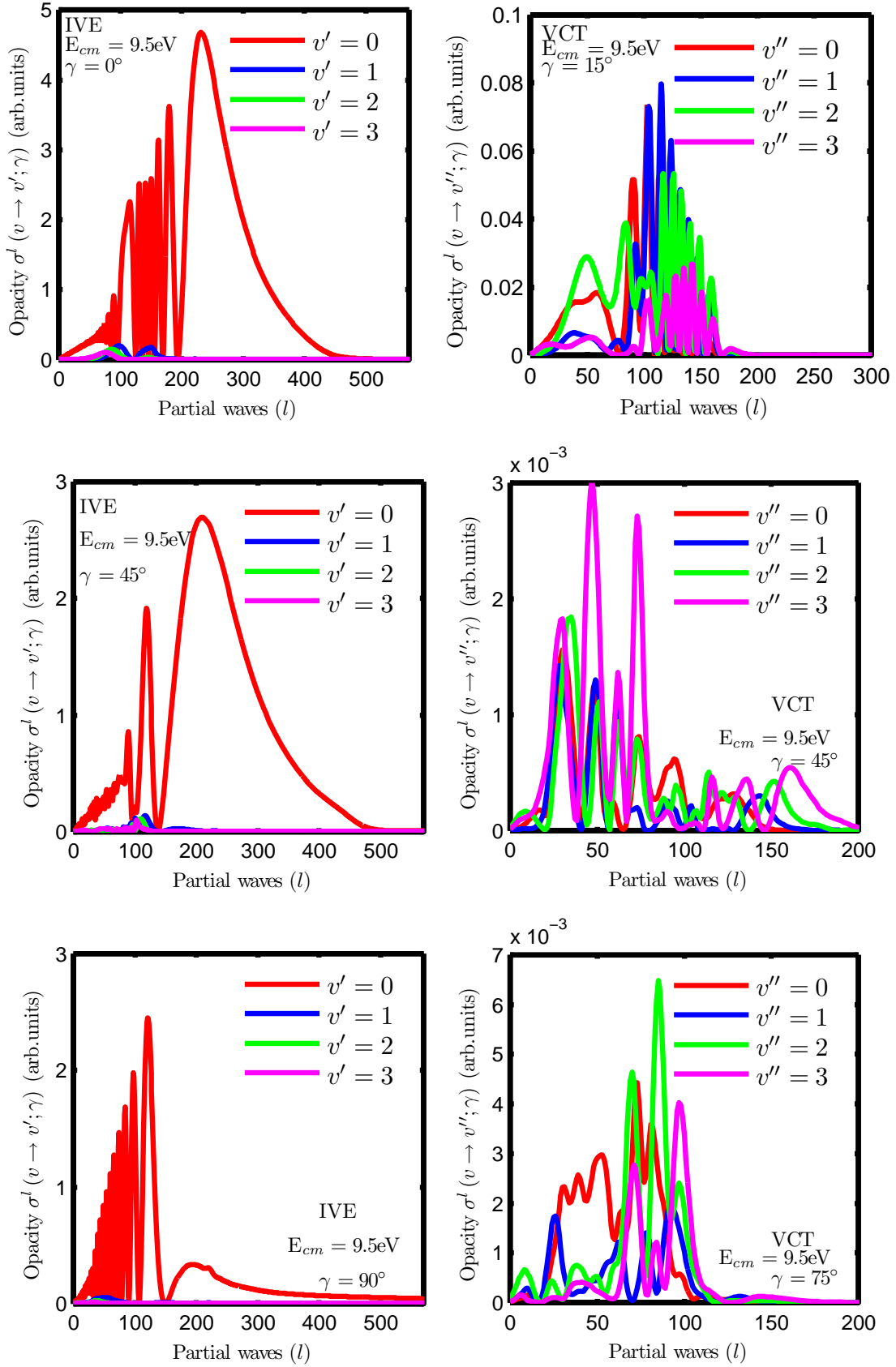


Figure 6.11: The opacity function as a function of partial waves (l , in the units of \hbar) for $\gamma = 0^\circ, \gamma = 45^\circ$ and $\gamma = 90^\circ$ orientations for the IVE channel, $\text{H}^+ + \text{O}_2(\text{X}^3\Sigma_g^-, v = 0) \rightarrow \text{H}^+ + \text{O}_2(\text{X}^3\Sigma_g^-, v')$ (left panel) and for $\gamma = 15^\circ, \gamma = 45^\circ$ and $\gamma = 75^\circ$ orientations for the first VCT channel, $\text{H}^+ + \text{O}_2(\text{X}^3\Sigma_g^-, v = 0) \rightarrow \text{H}(^2\text{S}) + \text{O}_2^+(\text{X}^2\Pi_g, v'')$ (right panel) at $E_{cm} = 9.5 \text{ eV}$.

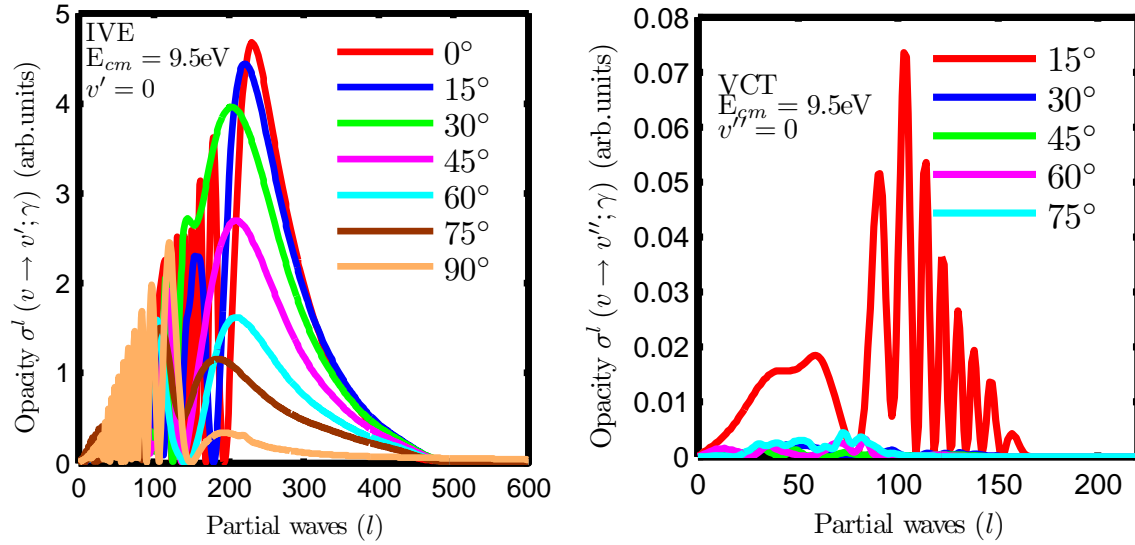


Figure 6.12: The comparison of opacity function among all the molecular orientations for the elastic collisions for the IVE channel $\text{H}^+ + \text{O}_2(\text{X}^3\Sigma_g^-, v = 0) \longrightarrow \text{H}^+ + \text{O}_2(\text{X}^3\Sigma_g^-, v')$ (left) and for first charge transfer collisions for the first VCT channel $\text{H}^+ + \text{O}_2(\text{X}^3\Sigma_g^-, v = 0) \longrightarrow \text{H}^{(2)\text{S}} + \text{O}_2^+(\text{X}^2\Pi_g, v'')$ (right) at $E_{cm} = 9.5 \text{ eV}$.

channel. It is being more than 1000 times higher for the IVE channel than for the first VCT channel, especially for $\gamma = 45^\circ$ and $\gamma = 75^\circ$ orientations. It also leads us to conclude that elastic collisions ($v = 0 \rightarrow v' = 0$) remains the most abundant of all the collisions for all the approaches. Considering the magnitudes of the opacities, we arrange the following order of vibrational excitation in the IVE channel : $v = 0 \rightarrow v' = 0 > v = 0 \rightarrow v' = 1 > v = 0 \rightarrow v' = 2 > v = 0 \rightarrow v' = 3$. The amount of elastic excitation decreases from $\gamma = 0^\circ$ to $\gamma = 90^\circ$ with collinear approach of H^+ ion favouring the elastic excitation more than the off-collinear approaches. The opacity function is converged only when the number of contributing partial waves ($l\hbar$) reaches 500 while for the VCT channel this value is just around $l \approx 200$, indeed, less number of partial waves needed to get convergence. The order of vibrational excitation is quite different in the VCT channel and is given for $\gamma = 15^\circ$ in the decreasing order of excitation for $v = 0 \rightarrow v'' = 1 > v = 0 \rightarrow v'' = 2 > v = 0 \rightarrow v'' = 0 > v = 0 \rightarrow v'' = 3$. For $\gamma = 45^\circ$ and $\gamma = 90^\circ$, there are not much oscillations in the

opacity function and order of excitation is different from what is given above for $\gamma = 15^\circ$. In the IVE process, elastic excitation is the most dominant process while in the VCT process, $v = 0 \rightarrow v'' = 1$, $v = 0 \rightarrow v'' = 3$ and $v = 0 \rightarrow v'' = 2$ excitation are the most dominant ones in $\gamma = 15^\circ$, $\gamma = 45^\circ$ and $\gamma = 75^\circ$ respectively. In Fig. 6.12, we show the comparison of opacity function of elastic, $v = 0 \rightarrow v' = 0$ (left) and first VCT, $v = 0 \rightarrow v'' = 0$ (right) process for all orientations and it is readily seen that the opacity for elastic process decreases gradually from $\gamma = 0^\circ$ to $\gamma = 90^\circ$ and vanishes to zero at about 600 partial waves, whereas, the same for first VCT process is relatively very high for $\gamma = 15^\circ$ and less for other orientations and vanishes to zero at about 200 partial waves. The magnitude of opacity is higher in IVE process than the VCT process as usual.

6.6.1.2 Rotationally-summed state-selective differential cross section (DCS)

The total differential cross section (TDCS) and state-selective differential cross sections (DCS) have been computed as a function of scattering angle θ_{cm} in center of mass (cm) frame of reference at the collision energy of $E_{cm} = 9.5$ eV, for the IVE channel, $\text{H}^+ + \text{O}_2(\text{X}^3\Sigma_g^-, v = 0) \longrightarrow \text{H}^+ + \text{O}_2(\text{X}^3\Sigma_g^-, v')$ and the VCT channel, $\text{H}^+ + \text{O}_2(\text{X}^3\Sigma_g^-, v = 0) \longrightarrow \text{H}(^2\text{S}) + \text{O}_2^+(\text{X}^2\Pi_g, v'')$ by employing the 4×4 coupled PESs. As discussed earlier in **section 5.7**, we report only such smoothed TDCS and state-selective DCSs in Fig. 6.13 for the IVE process (left) as well as the first VCT process (right) upto $v'(v'') = 5$. available for the TDCS and the state-to-state DCSs to be compared with the theoretical results at this collision energy. The TDCS computed by summing up the state-to-state DCSs upto 20 vibrational states of $\text{O}_2(^3\Sigma_g^-)$ and $\text{O}_2^+(^2\Pi_g)$ have been shown (red) lying above the state-to-state DCSs in both the channels. In the IVE channel, the TDCS and DCS for the elastic process, $v' = 0$, (blue) run parallel to each other with hardly any numerical differences till

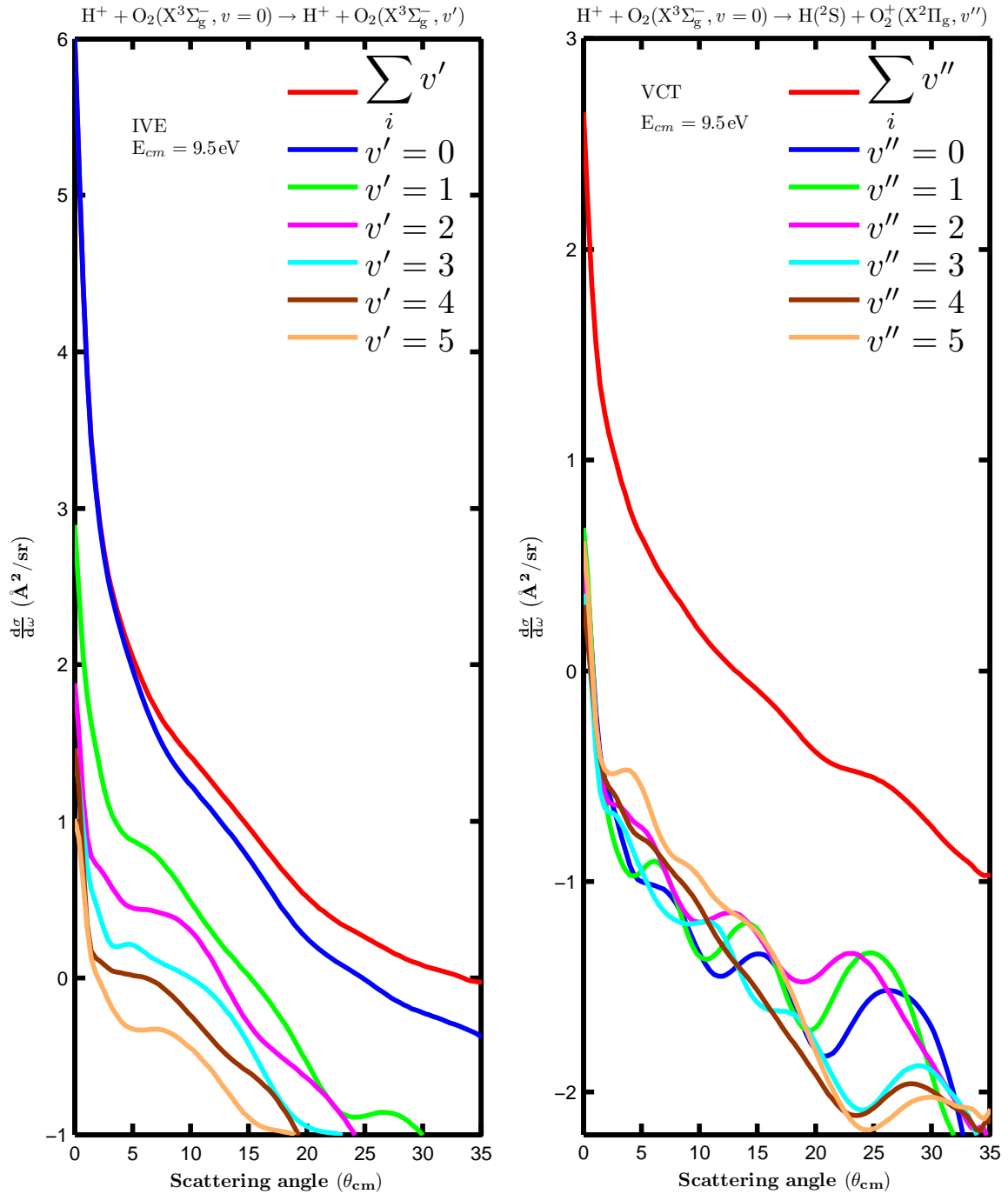


Figure 6.13: Rotationally-summed differential cross section (TDCS) and rotationally-summed state-to-state DCS as function of θ_{cm} for the IVE channel $\text{H}^+ + \text{O}_2(\text{X}^3\Sigma_g^-, v = 0) \longrightarrow \text{H}^+ + \text{O}_2(\text{X}^3\Sigma_g^-, v')$ (left) and for the first VCT channel $\text{H}^+ + \text{O}_2(\text{X}^3\Sigma_g^-, v = 0) \longrightarrow \text{H}(^2\text{S}) + \text{O}_2^+(\text{X}^2\Pi_g, v'')$ (right) at $E_{cm} = 9.5$ eV. The number in the ordinate indicate the powers of 10. There are no experimental data available to compare with theoretical results at this collision energy.

$\theta_{cm} \approx 7^\circ$ while in the VCT case, former is highly separated from the later throughout the entire range of scattering angle (θ_{cm}). The primary rainbow maximum in the TDCS curve which appeared at $\theta_{cm} \approx 12^\circ$ in the IVE channel in the two-state quantum dynamical model in **subsection 5.7.1.2** is now appeared quenched very much in the four-state quantum dynamics because of the influence of including two more ES PESs in the calculations. Similar is the case with VCT channel too wherein a strong primary rainbow structure was seen at $\theta_{cm} \approx 14.5^\circ$ in the two-state quantum dynamical computation. The quenching of rainbow in four-state calculation may be the result of competition among the three possible VCT processes and the dominance of elastic excitation during the scattering events. The presence of rainbow maxima feature, though of less intense, in the TDCS curve is the result of the appearance of the same feature in the state-to-state DCS in both the channels. The individual curves are laid out in the order starting from $v' = 0$ to $v' = 5$ one below one in Fig. 6.13 in the IVE channel (left) and their lay out in terms of decreasing DCS values are given as follows : $v' = 0 > v' = 1 > v' = 2 > v' = 3 > v' = 4 > v' = 5$. All the curves show monotonic decrease with scattering angle which is rather steep in the region upto $\theta_{cm} \approx 8^\circ$ and somewhat flatter at higher scattering angles. The individual curves in the VCT channel are laid out in a way different from IVE channel and the ordering of curves is given as $v'' = 2 > v'' = 1 > v'' = 0 > v'' = 3 > v'' = 5 > v'' = 4$ and at $\theta_{cm} = 0^\circ$, this ordering looks different from the above : $v'' = 1 > v'' = 5 > v'' = 0 > v'' = 2 > v'' = 3 > v'' = 4$. The TDCS drops sharply below $\theta_{cm} < 10^\circ$ and running almost flat with little variations after that and state-to-state DCS falls sharply below $\theta_{cm} < 3^\circ$ and then all of them runs closely spaced with oscillations.

6.6.1.3 Transition Probability

The relative state-to-state transition probability for IVE process, $P_{0 \rightarrow v'}(\theta_{cm})$ and for VCT process, $P_{0 \rightarrow v''}(\theta_{cm})$ have been computed as a function of scattering angle (θ_{cm}) from their respective state-to-state DCS values using the set of formulas given in Eq. (6.1).

$$P_{0 \rightarrow v'}(\theta_{cm}) = \frac{\left. \frac{d\sigma}{d\omega}(0 \rightarrow v') \right|_{\theta_{cm}}}{\sum_{v'=0}^{v_{max}} \left. \frac{d\sigma}{d\omega}(0 \rightarrow v') \right|_{\theta_{cm}}} \quad (6.1)$$

$$P_{0 \rightarrow v''}(\theta_{cm}) = \frac{\left. \frac{d\sigma}{d\omega}(0 \rightarrow v'') \right|_{\theta_{cm}}}{\sum_{v''=0}^{v_{max}} \left. \frac{d\sigma}{d\omega}(0 \rightarrow v'') \right|_{\theta_{cm}}}$$

The denominator involves the summation over state-to-state DCSs upto 20 vibrational states of $O_2(^3\Sigma_g^-)$ and $O_2^+(^2\Pi_g)$ molecules and the numerator involves the state-to-state DCS as a function of scattering angle (θ_{cm}) for a specific vibrational state and the division between the two gives us the relative state-to-state transition probability for the IVE and the first VCT channel. The transition probabilities for both the channels have been shown in Fig. 6.14 for the first five vibrational states along with the experimental data (Gianturco, Gierz, and Toennies, 1981) for the IVE channel alone. In the case of first VCT channel, where there is no experimental data available to compare with the theory. $P_{0 \rightarrow v''}(\theta_{cm})$ for the entire range of θ_{cm} for first five vibrational excitations in $O_2^+(^2\Pi_g)$ ion does not exceed 0.2 and almost all the excitations the order of excitation reflects the listing of favourable excitation and have been given in decreasing order of transition probability magnitude as $v = 0 \rightarrow v'' = 2 > v = 0 \rightarrow v'' = 1 > v = 0 \rightarrow v'' = 0 > v = 0 \rightarrow v'' = 3 > v = 0 \rightarrow v'' = 4$ and the most dominant excitation is found to be $v = 0 \rightarrow v'' = 2$, contrary to our expectations $v = 0 \rightarrow v'' = 0$. The probability ratio of most dominant VCT process to elastic process is

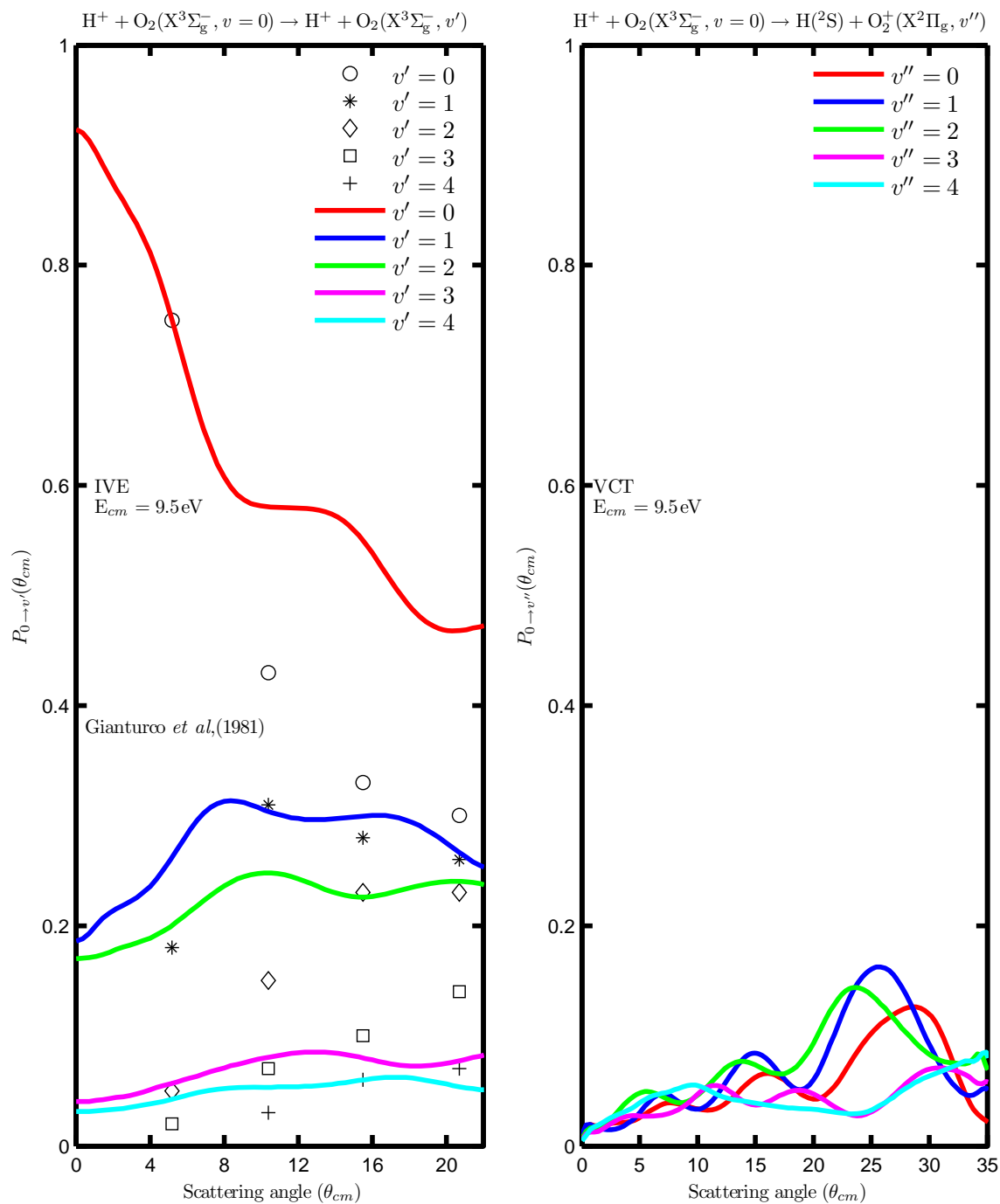


Figure 6.14: The transition probability for the IVE channel (left) $P_{0 \rightarrow v'}(\theta_{cm})$, $H^+ + O_2(v = 0) \rightarrow H^+ + O_2(v')$ and for the first VCT channel (right) $P_{0 \rightarrow v''}(\theta_{cm})$, $H^+ + O_2(v = 0) \rightarrow H(^2S) + O_2^+(v'')$ at $E_{cm} = 9.5\text{ eV}$ as a function of θ_{cm} . Theory and experiments are compared in the IVE channel alone (Gianturco, Gierz, and Toennies, 1981) and no experimental data are available for VCT channel.

0.2 : 0.8 roughly.

6.6.1.4 Average vibrational energy transfer

The average vibrational energy transfer $\overline{\Delta E}_{vib}(\theta_{cm})$ (in eV) is computed for the IVE and the first VCT processes using the set of formulas in Eq. (6.2) at the collision energy of $E_{cm} = 9.5$ eV. It is just the sum over the product of transition probability at specific vibrational state, and the corresponding vibrational energy of either $O_2(v')$ or $O_2^+(v'')$ as the case may be, as a function of θ_{cm} . The number of vibrational levels included in the computation is 20. Theoretically, computed average vibrational energy transfer $\overline{\Delta E}_{vib}(\theta_{cm})$ in both type

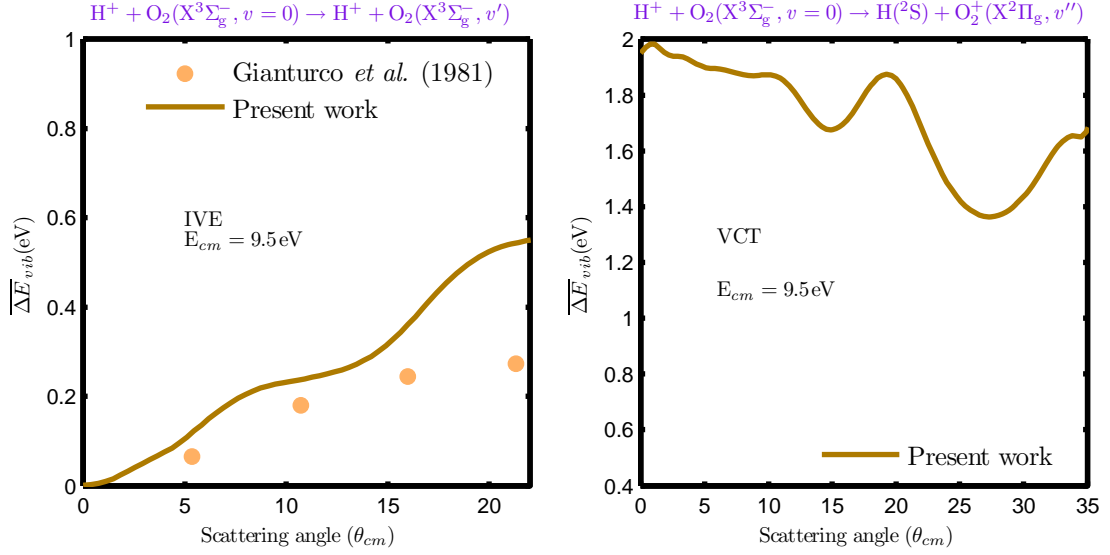


Figure 6.15: Average vibrational energy transfer $\overline{\Delta E}_{vib}(\theta_{cm})$ in eV as a function of scattering angle (θ_{cm}) for the IVE (left) and the first VCT (right) channels at $E_{cm} = 9.5$ eV. Theory and experiment (Gianturco, Gierz, and Toennies, 1981) are compared in the IVE channel

of processes have been shown in Fig. 6.15. The results for IVE channel is compared with experiments upto scattering angle $\theta_{cm} = 20^\circ$ and the results for VCT channel have been displayed in full range of θ_{cm} without any experimental data.

$$\overline{\Delta E}_{vib}(\theta_{cm}) = \sum_{v'=0}^{\infty} P_{0 \rightarrow v'}(\theta_{cm}) \Delta E(0 \rightarrow v') \quad (6.2)$$

$$\overline{\Delta E}_{vib}(\theta_{cm}) = \sum_{v''=0}^{\infty} P_{0 \rightarrow v''}(\theta_{cm}) \Delta E(0 \rightarrow v'')$$

The agreement between theory and experiment is quite encouraging in this four-state model relative to the two-state model in **subsection 5.7.1.4** and it explains the scattering angle dependency of the average vibrational energy transfer exactly over the specified range in IVE channel. The average vibrational energy transfer of VCT process is considerably changed from the two-state computations in **subsection 5.7.1.4** and it is found to be here strongly overestimated compared to the two-state model due to the influence of the ES PESs.

6.6.1.5 Intergral cross section

The rotationally summed state-to-state integral cross section (ICS) is computed using Eq. (3.32) on page 41 and is shown in Fig. 6.16 as a function of vibrational quantum number of $O_2(^3\Sigma_g^-, v')$ for the IVE channel, $H^+ + O_2(X^3\Sigma_g^-, v = 0) \longrightarrow H^+ + O_2(X^3\Sigma_g^-, v')$ (left) and as a function of vibrational quantum number of $O_2^+(^2\Pi_g, v'')$ for the first VCT channel, $H^+ + O_2(X^3\Sigma_g^-, v = 0) \longrightarrow H(^2S) + O_2^+(X^2\Pi_g, v'')$ (right) at the collision energy of $E_{cm} = 9.5$ eV. The numbers in the ordinate denote the power of 10. The four-state model gives us smaller values of ICS for both the IVE and the first VCT channel compared to that of two-state model. But here, the values for charge transfer channel are not smooth as in the case of those of the two-state model. We have summarized the absolute data of ICS in Table 6.17 and it shows a large difference between $v' = 0$ and $v' = 1$ in the IVE channel and between $v'' = 2$ and $v'' = 3$ in the VCT channel. The maximum occurs at $v' = 0$ (elastic excitation) in the IVE process and at $v'' = 2$ in the VCT process, suggestive of their dominance in the collisional events. The sum of integral cross sections for the IVE and the first VCT channel are computed to be at **104.05** and **0.581** respectively, almost close to the value of ICS for the elastic channel indicating its huge dominance over other inelastic channels. The Table 6.17 suggests that IVE channels dominate over VCT channels by two

orders of magnitude.

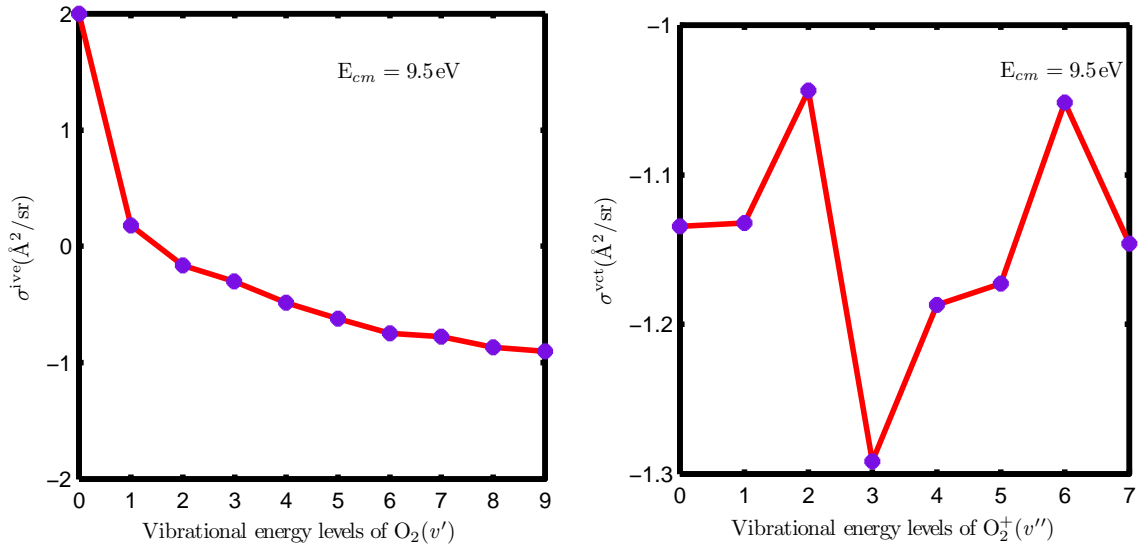


Figure 6.16: Integral cross section (σ) for the IVE, $\text{H}^+ + \text{O}_2(\text{X}^3\Sigma_g^-, v = 0) \longrightarrow \text{H}^+ + \text{O}_2(\text{X}^3\Sigma_g^-, v')$ (left) and VCT, $\text{H}^+ + \text{O}_2(\text{X}^3\Sigma_g^-, v = 0) \longrightarrow \text{H}^+ + \text{O}_2(\text{X}^2\Pi_g, v'')$ (right) processes as a function of vibrational energy levels of $\text{O}_2(\text{X}^3\Sigma_g^-)$ and $\text{O}_2^+(\text{X}^2\Pi_g)$ respectively at $E_{cm} = 9.5$ eV. The numbers in the ordinate indicate powers of 10.

Figure 6.17: The VCC-RIOSAs absolute state-to-state integral cross section (σ) for the IVE channel, $\text{H}^+ + \text{O}_2(\text{X}^3\Sigma_g^-, v = 0) \longrightarrow \text{H}^+ + \text{O}_2(\text{X}^3\Sigma_g^-, v')$ and the VCT channel, $\text{H}^+ + \text{O}_2(\text{X}^3\Sigma_g^-, v = 0) \longrightarrow \text{H}(^2\text{S}) + \text{O}_2^+(\text{X}^2\Pi_g, v'')$ at the $E_{cm} = 9.5$ eV for different vibrational states of $\text{O}_2(v')$ and $\text{O}_2^+(v'')$.

Integral cross section(\AA^2)		
$v'(v'')$	IVE	VCT
0	100.17	0.0734
1	1.51	0.0738
2	0.68	0.0904
3	0.50	0.0511
4	0.33	0.0650
5	0.24	0.0671
6	0.18	0.0887
7	0.17	0.0715
8	0.14	
9	0.13	
$\sum v'(v'')$	104.05	0.581

6.6.2 Dynamics at $E_{cm}=23$ eV

In this section, like the previous section, we will show and compare all the computed scattering attributes with those obtained from experiments (Noll and Toennies, 1986) and also with other theoretical studies performed earlier (Sidis, Grimbert, Sizun, and Baer, 1989; Gianturco, Palma, Semprini, Stefani, and Baer, 1990) at this collision energy along with the possible interpretations concerning the agreement between theory and experiment.

6.6.2.1 The orientation opacities

The VCC-RIOSAs angle-dependent opacity function as defined in Eq. (3.34) in **chapter 3** is shown in Fig. 6.18 as a function of partial waves (l) (in the units of \hbar) for the IVE channel, $H^+ + O_2(v = 0) \longrightarrow H^+ + O_2(v')$ for $\gamma = 0^\circ$, $\gamma = 45^\circ$ and $\gamma = 90^\circ$ orientations (left panel) and for the VCT channel, $H^+ + O_2(v = 0) \longrightarrow H(^2S) + O_2^+(v'')$ for $\gamma = 15^\circ$, $\gamma = 45^\circ$ and $\gamma = 75^\circ$ orientations (right panel) at $E_{cm} = 23$ eV. Note that since there is no radial coupling between the IVE and the VCT channels for $\gamma = 0^\circ$ and 90° there is no opening for any of the VCT channels for these angles and only the IVE process occur. The opacity is less at $E_{cm} = 23$ eV than that of $E_{cm} = 9.5$ eV in the IVE channel while the opposite is true in the VCT channel. At $E_{cm} = 23$ eV, more partial waves (l) are required to converge the opacity than at $E_{cm} = 9.5$ eV with $l_{max} = 800$ for IVE process and $l_{max} = 300$ for VCT process. The opacity follows the order of excitation in the IVE channel as given here : $v = 0 \rightarrow v' = 0 > v = 0 \rightarrow v' = 1 > v = 0 \rightarrow v' = 2 > v = 0 \rightarrow v' = 3$, suggestive of the dominance of elastic collisions over inelastic collisions, as it is the case at $E_{cm} = 9.5$ eV. The order of opacity in the VCT channel is sensitive to γ and follows the order, $v = 0 \rightarrow v'' = 1 > v = 0 \rightarrow v'' = 2 > v = 0 \rightarrow v'' = 0 > v = 0 \rightarrow v'' = 3$

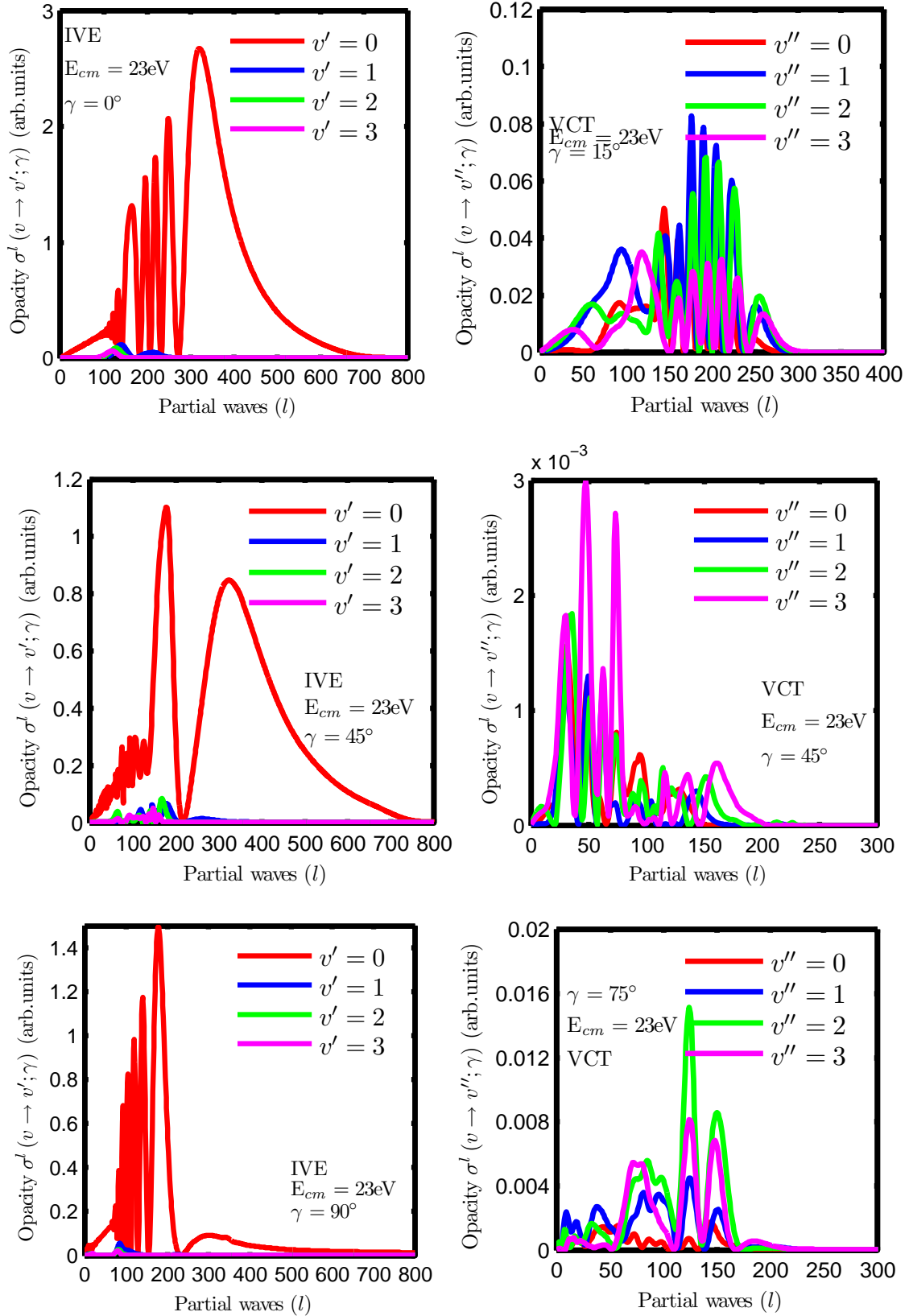


Figure 6.18: The opacity function as a function of partial waves (l , in the units of \hbar) for $\gamma = 0^\circ, \gamma = 45^\circ$ and $\gamma = 90^\circ$ orientations for the IVE channel, $\text{H}^+ + \text{O}_2(\text{X}^3\Sigma_g^-, v = 0) \rightarrow \text{H}^+ + \text{O}_2(\text{X}^3\Sigma_g^-, v')$ (left panel) and for $\gamma = 15^\circ, \gamma = 45^\circ$ and $\gamma = 75^\circ$ orientations for the VCT channel, $\text{H}^+ + \text{O}_2(\text{X}^3\Sigma_g^-, v = 0) \rightarrow \text{H}(^2\text{S}) + \text{O}_2^+(\text{X}^2\Pi_g, v'')$ (right panel) at $E_{cm} = 23\text{ eV}$.

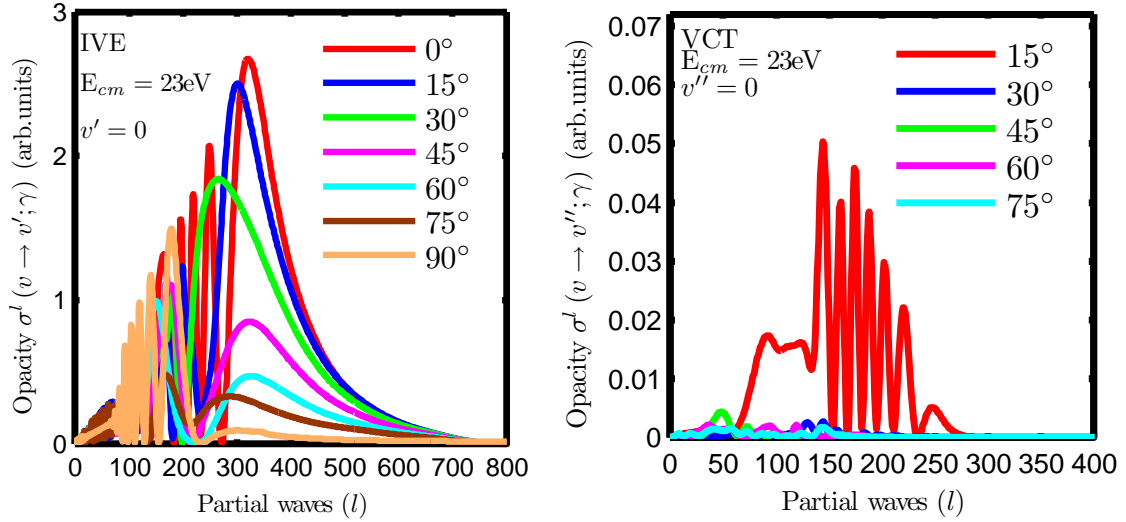


Figure 6.19: The comparison of opacity function among all the molecular orientations for the elastic collisions for IVE channel $\text{H}^+ + \text{O}_2(\text{X}^3\Sigma_g^-, v = 0) \rightarrow \text{H}^+ + \text{O}_2(\text{X}^3\Sigma_g^-, v')$ (left) and for first charge transfer collisions for the first VCT channel $\text{H}^+ + \text{O}_2(\text{X}^3\Sigma_g^-, v = 0) \rightarrow \text{H}(^2\text{S}) + \text{O}_2^+(\text{X}^2\Pi_g, v'')$ (right) at $E_{cm} = 23 \text{ eV}$.

for $\gamma = 15^\circ$ alone, the order, $v = 0 \rightarrow v'' = 3 > v = 0 \rightarrow v'' = 2 > v = 0 \rightarrow v'' = 1 > v = 0 \rightarrow v'' = 0$ for $\gamma = 45^\circ$ and the order $v = 0 \rightarrow v'' = 2 > v = 0 \rightarrow v'' = 3 > v = 0 \rightarrow v'' = 1 > v = 0 \rightarrow v'' = 0$ for $\gamma = 75^\circ$. This suggests that higher vibrational charge transfer ($0 \rightarrow v''$) dominates over $0 \rightarrow 0$ process in all three given orientations. We compare in Fig. 6.19 the opacity functions for the elastic (left) and the $v = 0 \rightarrow v'' = 0$ VCT (right) collisions for all the molecular orientations. The magnitude of opacity decreases with γ with the value for $\gamma = 0^\circ$ being the highest and that for $\gamma = 90^\circ$ being the lowest for the elastic collisions ($v = 0 \rightarrow v' = 0$) and the magnitude follows the order : $0^\circ > 15^\circ > 30^\circ > 45^\circ > 60^\circ > 75^\circ > 90^\circ$. It suggests that collinear approach promote elastic process very much. The magnitude for $v = 0 \rightarrow v'' = 0$ vibrational charge transfer collisions follows the order : $15^\circ > 75^\circ > 30^\circ > 45^\circ > 60^\circ$ suggesting that they are dominantly promoted by 15° orientations.

6.6.2.2 Rotationally-summed state-selective differential cross section (DCS)

The rotationally-summed total differential cross section (TDCS) and rotationally-summed state-selective differential cross sections (DCSs) have been computed as a function of scattering angle θ_{cm} at $E_{cm} = 23$ eV, for the IVE channel, $\text{H}^+ + \text{O}_2(\text{X}^3\Sigma_g^-, v = 0) \longrightarrow \text{H}^+ + \text{O}_2(\text{X}^3\Sigma_g^-, v')$ and the first VCT channel, $\text{H}^+ + \text{O}_2(\text{X}^3\Sigma_g^-, v = 0) \longrightarrow \text{H}(^2\text{S}) + \text{O}_2^+(\text{X}^2\Pi_g, v'')$. As mentioned earlier in **section 5.7** we report here smoothed data for the DCSs for both the IVE and the first VCT channels. In Fig. 6.20(b) we present our computed results for the IVE channels. Since the experimental results were reported on a relative scale we have normalized them with respect to our theoretical datum $\theta_{cm} = 11.72^\circ$ which is on the absolute scale and such normalized results are displayed in Fig. 6.20(a) (Noll and Toennies, 1986). The earlier theoretical works done by Gianturco *et al.* (1990) are given in Fig. 6.20(c) and the works done by Sidis *et al.* (1989) are given in Fig. 6.20(d) for comparison.

By considering the dynamics evolving on the four-state coupled PESs, we achieved remarkable improvements with respect to that obtained with two-state coupled electronic PESs and the agreement between theory and experiment. By employing the GS, the first, the second and the third ES PESs, we are able to bring about excellent agreement with experimental results over earlier reported theoretical results at $E_{cm} = 23$ eV. The rainbow feature is clearly visible though of less intensity in the TDCS curve at around $\theta_{cm} \approx 12^\circ$ which was completely absent in the two-state model. In the TDCS, the prediction of location of rainbow maximum by Gianturco *et al.* is roughly in agreement with experimental prediction of $\theta_{cm} = 11.72^\circ$. However, its size appears to be overestimated and for $\theta_{cm} > 12^\circ$ it shows a greater decline. Also, one see a pronounced rainbow maximum in their state-to-state DCSs which appears to be nearly absent in the experiments. Their DCSs appear to be jumbled

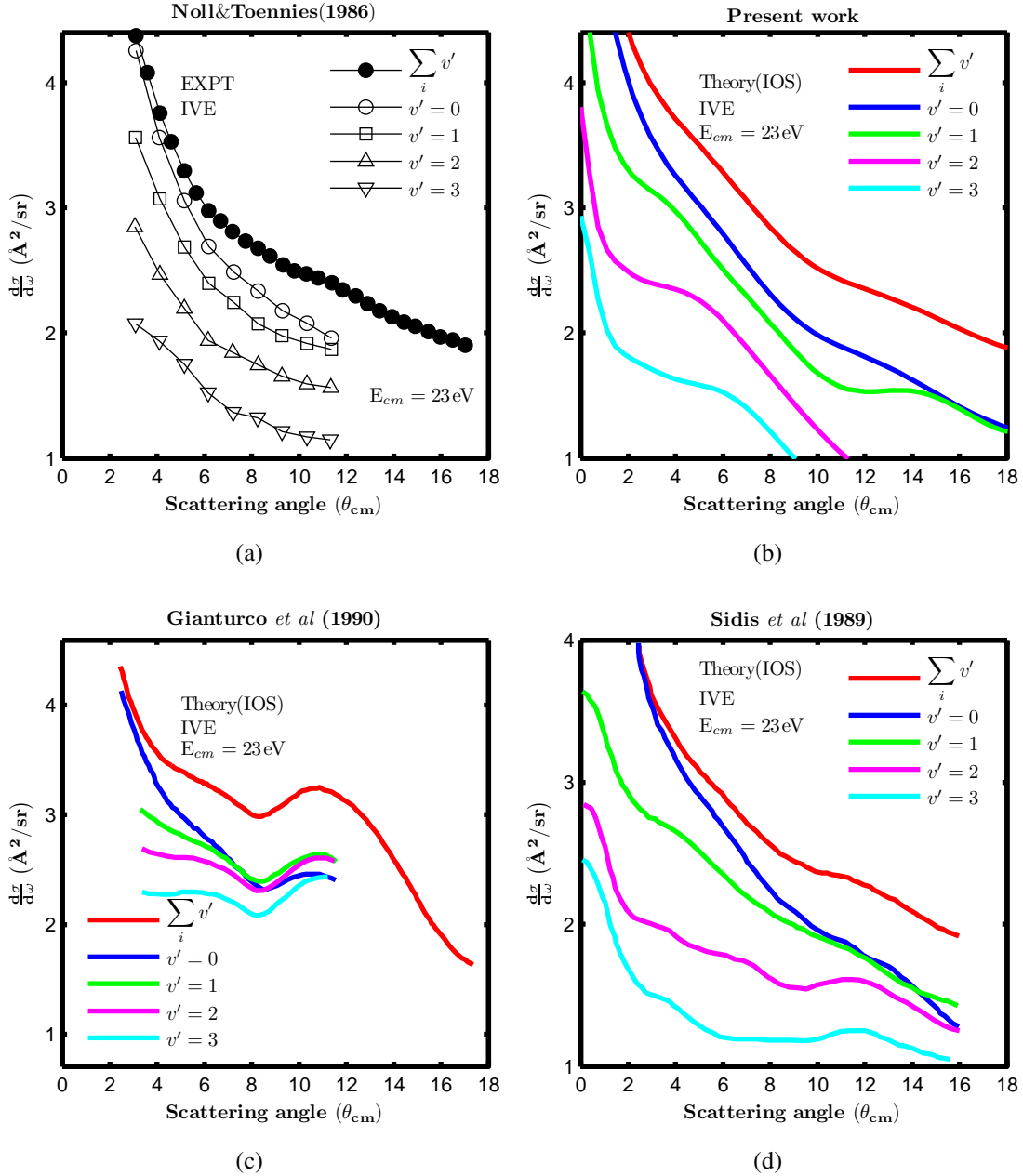


Figure 6.20: Rotationally-summed total differential cross section (TDCS) and rotationally-summed state-to-state DCS as function of θ_{cm} for IVE channel $H^+ + O_2(X^3\Sigma_g^-, v = 0) \rightarrow H^+ + O_2(X^3\Sigma_g^-, v')$ at $E_{cm} = 23$ eV along with the experimental and other two earlier theoretical results (Sidis, Grimbert, Sizun, and Baer, 1989; Gianturco, Palma, Semprini, Stefani, and Baer, 1990). The numbers in the ordinate denote powers of 10. See the text.

together in contrast to the experimental DCSs. The present data appear more or less similar to that of Sidis *et al.*. Both predict the rainbow maximum in the TDCS at higher θ_{cm} as compared to the experiments. But the size of the predicted rainbow maximum and its declining

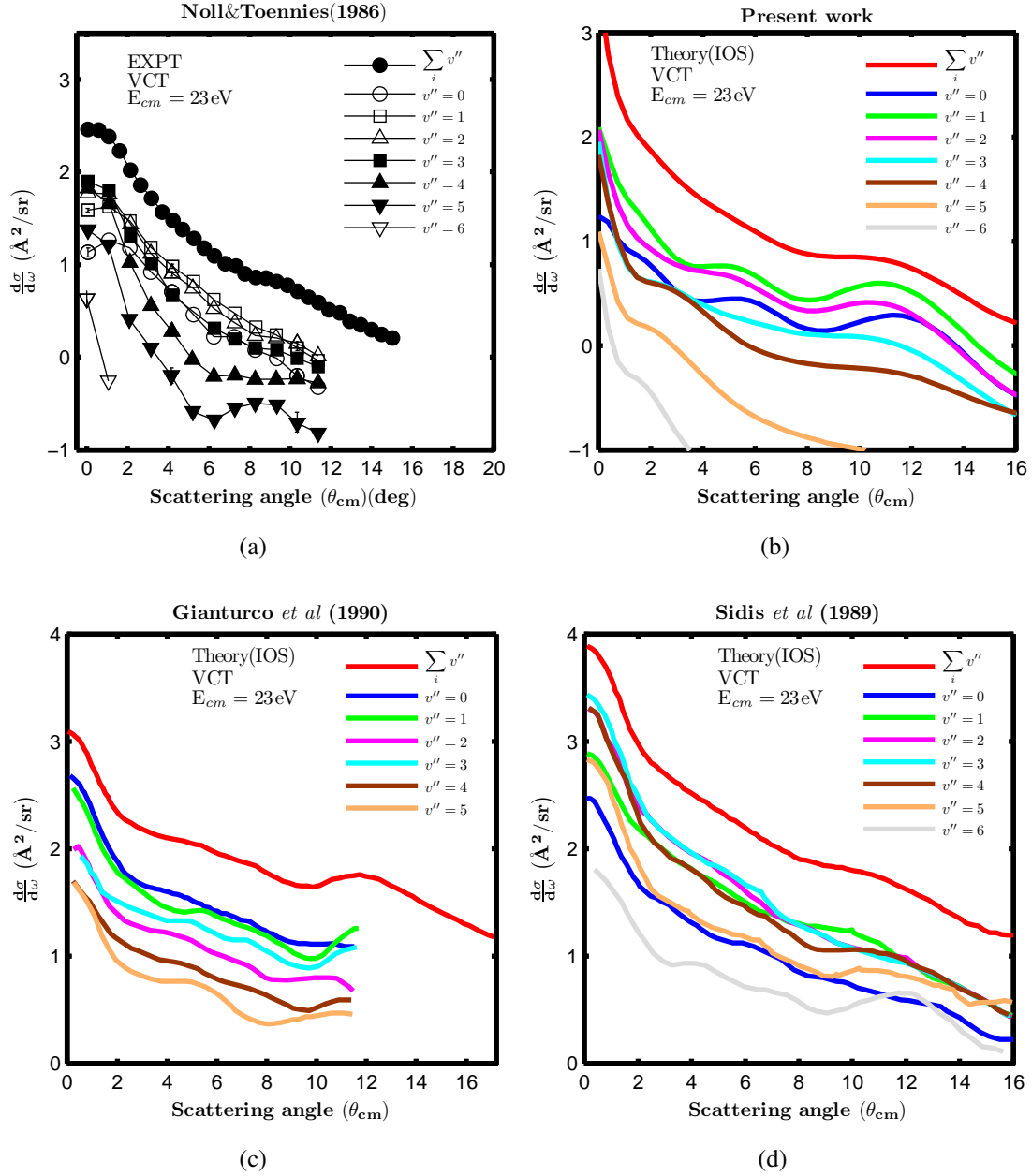


Figure 6.21: Rotationally-summed total differential cross section (TDCS) and rotationally-summed state-to-state DCS as function of θ_{cm} for the first VCT channel $\text{H}^+ + \text{O}_2(X^3\Sigma_g^-, v = 0) \rightarrow \text{H}(^2\text{S}) + \text{O}_2^+(X^2\Pi_g, v'')$ at $E_{cm} = 23$ eV along with experimental results and other two earlier theoretical works (Sidis, Grimbert, Sizun, and Baer, 1989; Gianturco, Palma, Semprini, Stefani, and Baer, 1990). The numbers in the ordinate denote powers of 10. See the text.

behaviour for larger θ_{cm} appear to be similar to that observed in the experiments. Also, the individual DCSs are well separated with each other and mostly follow the same order and trend as seen in the experiment.

For the charge transfer channel, $\text{H}^+ + \text{O}_2(\text{X}^3\Sigma_g^-, v = 0) \longrightarrow \text{H}(\text{2S}) + \text{O}_2^+(\text{X}^2\Pi_g, v'')$, we normalized the experimental data with respect to our theoretical datum value of TDCS at the experimental rainbow maximum at $\theta_{cm} = 9.0275^\circ$. Typical error estimates of the experimental data are given by the vertical bars. The rainbow maximum in the present TDCS occurs at around $\theta_{cm} \approx 11^\circ$ which is roughly 2° away from the rainbow maximum in the experimental curve and the intensity remains the same in both the case whereas it is overestimated in the work of Gianturco *et al.*; Its location and intensity is better estimated in the work of Sidis *et al.*. The order of layout of of state-to-state curves in terms of magnitudes of DCS in the present theory is well reproduced and is given as follows : $v'' = 1 > v'' = 2 > v'' = 0 > v'' = 3 > v'' = 4 > v'' = 5 > v'' = 6$ whereas this order is found to be altered in the other two theoretical works and not in agreement with experimental results. The TDCS and the DCSs in the experiment tend to a finite value after passing through a little maximum when θ_{cm} goes to zero. This feature is absent in the present work. There appears to be signatures of rainbow maximum in the experimental DCSs between $6^\circ - 12^\circ$ which is well marked for $v'' = 5$. All the theoretical sets show the existence of these rainbow maxima but at varying range of θ_{cm} as compared to those of experiments. The state-to-state DCS falls off steeply between $3^\circ \leq \theta \leq 6^\circ$ in the experiments and this is predicted by the present work. Hence, overall there is encouraging results obtained when moving from the two-state computation to the four-state computation.

6.6.2.3 Transition Probability

The detailed behaviour of the state-to-state probability for different processes as a function of scattering angle (θ_{cm}) is also a good tool to determine the quality of the present theoretical calculations in predicting the experimental behaviour. The computed state-to-state transition

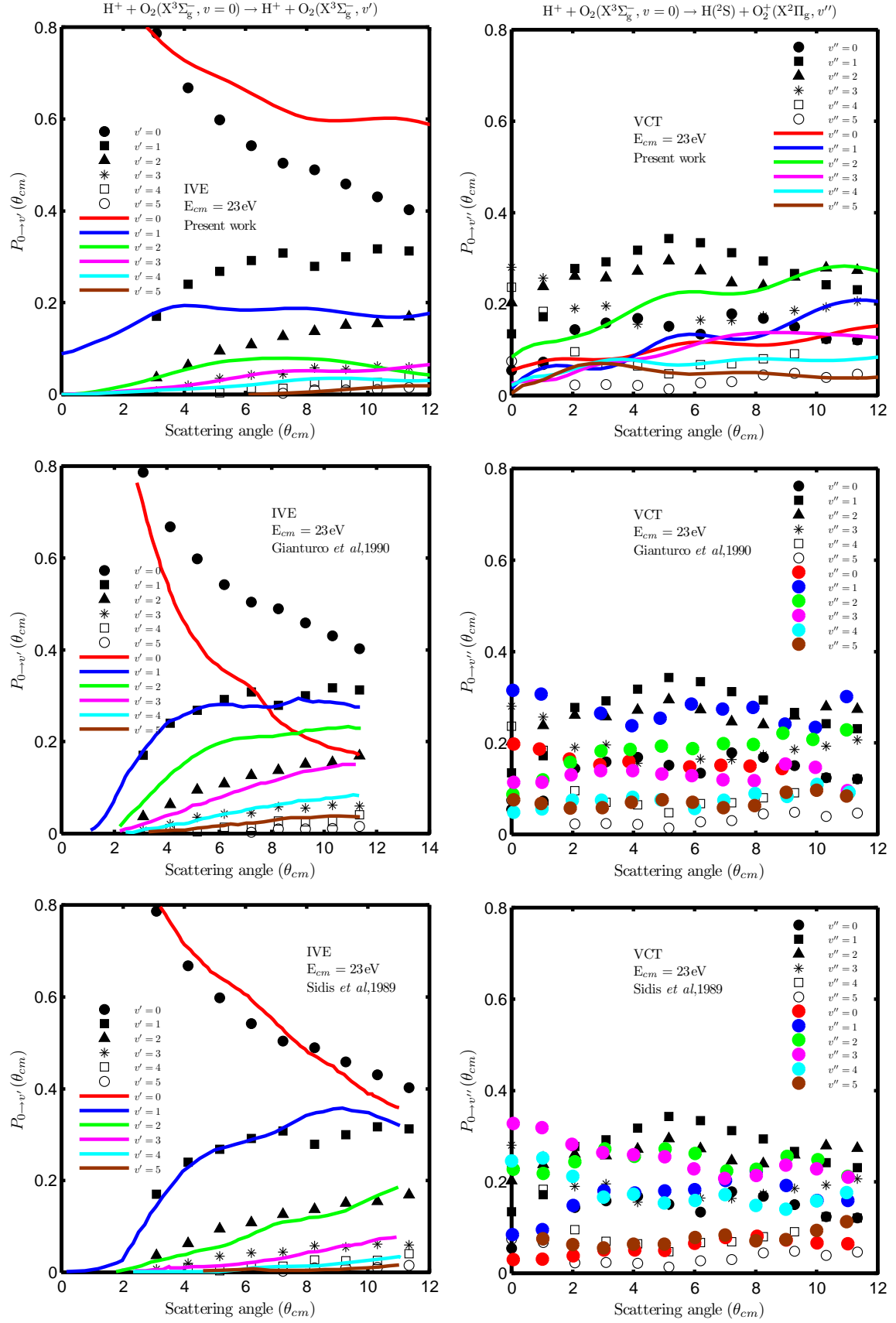


Figure 6.22: The transition probability, $P_{0 \rightarrow v'}(\theta_{cm})$, for IVE (left) and VCT (right) channel compared with experiment (Noll and Toennies, 1986) along with earlier theoretical works (Staemmler and Gianturco, 1985; Gianturco, Palma, Semprini, Stefani, and Baer, 1990). See the text.

probability and experimental values for the IVE channel, $\text{H}^+ + \text{O}_2(v = 0) \longrightarrow \text{H}^+ + \text{O}_2(v')$ (left) as well as the VCT channel $\text{H}^+ + \text{O}_2(v = 0) \longrightarrow \text{H}(^2\text{S}) + \text{O}_2^+(v'')$ (right) has been shown in in Fig. 6.22 at $E_{cm} = 23$ eV along with the two earlier theoretical results (Sidis, Grimbert, Sizun, and Baer, 1989; Gianturco, Palma, Semprini, Stefani, and Baer, 1990). The results of present calculations, Gianturco *et al.* and Sidis *et al.* are shown in the top, middle and bottom panels respectively. The experimental results (Noll and Toennies, 1986) are also shown in all plots and are denoted as markers, \bullet : $v'(v'') = 0$; \blacksquare : $v'(v'') = 1$; \blacktriangle : $v'(v'') = 2$; $*$: $v'(v'') = 3$; \square : $v'(v'') = 4$; \circ : $v'(v'') = 5$. The present data for the IVE and the VCT channel have also been tabulated in Table 6.3 and in Table 6.4, respectively, along with the experimental data.

From the behaviour of the $P_{0 \rightarrow v'}(\theta_{cm})$ for the IVE channel in Fig. 6.22(left), one can see that the elastic process is overestimated by present calculations (top). The earlier work of Gianturco *et al.* (1990) (middle) underestimates it whereas that of Sidis *et al.* (1989) (bottom) predicts well. The present computed values are found to be less than the experimental values for the inelastic processes, for, $v' = 1$, $v' = 2$ and $v' = 3$ excitations. The work of Gianturco *et al.* (1990) produces larger vibrational inelasticity for $v' = 2$ and $v' = 3$ excitations but well predicted by Sidis *et al.* (1989). The agreement for the present calculations is rather poor for the $P_{0 \rightarrow v''}(\theta_{cm})$ of the VCT channel relative to the IVE channel shown in Fig. 6.22 (right top). All the curves are underestimated in our calculations whereas in theory done by Gianturco *et al.* (1990)(middle), all the inelastic processes closely follow the experimental behaviour except at small angle regions where the probabilities are reduced considerably but not for elastic process which remain the dominant process and in work done by Sidis *et al.* (1989)(bottom), higher excitation are overestimated and low excitation process (including elastic) are underestimated and it correctly predicts the population of O_2^+

Table 6.3: Measured relative transition probabilities (Noll and Toennies, 1986) for vibrational excitation of O₂ by proton impact at E_{lab} = 23.7 eV for various scattering angles compared with our computed values for the inelastic channel, H⁺ + O₂(v = 0) → H⁺ + O₂(v') upto v' = 5 levels.

θ_{cm} (deg)	Expt (IVE)										Theory (IVE)				
	$P(0 \rightarrow v')$										$P(0 \rightarrow v')$				
	v' = 0	1	2	3	4	5	v' = 0	1	2	3	4	5			
3.09	0.786	0.170	0.037	0.007			0.790	0.173	0.033	0.012	0.008	0.000			
4.12	0.668	0.240	0.063	0.020	0.009		0.727	0.194	0.053	0.019	0.011	0.000			
5.15	0.598	0.268	0.095	0.035	0.004		0.692	0.188	0.069	0.029	0.015	0.000			
6.18	0.542	0.292	0.109	0.043	0.014		0.656	0.184	0.077	0.042	0.021	0.000			
7.21	0.504	0.308	0.127	0.044	0.014	0.003	0.618	0.187	0.079	0.050	0.029	0.003			
8.24	0.489	0.279	0.138	0.058	0.027	0.010	0.598	0.186	0.077	0.052	0.034	0.006			
9.28	0.458	0.300	0.151	0.055	0.025	0.010	0.597	0.176	0.069	0.051	0.035	0.009			
10.31	0.430	0.317	0.155	0.062	0.026	0.011	0.601	0.168	0.061	0.053	0.033	0.015			
11.34	0.402	0.313	0.169	0.060	0.041	0.015	0.599	0.169	0.049	0.060	0.030	0.018			

Table 6.4: The computed vibrational transition probabilities for the charge transfer process $\text{H}^+ + \text{O}_2(v=0) \longrightarrow \text{H}(^2\text{S}) + \text{O}_2^+(v'')$ at $E_{cm} = 23$ eV compared with the experimental values (Noll and Toennies, 1986) for the scattering angle $\theta_{cm} = 0^\circ - 11^\circ$.

θ_{lab} (deg)	Expt (VCT)						Theory (VCT)							
	$P(0 \rightarrow v'')$						$P(0 \rightarrow v'')$							
	$v'' = 0$	1	2	3	4	5	6	$v'' = 0$	1	2	3	4	5	6
0.00	0.055	0.135	0.203	0.280	0.237	0.075	0.015	0.055	0.015	0.084	0.026	0.022	0.005	0.015
1.03	0.073	0.172	0.238	0.257	0.184	0.067	0.009	0.075	0.061	0.115	0.033	0.043	0.036	0.071
2.06	0.144	0.278	0.261	0.190	0.096	0.023	0.010	0.079	0.064	0.129	0.053	0.061	0.058	0.092
3.09	0.158	0.292	0.258	0.196	0.070	0.024		0.077	0.063	0.148	0.070	0.078	0.069	0.053
4.12	0.168	0.318	0.272	0.156	0.065	0.022		0.087	0.099	0.187	0.080	0.077	0.062	0.040
5.15	0.151	0.343	0.295	0.149	0.047	0.014		0.106	0.124	0.219	0.092	0.068	0.050	0.026
6.18	0.134	0.334	0.273	0.165	0.067	0.027		0.117	0.133	0.226	0.115	0.069	0.047	0.020
7.21	0.178	0.312	0.247	0.164	0.069	0.030		0.113	0.123	0.221	0.131	0.077	0.050	0.021
8.24	0.168	0.294	0.240	0.174	0.080	0.045		0.110	0.135	0.235	0.137	0.080	0.050	0.017
9.28	0.150	0.267	0.259	0.186	0.091	0.048		0.119	0.170	0.263	0.136	0.077	0.043	0.010
10.31	0.124	0.242	0.279	0.193	0.124	0.039		0.135	0.200	0.282	0.134	0.076	0.040	0.008
11.34	0.121	0.231	0.274	0.207	0.121	0.046		0.145	0.208	0.282	0.129	0.079	0.038	0.009

molecules only at $v'' = 2$. Even though there is numerical mismatch the present work correctly explain the correct ordering of excitation of O_2^+ species as set out by the experiment unlike our two-state model case and hence in that aspect this model stand out as unique to the earlier one The order of excitation predicted by four-state model is $v = 0 \rightarrow v'' = 2 > v = 0 \rightarrow v'' = 1 > v = 0 \rightarrow v'' = 0 > v = 0 \rightarrow v'' = 3 > v = 0 \rightarrow v'' = 4 > v = 0 \rightarrow v'' = 5 > v = 0 \rightarrow v'' = 6$. This work seems to be fitting to $v'' = 4$ and $v'' = 5$ excitation more closely than any other, just as the work of Gianturco *et al.* with less numerical difference. The difference in probability for most probable excitations $v'' = 1$ and $v'' = 2$ is very high relative to that of Gianturco *et al.* and Sidis *et al.* work and also shape of the curves for these transitions are not similar to that of experiment. In spite of all these we have found overall the obtained results are encouraging and worth the attempt over our previous computation and still it is always advisable to redo the entire computation with more refined approach and may bring about more accuracy than the current one.

6.6.2.4 Average vibrational energy transfer

we computed the average vibrational energy transfer $\overline{\Delta E}_{vib}(\theta_{cm})$ as a function of scattering angle at $E_{cm} = 23$ eV in the same manner using Eq. (6.2) for the IVE channel, $H^+ + O_2(v = 0) \longrightarrow H^+ + O_2(v')$ and the VCT channel, $H^+ + O_2(v = 0) \longrightarrow H(^2S) + O_2^+(v'')$. The computed $\overline{\Delta E}_{vib}$ along with those of experimental data (Noll and Toennies, 1986) and earlier theoretical results (Gianturco, Palma, Semprini, Stefani, and Baer, 1990) are shown in Fig. 6.23 for the IVE (top) and the VCT (bottom) channels.

In Fig. 6.23(top) our four-state calculations explain well the angular dependency of the $\overline{\Delta E}_{vib}$ for the IVE channel which increases with the increase of θ_{cm} . For forward scattering,

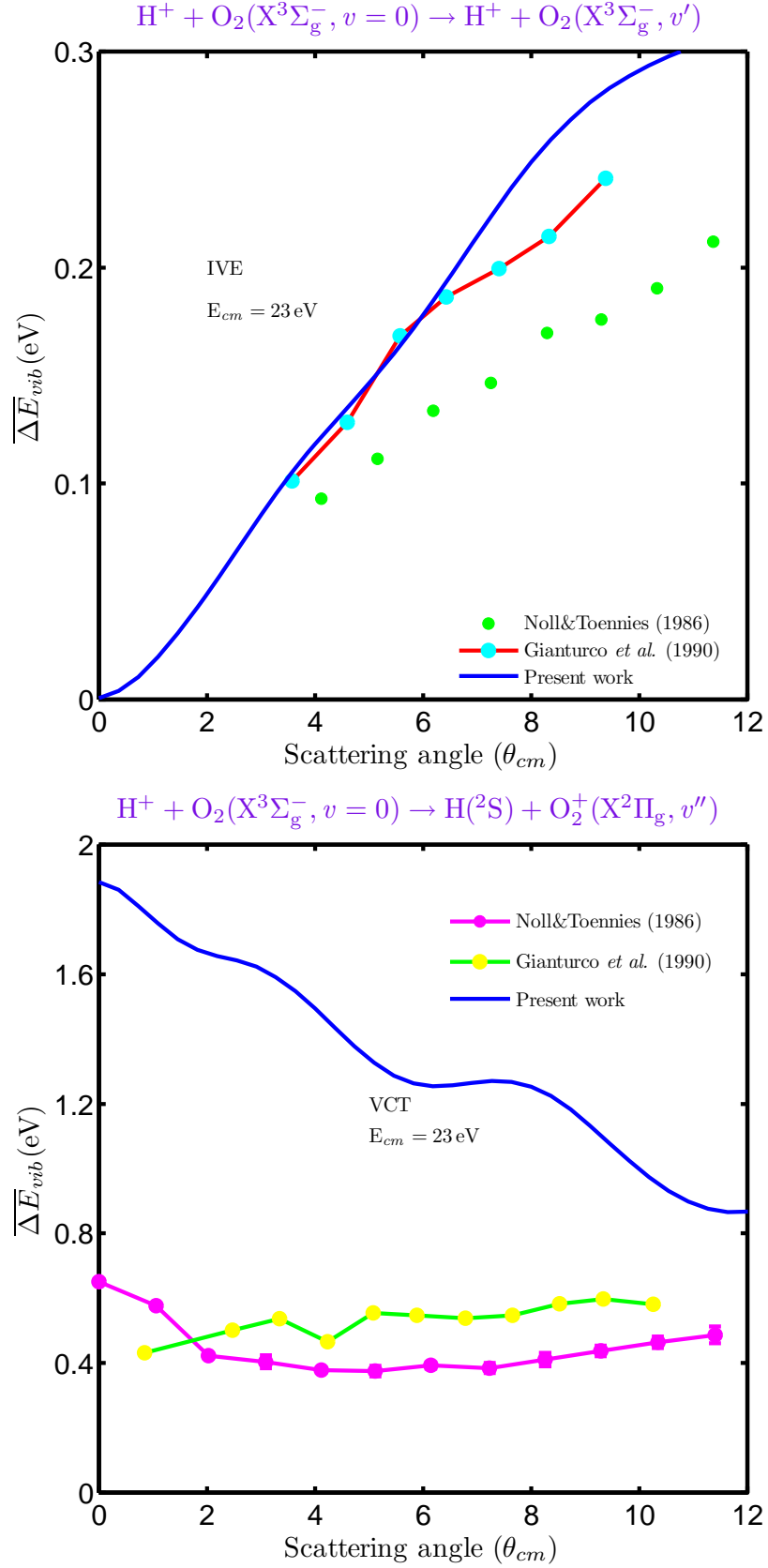


Figure 6.23: Average vibrational energy transfer $\overline{\Delta E_{vib}}(\theta_{cm})$ (in eV) as a function of scattering angle (θ_{cm}) at $E_{cm} = 23$ eV for the IVE (top) and the first VCT (bottom) channels along with experimental data (Noll and Toennies, 1986) as well as earlier theoretical work (Gianturco, Palma, Semprini, Stefani, and Baer, 1990).

it is almost zero primarily because of the dominance of the vibrationally elastic channel. The computed values in the present work are lying close to the values obtained by Gianturco *et al.* which are twice as large as the experimental ones. Though the numerical agreement seems to be the same as the two-state model the roughly linear shape of the curve makes us happy that the computed curve can be made to fit on the experimental one by a constant amount.

The trend observed in the VCT channel is different from that in the IVE channel in Fig. 6.23 (top). Even though we observe the trend to be the same as that of experiment at least in the small scattering angles the numerical agreement is not satisfactory and is highly overestimated relative to both experiment work as well as that of Gianturco *et al.*

6.6.2.5 Intergral cross section

Rotationally-summed integral cross section (ICS) for the IVE, $\text{H}^+ + \text{O}_2(\text{X}^3\Sigma_g^-, v = 0) \longrightarrow \text{H}^+ + \text{O}_2(\text{X}^3\Sigma_g^-, v')$ and the VCT, $\text{H}^+ + \text{O}_2(\text{X}^3\Sigma_g^-, v = 0) \longrightarrow \text{H}(^2\text{S}) + \text{O}_2^+(\text{X}^2\Pi_g, v'')$, is computed as a function of vibrational energy levels of target diatomic molecules O_2 and O_2^+ at $E_{cm} = 23$ eV in Fig. 6.24. There is no previously reported results from any theoretical work or experiments to be compared with. The ICS for the IVE channel decreases exponentially whereas that of VCT channel passes through a maximum at $v'' = 1$ followed by an exponential decay. The magnitude of the VCT being is less than that of the IVE process. We tabulate the absolute values of the state-to-state ICS at the collision energy of $E_{cm} = 23$ in the Table 6.25 for both channels and have found that sum over all vibrational states remain at **62.90** and **0.988**. As usual, the significant process is the elastic one in the IVE channel.

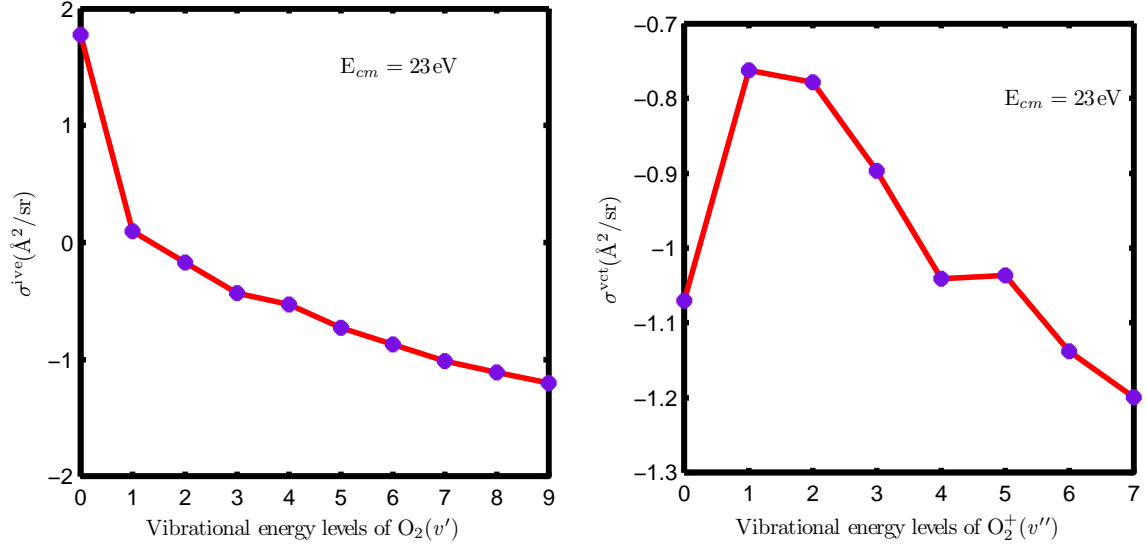


Figure 6.24: Integral cross section (σ) for the IVE (left) and VCT (right) processes as a function of vibrational energy levels of O_2 and O_2^+ respectively at $E_{cm} = 23$ eV. The numbers in the ordinate indicate powers of 10.

Figure 6.25: The VCC-RIOSAs absolute rotationally-summed state-to-state integral cross section (σ) for the IVE channel, $H^+ + O_2(X^3\Sigma_g^-, v = 0) \rightarrow H^+ + O_2(X^3\Sigma_g^-, v')$ and the VCT channel, $H^+ + O_2(X^3\Sigma_g^-, v = 0) \rightarrow H(^2S) + O_2^+(X^2\Pi_g, v'')$ at the $E_{cm} = 23$ eV for different vibrational states of $O_2(v')$ and $O_2^+(v'')$.

Integral cross section(\AA^2)		
$v'(v'')$	IVE	VCT
0	59.77	0.085
1	1.242	0.173
2	0.672	0.167
3	0.367	0.127
4	0.294	0.091
5	0.187	0.092
6	0.134	0.073
7	0.097	0.063
8	0.078	0.044
9	0.063	0.073
$\sum v'(v'')$	62.90	0.988

6.6.3 Dynamics : A comparison between 9.5eV and 23eV

In this section, we are going to discuss about how the scattering properties are influenced by the change of collision energy. Below we will compare one by one different scattering properties.

6.6.3.1 The orientation opacities

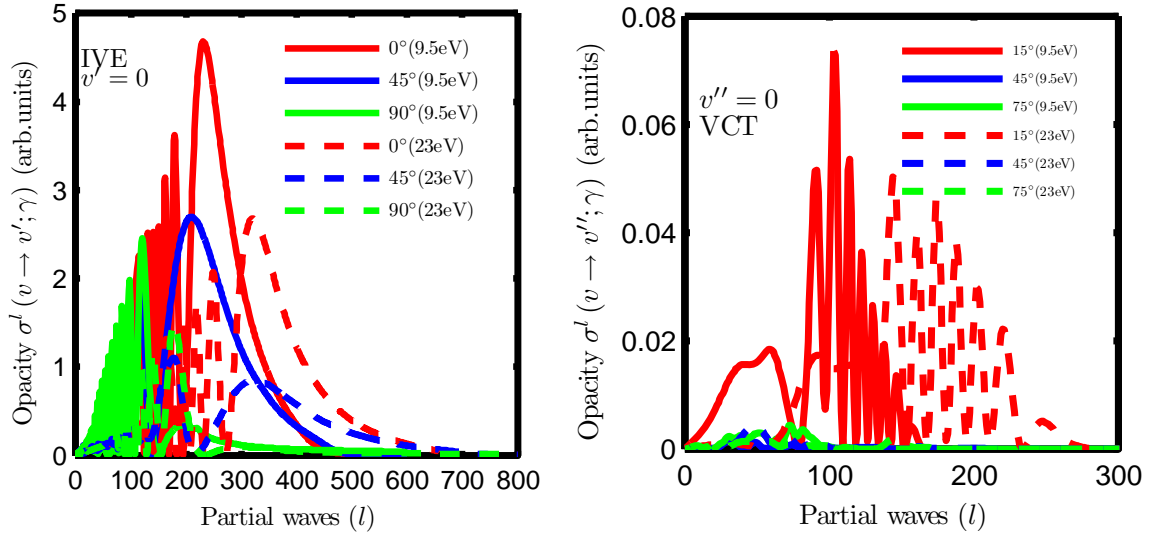


Figure 6.26: The comparison of opacity function between $E_{cm} = 9.5$ eV and $E_{cm} = 23$ eV for the elastic collisions for IVE channel (left) $H^+ + O_2(v = 0) \rightarrow H^+ + O_2(v')$ for $\gamma = 0^\circ, 45^\circ, 90^\circ$ and for first charge transfer collisions for VCT channel (right) $H^+ + O_2(v = 0) \rightarrow H(^2S) + O_2^+(v'')$ for $\gamma = 15^\circ, 45^\circ, 75^\circ$.

The opacity functions are compared at two different collision energies, $E_{cm} = 9.5$ eV and $E_{cm} = 23$ eV to see the changes it causes to the functions in Fig. 6.26 for both the channels. The opacity function is less and survives for large number of contributing partial waves at $E_{cm} = 23$ eV than at $E_{cm} = 9.5$ eV for the elastic collisions, $v = 0 \rightarrow v' = 0$ in the IVE channel. Similar is the case of first VCT channel too, $v = 0 \rightarrow v'' = 0$ where it is far displaced to right at $E_{cm} = 23$ eV for $\gamma = 15^\circ$. At $E_{cm} = 9.5$ eV and $E_{cm} = 23$ eV, the opacity follows the order : $0^\circ > 45^\circ > 90^\circ$ for IVE channel whereas for VCT channel, the order depends upon the collision energy and is given as $15^\circ > 45^\circ > 75^\circ$ at $E_{cm} = 23$ eV and as $15^\circ > 75^\circ > 45^\circ$ at $E_{cm} = 9.5$ eV. In general, the number of partial wave required for convergence is less for the first VCT channel than the IVE channel and independent of collision energy.

6.6.3.2 Rotationally-summed state-selective differential cross section(DCS)

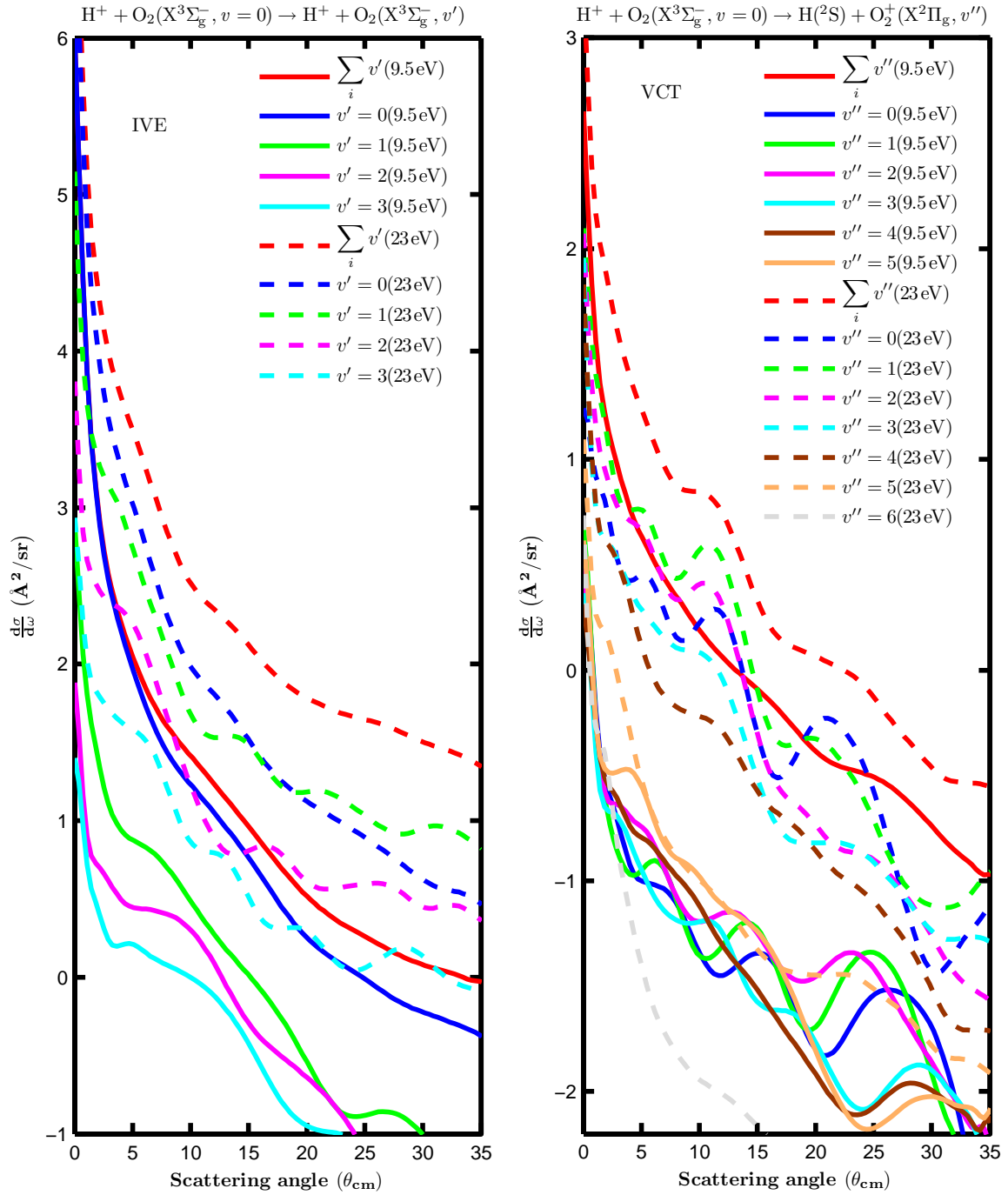


Figure 6.27: The comparison of state-to-state differential cross section (DCSs) and TDCS between $E_{cm} = 9.5\text{ eV}$ and $E_{cm} = 23\text{ eV}$ for IVE channel (left) $\text{H}^+ + \text{O}_2(v=0) \rightarrow \text{H}^+ + \text{O}_2(v')$ and for first VCT channel (right) $\text{H}^+ + \text{O}_2(v=0) \rightarrow \text{H}(^2\text{S}) + \text{O}_2^+(v'')$ as a function of scattering angle (θ_{cm}) (deg).

The state-to-state DCSs and TDCS are compared at $E_{cm} = 9.5\text{ eV}$ and $E_{cm} = 23\text{ eV}$

for the IVE and first VCT channel as a function of scattering angle (θ_{cm}) (deg) in Fig. 6.27. The magnitudes of TDCS and DCSs are always high at $E_{cm} = 23$ eV relatively than at $E_{cm} = 9.5$ eV for both channels. The rainbow maximum at $\theta_{cm} \sim 12^\circ$ is well marked in intensity at $E_{cm} = 23$ eV than at $E_{cm} = 9.5$ eV. The spacing between the TDCS and DCS for elastic channel is comparatively larger at $E_{cm} = 23$ eV than at $E_{cm} = 9.5$ eV. There is a flipping (cross over) of states of DCSs as a function of scattering angle at $E_{cm} = 23$ eV and no such flipping is observed at $E_{cm} = 9.5$ eV for IVE channel. At $\theta_{cm} = 0^\circ$, the magnitude of DCSs is higher at $E_{cm} = 23$ eV than at $E_{cm} = 9.5$ eV except elastic channel where the DCSs at these two collision energies seems almost similar. Below $\theta_{cm} = 5^\circ$, there is a steep increase in DCSs as well as TDCS curve at both energies but at higher angle, decrease is less at $E_{cm} = 23$ eV, looking roughly flat than at $E_{cm} = 9.5$. The TDCS curve is separated from state-to-state DCS widely at $E_{cm} = 9.5$ eV whereas at $E_{cm} = 23$ eV this separation is less. The rainbow is fully developed in TDCS curve at $E_{cm} = 23$ eV and is hardly visible at $E_{cm} = 9.5$ eV at $\theta_{cm} \sim 10^\circ$. The ordering of states predicted at the two energies differs a lot as a function of scattering angle and the individual DCS states are more closely packed at $E_{cm} = 9.5$ eV as a group than at $E_{cm} = 23$ eV. Upto $v'' = 4$, state-to-state DCSs curves are fully separated with a wide gap, with DCSs at $E_{cm} = 9.5$ eV being at bottom.

6.6.3.3 Transition Probability

The transition probability for the IVE channel (left) $P_{0 \rightarrow v'}(\theta_{cm})$, $H^+ + O_2(v = 0) \longrightarrow H^+ + O_2(v')$ and for VCT channel (right) $P_{0 \rightarrow v''}(\theta_{cm})$, $H^+ + O_2(v = 0) \longrightarrow H(^2S) + O_2^+(v'')$ at $E_{cm} = 9.5$ eV and $E_{cm} = 23$ eV are compared in Fig. 6.28 as a function of scattering angle θ_{cm} . The angular dependency of transition probability is followed in both channels approximately at both collision energies and is higher by slight margin at the collision energy

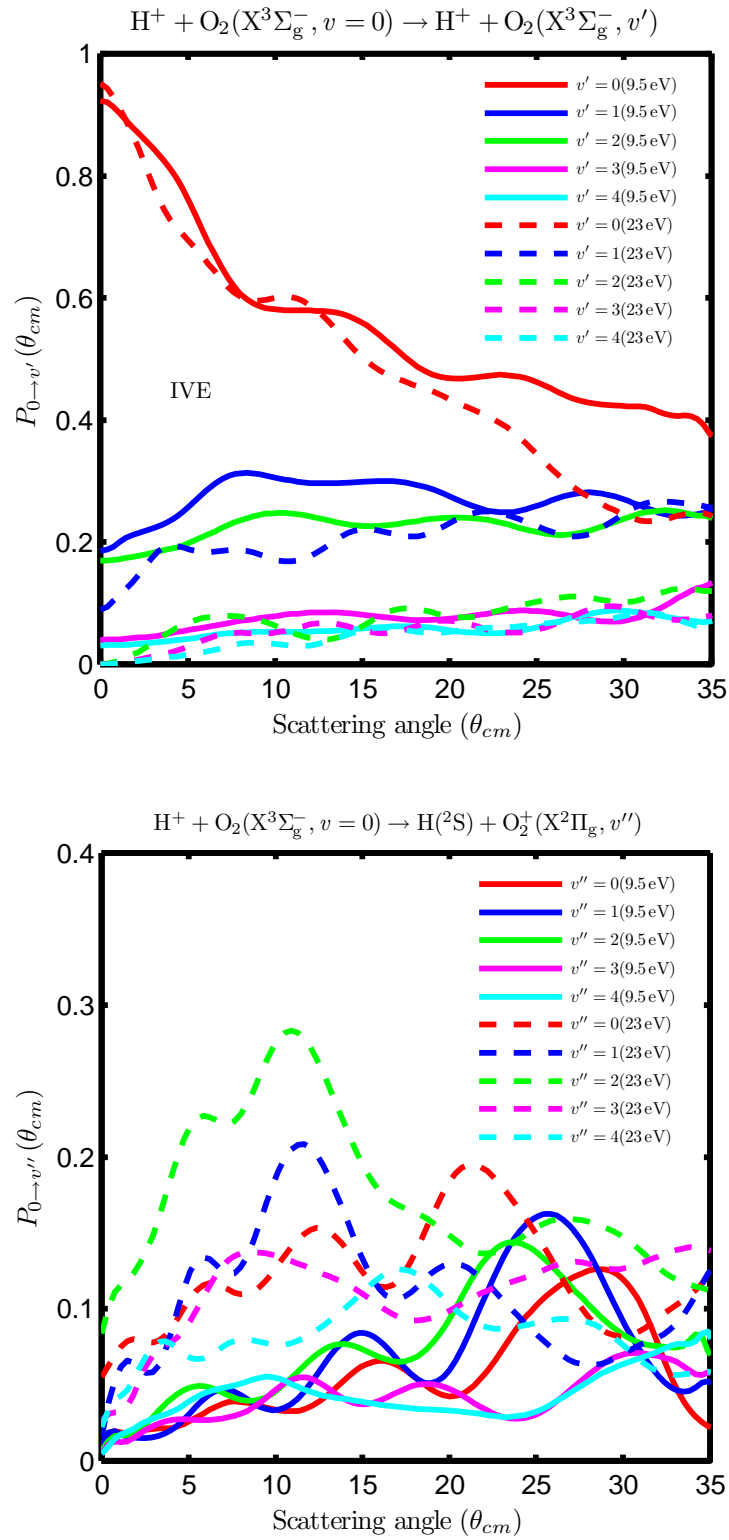


Figure 6.28: The transition probability for the IVE channel (left) $P_{0 \rightarrow v'}(\theta_{cm})$, $\text{H}^+ + \text{O}_2(v = 0) \rightarrow \text{H}^+ + \text{O}_2(v')$ and for VCT channel (right) $P_{0 \rightarrow v''}(\theta_{cm})$, $\text{H}^+ + \text{O}_2(v = 0) \rightarrow \text{H}^+(\text{S}) + \text{O}_2^+(v'')$ at $E_{cm} = 9.5 \text{ eV}$ and $E_{cm} = 23 \text{ eV}$ as a function of scattering angle θ_{cm} .

of $E_{cm} = 9.5$ eV than at the collision energy of $E_{cm} = 23$ eV for the IVE channel and remain almost the same at $v' = 4$ state. Both energies predict the same conclusion of highest probability for elastic channel. In the case of VCT channel, the transition probability never exceeds 0.3 and higher at $E_{cm} = 23$ eV upto $\theta_{cm} = 20^\circ$ for all states and order of probability remain almost the same at both energies

6.6.3.4 Average vibrational energy transfer

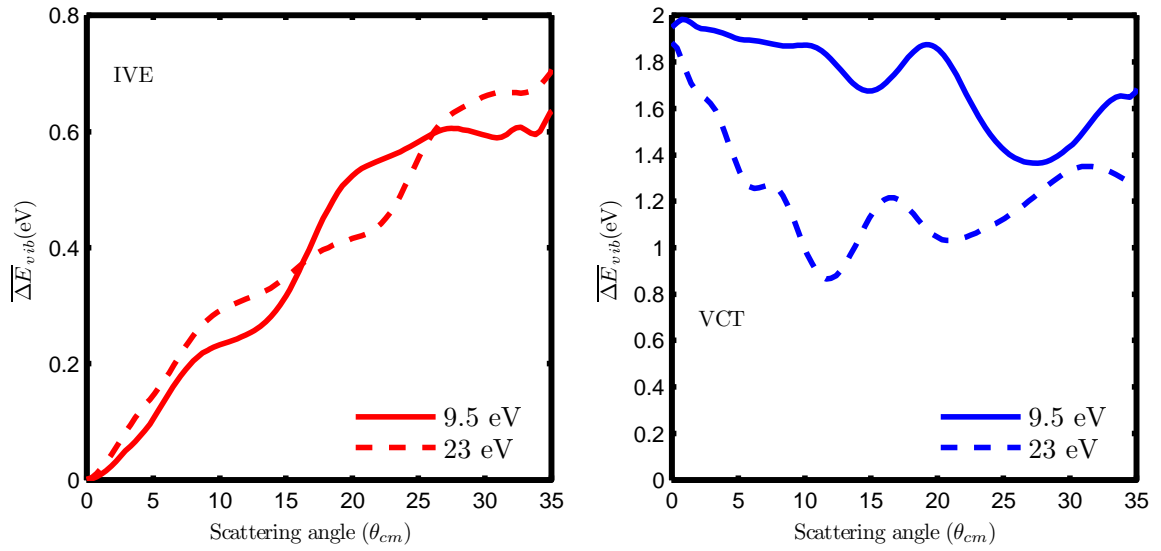


Figure 6.29: Average vibrational energy transfer $\overline{\Delta E}_{vib}(\theta_{cm})$ in eV as a function of scattering angle (θ_{cm}) for inelastic vibrational channel (IVE) (right), $H^+ + O_2(X^3\Sigma_g^-, v = 0) \longrightarrow H^+ + O_2(X^3\Sigma_g^-, v')$ and vibrational charge transfer (VCT) (left), $H^+ + O_2(X^3\Sigma_g^-, v = 0) \longrightarrow H(^2S) + O_2^+(X^2\Pi_g, v'')$ channels at $E_{cm} = 9.5$ eV and $E_{cm} = 23$ eV.

Average vibrational energy transfer $\overline{\Delta E}_{vib}(\theta_{cm})$ in eV as a function of scattering angle (θ_{cm}) at the collision energy of $E_{cm} = 9.5$ eV and $E_{cm} = 23$ eV for IVE (left) channel, $H^+ + O_2(X^3\Sigma_g^-, v = 0) \longrightarrow H^+ + O_2(X^3\Sigma_g^-, v')$, and VCT (right) channel, $H^+ + O_2(X^3\Sigma_g^-, v = 0) \longrightarrow H(^2S) + O_2^+(X^2\Pi_g, v'')$, have been shown in Fig. 6.29. They are very close together in the IVE channel and widely apart in the first VCT channel. The angular dependency at two collision energies remains the same, increase of average vibrational energy transfer with

increase of scattering angle in the IVE case and decrease with increase of scattering angle, at both collision energies. The dip in VCT at $E_{cm} = 23$ eV is somewhat more steeper than that at $E_{cm} = 9.5$.

6.6.3.5 Integral cross section

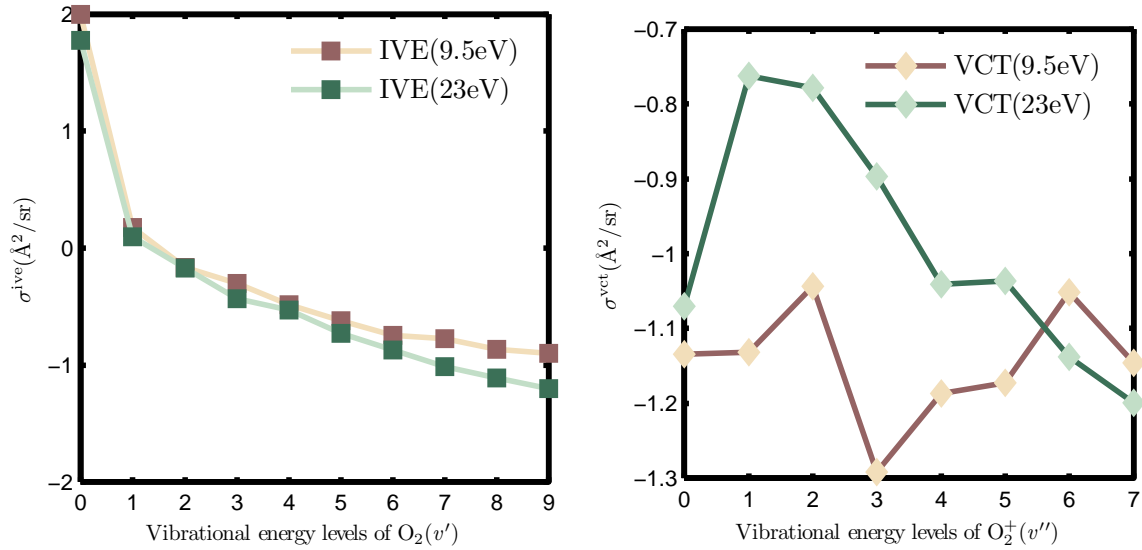


Figure 6.30: Integral cross section (σ) for the IVE (left) and VCT (right) processes as a function of vibrational energy levels of O_2 and O_2^+ respectively at $E_{cm} = 9.5$ eV and $E_{cm} = 23$ eV. The numbers in the ordinate indicate powers of 10.

The VCC-RIOSA absolute state-to-state integral cross section (ICS) (σ) for the IVE channel, $\text{H}^+ + \text{O}_2(v = 0) \longrightarrow \text{H}^+ + \text{O}_2(v')$ and the VCT channel, $\text{H}^+ + \text{O}_2(v = 0) \longrightarrow \text{H}(^2\text{S}) + \text{O}_2^+(v'')$ at $E_{cm} = 9.5$ eV and $E_{cm} = 23$ eV for different vibrational states of $\text{O}_2(v')$ and $\text{O}_2^+(v'')$ have been shown in Fig. 6.30. The state-to-state discrete values for both channels at these two collision energies have been summarized in Table 6.5. From the Fig. 6.30 and Table 6.5, we observe that the ICS values as a function of vibrational states for IVE channel is higher for $E_{cm} = 9.5$ eV than $E_{cm} = 23$ eV and though the ICS at both energies at lower states are roughly the same their gap increase with increase in quantum number and

Table 6.5: The VCC-RIOSAs absolute state-to-state integral cross section (σ) for the IVE channel, $\text{H}^+ + \text{O}_2(v=0) \rightarrow \text{H}^+ + \text{O}_2(v')$ and the VCT channel, $\text{H}^+ + \text{O}_2(v=0) \rightarrow \text{H}(^2\text{S}) + \text{O}_2^+(v'')$ at $E_{cm} = 9.5$ eV and $E_{cm} = 23$ eV for different vibrational states of $\text{O}_2(v')$ and $\text{O}_2^+(v'')$.

v'/v''	Integral cross section (\AA^2)			
	9.5 eV		23 eV	
	IVE	VCT	IVE	VCT
0	100.17	0.0734	59.77	0.085
1	1.51	0.0738	1.242	0.173
2	0.68	0.0904	0.672	0.167
3	0.50	0.0511	0.367	0.127
4	0.33	0.0650	0.294	0.091
5	0.24	0.0671	0.187	0.092
6	0.18	0.0887	0.134	0.073
7	0.17	0.0715	0.097	0.063
8	0.14		0.078	0.044
9	0.13		0.063	0.073
$\sum v'(v'')$	104.05	0.581	62.90	0.988

both curves generally decreases as a function of vibrational states. Note that there is big gap of ICS between $v' = 0$ and $v' = 1$ and the ICS at $v' = 0$ is the maximum at both energies. In the case of VCT channel, the ICS values for $E_{cm} = 9.5$ eV is lower than that at $E_{cm} = 23$ eV and it is maximum at $v'' = 1$ at $E_{cm} = 23$ eV and at $v'' = 2$ at $E_{cm} = 9.5$ eV. The curve for 9.5 eV are not smooth whereas that of 23 eV are smooth and keeps on decreasing after passing through a maximum at $v'' = 1$. The summed ICS for IVE channel at $E_{cm} = 9.5$ eV and $E_{cm} = 23$ eV is **104.05** and **62.90** and the same for VCT channel is **0.581** and **0.988** respectively.

6.7 Summary

In this chapter, we have presented some of the salient features of the adiabatic and quasi-adiabatic PECs and PESs of the GS and the lowest three excited states and analysed the

nonadiabatic interactions among them through the strength of the coupling potentials and NACME behaviour.

The VCC-RIOSAs calculations have been performed using the quasi-diabatic 4×4 coupling potential matrix to study the collision and energy transfer dynamics. A marked improvement is achieved in the present four-state quantum dynamics calculation as compared to that of two-state calculations of the collision attributes such as TDCS and state-to-state DCS against their experimentally observed trend and behaviour as a function of θ_{cm} . However, some quantitative discrepancies still remain in terms of the location of rainbow maxima and the relative magnitudes of the state-to-state DCS as a function of θ_{cm} . Yet, the discrepancy between theory and experiment exists for the production of transition probability as a function of θ_{cm} ; It is more in the case of the VCT channel since none of the theoretical sets are able to predict them correctly for the entire range of θ_{cm} .

At this point, it is desirable to discuss the likely reasons for the discrepancies and possible measures/suggestions which would improve the quantum dynamical results. It is worth pointing here that earlier quantum dynamics calculations were carried out within the VCC-RIOSAs framework on the coupled PESs involving the GS and the first ES. The corresponding quasi-diabatic PESs and the coupling were obtained employing the semi-empirical diatomics-in-molecules (DIM) method (Gianturco, Palma, Semprini, Stefani, and Baer, 1990) and the model effective potential procedures based on improved projected valence bond method (Sidis, Grimbert, Sizun, and Baer, 1989).

To the best of our knowledge, the present study reports for the first time in literature *ab initio* adiabatic and quasi-diabatic PESs for the four lowest electronic states of $^3A''$ symmetry. The constructions of the quasi-diabatic PESs have been achieved using the *ab initio*

procedure. It is generally debated that since the quasi-diabatic PESs cannot be determined uniquely and collision attributes such as rainbow maxima crucially depend on the topologies of these PESs, the origin of the discrepancies may lie on the determination of the quasi-diabatic potential matrix. However, it is worthwhile to point out here that the *ab initio* procedure suggested in the literature and presented in the thesis appears to be quite valid. In a recent study (Saieswari and Kumar, 2008a, 2007b, 2009) the quantum dynamics was performed for the IVE and the VCT processes in the $\text{H}^+ + \text{H}_2$ system on the two-state coupled quasi-diabatic PESs under the VCC-RIOSAs framework which were determined using the same *ab initio* procedure and the results obtained were in excellent agreement with experimental results settling some long-standing discrepancies between theory and experiments for the system. This lends credence to the *ab initio* procedure adopted in the present study. It is true that the quality of both the adiabatic and quasi-diabatic PESs depends crucially on the quality of the *ab initio* computations in terms of basis set and the methods adopted to account for the electron correlation. Comparisons and thereby excellent agreements of the equilibrium data for the diatoms as well as the bound HO_2^+ ion in the GS with those obtained from ultra high-level calculations give credence to and confidence in the quality of the present *ab initio* PESs. Therefore, we believe that the origin of discrepancy does not lie on the determination of *ab initio* PESs for the system.

It is clear from the present *ab initio* calculations that at $E_{cm} = 23$ eV at least three lowest ESs may be involved along with the GS in influencing the dynamics of the energy transfer processes. A two-state model involving the GS and the first ES may capture most of the intricacies of the dynamics but definitely would not be able to predict some of the crucial quantities like DCS and transition probabilities as a function of θ_{cm} . Therefore, quantum dynamics on the four-state electronically coupled PESs would be desirable and that is what

has been done in this chapter. It is also likely that VCC-RIOSAs framework does not hold good for the system. However, this would not be the case since it was able to capture the physics of the collision dynamics quite successfully in the $H^+ + H_2$ system. In this chapter we noted that magnitudes of opacities for the VCT were relatively larger for the collisions at $\gamma = 15^\circ$, or in other words, collisions for $0^\circ \leq \gamma \leq 45^\circ$ would be relatively richer in VCT processes. The present VCC-RIOSAs calculations were done for fixed γ in the range $0^\circ - 180^\circ$ at the interval of 15° , and the collision attributes were obtained from the γ -dependent scattering matrices. It could be possible that one needs to include more orientations averaging so that S-matrix could be properly obtained.

In the case of scattering being described on single electronic state PES, the intensity and the location of rainbow is mostly indentified with the location and well depth of the interaction well. For scattering involving multiple electronic states the attributes of rainbow can not be solely assigned to such patricular interaction well since the final outcome would be influenced by multiple processes which would average out the results. Therefore, in all likelihood, we believe that th origin of discrepancy lies mostly with the need for inclusion of more γ -dependent VCC-RIOSAs calculations and such a theoretical study would be mostly desirable for further study on this system.

CHAPTER 7

SUMMARY AND CONCLUSIONS

In this chapter, we provide concluding remarks regarding previous chapters, particularly, **chapter 4**, **chapter 5** and **chapter 6**, based on the outcome of our theoretical computation carried out on $H^+ + CO$ system using two-state coupled quasi-diabatic *ab initio* PESs and on $H^+ + O_2$ system using two-state as well as four-state coupled quasi-diabatic *ab initio* PESs, followed by future direction of research on this system with the aim of further improvement or refinement of results.

7.1 Concluding Remarks

In the present study we have undertaken an elaborate *ab initio* structural and quantum dynamics studies to study the energy transfer processes in the $H^+ + CO$ and $H^+ + O_2$ collision systems. In particular, we have studied the IVE and the VCT processes in these systems. For the $H^+ + CO$ system they are : $H^+ + CO (X^1\Sigma^+, v = 0) \longrightarrow H^+ + CO (X^1\Sigma^+, v')$ and $H^+ + CO (X^1\Sigma^+, v = 0) \longrightarrow H(^2S) + CO^+ (X^2\Sigma^+, v'')$, respectively and for the $H^+ + O_2$ system they are : $H^+ + O_2(X^3\Sigma_g^-, v = 0) \longrightarrow H^+ + O_2(X^3\Sigma_g^-, v')$ and $H^+ + O_2(X^3\Sigma_g^-, v = 0) \longrightarrow H(^2S) + O_2^+(X^2\Pi_g, v'')$, respectively.

One of the theoretical hurdles in studying the IVE and the VCT dynamics is that the collision dynamics evolves on coupled multi electronic PESs. For computational convenience one needs to carry out the dynamics on the corresponding coupled quasi-diabatic

PESs. The determination of quasi-diabatic PESs is not unique, and therefore many procedures have been proposed and their exactness and applicability have been discussed in the literature. In the present study, we have undertaken an *ab initio* procedure to describe the two-state and the four-state electronic coupling and the corresponding coupled potential matrices. This *ab initio* procedure has been utilized successfully for studying the dynamics of $\text{H}^+ + \text{H}_2$ collision system and the photodissociation of H_2S . The various aspects of adiabatic and quasi-diabatic transformations and the different methodologies for their transformation along with the *ab initio* procedure have been described in detail in the **chapter 2**.

One can perform the dynamics in the time-independent formulation of quantum mechanics using the full close-coupling methods. However, at the given range of collision energies, $E_{cm} = 9.5 - 30$ eV the full close-coupling method is not a feasible task computationally. Therefore, some physically valid assumption are invoked and the full close-coupling method is applied in the framework of the vibrational close-coupling rotational infinite-order sudden approximation (VCC-RIOSAs), which has been used quite successfully in the past for low and moderate energy collisions. In the present study, we have undertaken the quantum dynamics study within the VCC-RIOSAs framework. The formulation of the full close-coupling method and the various prescriptions and assumptions which lead to the VCC-RIOSAs have been discussed in detail in the **chapter 3**.

The *ab initio* and quantum dynamics results for the $\text{H}^+ + \text{CO}$ system are presented in **chapter 4**. The details of the *ab initio* computations of the adiabatic and quasi-diabatic PESs involving the GS and the first ES are given there along with the analysis of the nonadiabatic interactions in terms of the coupling potential and nonadiabatic coupling matrix elements. To the best of our knowledge these *ab initio* adiabatic and quasi-diabatic global PESs for the

two-state coupling suitable for scattering calculations have been obtained for the first time for the system. We have also analysed the various equilibrium structure properties of the bound molecular ions, HCO^+ and the HOC^+ , which are formed in the interaction wells of the GS PES and compared them with those obtained with high level *ab initio* computations focussed around describing the interaction well. The various parameters like barrier height and molecular configurations for the interconversions of $\text{HCO}^+ \rightleftharpoons \text{HOC}^+$ have been computed and compared with earlier theoretical results. Excellent agreement of these computed data with those obtained from high level *ab initio* computations ensures the quality of the newly obtained global PESs for the system.

The quantum dynamics has been performed within the VCC-RIOSAs framework using the two-state coupling potential at the experimental collision energies $E_{cm} = 9.5$ eV and $E_{cm} = 28.96$ eV. The dynamics has been examined in details in terms of various collision attributes such as opacities, DCS, ICS and transition probabilities. Since the present dynamics study happens to be perhaps the first quantum study of the IVE and the VCT processes on the two-state coupled PESs, extensive comparisons have been made for the computed collision attributes with those available from the experiment. Over all, there is a good agreement between the theory and the experiment for the IVE channel. For the VCT channel, although the theoretical predictions for the collision attributes follows the experimental trend qualitatively quite well, the quantitative agreement is still lacking.

We have undertaken quite an extensive and an elaborate *ab initio* study along with quantum dynamics for the $\text{H}^+ + \text{O}_2$ collision system computing the global adiabatic as well as quasi-diabatic PESs involving the GS and the three lowest ESs of $^3\text{A}''$ symmetries. Again, to the best of our knowledge, this is perhaps the first *ab initio* attempt to construct the four-

state *ab initio* global PESs for scattering studies. The earlier studies modelled the IVE and the VCT dynamics as a two-state processes involving the GS and the first ES and the PESs were constructed using the semi-empirical diatomics-in-molecules method and the model effective potential procedures based on the improved projected valence bond method. An *ab initio* attempt was made recently in our group to construct the two-state PESs. However, the NACME and the mixing angle showed a lot of irregularities indicating regions of avoided crossings of the first ES with the second ES. In order to model the dynamics purely as a two-state process these additional irregularities were smoothed and the global two-state PESs were obtained. The earlier and recent (in our group) quantum dynamics calculation with the VCC-RIOSAs framework on these set of PESs showed several quantitative discrepancies as compared to those of experimental results. Therefore, in order to test the applicability of the two-state modelling of the dynamics we first studied the quantum dynamics at the experimental collision energies, $E_{cm} = 9.5$ eV and $E_{cm} = 23$ eV by taking out the 2×2 coupling potential matrix involving the GS and the first ES from the computed 4×4 quasi-diabatic coupling potential matrix. There are some improvements but not up to the mark in the two-state dynamics calculations. The details of the four-state *ab initio* calculations involving the adiabatic PESs, NACMEs, and the quasi-diabatic PESs and the coupling potentials have been given in **chapter 5** along with the dynamics results. The various characteristics of the PECs/PESs for the GS and the first ESs have also been analysed and discussed therein. In **chapter 5**, we also studied the equilibrium structure of the bound HO_2^+ ion in the interaction well of the GS. Excellent agreement between the equilibrium structure data obtained from the present *ab initio* calculations and those obtained from highly refined *ab initio* calculations around the interaction well lends credence to our *ab initio* calculations for the system.

The various characteristics of the ES PECs/PESs of the $H^+ + O_2$ systems and their nonadiabatic interactions studied in terms of strength of NACMEs and the coupling potential have been analysed in detail in **chapter 6**. The details of quantum dynamics within the VCC-RIOSAs framework at the two experimental collision energies are also given therein. An extensive comparison has been made for the collision attributes obtained in the present four-state calculations. Significant improvements have been achieved in the four-state calculations, but some quantitative agreement between theory and experiment is still lacking. The likely reasons for the disagreement and the suggestions to improve the quality of theoretical calculations have been discussed in **section 6.7** of **chapter 6**.

7.2 Future direction of research

Our present study shows that there are still some issues which remain unresolved regarding the dynamics of $H^+ + CO$ and $H^+ + O_2$ systems. More refined experiments and more elaborate quantum mechanical calculations are desirable to address some of the issues described below.

In $H^+ + CO$ system, the experimental data on scattering quantities are not available at the collision energy of $E_{cm} = 9.5$ eV for IVE as well as VCT channel. Hence it would be desirable to carry out a fresh set of experiments at this collision energy to get the data on scattering quantities from the futuristic point of view. At $E_{cm} = 28.96$ eV, the experimental data on the VCT channel are not available and hence it would be worthy enough to perform the experiments for this channel at this collision energy and also at other collision energies from the point of view of extension of future work. For the VCT channel, the quantitative agreement between theory and experiment is lacking and it is proposed that quantum dynam-

ics calculations with further inclusion of other low-lying ESs would improve the theoretical predictions.

In $\text{H}^+ + \text{O}_2$ system, the experimental data on scattering quantities are not available at the collision energy of $E_{cm} = 9.5$ eV for IVE as well as VCT channel and hence it would be desirable to carry out a fresh experiments at this collision energy as well as at other collision energies in the range 0-30 eV. From the theoretical points of view, it is suggested that inclusion of more angle-dependent VCC-RIOSAs calculations particularly for γ in the range $0^\circ \leq \gamma \leq 45^\circ$ would further improve the dynamics results. This would need further *ab initio* calculations to generate the four-state PESS for these orientations.

APPENDIX A

VALIDITY OF VCC-RIOSIA IN THE PRESENT

CALCULATIONS

It may be argued whether or not the VCC-RIOSIA dynamics is valid and applicable for the present $\text{H}^+ + \text{CO}$ and $\text{H}^+ + \text{O}_2$ systems, particularly in view of the fact that for the $\text{H}^+ + \text{CO}$ system the potential anisotropy would be expressed in terms of long-range charge-dipole, charge-quadrupole and charge-polarizability interactions. It is generally believed, and as pointed out earlier in **section 3.2**, that the schemes of decoupling of angular momenta would work better for higher collision energies. The experimental results for the IVE and the VCT channels for the $\text{H}^+ + \text{CO}$ and the $\text{H}^+ + \text{O}_2$ systems are available for $E_{cm} = 28.96$ eV and $E_{cm} = 23.0$ eV, respectively. Compared to that of $\text{H}^+ + \text{CO}$ system, the long range interaction potential in the $\text{H}^+ + \text{O}_2$ system is much weaker in the absence of dipole moment of O_2 . Therefore, we carried out numerical tests for the validity of the infinite-order sudden (IOS) approximation in the $\text{H}^+ + \text{CO}$ system at $E_{cm} = 28.96$ eV against the coupled state (centrifugal sudden) (CS) decoupling scheme, (Parker and Pack, 1978) as it was done for the case of $\text{H}^+ + \text{H}_2$ system for E_{cm} as low as 3.7 eV.

It may be noted here that a real validation of any decoupling scheme would come from the comparison of collision attributes against those obtained from the full close-coupling calculations, which however still remain computationally formidable and prohibitive at these higher collision energies. In atom(ion)-molecule inelastic collisions the dimensionality of the problem increases from rapid proliferation of quantum channels associated with the

$(2j + 1)$ degeneracy of the energy levels of the rotating target. For the case of the atom-heteronuclear systems the problem splits up into the even-parity where the number of coupled equation is given by

$$N_{even} = \sum_{j=0}^{j_{max}} (j + 1) = \frac{(j_{max} + 1)(j_{max} + 2)}{2} \quad (\text{A.1})$$

For the odd-parity the total number is given by

$$N_{odd} = \sum_{j=0}^{j_{max}} j = \frac{j_{max}(j_{max} + 1)}{2} \quad (\text{A.2})$$

For even the most efficient algorithm, the labour of solving coupled equations goes as the cube of the number of equations to be solved. Therefore, it is obvious that the computational problem becomes rapidly intractable even for modest values of j_{max} .

As a consequence of this, the CS approximation has been extensively studied. It was called coupled states approximation in its earlier development stage while its simultaneous and independent introduction by Pack (Parker and Pack, 1978) was called the centrifugal sudden approximation. Further refinements and interpretations of its physical significance were indeed discussed by many authors in the literature and several computational applications have also been carried out for atom-diatomic systems. (McGuire, 1976; Schinke and McGuire, 1978a)

For a purely rigid rotor target interacting with a structureless atom, it is convenient to write the Hamiltonian in the body-fixed frame (Parker and Pack, 1978)

$$\hat{H}_{BF} = -\frac{1}{2\mu} \frac{1}{R} \frac{\partial^2}{\partial R^2} + \frac{\hat{l}^2}{2\mu R^2} - \frac{1}{2M} \nabla_r^2 + V(R, r, \gamma) \quad (\text{A.3})$$

where \hat{l} is the angular momentum operator for the KE term in the Hamiltonian and $-\frac{1}{2M}\nabla_r^2$ is the KE operator for the diatom. When the above operator is applied to the trial function expanded over the coupled molecular (rotational) states one sees that it would lead to purely radial equations on R if it were not for the \hat{l}^2 operator. Hence the lack of separation of the angular part of R is purely kinematic in origin and, in a sense, does not depend on the nature of the potential, even if the latter provides necessary coupling of radial functions.

In order to obtain the CS approximation, one now introduces an effective orbital angular momentum eigen value and approximates the centrifugal potential by

$$\frac{\hat{l}^2}{2\mu R^2} \approx \frac{l(l+1)}{2\mu R^2} \quad (\text{A.4})$$

This is also, of course, a sort of sudden approximation which eventually says that the relative KE is sufficiently large that the precise values of the centrifugal potential is not important. Whether this approximation is true or not, depends on how the different turning points for the different effective potentials are related. If the interaction potential is purely repulsive, then the rate of change of the turning points with various l is not large and therefore, the Eq. (A.4) is expected to be valid. For interactions exhibiting attractive wells one might encounter range of l values which have three turning points, all rapidly changing with l and therefore the fixed, effective eigenvalues of Eq. (A.4) is not a reliable approximation to that situation.

In the body-fixed equation one sees that Eq. A.4 provides a substantial simplification of those coupling matrix elements that are responsible for transitions between different helicity states,

$$\left\langle \Gamma_{j\Omega}^{JM} \left| \hat{l}^2 \right| \Gamma_{j,\Omega\pm 1}^{JM} \right\rangle \approx 0 \quad (\text{A.5})$$

where Γ is the body-fixed angular function and Ω stands for the helicity. J is the total angular momentum and $\hat{J} = \hat{l} + \hat{j}$. Here, one neglects the intermultiplet coupling provided by the different eigenvalues of \hat{l}^2 appearing in the \hat{H}_{BF} . Moreover, it further reduces the form of the coupling between states with the same helicity index to the following simpler expansion

$$\begin{aligned} \left\langle \Gamma_{j\Omega}^{JM} \left| \hat{l}^2 \right| \Gamma_{j,\Omega\pm 1}^{JM} \right\rangle &\sim J(j+1) \\ &\sim [J(j+1) + j(j+1) - 2\Omega^2] \end{aligned} \quad (\text{A.6})$$

according to whether one chooses Eq. (A.1),(A.2),(A.3) $l = J$ or the exact value of the diagonal matrix elements. The latter choice slightly complicates the long-range form of the asymptotic boundary conditions which require now spherical Bessel functions of the order λ , were $\lambda(\lambda+1) = J(J+1) + j(j+1) - 2\Omega^2$. The corresponding coupled equations in the body-fixed frame therefore become

$$\left\{ \frac{d^2}{dR^2} - \frac{l(l+1)}{R^2} + k_{jj'}^2 \right\} G_{j'\Omega}^{Jj\Omega}(R) = 2\mu \sum_{j''} \left\langle \Gamma_{j'\Omega}^{JM} \left| \hat{V} \right| \Gamma_{j''\Omega}^{JM} \right\rangle G_{j''\Omega}^{Jj\Omega}(R) \quad (\text{A.7})$$

where R is the distance vector of the projectile from the c.m. of the rigid rotor diatom, k is the wavevector, G is the translational wavefunction and \hat{V} stands for the interaction potential energy operator. The coupling matrix elements on the R.H.S of Eq. (A.7) exhibit now a simpler structure since they only contain the coupling between different j states via the interaction potential without the coriolis terms that cause coupling between different helicity states and that appear in the correct formulations in the correct body-fixed equations in the close-coupling formulations. Within the CS approximation the full coupling is independent of l as is zero between the states with different helicity, or different j_z -component on the

chosen axis of quantization. This is therefore the reason why this method is also called " j_z -conserving" approximation of coupled states approximation, in the sense that only coupling between different rotational states (and not between the substates) is allowed to appear in the dynamical treatment. It is important to note that the scattering formalism can also be achieved in the space-fixed frame by a unitary transformation to the corresponding body-fixed eigenfunctions.

The infinite-order sudden approximation has a long history in the molecular collision literature (Gianturco, 1979). It can be viewed as an energy sudden approximation to the results of the CS approximation discussed above. In the latter, in fact, the \hat{l}^2 operator is replaced by an effective eigenvalue form, thereby allowing one to use the closure property of the complete set of the partial wave expansion to simplify the sum over l and m_l . In the IOSA one further applies the same sort of approximation to the rotational energy. In the case of atom-rigid rotor diatom collision, $\frac{\hat{j}^2}{2I}$ (I is the moment of inertia of the diatom) is replaced by another effective eigenvalue form $j(j+1)$. Thus one has $k_{jj'}^2 \sim k_{jJ}^2$, for all j' . In this approximation, one completely decouples the angular momenta and one gets a constant term within the angular brackets. For example, in the case of linear rovibrator target one sets

$$\left\{ \frac{d^2}{dR^2} - \frac{l(l+1)}{R^2} + k_{jj'}^2 \right\} f_{v'}^{lJv}(R, \mathbf{r}, \mathbf{R}) = 2\mu \sum_{v''} \langle v' | \hat{V} | v'' \rangle_J^l f_{v''}^{lJv}(R, \mathbf{r}, \mathbf{R}) \quad (\text{A.8})$$

where new radial functions f now depend parametrically on the space-fixed orientation of \mathbf{R} and \mathbf{r} . Since the interaction potential only depends on $\cos \gamma = \mathbf{R} \cdot \mathbf{r}$, that is, on their relative orientation, the IOS wavefunction now becomes diagonal in the new rotational index j .

A.1 Numerical test calculations on the validity of IOSA in the $\text{H}^+ + \text{CO}$ system

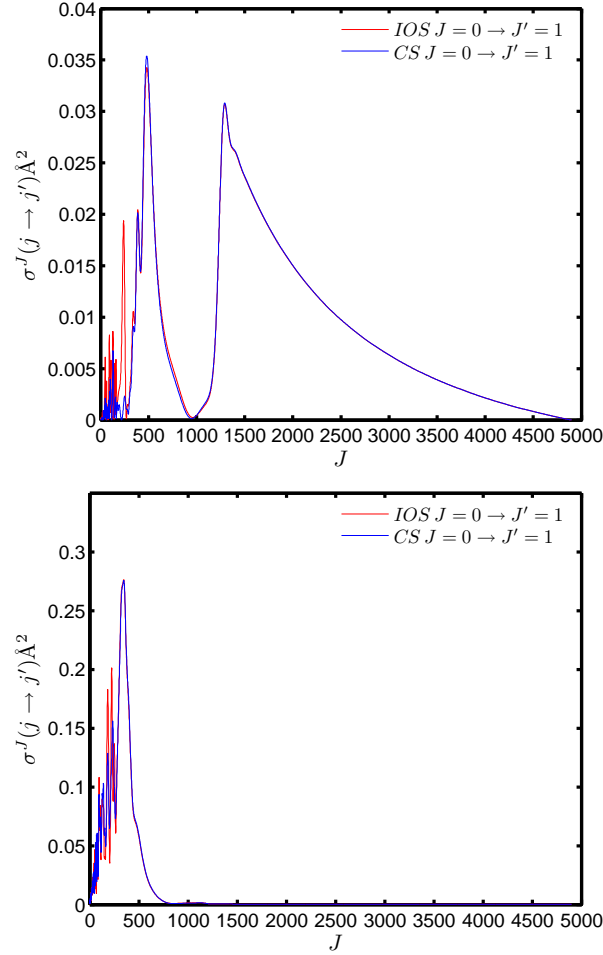


Figure A.1: IOS and CS partial cross sections as a function of the total angular momentum J for the $j = 0 \rightarrow j' = 0$ and $j = 0 \rightarrow j' = 1$ rotational excitations in the $\text{H}^+ + \text{CO}$ system at 28.96 eV.

In order to test the validity of the IOSA against the CS approximation in the $\text{H}^+ + \text{CO}$ system we have taken up the case for atom-rigid rotor (that is, considering CO molecule as a rigid rotor (RR)) collisions involving the GS interaction potential. It is generally expected that the IOSA would work fairly well for higher E_{coll} . Since the experimental results for both the IVE and the VCT channels are available only for $E_{coll} = 28.96$ eV, we have undertaken a numerical test involving the RR calculations at this energy only for the rotational excitations

in the ground vibrational state, $v = 0$ of CO. The general argument here is that if IOSA holds good for the RR in comparison with the corresponding CS calculations, it would also be valid for the vibrating CO molecule. This implies that the VCC-RIOSA would also hold good in comparison with the corresponding VCC-CS calculations. One point of objection that may arise at this point is whether energy sudden approximation would also be valid for the CO⁺ rotational states. However, $E_{coll}(= 28.96 \text{ eV})$ is quite high in value as compared to the ionization potential of CO which is 14 eV. Furthermore, considering the asymptotic limits of the CT channels, H(²S) + CO(X²Σ⁺) and the IVE channel, H⁺ + CO(X¹Σ⁺) which has energy separation of 0.4 eV, the energy sudden approximation is expected to hold good for the system.

Rigid rotor IOS and CS calculations were carried out with $j_{max} = 28$ for $E_{coll} = 28.96$ eV using the MOLSCAT code (Hutson and Green, 1994). For an illustration in Fig. A.1 we compare the partial cross section σ^J for $j = 0 \rightarrow j' = 0$ and $j = 0 \rightarrow j' = 1$ rotational excitations. It can be seen that for large impact parameters (larger J) both the IOS and CS calculations become almost identical while for smaller impact parameters (smaller J) the IOS appears to slightly overestimate the partial cross section values. Nevertheless, overall at this E_{coll} both the IOS and the CS calculations agree fairly well, thus largely validating the IOS approximation against the CS approximation.

Bibliography

- Adhikari, S.** and **G. D. Billing** (2002). Non-Adiabatic Effects in Chemical Reaction: Extended Born-Oppenheimer Equations and Its Applications. *Adv. Chem. Phys.*, **124**, 143.
- Alexander, M. H.** (1982). Rotationally inelastic collisions between a diatomic molecule in a $^2\Pi$ electronic state and a structureless target. *J. Chem. Phys.*, **76**, 5974–5988.
- Alexander, M. H.** and **C. G. Corey** (1986). Collision induced transitions between $^2\Pi$ and $^2\Sigma$ states of a diatomic molecules: Quantum theory and collisional propensity rules. *J. Chem. Phys.*, **84**, 100–113.
- Arthus, M.** and **A. Dalgarno** (1960). *Proc. R. Soc. A*, **256**, 540.
- Baer, M.** (1975). Adiabatic and diabatic representation for atom-molecule collisions: Treatment of the collinear arrangement. *Chem. Phys. Lett.*, **35**, 112–118.
- Baer, M.**, *Molecular Collision Dynamics*. Springer, Berlin, Heidelberg, 1983.
- Baer, M.** (2002a). The Electronic Non-Adiabatic Coupling Term in Molecular System: A Theoretical Approach. *Adv. Chem. Phys.*, **124**, 39–142.
- Baer, M.** (2002b). Introduction to the theory of electronic non-adiabatic coupling terms in molecular systems. *Phys. Rep.*, **358**, 75–142.
- Baer, M.** and **J. A. Beswick** (1979). Electronic transitions in the ion-molecule reaction $(\text{Ar}^+ + \text{H}_2 \longleftrightarrow \text{Ar} + \text{H}_2^+) \longrightarrow \text{ArH}^+ + \text{H}$. *Phys. Rev. A*, **19**, 1559–1567.
- Baer, M.**, **G. Niedner-Schatterburg**, and **J. P. Toennies** (1989). A three-dimensional quantum mechanical study of vibrationally resolved charge transfer processes in $\text{H}^+ + \text{H}_2$ at $E_{cm} = 20\text{eV}$. *J. Chem. Phys.*, **91**, 4182–4196.

- Baer, M., T. Vertesi, G. J. Halasz, A. Vibok, and S. Suhai** (2004). On diabaticization and the topological D-matrix: Theory and numerical studies of the H + H₂ system and the C₂H₂ molecule. *Faraday Discuss.*, **127**, 337–353.
- Balakrishana, N., M. Yan, and A. Dalgarno** (2002). Quantum-Mechanical study of Rotational and Vibrational Transitions in CO induced by H atoms. *Astrophys. J.*, **568**, 443–447.
- Balakrishnan, N., C. Kalyanaraman, and N. Sathyamurthy** (1997). Time-dependent quantum mechanical approach to reactive scattering and related processes. *Phys. Rep.*, **280**, 79–144.
- Balint-Kurti, G. G.** (1975). *International Review of Science (Ser 2)*, **1**, 286–326.
- Baragan, P., L. F. Errea, A. Macias, L. Mendez, I. Rabadan, A. Riera, J. M. Lucas, and A. Aguilar** (2004). Study of *ab initio* molecular data for inelastic and reactive collisions involving the H₃⁺ quasimolecule. *J. Chem. Phys.*, **121**, 11629–11638.
- Ben Houria, A., H. Gritli, N. Jaidane, Z. B. Lakdhar, G. Chambaud, and P. Rosmus** (2001). Electronic states of HNO⁺ and HON⁺. *Chem. Phys.*, **274**, 71–86.
- Bohme, D. K.**, *Interaction Between Ions and Molecules*. P. Ausloos, (Ed.), Plenum, 1975.
- Botschwina, P.**, *Ion and Cluster Ion Spectroscopy and Structure*. Elsevier: Amsterdam, 1989.
- Bruna, P. J.** (1975). Theoretical study of the properties of HCO⁺ at equilibrium. *Astrophys. Lett.*, **16**, 107–113.
- Bruna, P. J., S. D. Peyerimhoff, and R. J. Buenker** (1975). *Ab initio* investigation of HCO⁺ and HOC⁺ molecule ions structure and potential energy surfaces for dissociation in ground and excited states. *Chem. Phys.*, **10**, 323–334.
- Buenker, R. J., G. Hirsch, S. D. Peyerimhoff, P. J. Bruna, J. Römelt, M. Bettendorf, and C. Petrongolo** (1982). *Current Aspects of Quantum Chemistry*, **21**, p.81 Edition. Elsevier, Amsterdam.

- Buhl, D.** and **L. E. Snyder** (1970). Unidentified Interstellar Microwave Line. *Nature*, **228**, 267–268.
- Child, M. S.** (2002). Early Perspectives on Geometric Phase. *Adv. Chem. Phys.*, **124**, 1–38.
- Crutzen, P. J., I. S. A. Isaken,** and **G. C. Reid** (1975). Solar proton events. stratospheric sources of nitric oxide. *Science*, **189**, 457–459.
- Demkov, Y. N.** (1964). *Sov.Phys. JETP*, **18**, 138.
- Derouich, M.** (2006). Collisional depolarization of molecular lines. Application to SiO + H isotropic collisions. *Astronomy Astrophys.*, **449**, 1–7.
- Desouter-Lecomte, M., D. Dehareng,** and **J. C. Lorquet** (1987). Constructing approximately diabatic states from LCAO-SCF-CI calculations. *J. Chem. Phys.*, **86**, 1429–1436.
- Desouter-Lecomte, M., G. Galloy, J. C. Lorquet,** and **M. Vaz Pires** (1979). Nonadiabatic interactions in unimolecular decay. V Conical and Jahn-Teller intersections. *J. Chem. Phys.*, **71**, 3661–3672.
- Dhilip Kumar, T. J.** and **S. Kumar** (2004). Vibrationally inelastic collisions in $H^+ + CO$ system: Comparing quantum calculations with experiments. *J. Chem. Phys.*, **121**, 191–203.
- Dhilip Kumar, T. J., A. Saieswari,** and **S. Kumar** (2006). Elastic and charge transfer processes in $H^+ + CO$ collisions. *J. Chem. Phys.*, **124**, 034314(1)–034314(10).
- Domcke, S., D. R. Yarkony,** and **H. Köppel**, *Conical intersections: Electronic structure, dynamics and spectroscopy*. World Scientific, Singapore, 2004.
- Domcke, W.** and **C. Woywod** (1993). Direct construction of diabatic states in the CASSCF approach. Application to the conical intersection of the 1A_2 and 1B_1 excited states of ozone. *Chem. Phys. Lett.*, **216**, 362–368.
- Domcke, W., C. Woywod,** and **M. Stengle** (1994). Diabatic CASSCF orbitals and wavefunctions. *Chem. Phys. Lett.*, **226**, 257–262.

- Dunning, J. T. H.** (1989). Gaussian basis sets for use in correlated molecular calculations. I. the atoms boron through neon and hydrogen. *J. Chem. Phys.*, **90**, 1007–1023.
- Galloy, G.** and **J. C. Lorquet** (1977). Nonadiabatic interactions in unimolecular decay. III Selection and propensity rules for polyatomic molecules. *J. Chem. Phys.*, **67**, 4672–4680.
- Gao, R. S., L. K. Johnson, C. L. Hakes, K. A. Smith, and R. F. Stebbings** (1990). Collisions of kilo-electron-volt H^+ and He^+ with molecules at small angles: Absolute differential cross sections for charge transfer. *Phys. Rev. A*, **41**, 5929–5933.
- General Discussion** (2004). *Faraday Discuss.*, **127**, 81–121.
- Gianturco, F. A.**, *The transfer of molecular energies by collisions*. Springer, Berlin, 1979.
- Gianturco, F. A., U. Gierz, and J. P. Toennies** (1981). Anomalous vibrational excitation of O_2 in collisions with protons at 10 eV when compared with N_2 , CO and NO. *J. Phys. B: At. Mol. Phys.*, **14**, 667–677.
- Gianturco, F. A. and S. Kumar** (1995a). Dynamics of vibrationally inelastic collisions in $H^+ - H_2$: comparing quantum calculations with experiments. *Chem. Phys.*, **196**, 485–498.
- Gianturco, F. A. and S. Kumar** (1995b). Selective efficiency of vibrational excitations in ion-molecule collisions: A comparison of behaviour for $H^+ - H_2$ and $H^- - H_2$. *J. Chem. Phys.*, **103**, 2940–2948.
- Gianturco, F. A., S. Kumar, T. Ritschel, R. Vetter, and L. Zülicke** (1997). Interaction anisotropy and vibrational excitation in proton scattering from $N_2(^1\Sigma_g^+)$. *J. Chem. Phys.*, **107**, 6634–6645.
- Gianturco, F. A., S. Kumar, and F. Schneider** (1996). Correlated electronic potential energy surfaces for proton interactions with N_2 . *Chem. Phys.*, **211**, 33–46.
- Gianturco, F. A., U. T. Lamanna, and D. Ignazzi** (1980b). Proton-molecule collisional interactions: I. the $H^+ + CO(^1\Sigma^+)$ potential energy surface. *Chem. Phys.*, **48**, 387–397.

- Gianturco, F. A., A. Palma, E. Semprini, F. Stefani, and M. Baer** (1990). Coupled quantum treatment of vibrationally inelastic and vibronic charge transfer in proton-O₂ collisions. *Phys. Rev. A*, **42**, 3926–3939.
- Gianturco, F. A. and V. Staemmler**, *Intermolecular Forces*. pullman, Reidel, Dordrecht., 1981.
- Grimbert, D., B. Lassier-Givers, and V. Sidis** (1988). Model potentials and related diabatic states for the H⁺ + O₂ collisional system. *Chem. Phys.*, **124**, 187–204.
- Grunenberg, J., R. Streubel, G. V. Frantzius, and W. Marten** (2003). The strongest bond in the universe? Accurate calculation of compliance matrices for the ions N₂H⁺, HCO⁺ and HOC⁺. *J. Chem. Phys.*, **119**, 165–169.
- Hagstrum, H. D. and J. T. Tate** (1941). Ionisation and Dissociation of Diatomic Molecules by Electron Impact. *Phys. rev.*, **59**, 354–370.
- Handy, N. C. and A. M. Lee** (1996). The adiabatic approximation. *Chem. Phys. Lett.*, **252**, 425–430.
- Herbst, E.** (2001). The chemistry of interstellar space. *Chem. Soc. Rev.*, **30**, 168–176.
- Hermann, V., H. Schmidt, and F. Linder** (1978). Rotational and vibrational excitations in low-energy H⁺ + H₂ scattering experiments. *J. Phys. B.*, **11**, 493–506.
- Heumann, B. and R. Schinke** (1994). Emission spectroscopy of dissociating H₂S: Influence of nonadiabatic coupling. *J. Chem. Phys.*, **101**, 7488–7499.
- Heumann, B., K. Weide, R. Duren, and R. Schinke** (1992). Non-adiabatic effects in the photodissociation of H₂S in the first absorption band: An *ab initio* study. *J. Chem. Phys.*, **98**, 5508–5525.
- Hirsch, G., P. J. Bruna, R. J. Buenker, and S. D. Peyerimhoff** (1980). Nonadiabatic coupling matrix elements $\left\langle \psi^z \frac{\partial}{\partial q} \psi^\beta \right\rangle$ for large CI wavefunctions. *Chem. Phys.*, **45**, 335–347.

- Hirsch, G., R. J. Buenker, and C. Petrongolo** (1990). Part II: Non-adiabatic coupling between the two lowest $^2A'$ states and the construction of a diabatic representation. *Mol. Phys.*, **70**, 835–848.
- Hopkins, A. C., N. K. Holbrook, K. Yates, and I. G. Csizmadia** (1968). Theoretical study on the proton affinity of small molecules using Gaussian basis sets in the LCAO-MO-SCF framework. *J. Chem. Phys.*, **49**, 3596–3601.
- Hougen, J. T.**, *The Calculations of Rotational Energy Levels and Rotational Line Intensities in Diatomic Molecules (NBS Monograph 115)*. Washington DC: National Bureau of Standards, 1970.
- Huang, X. and T. J. Lee** (2008). A procedure for computing accurate *ab initio* quartic force fields: Application to HO_2^+ and H_2O . *J. Chem. Phys.*, **129**, 044312(1)–044312(14).
- Huber, K. P. and G. Herzberg**, *Molecular Spectra and Molecular Structure IV. Constants of Diatomic Molecules*. D. Van Nostrand Ccompany, New York, 1979.
- Hutson, J. M. and S. Green**, *MOLSCAT Computer code, Version 14 Project No. 6*. Engineering and Physical Sciences Research Council, UK, 1994.
- Jasper, A. W., C. Zhu, S. Nangia, and D. G. Truhlar** (2004). Introductory lecture: Non-adiabatic effects in chemical dynamics. *Faraday Discuss*, **127**, 1–22.
- Jenson, F.**, *Introduction to Computational Chemistry*. John Wiley and Sons, Chichester, 1999.
- Khare, V.** (1977). On the equivalence between the space fixed and body fixed formulations of the j_z -conserving approximation. *J. Chem. Phys.*, **67**, 3897–3900.
- Kimura, M., J. P. Gu, G. Hirsch, R. J. Buenker, and P. C. Stancil** (2000). Electron capture in collisions of protons with CO molecules in the keV region: The steric effect. *Phys. Rev. A*, **61**, 032708(1)–032708(9).
- Klemperer, W.** (1970). Carrier of the Interstellar 89.190 Ghz Line. *Nature*, **227**, 1230.

- Knowles, P. J. and H.-J. Werner** (1985). An efficient second-order MCSCF method for long configuration expansions. *Chem. Phys. Lett.*, **115**, 259–267.
- Knowles, P. J. and H.-J. Werner** (1988). An efficient method for the evaluation of coupling coefficients in configuration interaction calculations. *Chem. Phys. Lett.*, **145**, 514–522.
- Knowles, P. J. and H.-J. Werner** (1992). Internally contracted multiconfiguration-reference configuration interaction calculation for excited states. *Theor. Chim. Acta.*, **84**, 95–103.
- Köppel, H.** (2004). Regularized diabatic states and quantum dynamics on intersecting potential energy surfaces. *Faraday Discuss.*, **127**, 35–47.
- Köppel, H., W. Domcke, and L. S. Cederbaum** (1984). Multimode molecular dynamics beyond the born oppenheimer approximation. *Adv. Chem. Phys.*, **57**, 59–246.
- Kouri, D. J.**, *Atom-Molecule Collision Theory*. Plenum, New York, 1979.
- Kozin, I. N. and P. Jensen** (1994). Fourfold clusters of Rovibrational Energy Levels for H₂S Studied with a Potential Energy Surface Derived from Experiment. *J. Mol. Spec.*, **163**, 483–509.
- Krutein, J. and F. Linder** (1979). Measurements of vibrational excitation of N₂, CO and NO by low energy proton impact. *J. Chem. Phys.*, **71**, 599–604.
- Landau, L. D.** (1932). *Phys. Z. Sowjetunion*, **2**, 46.
- Lin, C. Y., P. C. Stancil, Y. Li, J. P. Gu, H. P. Liebermann, R. J. Buenker, and M. Kimura** (2007). Vibrationally resolved charge transfer for proton collision with CO and H collision with CO⁺. *Phys. Rev. A*, **76**, 012702(1)–012702(10).
- Loew, G. H., D. S. Berkowitz, and S. Chang** (1978). Candidate interstellar molecules formed from ion-molecule reaction of no. *Astrophys. J.*, **219**, 458–466.
- Ma, N. L., B. J. Smith, and L. Radom** (1992). Refined calculations of the structures and stabilities of the formyl (HCO⁺) and isoformyl (COH⁺) cations. *Chem. Phys. Lett.*, **197**, 573–580.

- Mahapatra, S.** and **H. Köppel**, Workshop on nonadiabatic effects. School of Chemistry, University of Hyderabad, 2002.
- Manaa, D. R.** and **D. Yarkony** (1992). On the intersection of potential energy surfaces in charge transfer reactions: A crossing seam for two states of the same symmetry in the reaction $\text{H}^+ + \text{NO}(X^2\Pi) \rightarrow \text{H}(^2\text{S}) + \text{NO}^+(X^1\Sigma^+)$. *J. Chem. Phys.*, **97**, 715–717.
- Marian, C., P. J. Bruna, R. J. Buenker,** and **S. D. Peyerimhoff** (1977). Comparison of the structure and spectra of the HNO^+ and NOH^+ ions using *ab initio* SCF and CI methods. *Mol. Phys.*, **33**, 63–74.
- Martin, J. M. L., P. R. Taylor,** and **T. J. Lee** (1993). Accurate *ab initio* quartic force fields for the ions HCO^+ and HOC^+ . *J. Chem. Phys.*, **99**, 286–292.
- McGuire, P.** (1976). Coupled states approximation study of inelastic H^+ - H_2 collisions at 3.7 eV. *J. Chem. Phys.*, **65**, 3275–3279.
- McLean, A. D., G. H. Loew,** and **D. S. Berkowitz** (1978). HNO^+ and HON^+ Potential energy surfaces for the lowest two electronic states including the barrier to isomerization. *Mol. Phys.*, **36**, 1359–1372.
- Mead, A.** and **D. Truhlar** (1982). Conditions for the definition of a strictly diabatic electronic basis for molecular systems. *J. Chem. Phys.*, **77**, 6090–6098.
- Mizushima, M.**, *The Theory of Rotating Diatomic Molecules*. Wiley, New York, 1975.
- Mladenović, M.** and **S. Schmatz** (1998). Theoretical study of the rovibrational energy spectrum and the numbers and densities of bound vibrational states for the system $\text{HCO}^+/\text{HOC}^+$. *J. Chem. Phys.*, **109**, 4456–4470.
- Mourik, T. V., T. H. J. Dunning,** and **K. A. Peterson** (2000). *Ab initio* characterization of the HCO^x ($x = -1, 0, +1$) species: Structures, vibrational frequencies, CH bond dissociation energies and HCO ionization potential and electron affinity. *J. Phys. Chem. A*, **104**, 2287–2293.

- Mulliken, R. S.** and **W. C. Ermler**, *Diatomic Molecules*. Academic, New York, 1977.
- Nakamura, H.**, *Dynamics of Molecules and Chemical Reactions*. Marcel Dekker, New York, 1996.
- Niedner, G., M. Noll, J. P. Toennies, and C. Schiler** (1987). Observation of vibrationally resolved charge transfer in $H^+ + H_2$ at $E_{cm} = 20$ eV. *J. Chem. Phys.*, **87**, 2685–2694.
- Niedner-Schatteburg, G. and J. P. Toennies** (1992). Proton energy loss spectroscopy as a state-to-state probe of molecular dynamics. *Adv. Chem. Phys.*, **82**, 553–646.
- Noll, M. and J. P. Toennies** (1986). Vibrational state resolved measurements of differential cross sections for $H^+ + O_2$ charge transfer collisions. *J. Chem. Phys.*, **85**, 3313–3325.
- Pacher, T., L. S. Cederbaum, and H. Köppel** (1988). Approximately diabatic states from block diagonalization of the electronic Hamiltonian. *J. Chem. Phys.*, **89**, 7367–7381.
- Pacher, T., L. S. Cederbaum, and H. Köppel** (1993). Adiabatic and Quasidiabatic States in a Gauge Theoretical Framework. *Adv. Chem. Phys.*, **84**, 293.
- Pack, R.** (1974). Space-fixed vs body-fixed axes in atom-diatom molecule scattering. Sudden approximations. *J. Chem. Phys.*, **60**, 633–639.
- Parker, G. and R. T. Pack** (1978). Rotationally and vibrationally inelastic scattering in the rotational IOS approximation. Ultrasimple calculation of total (differential, integral, and transport) cross sections for nonspherical molecules. *J. Chem. Phys.*, **68**, 1585–1601.
- Perić, M., M. Mladenović, C. M. Marian, and P. J. Bruna** (1982). A theoretical study of the vibronic structure in the electronic spectrum of HNO^+ . *Chem. Phys. Lett.*, **88**, 547–552.
- Petrongolo, C., G. Hirsch, and R. J. Buenker** (1990). Diabatic representation of the $\tilde{A}^2A_1\tilde{B}^2B_2$ conical intersection in NH_2 . *Mol. Phys.*, **70**, 825–834.

- Puzzarini, C., R. Tarroni, P. Palmieri, S. Carter, and L. Dore** (1996). Accurate *ab initio* prediction of equilibrium geometry of HCO^+ and of rovibrational energy levels of DCO^+ . *Mol. Phys.*, **87**, 879–898.
- Raine, G. P. and H. F. Schaefer III** (1984). The HO_2^+ molecular ion. Geometrical structure and vibrational frequencies. *J. Chem. Phys.*, **80**, 319–324.
- Reddy, R. R. and R. Viswanath** (1990). Estimation of the Dissociation Energy of CO^+ from Spectroscopic Data. *J. Astrophys. Astr.*, **11**, 67–72.
- Robbe, J. M., M. Monnerville, G. Chambaud, P. Rosmus, and P. J. Knowles** (2000). Theoretical spectroscopic data of the HO_2^+ ion. *Chem. Phys.*, **252**, 9–16.
- Romero, T., A. Aguilar, and F. X. Gadea** (1999). Towards the *ab initio* determination of strictly diabatic states, study for $(\text{NaRb})^+$. *J. Chem. Phys.*, **110**, 6219–6228.
- Rosen, N. and C. Zener** (1932). Double Stern-Gerlach Experiment and Related Collision Phenomena. *Phys. Rev.*, **40**, 502–507.
- Saieswari, A. and S. Kumar** (2007a). *Ab initio* study of $\text{H}^+ + \text{H}_2$: Elastic/inelastic and charge transfer processes. *Chem. Phys. Lett.*, **449**, 358–364.
- Saieswari, A. and S. Kumar** (2007b). Non-adiabatic collisions in $\text{H}^+ + \text{O}_2$ system: An *ab initio* study. *J. Chem. Sci.*, **119**, 423–431.
- Saieswari, A. and S. Kumar** (2007c). Vibrational inelastic and charge transfer processes in $\text{H}^+ + \text{H}_2$ system: An *ab initio* study. *J. Chem. Phys.*, **127**, 214304(1)–214304(10).
- Saieswari, A. and S. Kumar** (2008a). *Ab initio* potential energy surfaces and nonadiabatic collision dynamics in $\text{H}^+ + \text{O}_2$ system. *J. Chem. Phys.*, **128**, 154325(1)–154325(10).
- Saieswari, A. and S. Kumar** (2008b). *Ab initio* potential energy surfaces and nonadiabatic interactions in the $\text{H}^+ + \text{NO}$ collision system. *J. Chem. Phys.*, **128**, 124305(1)–124305(11).

- Saieswari, A. and S. Kumar** (2008c). Elastic/inelastic and charge transfer collisions of $H^+ + H_2$ at collision energies of 4.67, 6, 7.3, 10 eV. *J. Chem. Phys.*, **128**, 064301(1)–064301(11).
- Saieswari, A. and S. Kumar** (2008d). Quantum dynamics of inelastic excitations and charge transfer processes in the $H^+ + NO$ collisions. *J. Chem. Phys.*, **128**, 124306(1)–124306(7).
- Saieswari, A. and S. Kumar** (2009). Quantum dynamics of vibrational excitations and vibrational charge transfer processes in $H^+ + O_2$ collisions at collision energy 23 eV. *J. Chem. Sci.*, **121**, 797–803.
- Schinke, R., M. Dupuis, and W. A. Lester** (1980). Proton- H_2 scattering on an *ab initio* CI potential energy surface. i. Vibrational excitation at 10 eV. *J. Chem. Phys.*, **72**, 3909–3915.
- Schinke, R. and P. McGuire** (1978a). Combined rotationally sudden and vibrationally exact quantum treatment of proton- H_2 collisions. *Chem. Phys.*, **31**, 391–412.
- Schinke, R. and P. McGuire** (1978b). On the sudden centrifugal potential in the space-fixed system: Dependence of proton- H_2 cross sections on the choice of angular momentum parameter. *Chem. Phys.*, **28**, 129–145.
- Schmidt, H., V. Hermann, and F. Linder** (1976). Spectroscopy of low-energy $H^+ + H_2$ collisions: Rotational and vibrational excitations of H_2 . *Chem. Phys. Lett.*, **41**, 365–369.
- Schmidt, H., V. Hermann, and F. Linder** (1978). Crossed beam measurements of rotational quantum transitions in low-energy $H^+ - H_2$ scattering. *J. Chem. Phys.*, **69**, 2734–2738.
- Schneider, F., L. Zülicke, F. DiGiacomo, F. A. Gianturco, I. Páidarová, and R. Polák** (1988). DIM model calculations for (O_2H^+) interaction potentials. *Chem. Phys.*, **128**, 311–320.
- Sidis, V.** (1992). Diabatic potential energy surfaces for charge-transfer processes. *Adv. Chem. Phys.*, **82**, 73.

- Sidis, V., D. Grimbert, M. Sizun, and M. Baer** (1989). Quantal IOS calculations of differential cross sections for vibrational excitations and vibronic charge transfer in $\text{H}^+ + \text{O}_2$ collisions. *Chem. Phys. Lett.*, **163**, 19–22.
- Simah, D., B. Hartke, and H.-J. Werner** (1999). Photodissociation dynamics of H_2S on new coupled *ab initio* potential energy surface. *J. Chem. Phys.*, **111**, 4523–4534.
- Smith, F. T.** (1969). Diabatic and adiabatic representations for atomic collision problems. *Phys. Rev.*, **179**, 111–123.
- Staemmler, V. and F. A. Gianturco** (1985). Adiabatic SCF potential energy curves relevant to proton-oxygen molecular collisions. *Int. J. Quant. Chem.*, **28**, 553–564.
- Stogryn, D. E. and A. P. Stogryn** (1966). Molecular multipole moments. *Mol. Phys.*, **11**, 371–393.
- Stuckelberg, C. G.** (1932). *Helv. Phys. Acta.*, **5**, 369.
- Top, Z. H. and M. Baer** (1977). Incorporation of electronically nonadiabatic effects into bimolecular reactive systems. II. The collinear ($\text{H}_2 + \text{H}^+$, $\text{H}_2^+ + \text{H}$) system. *Chem. Phys.*, **25**, 1–18.
- Tully, J. C. and R. K. Preston** (1971). Trajectory surface hopping approach to nonadiabatic molecular collisions: The reaction of H^+ with D_2 . *J. Chem. Phys.*, **55**, 562–572.
- Udseth, H., C. F. Giese, and W. R. Gentry** (1974). Rotational excitation in the small angle scattering of protons from diatomic molecules. *J. Chem. Phys.*, **60**, 3051–3056.
- Ushakov, V., K. Nobusada, and V. I. Osherov** (2001). Electronically nonadiabatic transitions in a collinear $\text{H}_2 + \text{H}^+$ system: Quantum mechanical understanding and comparison with a trajectory surface hopping method. *Phys. Chem. Chem. Phys.*, **3**, 63–69.
- van Lenthe, J. H. and P. J. A. Ruttink** (1978). *Ab initio* calculations on the three lowest states of HO_2^+ . *Chem. Phys. Lett.*, **56**, 20–24.

- Varandas, A. J. C. and H. Szichman** (1998). A three-dimensional quantum mechanical study of the O + HO₂ atmospheric reaction: Infinite order sudden approximation and novel adiabatic approaches vs quasiclassical trajectories. *Chem. Phys. Lett.*, **295**, 113–121.
- Vazquez, G. J., R. J. Buenker, and S. D. Peyerimhoff** (1986). The electronic structure of HO₂⁺ an MRD-CI study. *Mol. Phys.*, **59**, 291–316.
- Vertesi, T., E. Bene, A. Vibok, G. J. Halasz, and M. Baer** (2005). N-state adiabatic-to-diabatic transformation angle: Theory and application. *J. Phys. Chem. A*, **109**, 3476–3484.
- Vibok, A., G. J. Halasz, T. Vertesi, S. Suhai, M. Baer, and J. P. Toennies** (2003). *Ab initio* conical intersections for the Na + H₂ system: A four-state study. *J. Chem. Phys.*, **119**, 6588–6596.
- Viegas, L. P., A. Alijah, and A. J. C. Varandas** (2007). Accurate *ab initio* based multi-sheeted double many-body expansion potential energy surface for the three lowest electronic singlet states of H₃⁺. *J. Chem. Phys.*, **126**, 074309(1)–074309(9).
- Wahlgren, U., P. K. Pearson, and H. F. Schaefer III** (1973). *Nature Phys. Sci.*, **246**, 4.
- Werner, H. J., B. Follmeg, and M. H. Alexander** (1988). Adiabatic and diabatic potential energy surfaces for collisions of CN (X²Σ⁺, A²Π) with He. *J. Chem. Phys.*, **89**, 3139–3151.
- Werner, H. J., B. Follmeg, M. H. Alexander, and P. Lemoine** (1989). Quantum scattering studies of electronically inelastic collisions of CN (X²Σ⁺, A²Π) with He. *J. Chem. Phys.*, **91**, 5425–5439.
- Werner, H.-J. and P. J. Knowles** (1985). A second order multiconfiguration SCF procedure with optimum convergence. *J. Chem. Phys.*, **82**, 5053–5063.
- Werner, H.-J. and P. J. Knowles** (1988). An efficient internally contracted multiconfiguration-reference configuration interaction method. *J. Chem. Phys.*, **89**, 5803–5814.

Werner, H. J., P. J. Knowles, M. Schütz, R. Lindh, P. Celani, T. Korona, G. Rauhut, F. R. Manby, R. D. Amos, A. Bernhardsson, A. Berning, D. L. Cooper, K. J. O. Deegan, A. J. Dobbyn, F. Eckert, C. Hampel, G. Hetzer, A. W. Lloyd, S. J. McNicholas, W. Meyer, M. E. Mura, A. Nicklaß, P. Palmieri, R. Pitzer, U. Schumann, H. Stoll, A. J. Stone, R. Tarroni, and T. Thorsteinsson (2002). MOLPRO is a package of *ab initio* programs.

Werner, H. J. and W. Meyer (1981). MCSCF study of the avoided curve crossing of the two lowest $^1\Sigma^+$ states of LiF. *J. Chem. Phys.*, **74**, 5802–5807.

Woods, R. C. (1988). *Phil. Trans. R. Soc. Lond. A*, **324**, 141.

Woods, R. C., T. A. Dixon, R. J. Saykally, and P. G. Szanto (1975). Laboratory microwave spectrum of HCO^+ . *Phys. Rev. Lett.*, **35**, 1269–1272.

Worth, G. A. and M. A. Robb (2002). Applying Direct Molecular Dynamics to Non-Adiabatic Systems. *Adv. Chem. Phys.*, **124**, 355–431.

Yamaguchi, Y., J. C. A. Richards, and H. F. Schaefer III (1994). High level *ab initio* study on the ground state potential energy hypersurface of the HCO^+ - HOC^+ system. *J. Chem. Phys.*, **101**, 8945–8954.

Yarkony, D. (1989). Nonadiabatic effects in the vicinity of multiple surface crossings. Evaluation of derivative couplings with respect to rotational and internal degrees of freedom. Application to the charge transfer reaction $\text{H}^+ + \text{NO} \rightarrow \text{H} + \text{NO}^+$. *J. Chem. Phys.*, **90**, 1657–1665.

Zener, C. (1932). *Proc. R. Soc. London: Ser. A.*, **137**, 696.

Zhang, Y. C., Z. H. Zhang, D. J. Kouri, and M. Baer (1987). Infinite order sudden approximation treatment of the $\text{H} + \text{D}_2 \rightarrow \text{HD} + \text{D}$ reactions. *Chem. Phys.*, **114**, 267–272.

LIST OF PAPERS BASED ON THESIS

1. **George F. and S. Kumar** Diabatic Potential Energy Surface of $H^+ + CO$. *J. Chem. Sci.*, **119**, 409-415, (2007).
2. **George F., T. J. DhilipKumar and S. Kumar** Scattering resonances in low-energy $H^+ + CO$ collisions. *Indian. J. Phys.*, **81(9)**, 889-900, (2007).

LIST OF PRESENTATIONS IN CONFERENCES

1. Study of Scattering Resonances in $H^+ + CO$ system, **F. George** and **S. Kumar** Discussion meeting on Spectroscopy and Dynamics of Molecules and Clusters, The International Centre Goa, March 30 - April 1, 2006.
2. The bound and long-lived scattering states (resonances) in $H^+ + CO$ system, **F. George** and **S. Kumar** Annual IIT Madras Chemistry Symposium & The first Mid-Year Meeting of the Chemical Research Society of India, IITM Chennai-36, July 12-13, 2006.
3. Elastic and Charge transfer collision in $H^+ + CO$ system, **F. George** and **S. Kumar** Theoretical Chemistry Symposium (TCS 2006), Bharathidhasan University Thiruchirappalli, December 11-13th, 2006.
4. Diabatic Potential Energy Surface of $H^+ + CO$ system, **F. George** and **S. Kumar** National Symposium on Quantum Chemistry, Soft Computation & Optimization, IACS Kolkatta, April 04-05, 2008.
5. Quantum dynamics of proton collisions with CO molecules, **F. George** and **S. Kumar** American Conference on Theoretical Chemistry, Northwestern University Evanston Illinois USA, July 19-23, 2008.

DOCTORAL COMMITTEE

GUIDE

Prof. Sanjay Kumar

Department of chemistry

MEMBERS

Prof. N. Chandrakumar

Department of chemistry

Prof. A. K. Mishra

Department of chemistry

Prof. P. B. Bisht

Department of Physics

Prof. C. Vijayan

Department of Physics

CURRICULUM VITAE

1. Name : **F George Densingh Xavier**
2. Date of Birth : 07-05-1973
3. Educational Qualification :
1993 : B.Sc in Chemistry from Manonmaniam Sundaranar University, Tirunelveli, Tamil Nadu, India.
1998 : M.Sc in Chemistry from Bharathidasan University, Trichirapalli, Tamil Nadu, India.
2009 : Ph.D in Chemistry from Indian Institute of Technology, Madras, India